The $t\bar{t}$ production
in pp collisions at $\sqrt{s} = 14$ TeV

Lars Sonnenschein

III.Physikalisches Institut der Technischen Hochschule Aachen

The $t\bar{t}$ production
in pp collisions at $\sqrt{s} = 14\,\text{TeV}$

Von der Fakultät für Mathematik, Informatik und Naturwissenschaften
der Rheinisch-Westfälischen Technischen Hochschule Aachen
zur Erlangung des akademischen Grades eines Doktors
der Naturwissenschaften genehmigte Dissertation

vorgelegt von
Diplom-Physiker
Lars Sonnenschein
aus Wuppertal

Berichter: Universitätsprofessor Dr. G. Flügge
Universitätsprofessor Dr. W. Bernreuther
Tag der mündlichen Prüfung: 23. Mai 2001

Diese Dissertation ist in der Hochschulbibliothek online verfügbar

Abstract

The proton proton collider LHC will operate at $\sqrt{s} = 14\,\text{TeV}$ center of mass energy which gives rise to a cross section of about $800\,\text{pb}$ for the production of $t\bar{t}$ events. This leads, already for a start-up luminosity of $\mathcal{L} = 10^{33}\,\text{cm}^{-2}\text{s}^{-1}$, to a huge production rate of $8 \cdot 10^6$ $t\bar{t}$ events per year, corresponding to an integrated luminosity of $10\,\text{fb}^{-1}$. Simulations including the CMS detector response show the expected precision in the determination of the top quark mass to be $900\,\text{MeV}$. Moreover, the measurement of the W boson helicity with an expected uncertainty at a percent level and the measurement of the $t\bar{t}$ spin correlation with an expected uncertainty below $15\,\%$ will allow to test the standard model interactions. The prospect of observing a heavy Higgs boson in the $t\bar{t}$ decay channel is investigated. A non standard model Higgs boson without coupling to vector bosons, like the supersymmetric pseudo scalar Higgs, with a mass not too far above $400\,\text{GeV}$ can be discovered (above the 5σ threshold) within less than half a year running at high luminosity ($\mathcal{L} = 10^{34}\,\text{cm}^{-2}\text{s}^{-1}$) under the assumption that the shape of the invariant mass spectrum and the cross section of the $t\bar{t}$ background is known to the percent level.

Kurzfassung

Der Proton-Proton-Speicherring LHC wird bei einer Schwerpunktsenergie von $\sqrt{s} = 14\,\text{TeV}$ betrieben werden. Der Wirkungsquerschnitt für die Produktion von $t\bar{t}$-Ereignissen beträgt dabei etwa $800\,\text{pb}$. Dies führt bereits bei einer anfänglichen Luminosität von $\mathcal{L} = 10^{33}\,\text{cm}^{-2}\text{s}^{-1}$ zu der großen Produktionsrate von $8 \cdot 10^6$ $t\bar{t}$ Ereignissen pro Jahr, entsprechend einer integrierten Luminosität von $10\,\text{fb}^{-1}$. Aufgrund von Simulationen, die die Eigenschaften des CMS-Detektors berücksichtigen, ist mit einer Präzision von $900\,\text{MeV}$ bei der Bestimmung der Top-Quarkmasse zu rechnen. Außerdem erlaubt die Messung der W-Bosonenhelizität mit einer erwarteten Präzision im Prozentbereich und die Messung der $t\bar{t}$-Spinkorrelation mit einer erwarteten Präzision von besser als $15\,\%$ die Wechselwirkungen im Standardmodell zu testen. Die Aussicht, ein schweres Higgs-Boson im $t\bar{t}$-Zerfallskanal zu beobachten, wird ebenfalls untersucht. Ein Higgs-Boson ausserhalb des Standardmodells, ohne Kopplung an Vektorbosonen, wie ein supersymmetrisches pseudoskalares Higgs mit einer Masse nicht sehr viel grösser als $400\,\text{GeV}$ kann innerhalb eines halben Jahres und schon eher bei hoher Luminosität ($\mathcal{L} = 10^{34}\,\text{cm}^{-2}\text{s}^{-1}$) entdeckt werden (oberhalb der 5σ Schwelle). Voraussetzung dafür ist die genaue Kenntnis der Form des invarianten Massenspektrums und des Wirkungsquerschnittes des $t\bar{t}$-Untergrundes im Prozentbereich.

Contents

Introduction

One of the outstanding merits of modern particle physics, especially relevant for collider physics, is the theory of strong interactions, Quantum Chromodynamics (QCD). It describes the interactions between quarks and gluons very successfully and provides an explanation for the observation of hadronic bound states. Particle colliders with their huge center of mass energies probe the structure of matter at shortest distances. At these scales, the strong, the weak and the electromagnetic interactions can be studied in detail. The quantitative understanding of QCD is very important at hadron colliders such as the LHC to fully exploit its physics potential. A primary goal of collider experiments at the LHC is the discovery of new heavy particles and new phenomena. Therefore the precise measurement of production rates of known heavy particles and their comparison to predictions of the theory is very important.

At present the information about c, b quarks and hadronic bound states containing them, comes mostly from the electron positron annihilation, since the signal to background ratio is better at electron positron colliders. The disadvantage of hadronically produced heavy quarks is the difficulty of distinguishing them amongst a large background of other hadrons. However, for certain measurements this is compensated by the large production rate of heavy quarks at hadron colliders.

Until a next linear collider (NLC) based on lepton beams is constructed, the production of the top quark will be reserved to hadron colliders. At the LHC about $8\,000\,000$ $t\bar{t}$ events are expected per $10\,\text{fb}^{-1}$ of integrated luminosity. This huge amount of statistics allows a precise investigation of the top quark and $t\bar{t}$ production without excessive interference from background processes.

The content is structered according to the following sequence:

In chapter 1 the collider and the detector, as currently implemented in the simulations, are described in some detail. Chapter 2 gives a short status of current experimental results and the motivation to improve existing measurements. The theoretical framework necessary for the understanding of the next two chapters is introduced. The theory necessary for the chapters 5 and 6 is postponed until their occurrence, since it relies on the following chapter which in turn relies on the present chapter. In chapter 3 the software tools and methods used are presented. After Monte-Carlo event generators have been introduced the implementation of matrix elements is discussed in detail. An extensive debate of parton distributions, generated with the implemented and the default matrix elements follows. In addition the different $t\bar{t}$ production mechanisms are compared. Chapter 4

demonstrates the determination of the top quark mass in the semileptonic decay channel of the $t\bar{t}$ production. A comprehensive survey of systematic uncertainties is given subsequent to the selection and reconstruction of the $t\bar{t}$ events. The precision is expected to be significantly better than what can be achieved at existing experiments. The determination of the W boson helicity in the semileptonic decay channel is covered in chapter 5. The $t\bar{t}$ production offers the opportunity to investigate the helicity states of an on-shell W boson coming from a polarized top quark. In chapter 6 the $t\bar{t}$ spin correlation is investigated in the dileptonic $t\bar{t}$ decay channel. The implemented matrix elements, which include the spin correlation in contrast to the default matrix elements of the Monte-Carlo event generators have been used. The scenario of a neutral Higgs boson with a mass just above the $t\bar{t}$ production threshold is presented in chapter 7. The observability of such a Higgs boson is investigated with the $t\bar{t}$ invariant mass spectrum based on the reconstruction of events in the semileptonic decay channel.

The unit system with $\hbar = c = 1$ typically used in elementary particle physics is applied throughout this thesis.

1

The CMS experiment at the LHC

In 1954 CERN[1] was founded as one of Europe's first joint ventures at Geneva. Today the laboratory for high energy physics can look back on a long tradition of experiments with international collaborations. Two of the most prominent are the UA1 and UA2 experiments at the S$\bar{\text{p}}$pS[2] where the $W^{\pm}$ bosons and the Z^0 boson were discovered in 1983 [UA183a], [UA283a], [UA183b], [UA283b]. From 1989 to 2000 LEP[4] has provided precise measurements in the electroweak and the strong sector including the precise determination of the W and Z boson masses and the measurement of running α_s.

1.1 The Large Hadron Collider

The LHC[5] will be the biggest hadron collider in the world at the planned beginning of operation in 2005. It will collide protons, which are brought to collision at a center of mass energy of $\sqrt{s} = 14\,\text{TeV}$. The facility will be housed in the already existing LEP tunnel with a circumference of $26\,658.88\,\text{m}$, taking the nominal beam position as measure. Two separate beam channels, with fields equal in strength but opposite in directions, are required. Superconducting magnets containing the two beam channels and their corresponding sets of coils inserted in a unique structure with a single cryostat are foreseen [Per86, Ler93]. The magnets are cooled with superfluid helium at a temperature of 1.9K to allow an operating magnetic field of $8.4\,\text{T}$.

To supply the LHC with pre-accelerated protons, existing CERN facilities are used [Bro93]. After upgrading the source and the RF[6] systems of the Linac[7] 2, protons of $50\,\text{MeV}$ energy with an intensity of $180\,\text{mA}$ in pulses of some $20\,\mu\text{s}$ duration will be delivered and the PS[8] Booster will be modified to prepare the proton beam for injection into the PS. One possible scenario for the modification is to upgrade the output energy from 1 to $1.4\,\text{GeV}$. Two new RF systems will be placed in the PS, one working at

---

[1]**C**entre **E**uropéen pour la **R**echerche **N**ucléaire
[2]**S**uper $\bar{\text{p}}$ **p** **S**ynchrotron, which was later transformed to the SPS[3]
[3]**S**uper **P**roton **S**ynchrotron
[4]**L**arge **E**lectron **P**ositron collider
[5]**L**arge **H**adron **C**ollider
[6]**R**evolution **F**requency
[7]**Lin**ear **ac**celerator
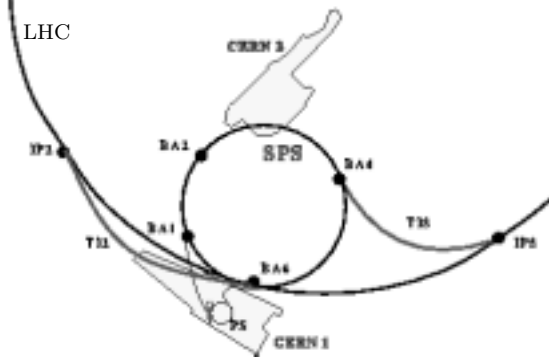[8]**P**roton **S**ynchrotron

Figure 1.1: The PS which provides the protons for the SPS which in turn supplies the LHC with protons. To deliver the protons to the LHC from the SPS which lies 72 m above, the new transfer line TI2 and the existing transfer line TI8 with a length of 2.8 km and 2.6 km respectively will be used.

40 MHz for the adiabatic capture of the beam and generation of the bunchstructure and another one working at 80 MHz for the compression of the 84 bunches. The compression is necessary to fit the bunches into the 200 MHz buckets of the SPS. The proton beam will be ejected in bunches of 25 ns spacing with an energy of 26 GeV. To compress the bunches to a longitudinal emittance of 1 eV·s, the SPS will be upgraded with a new superconducting RF system, which accelerates the protons to an energy of 450 GeV. Since the SPS is limited in the total amount of particles that can be accelerated, only 3/11 parts of its circumference will be filled. This is done in three PS cycles. In turn the SPS needs twelve cycles to fill one LHC ring. See figure 1.1 for the layout of the PS and the SPS with its transfer lines to the LHC. To fill both LHC rings 24 SPS cycles are needed. This requires 72 PS cycles and 144 PS Booster cycles. To take into consideration the rise and fall time of the kicker magnets the nominal number of bunches in one LHC ring is 2835, whereas 3564 bunch places are available. The nominal number of protons per bunch is 10^{11}. While the complete filling procedure takes about seven minutes, the beam lifetime is about 22 hours. However the time of data taking is restricted to about 10 hours since

Parameter	Variable	Unit	Value
Luminosity	L	[cm^{-2}s^{-1}]	10^{34}
Number of bunches	k_b		2835
Bunch spacing	τ_b	[ns]	24.95
Particles per bunch	n_b		$1.05 \cdot 10^{11}$
Normalised transverse emittance	ϵ_n	[μm·rad]	3.75
R.m.s. bunch length	$< l_b >$	[cm]	7.5
Transverse beam size at I.P.	σ	[μm]	15.9
β at I.P.	β^*	[m]	0.5
Crossing angle	ϕ	[μrad]	200
Beam lifetime	τ_{beam}	[h]	22
Luminosity lifetime	τ_L	[h]	10

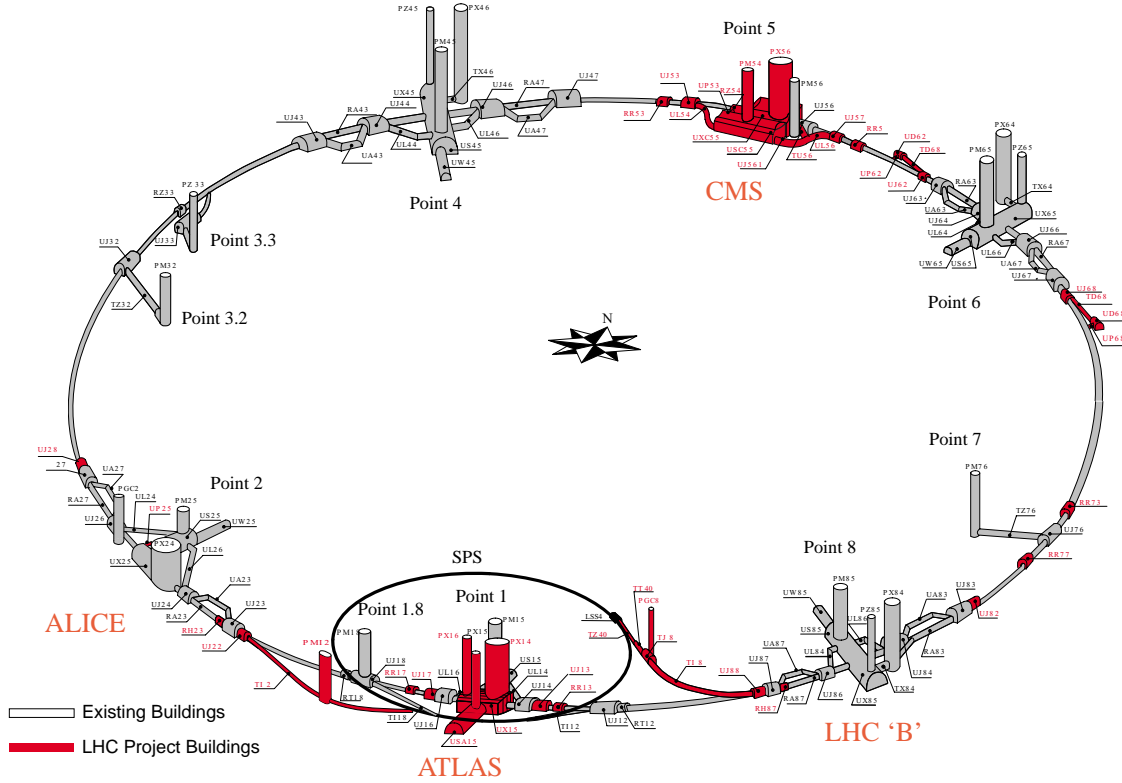*Table 1.1: Summary of important LHC design parameters.*

Figure 1.2: The LHC in the underground with a circumference of about 26.7 km. The caverns for the new experiments CMS and ATLAS are under construction at points 5 and 1 respectively. The LHC experiment ALICE replaces the LEP experiment L3 at point 2 and the experiment LHCb replaces the LEP experiment DELPHI at point 8. The cavern of the LEP experiment ALEPH at point 4 will be used to house the RF systems and at point 6 (LEP experiment OPAL) the beam dump will be installed. In the foreground around the experiment ATLAS and 72 m higher the SPS which delivers the proton beams to the LHC is visible.

the luminosity is continuously decreasing due to collisions. The RF system of the LHC operates at $400 \, \text{MHz}$ with a voltage of $8 \, \text{MV}$ at injection to $16 \, \text{MV}$ in collision. At the same time the longitudinal bunch emittance increases from $1 \, \text{eV·s}$ at injection to $2.5 \, \text{eV·s}$ in collision while the bunch length decreases from $13 \, \text{cm}$ at injection to $7.5 \, \text{cm}$ in collision. The luminosity is given by

$$L = \frac{N^2 k_b f \gamma}{4\pi \epsilon_n \beta^*} F \, , \tag{1.1}$$

where N is the number of protons per bunch, k_b the number of bunches, f the revolution frequency, γ the relativistic factor, ϵ_n the normalised transverse emittance , β^* the value of the betatron function at the interaction point and $F \approx 0.9$ the reduction factor caused by the crossing angle ϕ of the beams [Lef95]. The nominal parameters of the LHC performance are listed in table 1.1. After the first three years of running at low luminosity $L = 10^{33} \, \text{cm}^{-2}\text{s}^{-1}$ the LHC will operate at the design luminosity $L = 10^{34} \, \text{cm}^{-2}\text{s}^{-1}$ for

further three years. Afterwards heavy ion collisions with calcium and lead will take place. The ALICE[9] experiment is dedicated to study the physics of strongly interacting matter at extreme energy densities as produced in $Pb - Pb$ collisions. LHCb[10] is optimized for the precise measurement of CP violation and rare b decays. ATLAS[11] and CMS[12] are multi purpose detectors which cover a huge domain of particle physics. See figure 1.2 for details of the LHC and the experiments.

1.2   The CMS detector

In October 1990 the concept of a compact detector for the LHC based on a solenoid, the Compact Muon Solenoid was presented at the LHC workshop in Aachen [Pim90]. Since this workshop many institutes joined the collaboration and the demands on the detector were able to grow with the number of members. The design goals of the CMS detector are a high precision and redundant muon system, the best achievable electromagnetic calorimeter and a high quality central tracking system for secondary vertex tagging and the precise measurement of tracks.
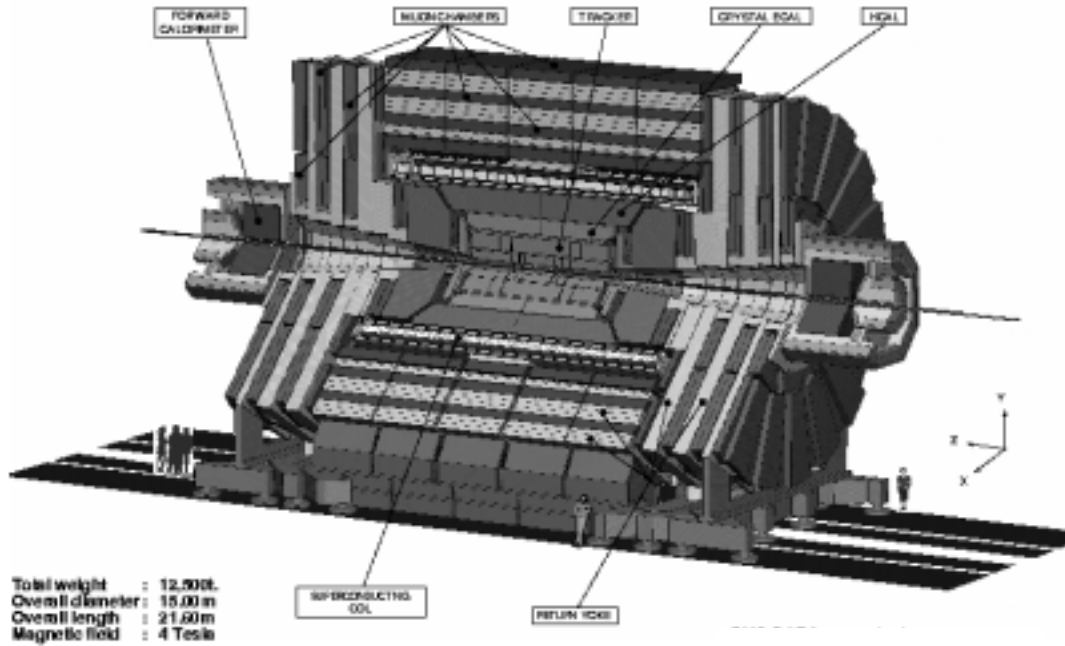
Figure 1.3: The CMS detector in an elevation view. The z axis is parallel oriented to the beam which is circulating counter-clock wise in the collider seen from a bird's-eye view as depicted in figure 1.2. The x axis is oriented to the center of the collider and to complete the right handed coordinate system the y axis points upwards.

[9]**A L**arge **I**on **C**ollider **E**xperiment
[10]**LHC b**eauty experiment
[11]**A T**orroidal **L**HC **A**pparatus
[12]**C**ompact **M**uon **S**olenoid
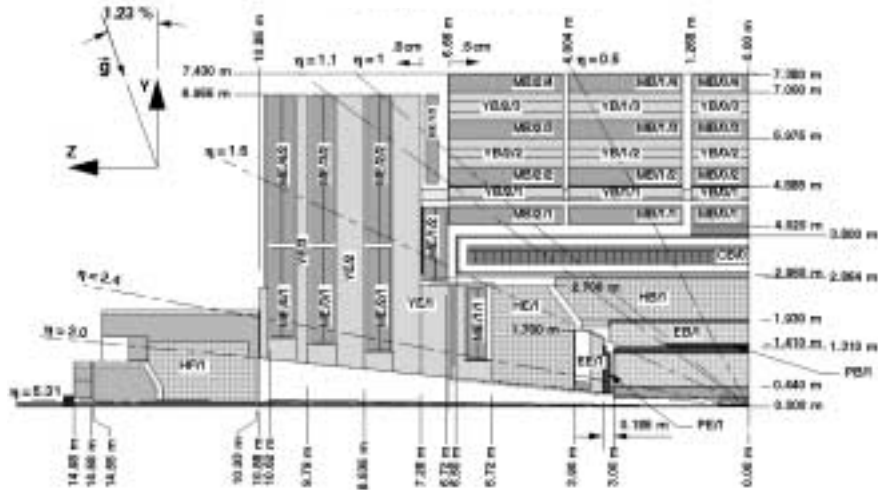
Figure 1.4: Cross section of the CMS detector along the z axis (only a quarter is drawn). The pseudo rapidity range η of the different sub-detector systems is indicated.

To obtain a good momentum resolution, a strong magnetic field is required. In accordance with a compact design this is achieved by a superconducting 13 m long solenoid [CMS94] with an inner diameter of 5.9 m. The solenoid is cooled with liquid helium by the surrounding cryogenic system and operates at a nominal magnetic field of 4 T. A quench protection system protects the coil against damages caused by the release of the huge amount of stored energy (2.7 GJ) in case of quenching [CMS97a]. In figure 1.3 the CMS detector is presented in an elevation view. Its weight is about 12 500 t, the over all diameter measures 15 m and the length without the forward calorimeters amounts to 21.60 m. Closest to the beam pipe, in the center of the detector, a silicon pixel vertex detector is placed. In the low luminosity phase three pixel layers are under discussion at 4 cm, 7 cm and 11 cm radius from the nominal beam position. The vertex detector is essential for the b tagging relying on a precise impact parameter measurement of tracks. It is surrounded by a silicon strip tracker up to the outer radial region of the central tracking system. The tracker is dedicated to the reconstruction of charged tracks. It is surrounded by the electromagnetic calorimeter which consists of scintillating crystals. Its purpose is a very precise measurement of energy deposits coming from photons and charged particles as electrons, pions and others. In front of the endcaps a preshower detector will be placed from the beginning of LHC operation with low luminosity. Its acceptance can be expressed in terms of the pseudo rapidity

$$\eta = \frac{1}{2} \ln \left(\frac{|\vec{p}| + p_z}{|\vec{p}| - p_z} \right) = -\ln \left(\tan \left(\frac{\theta}{2} \right) \right) , \qquad (1.2)$$

where $\vec{p}$ is a particle momentum and p_z its longitudinal component with respect to the nominal interaction point. θ is the polar angle with respect to the z axis. The preshower detector covers the range $1.65 < |\eta| < 2.61$. If the activity of minimum bias events at low luminosity shows the necessity, in the high luminosity phase an additional preshower

7

detector will be installed between the outer tracker and the electromagnetic calorime-
ter in the barrel region ($|\eta| < 0.9$) to improve the electron identification by rejecting
pions and enhancing the resolution of the electron and photon position in front of the
electromagnetic calorimeter. Between the electromagnetic calorimeter and the solenoid
the hadronic calorimeter consisting of copper alloy and stainless steel instrumented with
plastic scintillators is located. It measures mainly the hadronic components of showers
coming from gluons and quarks. In combination with the electromagnetic and the for-
ward calorimeter which lies outside of the muon system the missing transverse energy
is measured. A muon system for the precise measurement of muon momenta is placed
outside of the solenoid. It consists of four muon stations at different radii integrated in
the return yoke of the magnet. The muon stations will utilize three different technologies,
drift tubes, cathode strip chambers and resistive plate chambers to respect the different
strengths of the magnetic field in the different η regions. The measurement of the total
cross section and the luminosity at CMS in the low luminosity phase is addressed by the
TOTEM project [CMS99]. Two telescopes T1 are placed in the vacuum cones around the
beam pipe between the hadronic calorimeter and the forward calorimeter at each side of
the CMS detector. They cover the range $3 < |\eta| < 5$. Two telescopes T2 at the outer
sides of the forward calorimeters cover the range $5 < |\eta| < 7$. Details of the different
detectors are given below. Their η range can be extracted from figure 1.4.

1.2.1   The pixel vertex detector

The pixel detector is primarily dedicated to the efficient tagging of jets originating from
the decay of heavy hadrons containing b and c quarks. Due to the high particle fluxes
near the primary vertex, pixel devices are required to get space point information with
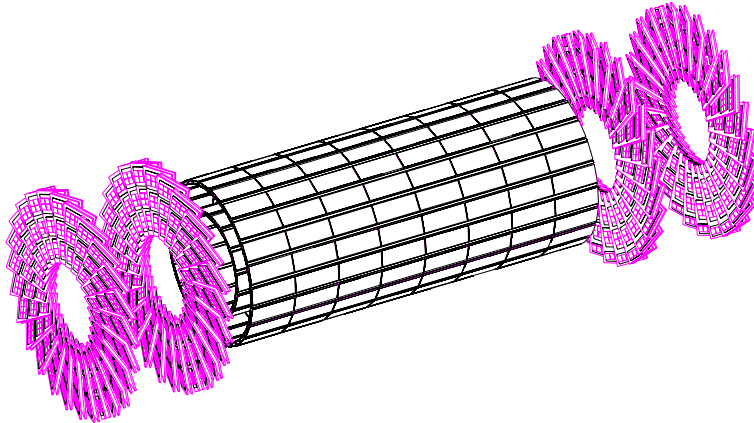high resolution. To identify secondary vertices of long-lived objects like heavy hadrons or

Figure 1.5: *The pixel vertex detector in high luminosity configuration with the inner barrel
layer at* $70 - 74$ *mm and the outer layer at* $107 - 112$ *mm. The disks are placed in front of
the barrel at* $z = \pm 32.5$ *cm and* $z = \pm 46.5$ *cm. The length of the barrel is* 100 *cm for the
low and the high luminosity configuration.*

τ leptons and to distinguish them against jets originating from light quarks and gluons, at least two pixel hits per track are required. Therefore the detector has to consist of at least two barrel layers and two end disks on each side of the barrel. In the low luminosity configuration even three barrel layers are under discussion. The inner layer resides at $41 - 45\,\mathrm{mm}$, the middle layer at $70 - 74\,\mathrm{mm}$ and the outer layer at $107 - 112\,\mathrm{mm}$ radius from the nominal beam axis while in the high luminosity configuration the inner barrel layer will be removed as shown in figure 1.5. The endcap disks with a radius from 60 to $150\,\mathrm{mm}$ are placed at $\pm 32.5\,\mathrm{cm}$ and $\pm 46.5\,\mathrm{cm}$ in z direction. Due to radiation damage all components at radii smaller than $10\,\mathrm{cm}$ to the beam axis have to be replaced at least once during the expected lifetime of the experiment. As a compromise between radiation hardness and cost silicon is chosen as detector material (GaAs turned out to be too susceptible to charged hadrons and diamond is too expensive). The coverage in pseudo rapidity for tracks with two pixel hits originating from the collision point within 1σ deviation goes up to $|\eta| = 2.4$. With a pixel size of $150\,\mu\mathrm{m} \times 150\,\mu\mathrm{m}$ an overall tracking precision of $15\,\mu\mathrm{m}$ in the cylinder coordinates $r\phi$ is expected under the assumption of an overall alignment precision within $10\,\mu\mathrm{m}$ [CMS98]. The effect of increasing the effective doping of the silicon pixel vertex detector can be controlled by keeping the detector at an appropriate temperature of $-10°\mathrm{C}$. To ensure this temperature the total power of about $3\,\mathrm{kW}$ is removed by a heat transfer liquid with short radiation length.

1.2.2 The silicon strip tracker

To achieve a clean identification and a precise measurement of leptons, photons and jets, robust tracking in addition to the detailed vertex reconstruction is essential. In conjunction with the pixel vertex detector the tracker is also useful to reconstruct primary and secondary vertices. In December 1999 the decision was taken to abandon the previous
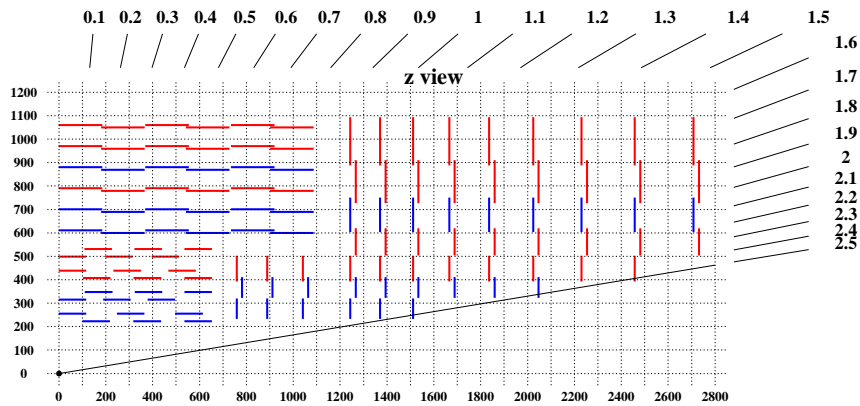

Figure 1.6: *Longitudinal cross section of the silicon tracker layout (one quarter) as modelled in the Monte-Carlo including the vertex detector in the center, surrounded by the inner silicon strip tracker which in turn is surrounded by the outer silicon tracker.*
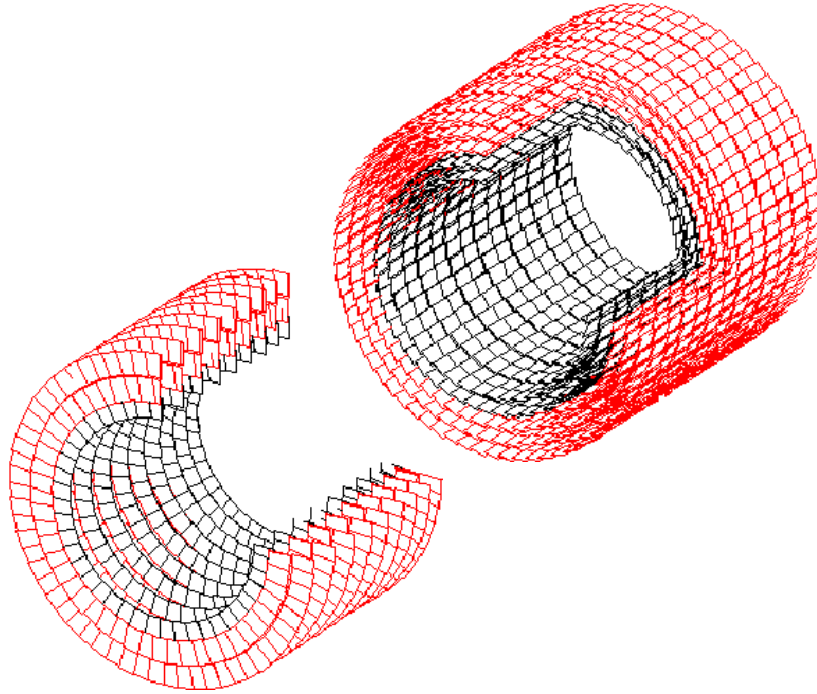
Figure 1.7: *In the front the outer endcap stations and behind the outer barrel section of the all silicon tracker layout as modelled in the Monte-Carlo. The innermost ring in each station of the endcap and the two innermost layers of the barrel are equipped with sensors mounted back-to-back.*

baseline design with an outer MSGC[13] tracker surrounding the inner silicon strip tracker in favour of an all-silicon tracker. The silicon strip tracker consists of an inner silicon strip tracker and an outer silicon tracker with ten barrel layers in all and nine disks in each outer endcap.

The inner silicon strip tracker (see figure 1.6) consists of $300\,\mu$m thick silicon detectors tilted by nine degrees to compensate the Lorentz effect. The pitch varies for different module types between 60 and $270\,\mu$m and the length varies between 7 and 12.5 cm. The barrel reaches a radius of 0.54 m and a length of 1.22 m which is extended by the endcaps to 5.39 m. This allows to cover a pseudo rapidity range up to $|\eta| = 2.5$ consistent with the other detector components [CMS98].

The outer silicon strip tracker (see figure 1.7) consists of $500\,\mu$m thick detectors which are not tilted. The outer radius of the barrel is 1.2 m and the length is 2.41 m. Together with the endcaps a total length of 5.87 m is reached to cover the pseudo rapidity range up to $|\eta| = 2.5$.

Some of the inner layers of the inner and the outer tracker are instrumented with back-to-back sensors to provide space point measurements [CMS00a]. The performance of the entire silicon tracker is comparable or even slightly better than the performance of

---

[13]**M**icro **S**trip **G**as **C**hamber

the MSGC tracker layout with a transverse momentum[14] resolution of

$$\frac{\Delta p_\perp}{p_\perp} = 0.15 p_\perp [\text{TeV}] \oplus 0.5\% \tag{1.3}$$

for isolated charged leptons. The recognition and reconstruction of tracks is guaranteed down to transverse momenta of about $1\,\text{GeV}$. The momentum resolution for the entire silicon tracker ranges for single charged lepton tracks with $p_\perp = 1\,\text{GeV}$ from 0.6% at $|\eta| = 0.1$ to 1.6% at $|\eta| = 2.3$. This relatively low transverse momentum is typical for the multitude of soft tracks in jets. For $200\,\text{GeV}$ transverse momentum jets the track finding efficiency varies between $85\,\%$ and $94\,\%$ depending on the pseudo rapidity and the reconstruction method, whereas central pseudo rapidities yield enhanced efficiencies. Further momentum resolutions and comparisons of track finding efficiencies can be found in [CMS00a].

1.2.3 The electromagnetic calorimeter

The electromagnetic calorimeter (ECAL) is designed to measure the energy and directions of electrons and photons with high precision [CMS97b]. The desired energy resolution can be achieved using scintillating crystals, where the energy of electrons and photons is deposited within the homogeneous crystal volume of the calorimeter. To meet the requirements of radiation hardness and high speed for the huge amount of particles which will be produced every $25\,\text{ns}$, lead tungstate ($PbWO_4$) was chosen as material for the
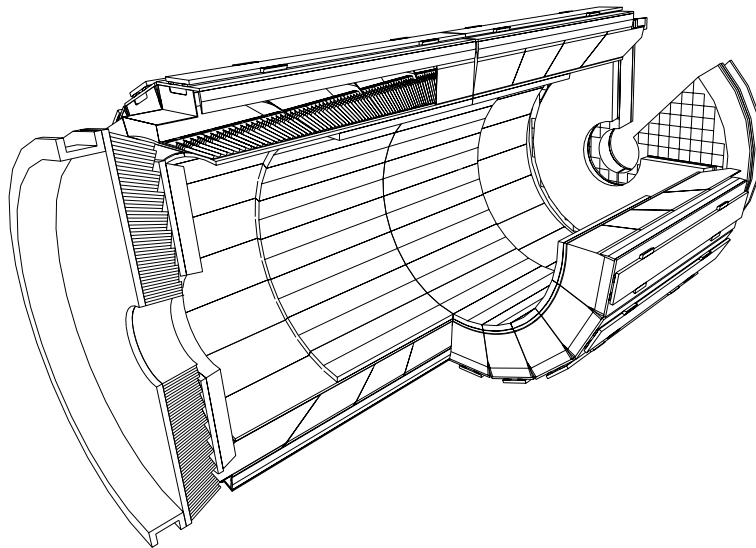

Figure 1.8: The electromagnetic calorimeter in an elevation view. The inner radius of the ECAL is $1.24\,m$, the outer radius is $1.75\,m$ and the total length extends to $7.8\,m$.

---

[14]This is the momentum transverse to the z axis given by $p_\perp = \sqrt{p_x^2 + p_y^2} = |\vec{p}|\sin\theta$
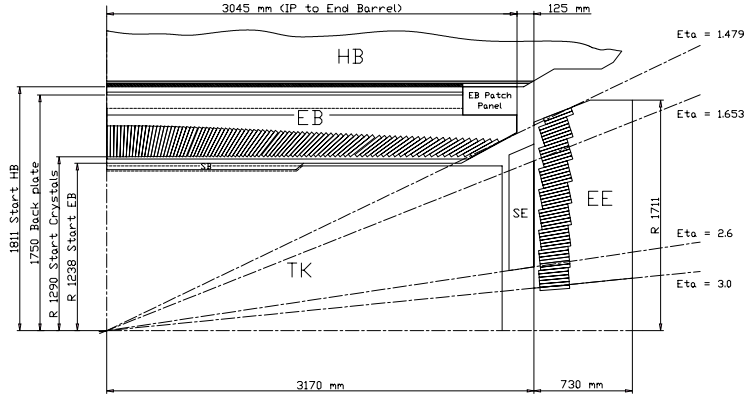
Figure 1.9: Longitudinal cross section of the electromagnetic calorimeter with marks for the accessible pseudo rapidity range. The preshower detector in front of the ECAL in the endcap and the optional one in the barrel are also displayed. The tokens in the figure stand for HB = HCAL Barrel, EB = ECAL Barrel, TK = Tracker, SE = (Pre)Shower Endcap and EE = ECAL Endcap.

crystals. $PbWO_4$ is a fast scintillator characterized by its short radiation length. In the barrel a radiation length of $25.8X_0$ and in the endcap a radiation length of $24.7X_0$ is achieved, corresponding to the crystal length of $230\,\text{mm}$ and $220\,\text{mm}$ respectively. The small Molière radius of $21.9\,\text{mm}$ matches the crystal front face of about $22 \times 22\,\text{mm}^2$. The $61\,000$ crystals of the ECAL are grouped in 36 supermodules consisting of 20×85 crystals. One supermodule is divided in four modules which in turn consist of 170 submodules. The granularity is accommodated to the physical relevant segmentation of the geometrical phase space in units of the pseudo rapidity η and the azimuthal angle ϕ. It is given by $\Delta\eta \times \Delta\phi = 0.0175 \times 0.0175$ in the barrel and increases monotonic to $\Delta\eta \times \Delta\phi = 0.05 \times 0.05$ in the endcap at the outer most pseudo rapidity of $|\eta| = 3.0$ while the crystal front surface is kept unchanged. Although the geometrical crystal coverage extends to $|\eta| = 3.0$, the precise energy measurement of electrons and photons will be carried out to $|\eta| = 2.5$ matching the acceptance of the tracker. This is important to distinguish the charged electrons from the neutral photons without track information. The reduced pseudo rapidity range for the precise measurement is caused by the radiation and pile-up energy in the forward direction. The ECAL trigger towers are grouped to 5×5 crystals in the barrel to match the HCAL tower granularity (see subsection 1.2.4). In the endcaps, below $|\eta| = 2.1$ the trigger towers have the same $\Delta\eta \times \Delta\phi$ granularity. Beyond $|\eta| = 2.1$ the trigger towers have a granularity of $\Delta\eta \times \Delta\phi = 2 \cdot 0.087 \times 0.087 = 0.174 \times 0.087$. See figure 1.8 for a detailed view of the calorimeter equipped with crystals.

From the start-up of the LHC a preshower detector is placed in front of the endcaps at $|z| = 3.05\,\text{m}$. If during the low luminosity phase the pile-up activity indicates the necessity, a further preshower detector will be placed in front of the barrel ECAL as indicated in figure 1.9. The preshower detector contains lead converters followed by detector planes of silicon strips with a pitch of less than $2\,\text{mm}$. For a total energy deposition of $20\,\text{GeV}$

in the CMS detector an energy fraction of typically 5% is deposited in the preshower. The fraction decreases with increasing incident energy. The space resolution of electrons and photons is improved exploiting the spatial precision of the preshower detector. The radiation length of $3.0X_0$ lead converter initialises the preshower and increases the spatial precision for electrons. The improved spatial resolution ranges from about $410\,\mu$m at $15\,$GeV incident electron energy to about $250\,\mu$m at $120\,$GeV. The separation between neutral pions and photons is improved as well. The lateral shower shape in the preshower and the ECAL is used to reject π^0 mesons which decay dominantly into two photons and therefore show broader energy deposits.

The energy resolution of the ECAL can be parameterised as

$$\frac{\Delta E}{E} = \frac{a}{\sqrt{E[\text{GeV}]}} \oplus \frac{\sigma_n}{E[\text{GeV}]} \oplus c \tag{1.4}$$

where a is a stochastic term due to shower containment, preshower sampling and photo-statistics. The value increases from $a = 2.7\,\%$ in the barrel to $5.7\,\%$ in the endcap. σ_n is the electronic noise arising from the preamplifiers and pile-up. The noise term corresponding to the reconstructed energy in a 5×5 crystal array is expected to be about $155\,$MeV in the barrel and about $205\,$MeV in the endcap at low luminosity. At high luminosity the values in the barrel and endcap are about $30\,\%$ and $20\,\%$ higher respectively. The small constant term $c = 0.55\,\%$ is achieved assuming the contributions from intercalibration errors to be smaller than $0.4\,\%$, from crystal non-uniformity to be smaller than $0.3\,\%$ and from shower leakage and others to be smaller than $0.2\,\%$.

The absolute calibration of the ECAL is expected to be limited in the start-up period of the LHC by systematics to $0.3\,\%$, which is better than the design goal of $0.5\,\%$. Using the Z mass constraint, two isolated high transverse momentum leptons from the process $Z \to e^+e^-$ will allow to achieve an intergroup calibration precision of $0.3\,\%$ after a few weeks of low luminosity.

1.2.4   The hadronic calorimeter

The hadronic calorimeter system [CMS97c] consists of the barrel and endcap calorimeter (HCAL) and the forward calorimeter (FH). By measuring the energy and direction of particle jets and the missing transverse energy the system determines quark, gluon and transverse neutrino directions and energies. In conjunction with the ECAL and the muon system the hadronic calorimeter system is also useful for the identification of electrons, photons and muons.

The hadronic calorimeter HCAL

The HCAL is placed outside of the ECAL and surrounded by the solenoid. The barrel (depicted in figure 1.10) ranges from an inner radius of $1.8\,$m to $2.86\,$m. Including the endcaps a length of $11.4\,$m is reached. The pseudo rapidity range of the HCAL extends to $|\eta| = 3$. The calorimeter is exposed to the entire $4\,$T field of the solenoid and hence

a)   b)
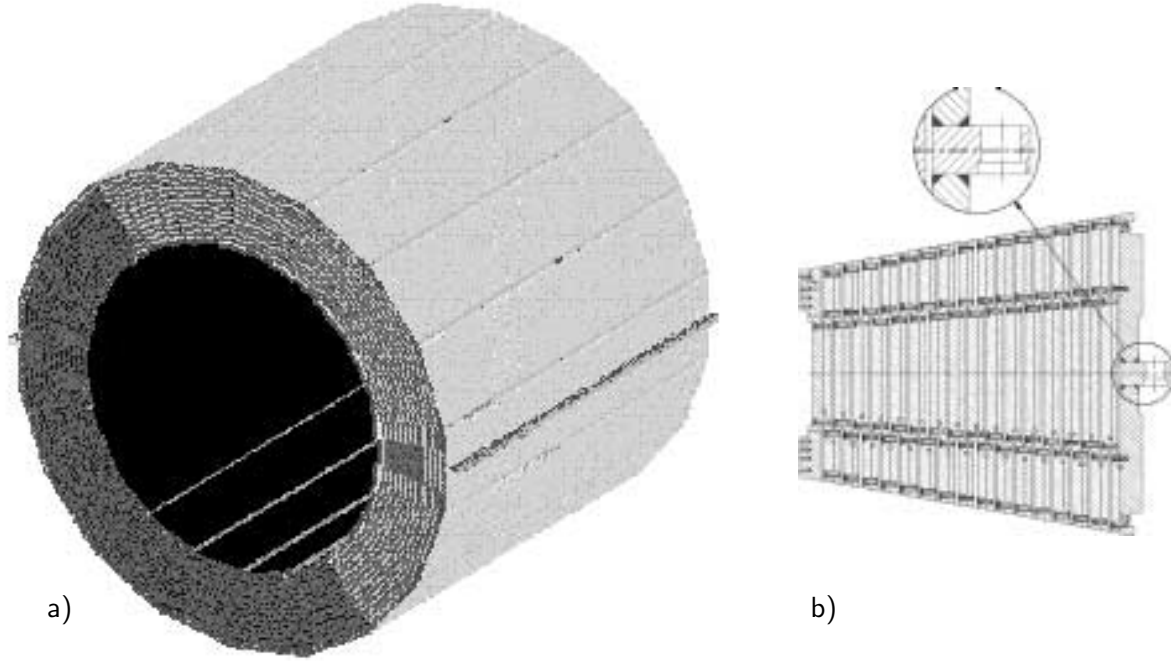
Figure 1.10: One half of the HCAL barrel in an perspective view (a) and a cut through one of the 36 barrel layer wedges (b). The support structure for rail mounting is built on the back plate of four special wedges as shown in detail.

made of non-magnetic materials which are copper alloy and stainless steel. The HCAL is a sampling calorimeter consisting of active material embedded between copper absorber plates of 5 cm and 8 cm thickness in the barrel and endcaps respectively. 4 mm thick plastic scintillator tiles serve as active material. They are read out by wavelength-shifting plastic fibres. At $\eta = 0$ the calorimeter is 79 cm thick, which corresponds to 5.15 λ nuclear interaction lengths. An optional configuration which exploits available space inside the cryostat allows a sampling depth of 89 cm corresponding to 5.82 λ. To ensure a sufficient sampling depth over the entire pseudo rapidity range up to $|\eta| = 3$, the first muon chamber absorber layer is instrumented with scintillator tiles. The cylindrical structure of each half barrel is divided into 18 wedges covering 20° in ϕ. Each barrel wedge is composed of 31 copper alloy plates, whereas the inner and outer plates are made of stainless steal to improve the mechanical stability. The plates have slots for the scintillators. The endcap is made of 18 absorber sectors and 18 spacers in alternating layers divided into segments of 20° in ϕ as the barrel. The 18 brass spacers have insertion gaps of 10° in ϕ for the scintillator. For the barrel and the endcap the scintillators are segmented into towers of about $\Delta\eta \times \Delta\phi = 0.087 \times 0.087$ to match the lateral granularity of the ECAL.

The forward calorimeter FH

The forward hadron calorimeter FH is placed outside of the muon system around the beam pipe with a radius of 10 cm. The FH itself measures an inner radius of 12.5 cm, an outer

radius of 1.5 m and a length of about 3 m. Its acceptance meets the pseudo rapidity range of the hadronic calorimeter endcaps at $|\eta| = 3$ and extends the hermiticity of the HCAL to the pseudo rapidity of $|\eta| = 5.3$ to improve the measurement of missing transverse energy. Moreover, the calorimeter is useful to tag high transverse momentum jets in the forward direction and to apply jet vetos for signal processes without associated jet production in the forward direction. The forward calorimeter consists of quartz fibres as active medium embedded in a copper absorber matrix. In the high radiation environment it is predominantly sensitive to Cerenkov light from neutral pions resulting in a very localised response to hadronic showers. In conjunction with Roman Pots $300 - 400$ m upstream of the low beta insertion, the forward calorimeter is also used to monitor the luminosity.

Energy resolution of the complete calorimeter system

Test beam studies indicate that for the complete calorimeter system including the ECAL an energy resolution of

$$\frac{\Delta E}{E} = \frac{100\,\%}{\sqrt{E[\text{GeV}]}} \oplus 4.5\% \tag{1.5}$$

can be achieved for energies between 30 GeV and 1 TeV. There are various methods to calibrate the hadronic calorimeter. In the test beam the response of several wedges is measured with muons and hadrons versus moving radioactive wire sources. With laser calibration and light injection the uncertainty of the absolute energy scale will be reduced to less than 3 %. With further optimization the precision is expected to reach 1 %. With calibration through physics events, e.g. τ leptons balanced by jets, resonances decaying into two jets and pions not interacting in the ECAL in comparison to the momentum measured in the tracker, the accuracy of 1 % can be achieved [Kin97] (2 % using pions interacting in the ECAL).

1.2.5 The muon system

The basic concept of the CMS detector is to trigger and reconstruct muons which deliver an unambiguous signature in most of the physics processes to be investigated at the LHC. Precision tracking in the central barrel region and triggering on muons through their bending in the transverse plane is facilitated by the solenoidal magnetic field. The muon system [CMS97d] uses three different technologies for the detection and measurement of muons. In the barrel region DT's[15] were chosen in consideration of the expected low rate and the relatively low intensity of the magnetic field. The endcaps consist of CSC's[16] providing precise space time information in the presence of a high magnetic field and particle rate. In the barrel and the endcaps the RPC's[17] with their very fast response time comparable to those of scintillators are installed. They provide an unambiguous

---

[15]**D**rift **T**ube

[16]**C**athode **S**trip **C**hamber

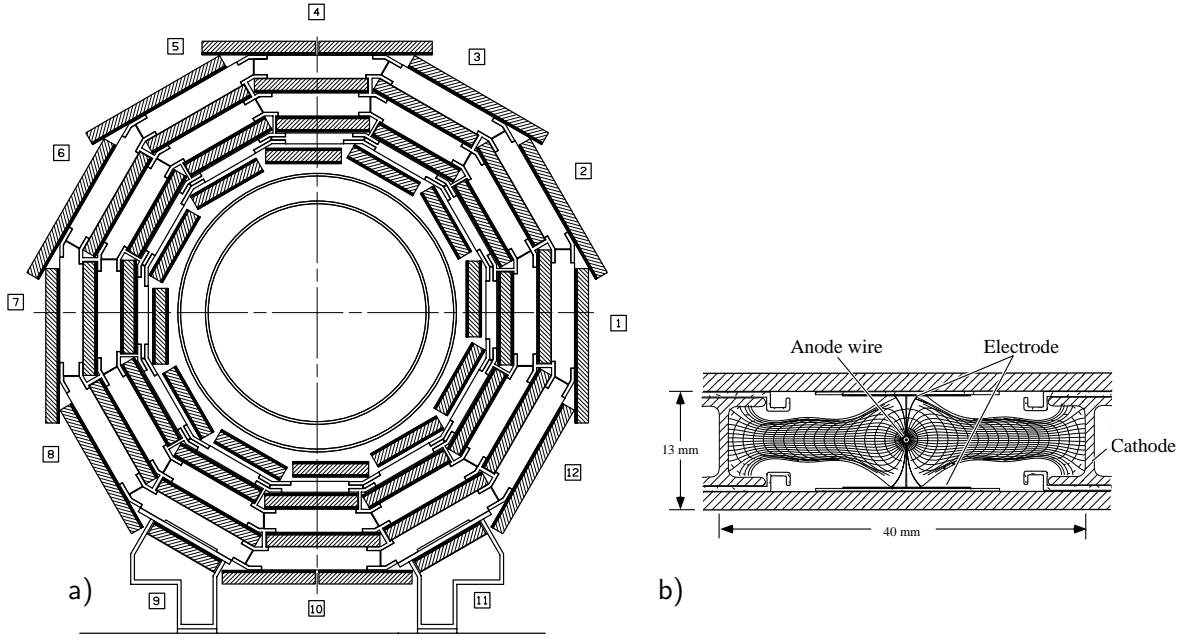[17]**R**esistive **P**late **C**hamber

Figure 1.11: A cross section of the muon barrel system perpendicular to the beam axis is shown in sketch a). Two of the four muon stations are mounted on the inner and outer face of the return yoke. The other two stations are located in slots inside the iron. The system is highly redundant to cover inefficiencies due to the support structure. A transverse view trough a baseline drift cell is shown in sketch b). The drift lines and isochrones for a typical voltage configuration of the electrodes are indicated.

assignment of the bunch crossing and measure the transverse momentum at trigger time. Hence candidate muon tracks can be triggered with high efficiency. All muon chambers are aligned to allow the muon trajectories to traverse the chambers rather perpendicular than parallel. Besides, the chambers are distributed to provide hermetic coverage over the whole pseudo rapidity range of $0 \leq |\eta| < 2.4$.

The barrel system consists of four muon stations integrated in the return yoke of the magnet as shown in figure 1.11 on the left. Each station is $2.5\,\mathrm{m}$ long according to the segmentation of the iron yoke in five rings. While the inner three stations are composed of 60 chambers, the outer station counts 10 more chambers due to the feet of the yoke. The chambers are equipped with drift cells (see figure 1.11 right) of approximately $400\,\mathrm{ns}$ maximum drift time. Each chamber consists of twelve planes of drift tubes which are grouped into three independent units of super layers, each consisting of four planes with parallel wires. The two outer super layers are dedicated to measure the coordinate in the bending plane (ϕ super layer) while the super layer in the middle measures the track coordinate along the z axis (z super layer). The distance of the two outer super layers is maximized to about $23\,\mathrm{cm}$ to achieve the best angular resolution. Between the super layers thick honeycomb plates are placed as spacer. The four planes of a super layer are shifted by half a cell to allow the computation of the coordinate and the angle of crossing tracks. For this the correlation of the drift times in the different planes is exploited. The drift cells are filled with an Ar/CO_2 gas mixture at atmospheric pressure. They are

contacted with two electrodes on the side walls, one on the top and one on the bottom wall. A resolution of $250\,\mu$m is achieved per layer and about $100\,\mu$m per chamber.

The endcaps have four muon stations consisting of trapezoidal CSC's, arranged in series of concentric rings centered around the beam line. The stations are separated by the three iron disks of the return yoke which are also useful to isolate electrons in showers. The outermost muon station is followed by a 100 mm thick iron disk, predominantly to shield the station against backsplash backgrounds induced by particles scattered at small angles and interacting with material in the forward direction (beampipe, quadrupoles, forward calorimeter, etc). The innermost station is built of three rings, the others are built of two rings. All chambers but the outermost ring of the inner station overlap in ϕ to form rings without dead areas in azimuth. The outer three stations consist of 36 chambers in the outer ring covering $10°$ in ϕ and of 18 chambers in the inner ring covering $20°$. The radial cracks between the chamber rings are misaligned to guarantee at least three chambers on one muon path. In each CSC six layers of angular tangential aligned wires with approximately constant spacing are sandwiched between six cathode panels of radially aligned strips (perpendicular to the wires). The precision requirement for the chambers is $75\,\mu$m in the two inner rings of the innermost station and $150\,\mu$m anywhere else.

To provide an additional, complementary trigger, RPC's are added in the barrel and the endcaps. They consist of gaseous parallel plate chambers with reasonable spatial and excellent time resolution. The trigger signals from the drift tubes, cathode strip chambers and the resistive plate chambers reach the trigger logic in parallel to achieve a higher efficiency and larger rate capabilities. A RPC is constructed from two parallel phenolic resin plates. The resin material is coated with conductive graphite to form electrodes which are read out by insulated aluminium strips positioned outside in the middle of the plates. Two plates placed back to back build a sandwich. To use the chambers in the high rate environment of CMS, they operate in the avalanche mode with lower gas amplification and smaller pulses. Due to the low costs of the devices they can be sufficiently highly segmented to allow the measurement of the transverse momentum at trigger time. In addition the bunch crossings can be assigned with high efficiency.

The momentum resolution $\Delta p_\perp / p_\perp$ of muon tracks in the muon system depends strongly on the pseudo rapidity since for $|\eta| \geq 1.5$ the tracks are less bent because they exit the end of the solenoid. For muons with a transverse momentum of 10 GeV the resolution ranges from $7\,\%$ at the barrel center to $24\,\%$ at $|\eta| = 2.4$. In combination with the central tracker the resolution of 10 GeV muons improves to about $1.5\,\%$ with smaller dependence on the pseudo rapidity range. The momentum resolution of the combined muon system with the inner tracker can approximately be expressed by the simple parameterization

$$\frac{\Delta p}{p} = 4.5\,\%\sqrt{p\,[\text{TeV}]} \tag{1.6}$$

In the endcap where the measurement is limited by multiple scattering in the forward tracker the formula is only adequate for particle momenta above 70 GeV. A constant value of $\Delta p/p = 1.2\,\%$ turns out to describe the resolution in this case.

1.3 The trigger

Since the rate of the on-line computer farm is limited to $100\,\mathrm{kHz}$, the huge input rate of interactions due to bunch crossings every $25\,\mathrm{ns}$ has to be reduced. This is done in two steps. At the first level all data is stored for $3.2\,\mu s$ to be passed with no more than $100\,\mathrm{kHz}$ to the higher level triggers [CMS00b]. In the first step the L1[18] trigger system

Process	Trigger Efficiency (%)
$pp \rightarrow t\bar{t} \rightarrow eX$	99.3
$pp \rightarrow t\bar{t} \rightarrow H^{+}X$	99.0
$pp \rightarrow bb \rightarrow eX$	0.2
SUSY Neutral Higgs ($10 \leq \tan\beta \leq 30, 100 \leq m_H \leq 400\,\mathrm{GeV}$)	45-98

Table 1.2: *The trigger efficiencies of some signal processes at low luminosity.*

uses coarsely segmented data from the calorimeter and the muon system while holding the precise data in pipeline memories. At initial operation, the L1 trigger will be restricted to $75\,\mathrm{kHz}$. In the second step the HLT[19] system exploits the more complete information, not available on the time scale of the L1 trigger decision. The system is designed to achieve a rejection factor of 10^3 and to write up to 100 events per second to mass storage.

The trigger efficiencies of some physics processes are summarized in table 1.2. The values correspond to the representative set of trigger transverse momentum cutoffs as shown in table 1.3 [Das98].

Trigger channel	cut-off $p_\perp$ (GeV)
Missing transverse energy	40
Electron	12
Single jet	50
Two jets	30
Three jets	20
Four jets	15

Table 1.3: *Representative set of trigger $p_\perp$ cut-offs at low luminosity.*

---

[18]**Level 1**
[19]**H**igher **L**evel **T**rigger

2

The top quark at the LHC

The top quark was discovered at the Tevatron in 1995 [CDF95], completing the third generation of quarks within the standard model. It is the heaviest elementary particle yet discovered with a mass close to the scale of electroweak symmetry breaking, recently determined by direct Tevatron measurements to $m_t = 174.3 \pm 5.1$ GeV [Gro00]. At present the statistical error is still dominating, but in the future (Tevatron Run II) the uncertainty on the jet energy calibration will set systematic limits on the achievable accuracy in the top mass measurement. In contrast at the LHC, which will be a top factory, this systematic uncertainty can be essentially reduced by the requirement of considerably higher transverse jet momenta. Here the theoretical uncertainty on the transverse momentum spectrum of the top quark in the $t\bar{t}$ production constitutes the dominating contribution as will be shown in chapter 4.

One of the most interesting top measurements will be the precise determination of the top quark mass (chapter 4), which allows in particular the improvement of the accuracy of supersymmetric exclusion limits. The measurement of the helicity states of the W boson from the top quark decay within the percent level (chapter 5) will allow to search for deviations of the standard model. The measurement of the $t\bar{t}$ spin correlation (chapter 6) constitutes the direct check of the top quark spin one half and thus a fundamental test of the quark spins in general and the QCD itself. Moreover, the investigation of the cross section of the heavy quark production in high energetic hadronic collisions is important for the design of experiments at existing and future accelerators and also in the domain of cosmic ray physics [Rys00]. Beyond the standard model, a heavy Higgs boson above the $t\bar{t}$ production threshold may become relevant (chapter 7).

The mass of the top quark can also be inferred from electroweak measurements at LEP and SLD for example. The ratio of the Z boson decay width into $b\bar{b}$ pairs to its decay width into hadrons $R_b = \frac{\Gamma(Z \to b\bar{b})}{\Gamma(Z \to \text{hadr.})}$ is sensitive to the top quark mass through loop corrections including contributions from highly virtual top quarks. The combined analysis yields $m_t = 150 \pm 25$ GeV [Cla00]. Kinematical fits to precisely measured electroweak observables at LEP lead to the limits $m_t = 172^{+14}_{-11}$ GeV [Abb00]. Further aspects and properties of the top quark are described in the following.

2.1 Properties of the top quark

According to the standard model the top quark is a spin 1/2 fermion with charge $+2/3$. Together with the bottom quark it constitutes the weak isospin quark doublet of the third generation. The top quark aquires its mass via the Yukawa coupling $g_t = 2^{3/4}G_F^{1/2}m_t$ to a Higgs boson after spontaneous symmetry breaking. However its value cannot be predicted by the standard model since particle masses are free parameters which have to be determined experimentally. Beside the top quark pole mass, which is defined as the particle pole in the perturbative top quark propagator, the renormalized top quark mass $\overline{m}_t(\mu)$ given at a renormalization scale μ defined in the $\overline{\text{MS}}$ scheme is convenient. At the scale $\mu = \overline{m}_t$ the renormalized mass is $\overline{m}_t \simeq 165\,\text{GeV}$ and the difference to the pole mass $m_t - \overline{m}_t$ is about $10\,\text{GeV}$. In view of such big differences in different mass conventions any observable supposed to measure the top quark mass with an accuracy of $1 - 2\,\text{GeV}$ has to tell which mass is actually determined. A particular measurement determines a mass parameter accurately to the extent to which higher order corrections to matrix elements of the process are small. Measuring the top quark mass through pair production near
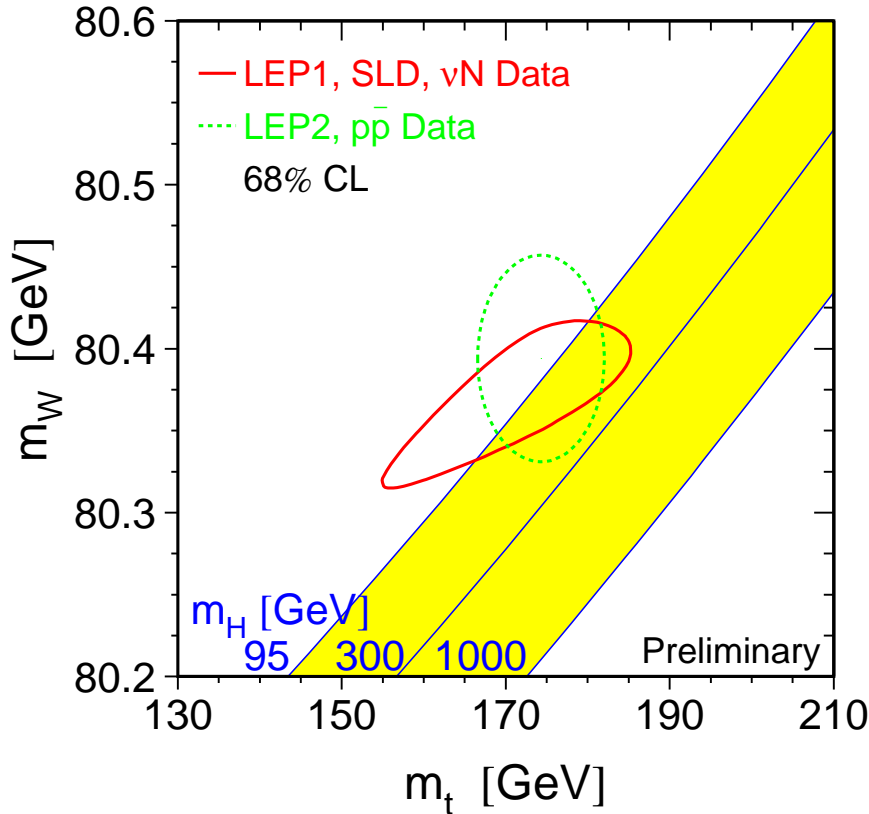

Figure 2.1: *Constraints on the Higgs mass using the measured top quark and W boson masses. The closed curves correspond to experimental limits on m_t and m_W. The shaded band indicates for different Higgs masses the values allowed in the standard model.*

threshold in e^+e^- collisions at future linear colliders, the theoretical uncertainty of the renormalized top mass $\overline{m}_t$ in the $\overline{\text{MS}}$ scheme is $0.15\,\text{GeV}$. This uncertainty is less than half of what could be achieved by parameterizing the cross section with the top quark pole mass [Alt00] (p. 441). The reason for the larger uncertainty using the concept of the pole mass lies in the intrinsic ambiguity of the pole mass of the order Λ_{QCD}. This will take affect at the LHC and future colliders with still improved precision.

The decay width of the top Γ_t will be difficult to measure but its theoretical accuracy lies within $1\,\%$. Since the mass of the top quark exceeds the Wb production threshold its decay width is expected to be dominated by the two-body decay $t \to Wb$. Neglecting higher order corrections and the b quark mass the prediction of the standard model is given by

$$\Gamma(t \to bW) = \frac{G_F m_t^3}{8\pi\sqrt{2}} \left(1 - \frac{m_W^2}{m_t^2}\right)^2 \left(1 + 2\frac{m_W^2}{m_t^2}\right) \tag{2.1}$$

[Jar90] (vol. II, p. 314). The numerical value of the top width for a mass of $m_t = 175\,\text{GeV}$ is $\Gamma_t = 1.54\,\text{GeV}$, corresponding to a lifetime of about $\tau_t = 1/\Gamma_t \simeq 4.23^{-25}\,\text{s}$. This is much shorter than the typical hadronisation time $\tau_{\text{hadr.}} \sim 1/\Lambda_{\text{QCD}}$. Thus no top flavoured hadrons or $t\bar{t}$ quarkonium bound states can be formed.

Since the top quark mass in combination with the W boson mass allows to test the standard model and to set constraints on the mass of the Higgs boson it is very important to improve the precision of the measured top quark mass. The Higgs boson, the W boson and the top quark contribute via radiative corrections to observables already measured at LEP and SLC, so that the measured observables together with the measured values of the W and top mass restrict the allowed mass range of the Higgs boson as shown in figure 2.1. Recent experimental constraints on the Higgs boson mass are consistent with the standard model [Abb00]. Providing valuable input for future experiments with a final precision of the W mass from LEP expected to be $\sim 40\,\text{MeV}$, a precision of about $1\,\text{GeV}$ in the top mass would yield a prediction in the Higgs boson mass of $\delta m_H/m_H \leq 40\,\%$ [Sim99b].

2.2 Top quark decay

The fraction of top quarks decaying into b quarks

$$B_b \equiv \frac{\Gamma(t \to bW)}{\Gamma(t \to qW)} \tag{2.2}$$

has been measured by CDF to $B_b = 0.99 \pm 0.29$ [Tol98]. Within the three generation standard model this ratio can be expressed by the CKM matrix elements as

$$B_b \equiv \frac{|V_{tb}|^2}{|V_{tb}|^2 + |V_{ts}|^2 + |V_{td}|^2} \tag{2.3}$$

where the denominator equals to exactly 1.0 due to unitarity of the CKM matrix. Measurements in combination with the CKM unitarity yield $0.9990 < |V_{tb}| < 0.9993$ [Gro00],

i.e. the top quark decays almost exclusively (about 99.83 %) into a b quark and a W boson. In an extended standard model with a fourth generation of quarks the three generation unitarity does no longer hold and the denominator of equation (2.3) can be smaller than 1.0. Measurements from D∅ constrain a fourth generation b' quark to have a mass greater than $m_t - m_W$. Thus the top quark decay into b' would be suppressed and the original expression of equation (2.3) is still valid. Measurements in combination with a four generation CKM matrix yield the weak constraint $0.05 < |V_{tb}| < 0.9993$. Therefore the direct measurement of $|V_{tb}|$ is useful to search for physics beyond the standard model.

Rare top decays via flavour changing neutral current (FCNC) transitions are highly suppressed in the top quark decay of the standard model, but beyond a two Higgs doublet model would yield $\mathrm{Br}(t \rightarrow \gamma(Z)q) \sim 10^{-8}$. An R parity violating supersymmetric model would reach $\mathrm{Br}(t \rightarrow \gamma(Z)q) \sim 10^{-4}$. The current constraints from LEP and CDF are not very stringent but at the LHC the sensitivity will be about four orders of magnitude better [Son01].

2.3 $t\bar{t}$ production

The leading order processes for the production of a $t\bar{t}$ pair in hadron-hadron collisions are

$$q(p_1) + \bar{q}(p_2) \quad \rightarrow \quad t(p_3) + \bar{t}(p_4) \tag{2.4}$$
$$g(p_1) + g(p_2) \quad \rightarrow \quad t(p_3) + \bar{t}(p_4) \tag{2.5}$$

where the four momenta $p = (E, p_x, p_y, p_z)$ of the partons as defined in figure 2.2 are given in brackets. The Feynman graphs contributing to the matrix elements in $\mathcal{O}(\alpha_\mathrm{s})$ are shown in the figures 2.4 and 2.3. The squared matrix elements averaged over initial and summed over final colour and spin states are given by

$$|\overline{\mathcal{M}}|^2(q\bar{q} \rightarrow t\bar{t}) \quad = \quad (4\pi\alpha_\mathrm{s})^2 \frac{8}{9} \left(2\frac{(p_1 \cdot p_3)^2 + (p_2 \cdot p_3)^2}{(p_1 + p_2)^4} + \frac{m_t^2}{(p_1 + p_2)^2} \right) , \tag{2.6}$$
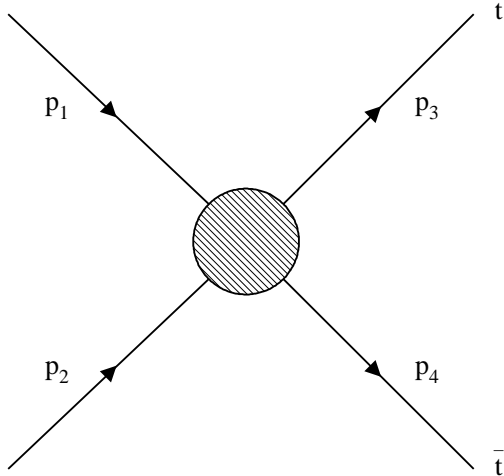

Figure 2.2: The production of a $t\bar{t}$ pair. The two incoming partons of the hard sub process, either two gluons or a quark antiquark pair, carry the four momenta p_1 and p_2. The amplitude of the parton scattering is visualized by the hatched circle. The outgoing top and antitop quarks carry the four momenta p_3 and p_4.
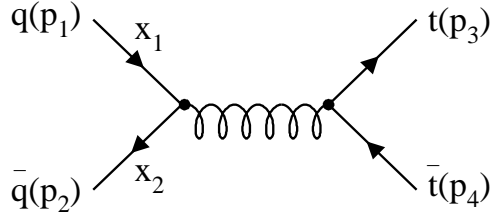
Figure 2.3: *Feynman graph for the production of a tt̄ pair via quark antiquark annihilation in lowest order. About 13 % of the tt̄ pairs are expected to be produced by this process at LHC energies.*

$$\overline{|\mathcal{M}|}^2(gg \to t\bar{t}) = (4\pi\alpha_\mathrm{s})^2 \left(\frac{(p_1 + p_2)^4}{24(p_1 \cdot p_3)(p_2 \cdot p_3)} - \frac{3}{8} \right)$$
$$\times \left(4\frac{(p_1 \cdot p_3)^2 + (p_2 \cdot p_3)^2}{(p_1 + p_2)^4} + \frac{4m_t^2}{(p_1 + p_2)^2} - \frac{m_t^4(p_1 + p_2)^4}{(p_1 \cdot p_3)^2(p_2 \cdot p_3)^2} \right) \quad (2.7)$$

with the four vector product defined as $(p_a \cdot p_b) = E_a E_b - \vec{p_a}\vec{p_b}$. The differential partonic cross section

$$d\hat{\sigma} = \frac{1}{2(p_1 + p_2)^2} \frac{d^3 p_3}{(2\pi)^3 2E_3} \frac{d^3 p_4}{(2\pi)^3 2E_4} (2\pi)^4 \delta^4(p_1 + p_2 - p_3 - p_4)\overline{|\mathcal{M}|}^2 \quad (2.8)$$

is obtained by including the flux factor for the incoming partons $2(p_1+p_2)^{-2}$ and the terms arising from the phase space of the $2 \to 2$ scattering process. The differential hadronic cross section
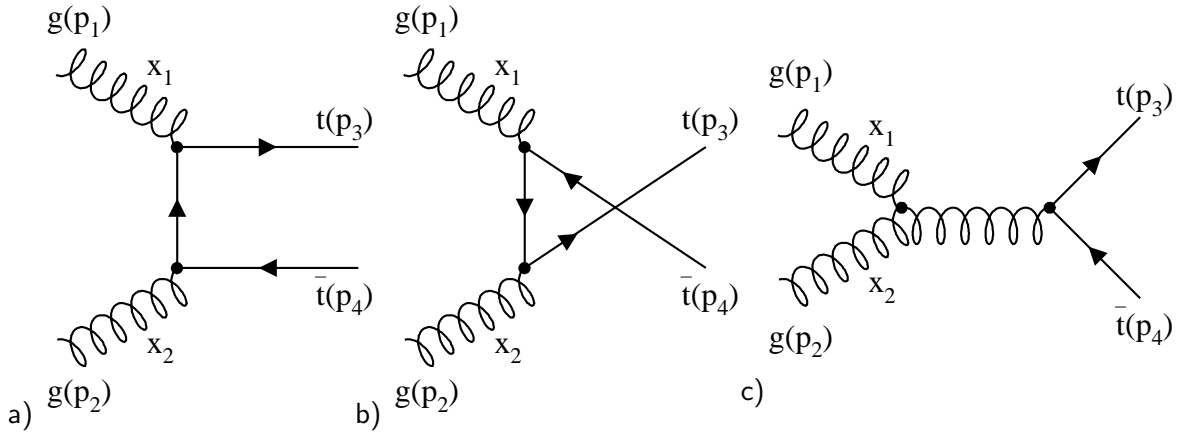

Figure 2.4: *Feynman graphs for the production of a tt̄ pair via the gluon fusion in lowest order. The t channel amplitude (a), the u channel amplitude (b) and the three gluon vertex (c). The bulk of the tt̄ pairs, about 87 %, is expected to be produced by these processes at the LHC.*

$$d\sigma = \int_0^1 \int_0^1 dx_1 dx_2 f_1(x_1, Q^2) f_2(x_2, Q^2) d\hat{\sigma} \qquad (2.9)$$

follows from the partonic one by folding it with the parton density functions of the incoming protons, which give the probability of finding a parton ($q, \bar{q}$ or g) with momentum fraction $x \in (0,1)$ in the proton at a given Q^2 scale which is ambiguous but of the order of the invariant top quark mass squared.

The $t\bar{t}$ production at the LHC with a hadronic center of mass energy of $\sqrt{s} = 14\,\text{TeV}$ yields a LO cross section of about $560\,\text{pb}$ assuming a top mass of $m_t = 175\,\text{GeV}$. Calculations of the NLO cross section predict about $800\,\text{pb}$. A variation of the top mass of $\pm 5\,\text{GeV}$ yields a change in the cross section of about $12\,\%$ with decreasing cross section for increasing top masses [Alt00] (p. 426). Furthermore the variation of the renormalization and factorisation scale in the calculation of the NLO cross section, which is of the order $\mathcal{O}(\alpha_{\text{s}}^3)$ gives rise to higher order corrections. In detail, a variation of the scale $\mu = m_t$ by a factor of two yields a $10\,\%$ variation of the cross section [Alt00] (p. 429) using the MRST99 parton density functions [MRS99].

For the production of an on-shell $t\bar{t}$ pair the energy equivalent of two top masses is sufficient. Just above this threshold the production reaches its maximum and low proton momenta fractions below $x \simeq 0.03$ are favoured. The gluon density of the proton dominates in this range and one expects that about $87\,\%$ of the $t\bar{t}$ events are produced by the gluon gluon fusion processes of figure 2.4. The remaining fraction is expected to be produced by the quark antiquark annihilation of figure 2.3 (In chapter 6 it will be shown that the fractions depend, to the percent level, on the parton density functions used). This is different at the Tevatron, where the $p\bar{p}$ center of mass energy is $\sqrt{s} = 1.8\,\text{TeV}$ (Run I). Here the quark antiquark annihilation process dominates with about $90\,\%$ over the gluon fusion [Cho99]. This large fraction will be slightly reduced (about $2\,\%$) in the new Run II with $\sqrt{s} = 2\,\text{TeV}$ due to the rise of the gluon density in the proton towards lower x while the valence quark density (and antiquark density in the antiproton) decreases. On the other hand an optional upgrade of the LHC, to a center of mass energy of $\sqrt{s} = 28\,\text{GeV}$ would lead to a further increase of the already dominating gluon fusion in the $t\bar{t}$ production (about $5\,\%$). This may slightly increase the systematic uncertainty in the mass of the reconstructed top due to the uncertainty in the gluon density (see the discussion about the parton density functions in section 4.3). It constitutes also an important issue in the investigation of the $t\bar{t}$ spin correlation and its improvement [Alt00] (p. 472) 6.

2.4 $t\bar{t}$ event topology

Taking the two incoming partons from the protons as longitudinal axis the produced $t\bar{t}$ pair is balanced in $p_\perp$, i.e. their momentum vectors are back-to-back in the plane transverse to the longitudinal axis. Since the partons can have a primordial transverse momentum and initial state radiation can provide additional $p_\perp$ the longitudinal axis does not necessarily coincide with the z axis of the lab system. As already explained

$t\bar{t} \rightarrow (W^+b)(W^-\bar{b})$			$W^+ \rightarrow$				
			e^+, ν_e	μ^+, ν_μ	τ^+, ν_τ	u, d	$c, \bar{s}$
			1/9	1/9	1/9	3/9	3/9
$W^- \rightarrow$	$e^-, \bar{\nu}_e$	1/9	1/81	1/81	1/81	3/81	3/81
	$\mu^-, \bar{\nu}_\mu$	1/9	1/81	1/81	1/81	3/81	3/81
	$\tau^-, \bar{\nu}_\tau$	1/9	1/81	1/81	1/81	3/81	3/81
	$\bar{u}, d$	3/9	3/81	3/81	3/81	9/81	9/81
	$\bar{c}, s$	3/9	3/81	3/81	3/81	9/81	9/81

Table 2.1: The possible W boson decay modes of the $t\bar{t}$ system and their fractions.
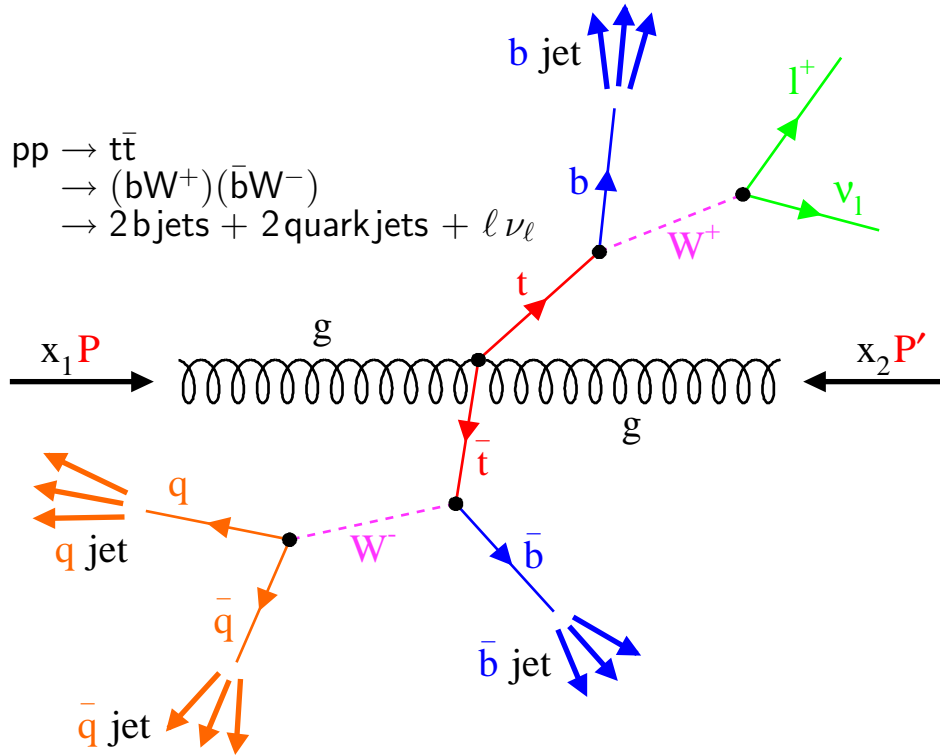
Figure 2.5: Sketch of the $t\bar{t}$ decay topology in the case of the semileptonic decay channel. The two incoming gluons carrying the proton momentum fractions x_1P and x_2P' respectively produce a $t\bar{t}$ pair which is balanced in $p_\perp$ taking the two incoming gluons as longitudinal axis. The top quarks decay in a W boson and a b quark. Here one W boson decays to a charged lepton and the corresponding (anti-)neutrino. The other W boson decays into a light $q\bar{q}$ pair which will be detected as the b quark through the jets of their fragmentation products.

the top quark decays almost exclusively into a b quark and a W boson. While the W boson decays into a fermion antifermion pair of a weak isospin doublet as indicated in table 2.1, the relatively long living b quark builds a hadronic bound state before it decays. Taking into account the three different lepton generations, about 33% of all W bosons decay leptonically. The remaining 67% of W bosons decay into a quark antiquark pair, predominantly of the first two quark generations, where a degeneration factor of three according to the three colours of the strong interaction has to be taken into account. Here about 11% of all $t\bar{t}$ events decay dileptonically. The remaining fraction of $t\bar{t}$ events decay to about 44% fully hadronically and semileptonically respectively. Neglecting the τ lepton which in turn decays only to about 35% into an electron or muon, the fraction of semileptonically decaying $t\bar{t}$ pairs decreases to 30%. As an example, the production and decay of a $t\bar{t}$ pair in the semileptonic decay channel is shown in figure 2.5. The fractions of all $t\bar{t}$ decay modes are summarized in table 2.1.

3

Simulation tools and methods

This chapter gives an overview of the tools and methods necessary to carry out a self-contained analysis from the generation of scattering processes to the reconstruction of observables including the processing of events through the detector simulation. Among other things it will be explained how to implement matrix elements in an Monte-Carlo event generator. Therefore a brief insight into the kinematics of hard subprocesses is useful.

3.1   Kinematics of $2 \rightarrow 2$ processes

The beam protons at the LHC will have an energy of $E = 7\,\text{TeV}$ which gives rise to a total center of mass energy of

$$\sqrt{s} = 2E = 14\,\text{TeV} \tag{3.1}$$

for the collision of two protons. However, the two partons entering into the hard interaction carry only a fraction x_1 and x_2 of the proton momenta. Their four momenta can be described by

$$
\begin{aligned}
p_1 &= E(x_1, 0, 0, x_1)\,, \\
p_2 &= E(x_2, 0, 0, -x_2)
\end{aligned}
\tag{3.2}
$$

assuming particle one flying in positive and particle two flying in negative z direction. A sketch of the partons with their four momenta is shown in figure 3.1. The incoming partons are not put on mass shell since their corresponding four vectors would be time-like but the partons inside a particle as the proton are always virtual and thus space-like. These space-like virtualities are introduced in the framework of the initial state parton shower. The squared center of mass energy of the two incoming partons is defined by

$$\hat{s} = (p_1 + p_2)^2 = x_1 x_2 s\,. \tag{3.3}$$

The fractions x_1 and x_2 can also be expressed by the variables

$$\tau = x_1 x_2, \qquad y = \frac{1}{2}\ln\frac{x_1}{x_2}\,, \tag{3.4}$$

whereas τ in turn can be written in the convenient form
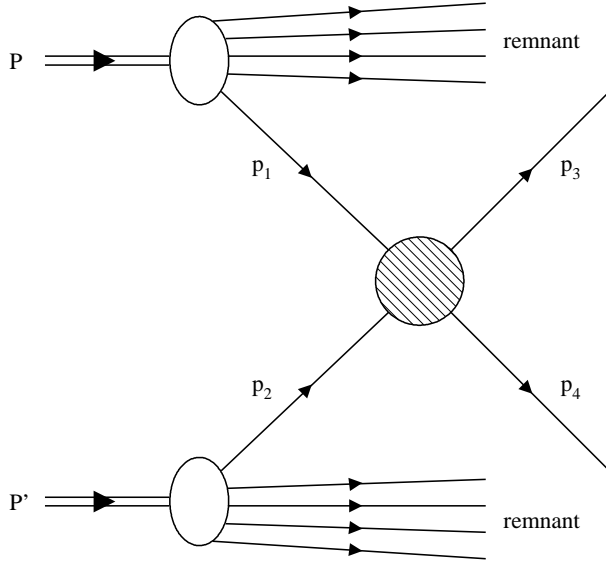
$$\xi = \ln(\tau)\,. \tag{3.5}$$

Figure 3.1: The $2 \rightarrow 2$ scattering process at the LHC. Two partons coming from the protons undergo a hard scattering process. They carry only the proton momentum fractions x_1 and x_2 respectively. The remaining fractions are kept by the proton remnants. The incoming partons of the hard subprocess carry the four momenta p_1 and p_2 and the produced outgoing partons carry the four momenta p_3 and p_4. The amplitude of the parton scattering is visualized by the hatched circle.

These transformed variables turn out to be very useful as will be shown in section 3.5. To complete the kinematics of a $1+2 \rightarrow 3+4$ process two more variables are necessary. These are the azimuthal angle ϕ around the beam axis by which the whole scattering process may be rotated and the polar angle $\hat{\theta}$ of the outgoing partons. The azimuthal angle ϕ is isotropically distributed for unpolarized beams as at the LHC and no more considered here. The hard scattering process can also be expressed in terms of the Mandelstam variables $\hat{s}$ of equation (3.3) and

$$\hat{t} \;=\; (p_1 - p_3)^2 \;=\; (p_2 - p_4)^2 \;=\; -\frac{\hat{s}}{2}\left((1 - 2\frac{m_t^2}{\hat{s}}) - \beta_{34}\cos\hat{\theta}\right) , \qquad (3.6)$$

$$\hat{u} \;=\; (p_1 - p_4)^2 \;=\; (p_2 - p_3)^2 \;=\; -\frac{\hat{s}}{2}\left((1 - 2\frac{m_t^2}{\hat{s}}) + \beta_{34}\cos\hat{\theta}\right) . \qquad (3.7)$$

with

$$\beta_{34} = \sqrt{1 - 4\frac{m_t^2}{\hat{s}}} . \qquad (3.8)$$

Only two of the three variables are independent since they are related via the equation

$$\hat{s} + \hat{t} + \hat{u} = 2m_t^2 . \qquad (3.9)$$

The equations hold also in the case of massless outgoing particles where the top mass m_t has to be set to zero. The cross section for the process $1 + 2 \rightarrow 3 + 4$ can now be written as

$$\sigma \;=\; \int_0^1 dx_1 \int_0^1 dx_2 \int_{-s}^0 d\hat{t}\, f_1(x_1, Q^2) f_2(x_2, Q^2)\frac{d\hat{\sigma}}{d\hat{t}} , \qquad (3.10)$$

$$=\; \int_0^1 \frac{d\tau}{\tau} \int_{-\infty}^\infty dy \int_{-1}^1 d\cos\hat{\theta}\, x_1 f_1(x_1, Q^2)\, x_2 f_2(x_2, Q^2)\frac{d\hat{\sigma}}{d\cos\hat{\theta}} . \qquad (3.11)$$

The choice of the Q^2 scale at which the parton density functions $f_i(x, Q^2)$ of the two protons have to be evaluated is not unique, but since the partonic center of mass system is in general longitudinally boosted by the Lorentz factor

$$\gamma = \cosh \psi = \frac{x_1 + x_2}{2\sqrt{\tau}} \, , \tag{3.12}$$

against the hadronic center of mass system which coincides at the LHC with the lab system it is convenient to express the scale in form of transverse variables which are invariant under such a boost. In the case of outgoing massive particles the Q^2 scale is here chosen to be [Sjo94]

$$Q^2 = \hat{m}_\perp^2 = m_t^2 + \hat{p}_\perp^2 = m_t^2 + \frac{\hat{t}\hat{u} - m_t^4}{\hat{s}} = m_t^2 + \frac{\hat{s}}{4} \beta_{34}^2 \sin^2 \hat{\theta} \, , \tag{3.13}$$

where $\hat{m} \equiv m_t^2 + \hat{p}_\perp^2$ is the transverse mass of the hard subprocess. For massless particles the expression simplifies to $Q^2 = \hat{p}_\perp^2$. After the cross section has been considered it can be related to the number of expected events in a specific experiment. An important aspect of the performance of the LHC collider is given by the luminosity L of equation (1.1). For a given process with cross section σ of equation (3.11) the number of events expected during a considered time period is given by

$$N = \sigma \int L dt = \sigma \mathcal{L} \, . \tag{3.14}$$

where $\mathcal{L}$ is the time integrated luminosity [Loh90].

3.2   The parton shower approach

Since matrix elements are only calculated to finite order of perturbation theory of radiative corrections an additional model based on the technique of parton showering [Ell96] can be used to take into account contributions of all orders of α_s. The model is applied at squared four momentum vectors above an infra-red cut-off parameter $Q^2_{\min}$ which is typically set to $1 \, \text{GeV}^2$. Subsequently, a phenomenological model can be appended for the hadronisation of partons. In an intermediate evolution step of the showering the relative $p_{\perp i}$ of a daughter particle i is restricted by the condition $p_{\perp \max} = Q_i/2$. To match this condition to the transverse momentum of the matrix element with its scale $Q^2 = m_t^2 + \hat{p}_\perp^2$, the shower begins at the scale $Q^2_{\max} = 4\hat{p}_\perp^2 = 4(Q^2 - m_t^2)$. In case of $2 \to 1 \to 2$ processes with an intermediate resonance which is in a colour singlet, the $Q^2_{\max}$ scale for the final state radiation would simply have to be set to the squared mass of the resonance. As for the matrix element, the choices of the $Q^2_{\max}$ scales for the initial and final state shower evolutions are not unambiguous. The branching of the partons

$$\left. \begin{array}{c} q \to qg \\ g \to gg \\ g \to q\bar{q} \end{array} \right\} \quad QCD \tag{3.15}$$

$$\left.\begin{array}{c} q \to q\gamma \\ \ell \to \ell\gamma \end{array}\right\} \quad QED \tag{3.16}$$

is described by the corresponding splitting kernels which provide the probability for the splitting at a given momentum and energy distribution between the two daughter particles. The outgoing partons build time-like showers, the final state radiation which begins at the matching scale $Q^2_{\max}$ and developes towards decreasing scales down to the cut-off parameter $Q^2_{\min}$. In contrast the incoming partons develop space-like showers which are backward evoluted from the matching scale to a given cut-off parameter. This is the initial state radiation.

3.3   The hadronisation

After the partons have been evolved to their final state they have to be transformed into observable hadrons. The hadronisation processes take place at low momentum transfers corresponding to long distance scales. This non perturbative regime will be described by models.

Independent fragmentation

The most simple method for generating hadron distributions from parton distributions is to assume that the partons fragment independently from each other [Fie91]. A fragmenting quark builds a meson with an antiquark from a $q\bar{q}$ pair of the vacuum. The energy will be shared between the meson and the remaining quark of the vacuum which in turn fragments in the same way. This process continues until the remaining energy fraction falls below a cut-off value. The limited transverse momentum results from the relative transverse momentum of the produced $q\bar{q}$ pair which is assumed to be Gaussian distributed. A gluon fragments by splitting into a $q\bar{q}$ pair with subsequent fragmentation as described above. One problem of the model is the absence of colour treatment.

String fragmentation

Within the string model [And86] the hadronisation is described by colour strings between a $q\bar{q}$ pair, or a quark (antiquark) and the proton remnant. Two partons lose energy to the colour string which is stretched between them and the energy is uniformly distributed over the whole length of the string. By spontaneous production of $q\bar{q}$ pairs and di-quark pairs the string breaks up into fragments of hadron size. These fragments are combined to colourless mesons in case of $q\bar{q}$ pairs or baryons in case of di-quark pairs in conjunction with an additional quark q. Gluons form kinks in a colour string which take the energy and momentum of the gluons. The fragmentation of kinked strings yields an angular distribution of hadrons different from that of the independent fragmentation model and in better agreement with experimental results.

Cluster fragmentation

The cluster hadronisation model [Web84] forms colour singlets of the partons after their production through the formation of clusters. Every cluster corresponds to a colour singlet which decays into hadrons. The formation of colour singlets is achieved by non-perturbative splitting of gluons remaining after the parton shower. After the splitting neighbouring quarks and antiquarks can be combined to colour singlets. The mass spectrum of the cluster is steeply falling for large masses and typical cluster masses have two to three times the value of the cut-off parameter $\sqrt{Q_{\min}^2}$. For low cut-off values of the order 1 GeV the cluster can be treated as a superposition of meson resonances which decay into mesons and baryons according to their available phase space. The energy and transverse momentum distribution is in good agreement with experimental results.

3.4   Monte-Carlo event generators

To generate the $t\bar{t}$ signal events the Monte-Carlo event generators PYTHIA 5.7 [Sjo94], PYTHIA 6.1 [Sjo00] and HERWIG 6.1 [Cor99] have been used. All these event generators treat the signal events in LO with $2 \to 2$ matrix elements (two incoming partons and two outgoing partons, the top quarks) as shown in the figures 2.4 and 2.3. The event generators have been used with their default settings. Only the masses of the t, b quarks and the W boson have been modified according to table 3.1 and the parton densities of CTEQ4L [Lai97] have been used as default. Further parameters are varied in section 4.3 for the investigation of systematic uncertainties on the top mass.

Particle	Initial settings of PYTHIA 5.7 [GeV]		Used as default values [GeV]	
	Pole mass	Total width	Pole mass	Total width
t	160.0	1.123	175.0	1.542
b	5.0	—	4.6	—
W	80.25	2.068	80.41	2.072

Table 3.1: *Modified input parameters of the event generators used.*

3.5   Implementation of matrix elements in PYTHIA

For investigations beyond the $2 \to 2$ matrix elements of the $t\bar{t}$ production, several $2 \to 6$ matrix elements were implemented in PYTHIA 5.7. These are the $gg, q\bar{q} \to t\bar{t} \to 6$ fermions matrix elements in the on-shell approximation for the intermediate top quark and W boson from M. Flesch [Ber98a]. In the partonic final state they include beside the b quarks the fermion antifermion pairs coming from the W bosons. These matrix elements also allow to switch on an intermediate neutral Higgs boson with adjustable vector boson, scalar and pseudoscalar Yukawa coupling strengths. In addition

the $gg, q\bar{q} \rightarrow t\bar{t} \rightarrow 6$ fermions matrix elements, realized by S. Slabospitsky were implemented in PYTHIA 5.7 [Sla01]. According to Kleiss and Stirling [Kle88] they dispose of a Breit-Wigner smeared top mass and off-shell W boson masses. The investigation of background processes was done using the CompHEP [Puk99] package, the event generator PYTHIA 5.7 and additional matrix elements. These are some $2 \rightarrow 5$ matrix elements for the single top production and some $2 \rightarrow 4$ matrix elements for the W boson production implemented in PYTHIA [Sla01].

As an example the implementation of the $gg, q\bar{q} \rightarrow t\bar{t} \rightarrow 6$ fermions matrix elements from [Ber98a] into PYTHIA 5.7 is explained below. Before the initialisation of the event generator via a call to the subroutine PYINIT, the external processes $gg \rightarrow t\bar{t}$ and $q\bar{q} \rightarrow t\bar{t}$ have to be declared by a call to the subroutine PYUPIN, e.g.

$$\text{PYUPIN}(191,\text{'qq\textasciitilde}-> \text{tt\textasciitilde}-> 6 \text{ fermions'}, \text{qqsigmamax}) \tag{3.17}$$

$$\text{PYUPIN}(192,\text{'gg}\quad-> \text{tt\textasciitilde}-> 6 \text{ fermions'}, \text{ggsigmamax}) \tag{3.18}$$

where the unused process numbers 191 and 192 are assigned to the external processes. The process numbers N are followed by a comment string and the maximum of the differential cross section $d\sigma/dV_n$ multiplied by the considered volume $\int dV_n$ of the n dimensional phase space. Their values can be found by an extrapolatory run. The external processes can be switched on as usual by setting

$$\text{MSUB}(191)=1 \tag{3.19}$$

$$\text{MSUB}(192)=1 \tag{3.20}$$

before the call of the subroutine PYINIT. For the generation of a hard scattering process the user has to provide the subroutine

$$\text{PYUPEV}(\text{N}, \frac{d\sigma}{dV_n} \int dV_n) \quad , \tag{3.21}$$

which has to treat the relevant process N chosen from PYTHIA and returns the value $d\sigma/dV_n \int dV_n$ which averaged over a large number of events corresponds to the total cross section of the given process. The generated events will be accepted by PYTHIA with a probability $(\frac{d\sigma}{dV_n} \int dV_n)/\text{qqsigmamax}$ or $(\frac{d\sigma}{dV_n} \int dV_n)/\text{ggsigmamax}$ respectively. The application of this acceptance/rejection method separately for each individual subprocess allows the generation of several processes together in the right mixture. Since the differential cross section for the considered processes is strongly peaked in a few phase space regions the probability to accept an event is on average small and the phase space variables have to be transformed into smoother ones. The differential phase space for the implemented $2 \rightarrow 6$ processes

$$dV_n = dx_1 \, dx_2 \, d\cos\hat{\theta} \, d\theta^*_{\ell+} \, d\phi^*_{\ell+} \, d\theta^*_{\ell-} \, d\phi^*_{\ell-} \, d\theta^*_b \, d\phi^*_b \, d\theta^*_{\bar{b}} \, d\phi^*_{\bar{b}} \tag{3.22}$$

counts $n = 11$ variables neglecting the rotation of the whole event by an arbitrary angle ϕ around the longitudinal axis. The first three variables have already been introduced and
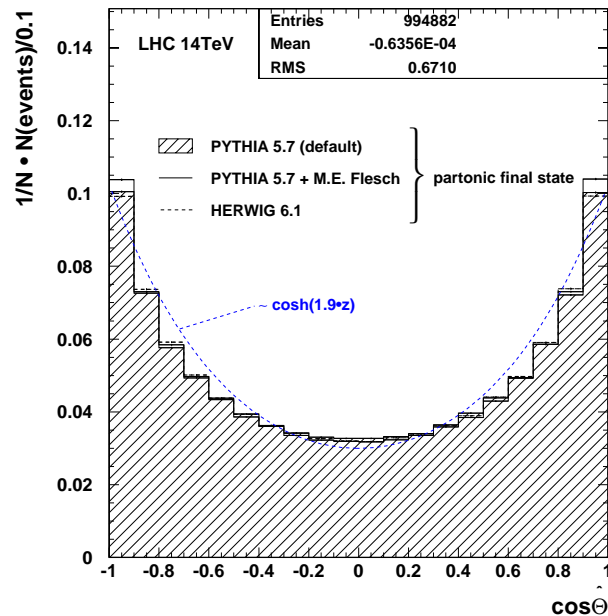
Figure 3.2: The distribution of the uniformly generated random variable $\cos\hat{\theta}$ of the hard subprocess for the event generators HERWIG 6.1, PYTHIA 5.7 with its default $2 \to 2$ matrix elements and with the implemented $2 \to 6$ matrix elements in the on-shell approximation. The distributions agree quite well. The distribution of the implemented matrix elements disposes of slightly enhanced populations in the edges. The plotted distribution $z = \cos\hat{\theta}$ can be approximately described with the function $\cosh(1.9z)$. Generating the random variable z according to this function would yield an improved efficiency.

the others are the polar and azimuthal angles of the two leptons in the case of a dileptonic event and the b, $\bar{b}$ quarks. The angles here have to be evaluated in the rest frame of their parent top quark respectively. The differential cross section can then be written as

$$\frac{d\sigma}{dV_n} = \sum_{ij} f_i(x_1, Q^2) f_j(x_2, Q^2) \frac{d\hat{\sigma}_{ij}}{dx_1 dx_2 d\cos\hat{\theta} d\theta^*_{\ell^+} d\phi^*_{\ell^+} d\theta^*_{\ell^-} d\phi^*_{\ell^-} d\theta^*_{b} d\phi^*_{b} d\theta^*_{\bar{b}} d\phi^*_{\bar{b}}} \ , \quad (3.23)$$

which is the product of the parton distributions and the matrix elements, summed over all allowed incoming parton flavours i and j. The event generation begins with the selection of explicit values of the variables, uniformly distributed in the phase space $\int dV_n$, i.e. $0 < x_1, x_2 < 1$, $-1 < \cos\hat{\theta} < 1$, $0 < \theta^*_{\ell^+}, \theta^*_{\ell^-}, \theta^*_b, \theta^*_{\bar{b}} < \pi$ and $0 < \phi^*_{\ell^+}, \phi^*_{\ell^-}, \phi^*_b, \phi^*_{\bar{b}} < 2\pi$. The matrix element has to be evaluated at the chosen point in the phase space and returns the corresponding differential partonic cross section $d\hat{\sigma}/dV_n$. The value which is returned to PYTHIA is the product of the phase space volume $\int dV_n$ and the differential hadronic cross section $d\sigma/dV_n$ which in turn is obtained by multiplication of the partonic differential cross section with the parton distributions. With the variables above, the acceptance of an event by PYTHIA is very low, and the generation of a few events takes hours. Therefore the most peaking variables x_1, x_2 and $\cos\hat{\theta}$ are transformed. Note, that it is not necessary to find an exact (analytical) transformation to the phase space of perfectly homogeneous distributed variables. It is sufficient to find a simple transformation into a phase space where the variables are smoother behaved. The loss in efficiency will be acceptable while the physics results remain unchanged in any case. According to the inverse transformation method [Pre94] a desired distribution $f(z)$ can be obtained for the random variable z by choosing a uniformly distributed random variable u which corresponds to the integral function of the desired distribution $u = F(z)$. The original random variable z is then given by the inverse of the integral function $F^{-1}(z)$. To obtain the new phase space $\int dV'_n$
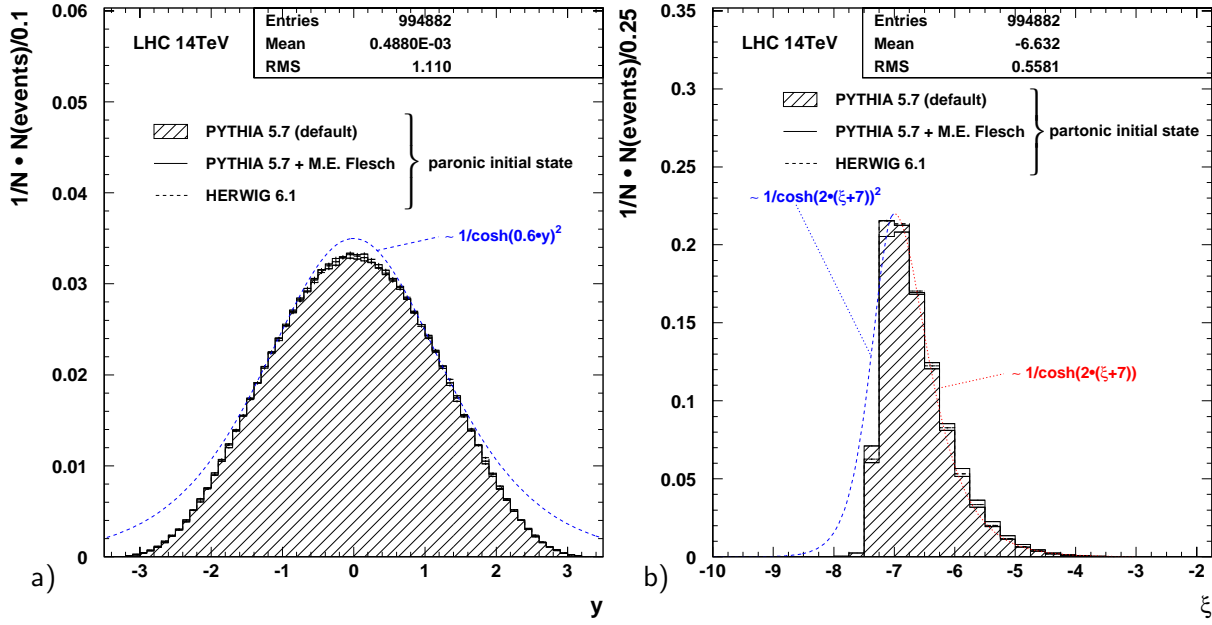
Figure 3.3: *The distributions of the transformed variables y and ξ of the equations 3.4 and 3.5. The distributions of the different used matrix elements are in good agreement. The used functions for a more effective generation of the random numbers are also indicated.*

the differential variable dz has to be substituted by the transformed one through

$$dz = \left| \frac{\partial z}{\partial u} \right| du \ , \tag{3.24}$$

where the Jacobian determinant $|\partial z / \partial u|$ ensures that the result does not depend on the choice of a specific random variable. So the usage of the transformed variable u implies an additional multiplicative factor which has to be taken into account by the evaluation of the differential cross section.

As an explicit example lets consider the cosine of the top scattering angle θ of the hard subprocess. The distribution is shown in figure 3.2 for the event generators HERWIG 6.1 and PYTHIA 5.7 with its default $2 \to 2$ matrix elements and with the implemented $2 \to 6$ matrix elements in the on-shell approximation. The variable $z = \cos \hat{\theta}$ which has to be uniformly chosen in the interval $-1 \leq z \leq 1$ can be approximately described by the function

$$f(z) = \cosh(1.9z) \ . \tag{3.25}$$

Its integrated function is then given by

$$F(z) = \frac{\sinh(1.9z)}{1.9} = u \ , \tag{3.26}$$

whereas the transformed variable has to be chosen in the interval

$$u_a = \frac{-\sinh(1.9)}{1.9} \leq u \leq \frac{\sinh(1.9)}{1.9} = u_b \ . \tag{3.27}$$

The original variable z which has to be provided for the explicit calculation of the matrix element can be obtained by inversion of equation (3.26) as

$$z = \frac{\text{arsinh}(1.9u)}{1.9} = \frac{\ln(1.9u) + \sqrt{(1.9u)^2 + 1}}{1.9} \ .$$
(3.28)

Now the the Jacobian determinant can be determined according to the inverse mapping theorem by its inversion as

$$\left|\frac{\partial z}{\partial u}\right| = \frac{1}{\left|\frac{\partial u}{\partial z}\right|} = \frac{1}{\cosh(1.9z)} \ .$$
(3.29)

The new phase space can be written as

$$\int dV_n' = \int du \, dV_{n-1}' = \int du \int dV_{n-1}'$$
(3.30)

with $\int_{u_a}^{u_b} du = u_b - u_a = 2\sinh(1.9)/1.9$ and finally the product of the differential cross section, the Jacobian determinant and the new phase space

$$\frac{d\sigma}{dV_n'}\left|\frac{\partial z}{\partial u}\right|_{z=z_0} \int dV_n' = \frac{d\sigma}{dV_n'}\bigg|_{V'0} \frac{1}{\cosh(1.9z_0)} \frac{2\sinh(1.9)}{1.9} \int dV_{n-1}'$$
(3.31)

has to be returned to PYTHIA. The differential cross section and the Jacobian determinant have to be evaluated at the chosen random variables. No integration is carried out over the phase space of the remaining $n - 1$ random variables, since two of them, the variables x_1 and x_2 will be transformed, too.

The Jacobian determinant for the transformation of the variables x_1, x_2 into the variables y and ξ which are plotted in figure 3.3 is given by

$$\left|\frac{\partial x_1 \partial x_2}{\partial y \ \partial \xi}\right| = \frac{1}{\left|\frac{\partial y \ \partial \xi}{\partial x_1 \partial x_2}\right|} = \frac{1}{\begin{vmatrix} \frac{1}{2x_1} & -\frac{1}{2x_2} \\ \frac{1}{x_1} & \frac{1}{x_2} \end{vmatrix}} = x_1 x_2 \ .$$
(3.32)

For the production of an on-shell $t\bar{t}$ pair the partonic center of mass energy squared is restricted to

$$4m_t^2 \leq \hat{s} \leq s \ ,$$
(3.33)

which can be translated to the phase space limits

$$\xi_a = \ln\left(\frac{4m_t^2}{s}\right) \leq \xi \leq 0 = \xi_b \ .$$
(3.34)

Assuming that one proton fraction reaches its maximum at 1, e.g. $x_1 = 1$, the fraction x_2 has to be greater than $\exp(\xi)$. Insertion in equation 3.4 (right) results in the limits

$$y_a = \frac{\xi}{2} \leq y \leq -\frac{\xi}{2} = y_b \ .$$
(3.35)

The original variables x_1 and x_2 can be obtained by the equations

$$x_1 = \exp(\frac{\xi}{2} + y), \qquad x_2 = \exp(\frac{\xi}{2} - y) \ . \tag{3.36}$$

The restricted phase space of the new variables and their smoother behaviour already leads to an important improvement of the efficiency. But it can be further improved by a transformation of the variables y and ξ. For the variable y the function

$$f(y) = \frac{1}{\cosh^2(0.6y)} \tag{3.37}$$

describes the distribution approximately. The transformed variable, designated as r is given by the integrated function

$$F(y) = \frac{1}{0.6} \tanh(0.6y) = r \tag{3.38}$$

and has to be chosen uniformly in the interval

$$r_a = \frac{1}{0.6} \tanh(0.6y_a) \leq r \leq \frac{1}{0.6} \tanh(0.6y_b) = r_b \ , \tag{3.39}$$

which gives the new partial phase space $\int dr = r_b - r_a$. The original variable y is then obtained by the inverse function

$$y = \frac{1}{0.6} \text{artanh}(0.6r) = \frac{1}{0.6} \ln \left(\sqrt{\frac{1 + 0.6r}{1 - 0.6r}} \right) \tag{3.40}$$

and the Jacobian determinant is given by

$$\left| \frac{\partial y}{\partial r} \right| = \frac{1}{\left| \dfrac{\partial r}{\partial y} \right|} = \cosh^2(0.6y) \ . \tag{3.41}$$

The last variable which has to be transformed is ξ. The asymmetric distribution is divided into two intervals I below and above $\xi_i = -7$ (see figure 3.3) to optimize the efficiency. The two intervals cover the ranges

$$I_\alpha = \{\xi \in \mathbb{R} : \xi_a = \leq \xi \leq \xi_i = -7\} \tag{3.42}$$

and

$$I_\beta = \{\xi \in \mathbb{R} : \xi_i = -7 \leq \xi \leq \xi_b = 0\} \ , \tag{3.43}$$

where the values for ξ_a and ξ_b have already been evaluated in (3.34). The choice of the interval which has to be evaluated is free. If the ratio, with which the intervals I_α and I_β are randomly chosen is given by p_α / p_β, the choice can be accomplished by a random number generated in the interval $[0, p_\alpha + p_\beta]$ and subsequent branching to I_α (I_β) in the

case of a random number smaller (greater) than p_α. To compensate for the smaller phase space of the chosen interval I_α (I_β) the weighting factor $\frac{p_\alpha+p_\beta}{p_\alpha}$ ($\frac{p_\alpha+p_\beta}{p_\beta}$) has to be taken into account by multiplying with the partial phase space. Following this procedure the intervals decouple and they can be treated independently. The two functions

$$f_\alpha(\xi) \quad = \quad \frac{1}{\cosh^2(2(\xi+7))} \qquad \forall\, \xi \in I_\alpha \tag{3.44}$$

$$f_\beta(\xi) \quad = \quad \frac{1}{\cosh(2(\xi+7))} \qquad \forall\, \xi \in I_\beta \tag{3.45}$$

are used for an efficient generation of the ξ distribution of figure 3.3 (b). The function f_α of the left interval I_α does not describe the distribution very well but it is easy to integrate with the result

$$F_\alpha(\xi) = \frac{1}{2}\tanh(2(\xi - \xi_i)) = t_\alpha \tag{3.46}$$

and also its inverse function can be given in the closed form

$$\xi = \frac{1}{2}\mathrm{artanh}(2t_\alpha) + \xi_i\,. \tag{3.47}$$

The new random variable t_α has to be chosen in the interval

$$t_{\alpha a} = \frac{1}{2}\tanh(2(\xi_a - \xi_i)) \leq 0 = t_{\alpha b} \tag{3.48}$$

of the new partial phase space $\int dt_\alpha = t_{\alpha b} - t_{\alpha a}$ and the Jacobian determinant

$$\left|\frac{\partial \xi}{\partial t_\alpha}\right| = \frac{1}{\left|\frac{\partial t_\alpha}{\partial \xi}\right|} = \cosh^2(2(\xi - \xi_i)) \tag{3.49}$$

has to be taken into account. If the second interval I_β has been chosen, the function f_β is relevant and its integration yields

$$F_\beta(\xi) = \arctan(\exp(2(\xi - \xi_i))) = t_\beta\,. \tag{3.50}$$

The inverse function is given by

$$\xi = \frac{\ln\left(\tan(t_\beta)\right)}{2} + \xi_i \tag{3.51}$$

and the new random variable t_β has to be chosen in the interval

$$t_{\beta a} = \frac{\pi}{4} \leq t_\beta \leq \arctan(\exp(-2\xi_i)) = t_{\beta b} \tag{3.52}$$

of the new partial phase space $\int dt_\beta = t_{\beta b} - t_{\beta a}$. The Jacobian determinant is given by

$$\left|\frac{\partial \xi}{\partial t_\beta}\right| = \frac{1}{\left|\frac{\partial t_\beta}{\partial \xi}\right|} = \cosh(2(\xi - \xi_i))\,. \tag{3.53}$$
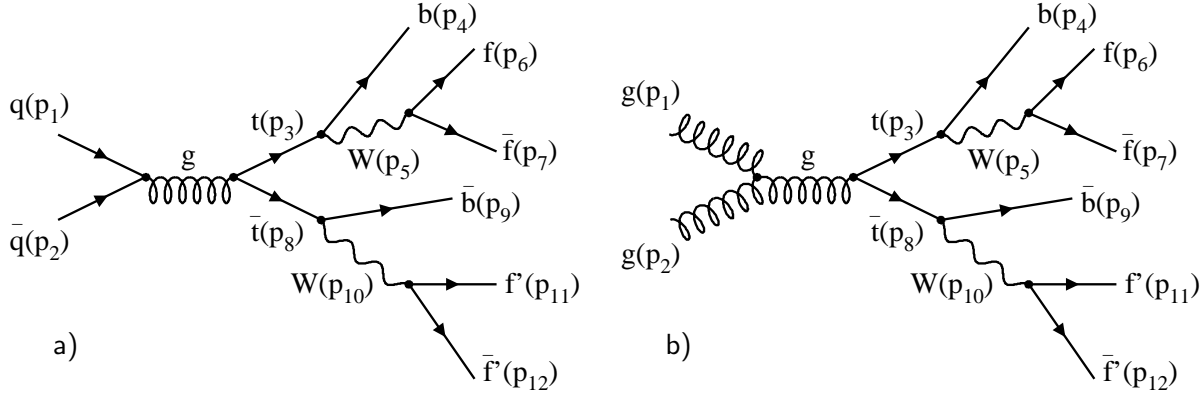
Figure 3.4: The implemented matrix element $q\bar{q} \to t\bar{t} \to 6f$ of the process number 191 (a) and exemplary for the gluon fusion process (number 192) the implemented three gluon vertex matrix element $gg \to t\bar{t} \to 6f$ (b). The particle momenta are enumerated as used in the subroutine PYUPEV.

It is convenient to choose the branching fractions p_α and p_β of the intervals I_α, I_β to be

$$p_\alpha = \int_{t_{\alpha a}}^{t_{\alpha b}} dt_\alpha \; , \tag{3.54}$$

$$p_\beta = \int_{t_{\beta a}}^{t_{\beta b}} dt_\beta \; , \tag{3.55}$$

since the product of the partial phase space and the weighting factor yields unity and thus does not have to be considered further. Having the three most peaking variables transformed, the efficiency of the acceptance rejection method for the implemented $2 \to 6$ on-shell matrix elements is even (slightly) faster than the default $2 \to 2$ matrix elements implemented in PYTHIA corresponding to a gain in speed of more than three orders of magnitude. It should be mentioned that the transformations are tuned to the top mass of $m_t = 175$ GeV such that artificially large differing top masses (by more than $10\,\%$) slow down the generation speed considerably. The remaining eight not transformed random variables, i.e. the azimuthal and polar angles of the leptons and the b quarks yield the partial phase space $\int dV_{n-3} = \int dV'_{n-3} = 16\pi^8$ and finally the expression

$$\left. \frac{d\sigma}{dV'_n} \right|_{V'^0} \left(\left| \frac{\partial z}{\partial u} \right|_{z_0} \left| \frac{\partial x_1 \partial x_2}{\partial y \partial \xi} \right|_{x_{1,2_0}} \left| \frac{\partial y}{\partial r} \right|_{y_0} \left| \frac{\partial \xi}{\partial t} \right|_{\xi_0} \right) \left(\int_{u_a}^{u_b} du \int_{y_a}^{y_b} dy \int dV'_{n-3} \right) \tag{3.56}$$

has to be returned to PYTHIA. The convenient circumstance that the Jacobian determinant of (3.32) equals to the product of the proton fractions $x_1 x_2$ can be exploited for the evaluation of the parton density functions which return the product $x \cdot f_i(x, Q^2)$ of the parton densities and the proton fractions, i.e. the Jacobian determinant is already included in the product of the two evaluated proton density functions and does not have to be multiplied explicitly.
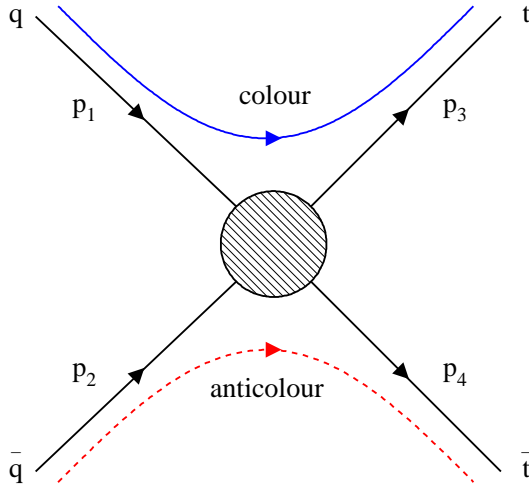
Figure 3.5: Colour flow from the incoming quark antiquark pair of the hard sub process to the outgoing $t\bar{t}$ pair. The flow is unequivocal and it propagates immediately from the top quarks to the corresponding b quarks of the final state of the $2 \rightarrow 6$ matrix element since the W bosons do not couple strongly and the colour charge has to be conserved. Therefore all necessary information about the colour flow is contained in the here displayed $2 \rightarrow 2$ process.

After the evaluation of the matrix element at the chosen values of the random variables, the fixed four vectors of the partons are also provided by the implemented matrix element routines, and their values have to be made accessible for PYTHIA by inserting them into the common block

$$\text{COMMON/PYUPPR/NUP,KUP(20,7),PUP(20,5),NFUP,IFUP(10,2),Q2UP(0:10)} \, , \quad (3.57)$$

with NUP the number of particles, which is twelve in the case of the implemented $2 \rightarrow 6$ matrix elements. By default 20 particle entries are allowed. The index of the matrix element partons is assigned as indicated in figure 3.4. In the KUP array the state, flavour code, position of the mother particle and the colour connected partner particle have to be stored. In case of $t\bar{t}$ production through quark antiquark annihilation the colour flow can be assigned without ambiguities as depicted in figure 3.5. However in case of the gluon gluon fusion there remain two possibilities to assign the colour flow from the gluons to the top quarks as can be extracted from figure 3.6 a) and b). The denominators

$$\text{den}(t) = m_t^2 - (p_1 - p_3)^2 \overset{\text{on-shell}}{\longrightarrow} 2(p_1 \cdot p_3) = \frac{\hat{s}}{2}(1 - \cos\hat{\theta}) \, , \quad (3.58)$$

$$\text{den}(u) = m_t^2 - (p_2 - p_3)^2 \overset{\text{on-shell}}{\longrightarrow} 2(p_2 \cdot p_3) = \frac{\hat{s}}{2}(1 + \cos\hat{\theta}) \quad (3.59)$$

from the virtual top quark propagators corresponding to the t and u channel diagrams of figure 2.4 are considered to take a decision [Sjo94]. If $|\text{den}(t)|$ is smaller than $|\text{den}(u)|$ the t channel dominates over the u channel and the colour flow is chosen as depicted in figure 3.6 a). For the three gluon vertex (figure 2.4 a) it is assumed that the colour flow is the same as for the t and u channel amplitudes. The four momenta and masses of the particles of the hard subprocess have to be assigned to the array PUP. The variable NFUP has to be set to the number of parton pairs that undergo final state showers. It is not possible
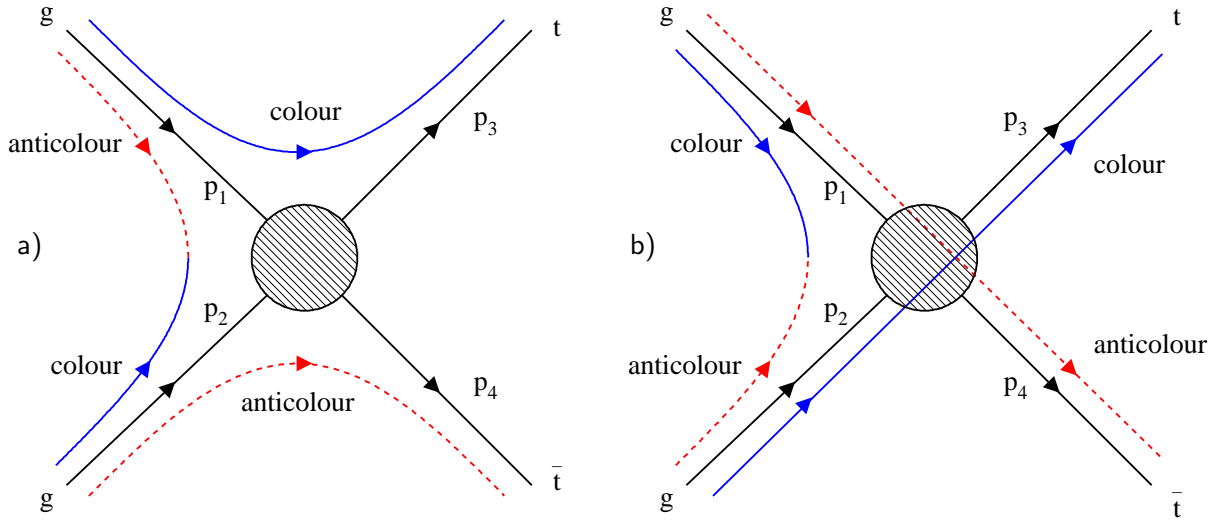
Figure 3.6: Colour flow from the incoming gluons of the hard subprocess to the outgoing $t\bar{t}$ pair. The gluons with a colour charge and anticharge provide the two possibilities of colour flow depicted in a) and b).

to shower a single particle since the energy and momentum of the shower would not be conserved. The fermion pairs of the W boson decays build shower pairs. The b quarks would have to be assigned correctly to the W bosons, but they are only intermediate states in the implemented $2 \rightarrow 6$ matrix elements and thus they can't shower in PYTHIA. As a temporary solution the two b quarks are treated as a shower pair. In the array IFUP the positions of the showering parton pairs have to be assigned and finally in the array Q2UP the Q^2 scales for the shower pairs (Q2UP(0) for the initial state radiation of the two incoming partons) have to be set. For the fermion pairs of the W boson resonances the choice of the scale has to be $Q^2 = m_W^2$. For the b quarks the mass of the parent particles, the top quark pole mass, squared was chosen.

3.6   Parton distributions

After the Monte-Carlo event generators are introduced and some matrix elements are discussed in detail the distributions of characteristic observables like partonic center of mass energies, masses, transverse momenta and pseudo rapidities of the hard partons, i.e. the non radiative partons of the matrix elements help to understand the kinematics of the $t\bar{t}$ production. The used event generators HERWIG 6.1, PYTHIA 5.7 and the $2 \rightarrow 6$ on-shell matrix elements implemented in PYTHIA are compared in this section. Furthermore the different contributions from the gluon gluon fusion and the quark antiquark annihilation processes are shown in comparison.

First the generated distributions of the proton momentum fractions $x_{1,2}$ are discussed

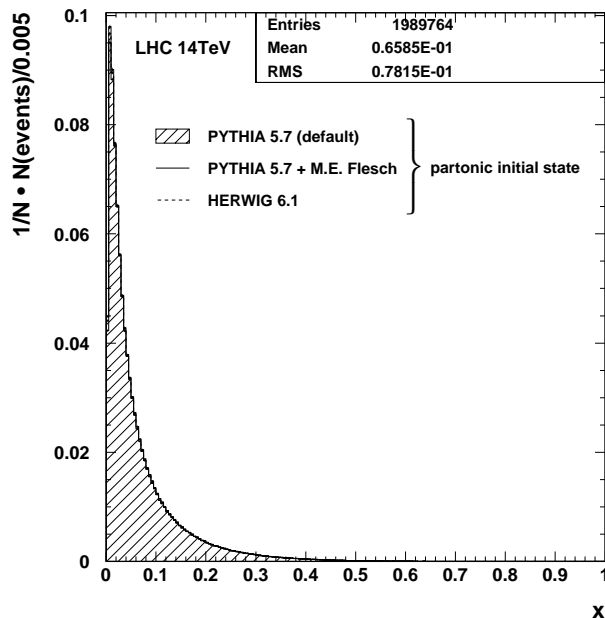*Figure 3.7: Distribution of the generated proton momentum fractions $x_{1,2}$ for the event generators used and the $2 \rightarrow 6$ on-shell matrix elements implemented in PYTHIA. The distributions reach their maximum at very small momentum fractions and they are falling very steeply towards greater momentum fractions. Already at momentum fractions of about $x = 0.4$ the distributions assume negligible values.*

(see figure 3.7). They peak near vanishing momentum fractions and fall steeply towards greater momentum fractions. The same plot presented with logarithmic ordinate can be found in the appendix, figure A.2 a).

Compared to the gluon fusion processes the quark antiquark annihilation processes dominate beyond $x \simeq 0.12$ while they are dominated by the gluon fusion processes below the crossing point as shown in figure 3.8 a). The plots b) c) and d) of the figure show the $\cos\hat{\theta}$, y and ξ distributions respectively. The $\cos\hat{\theta}$ distribution of quark antiquark annihilation processes shows less pronounced maxima at the edges ($\cos\hat{\theta} = \pm 1$) than the distribution of gluon gluon fusion processes. The reason can be found in the denominators of the t and u channel diagramms of the gluon gluon fusion (see equations (3.58) and (3.59)). They appear in the squared and averaged matrix element of the gluon gluon fusion given by equation (2.7). While the t channel provides enhanced scattering amplitudes for $\cos\hat{\theta} = +1$ the u channel dominates at $\cos\hat{\theta} = -1$. Together the gluon gluon fusion favours $\cos\hat{\theta}$ values at the edges. The y distribution of quark antiquark annihilation processes has a broader plateau in the center and its ξ distribution dominates at smaller (more negative) values in comparison to the gluon fusion. The broader rapidity distribution of quark antiquark annihilation processes reflects the broad spectrum of proton momentum fractions x comprising the unbalanced case of valence quark sea antiquark scattering. In contrast the rapidity distribution of gluon gluon fusion processes peaks at vanishing rapidities due to balanced low proton momentum fractions of the gluons. The differences between the $\cos\hat{\theta}$ and y distributions of the two different $t\bar{t}$ production mechanisms could also be used for a separately optimized generation of the phase space variables which would lead to a still improved efficiency. This may be necessary for more difficultly behaved phase space variables of other matrix elements.

The partonic center of mass energy $\sqrt{\hat{s}}$ of figure 3.9 a) shows a steep rise from the production threshold (exactly $2m_t$ for the $2 \rightarrow 6$ on-shell matrix elements) and reaches its
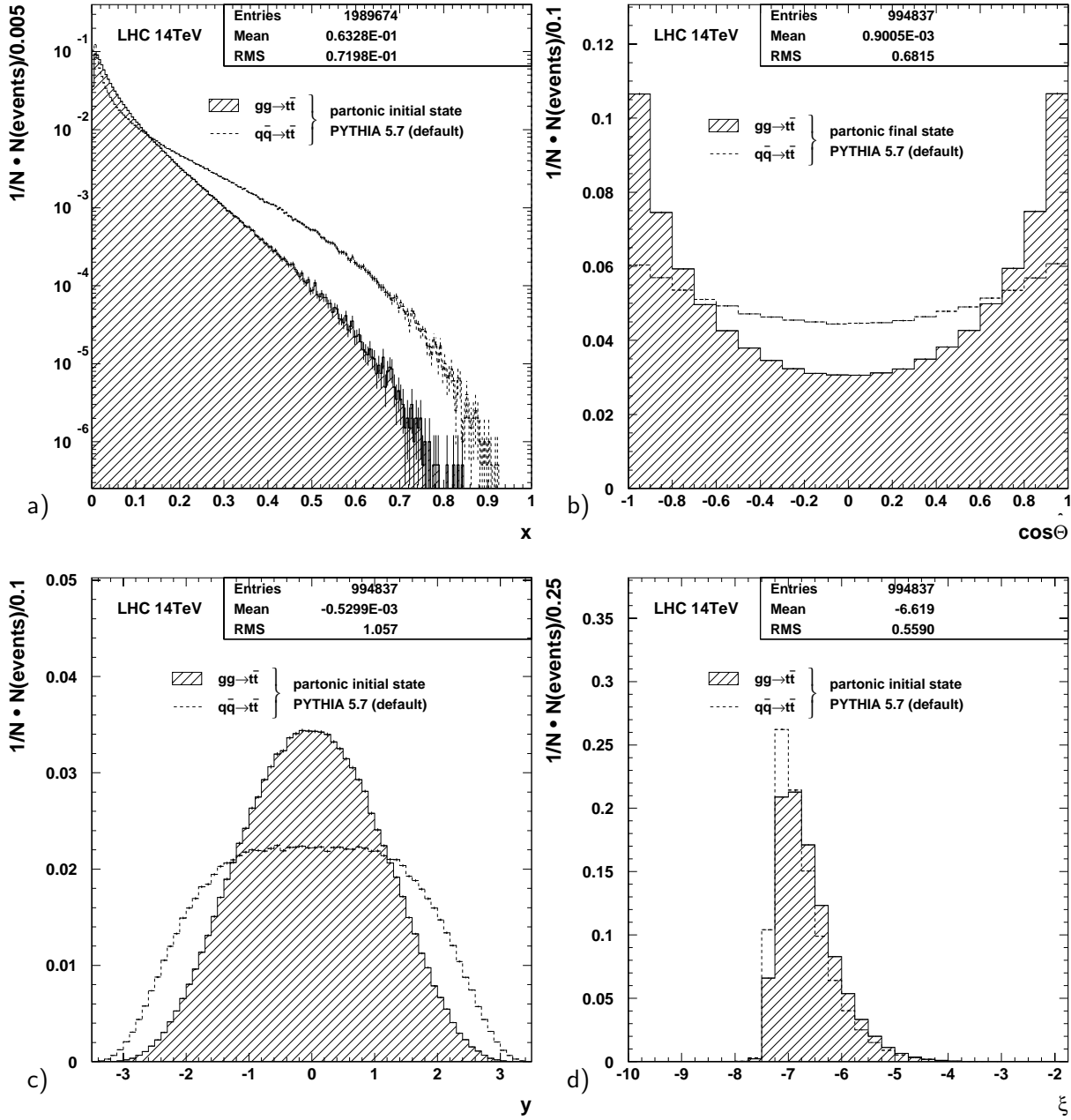
Figure 3.8: *Comparison between the contributions of the gluon gluon fusion and the quark antiquark annihilation processes to the x, $\cos\hat{\theta}$, y and ξ distributions using the event generator PYTHIA 5.7. The proton momentum fractions of the quark antiquark annihilation dominate beyond $x \simeq 0.12$ the gluon fusion. The $\cos\hat{\theta}$ distribution of the quark antiquark annihilation processes shows less pronounced maxima in the edges, its y distribution shows a broader plateau in the center and its ξ distribution dominates at smaller values in comparison to the gluon fusion processes.*
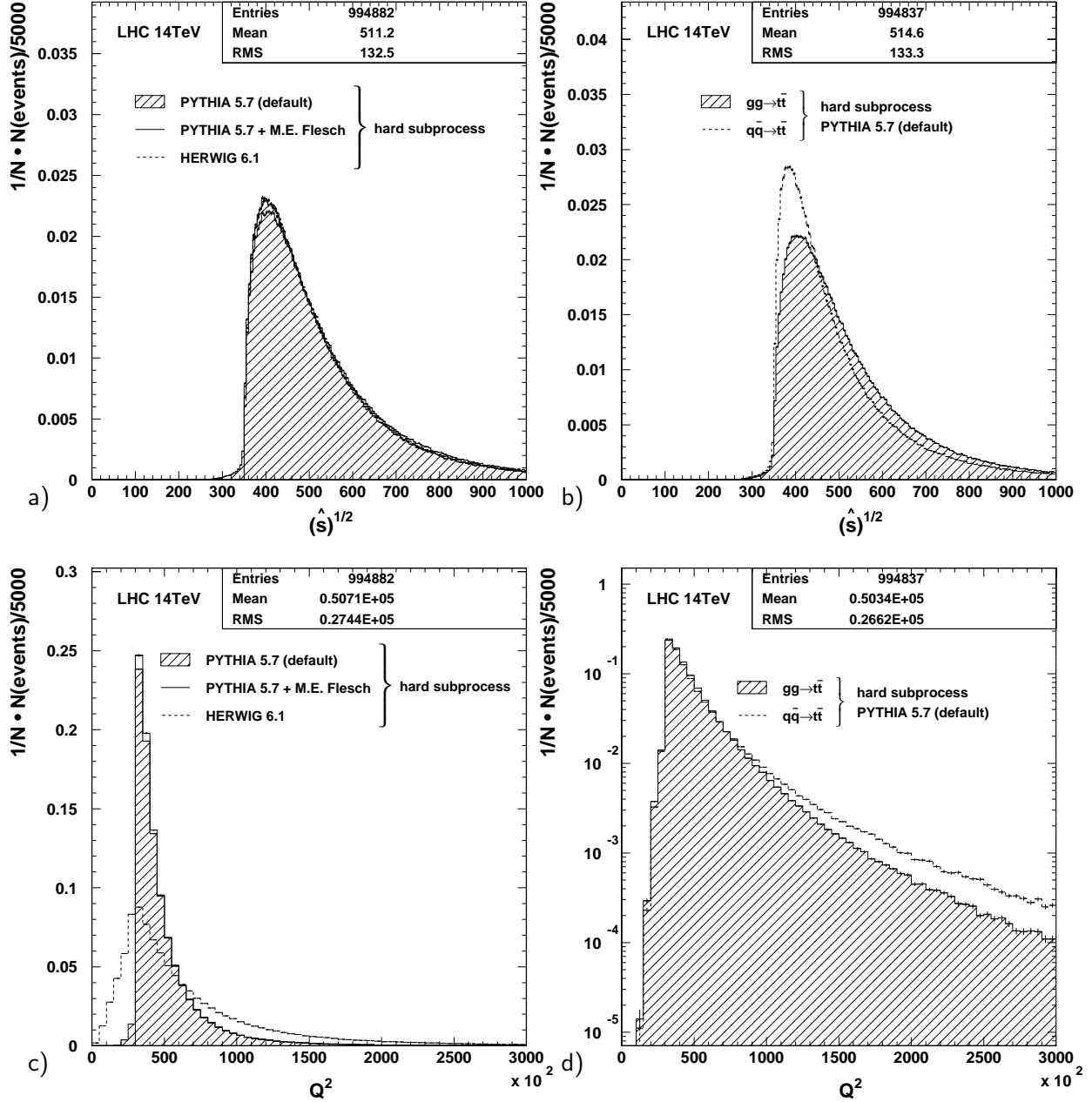
Figure 3.9: The partonic center of mass energy $\sqrt{\hat{s}}$ (top) and the Q^2 distribution of the hard subprocess (bottom). The used event generators agree quite well for $\sqrt{\hat{s}}$. The distribution increases steeply from the $t\bar{t}$ production threshold and reachs its maximum close to it. In comparison to the gluon gluon fusion processes, the quark antiquark annihilation processes show a much more pronounced maximum in the $\sqrt{\hat{s}}$ distribution. The Q^2 scales of HERWIG 6.1 differ quite a bit from the PYTHIA ones due to another definition of the Q^2 scale of the hard subprocess (see text for details). Towards higher Q^2 scales the quark antiquark annihilation processes dominate over the gluon gluon fusion processes.
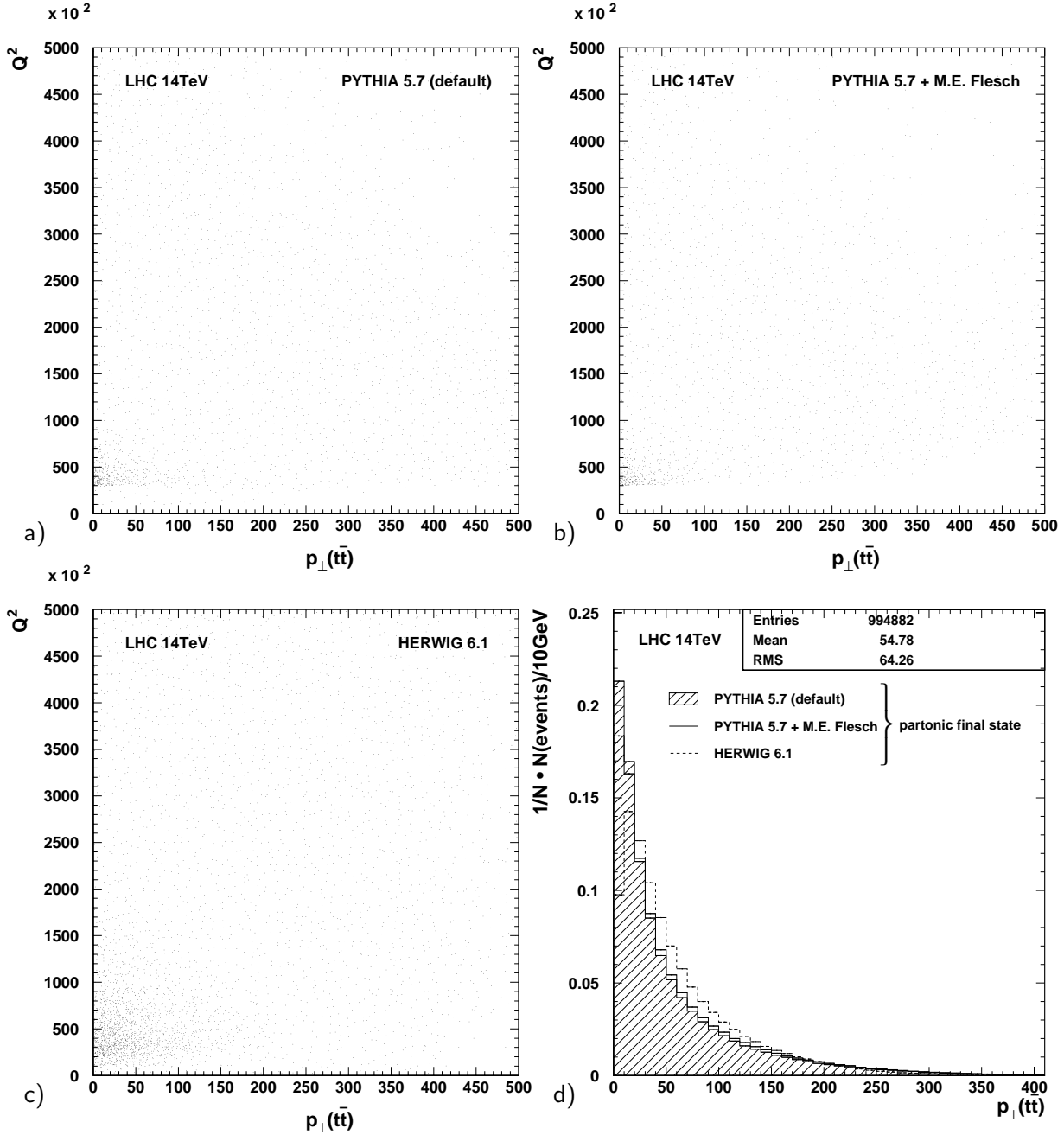
Figure 3.10: *Correlation between the Q^2 scale of the hard subprocess and the transverse momentum of the $t\bar{t}$ system due to initial state radiation for the different event generators (matrix elements) used in the plots a), b) and c). The phase space region at lower Q^2 and $p_\perp(t\bar{t})$ values shows an enhanced population. Apart from that the generated events are rather flatly distributed over a broad range. In plot d) the $p_\perp(t\bar{t})$ spectra of default PYTHIA 5.7 and the implemented $2 \to 6$ on-shell matrix elements are compared. They agree quite well. The prediction of HERWIG 6.1 is shifted towards larger transverse momenta according to the different choice of the Q^2 scale.*
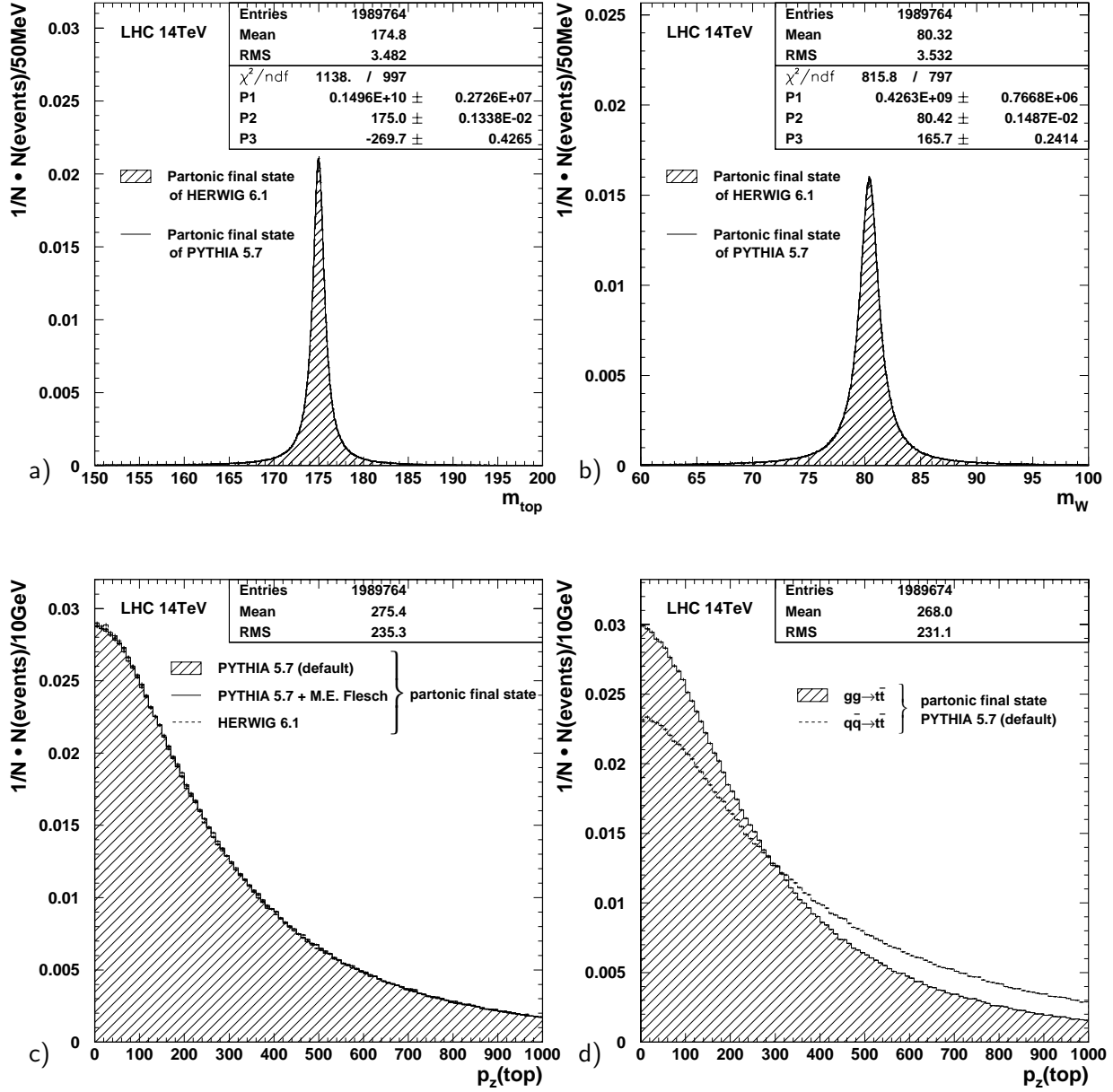
Figure 3.11: The off-shell mass distributions of the top quark (a) and the W boson (b) for the event generators PYTHIA 5.7 and HERWIG 6.1, the top quark longitudinal momentum distributions (c) and the gluon gluon fusion and quark antiquark annihilation processes in comparison for PYTHIA 5.7 (d). The fit of the masses with a relativistic Breit-Wigner function reproduces the parameter settings of the event generators as listed in table 3.1. The central mass value is given by the fit parameter P_2 and the total width is given by the absolute value of the fraction of the fit parameters $|P_3/P_2|$. The longitudinal momenta of the top quarks produced by the quark antiquark annihilation dominate at larger momenta.

Figure 3.12: *The top quark $p_\perp$ spectra (top) and pseudo rapidity distributions (bottom) for different event generators (left) and separately for the gluon gluon fusion and the quark antiquark annihilation processes (right). The plotted parton momenta and pseudo rapidities correspond to the non radiative partonic final state, i.e. to the partons of the hard subprocess before final state radiation.*

Figure 3.13: *The W boson $p_\perp$ spectra (top) and the pseudo rapidity distributions (bottom) for different event generators (left) and separately for the gluon gluon fusion and the quark antiquark annihilation processes (right). The plotted parton momenta correspond to the non radiative partonic final state, i.e. to the partons of the hard subprocess before final state radiation.*

maximum at about $400\,\mathrm{GeV}$. Towards higher energies the distribution decreases continuously due to lower parton densities in the proton at higher momentum fractions which are necessary for more energetic reactions. The squared energy $\hat{s}$ is shown in the appendix, figure A.2 bottom for completeness. The event generators used and the $2 \to 6$ on-shell matrix elements implemented in PYTHIA 5.7 are in good agreement apart from the lower production threshold of the off-shell matrix elements which is marginally populated. The distributions of the quark antiquark annihilation processes show a more pronounced peak in comparison to the distributions of the gluon gluon fusion processes (see figures 3.9 b) and A.2 d).

The Q^2 scale of the hard subprocess has already been described in section 3.5 for the event generator PYTHIA. The distributions have their maximum at the top pole mass squared $m_t^2 \simeq 30\,000\,\mathrm{GeV}^2$. The distributions from default PYTHIA and the $2 \to 6$ on-shell matrix elements implemented agree quite well, while the prediction of HERWIG 6.1 is different. This is due to the fact that HERWIG uses the expression

$$Q^2 = \frac{4\hat{s}\hat{t}\hat{u}}{\hat{s}^2 + \hat{t}^2 + \hat{u}^2} \tag{3.60}$$

for the evaluation of the parton density functions in the heavy quark production (for light fermion production the factor 4 has to be changed to a factor of 2). Towards larger Q^2 scales the quark antiquark annihilation processes dominate slightly over the gluon gluon fusion processes. The same plot with a logarithmically scaled ordinate is given in the appendix, figure A.2 b).

After the Q^2 scale distributions have been discussed the correlation between them and the transverse momentum of the $t\bar{t}$ system due to initial state radiation can be considered (see figure 3.10 a), b) and c). For the event generators used and the $2 \to 6$ on-shell matrix elements implemented in PYTHIA 5.7 the distributions are similar. The phase space region at lower Q^2 scales and $t\bar{t}$ transverse momenta shows an enhanced population which gets diluted towards greater values of the phase space variables. The $p_\perp(t\bar{t})$ spectrum (figure 3.10 d) of the PYTHIA 5.7 event generator with default matrix elements and the implemented one agree quit well. The biggest difference in the first bin can be explained by the on-shell approximation used in the matrix elements of [Ber98a] which is responsible for a hard cut-off of the Q^2 scale at the lower edge $Q^2_{\min} = (m_t^{\mathrm{pol.}})^2$. The event generator HERWIG 6.1 uses its own Q^2 scale which is responsible for the different momentum distribution shifted towards higher transverse momenta.

Next the masses of the top quarks and the W boson resonances are considered. With the given on-shell mass parameter values of table 3.1 the event generators PYTHIA and HERWIG provide the Breit-Wigner mass distributions for the top quark and the W boson as shown in figure 3.11 a) and b). The distributions are fitted with a relativistic Breit-Wigner function (see [Ber92], [Don96])

$$\frac{1}{\left((m_t^{\mathrm{inv.}})^2 - (m_t^{\mathrm{pol.}})^2\right)^2 + (m_t^{\mathrm{pol.}}\Gamma_t)^2} \sim \frac{P_1}{\left((m_t^{\mathrm{inv.}})^2 - P_2^2\right)^2 + P_3^2} \,, \tag{3.61}$$
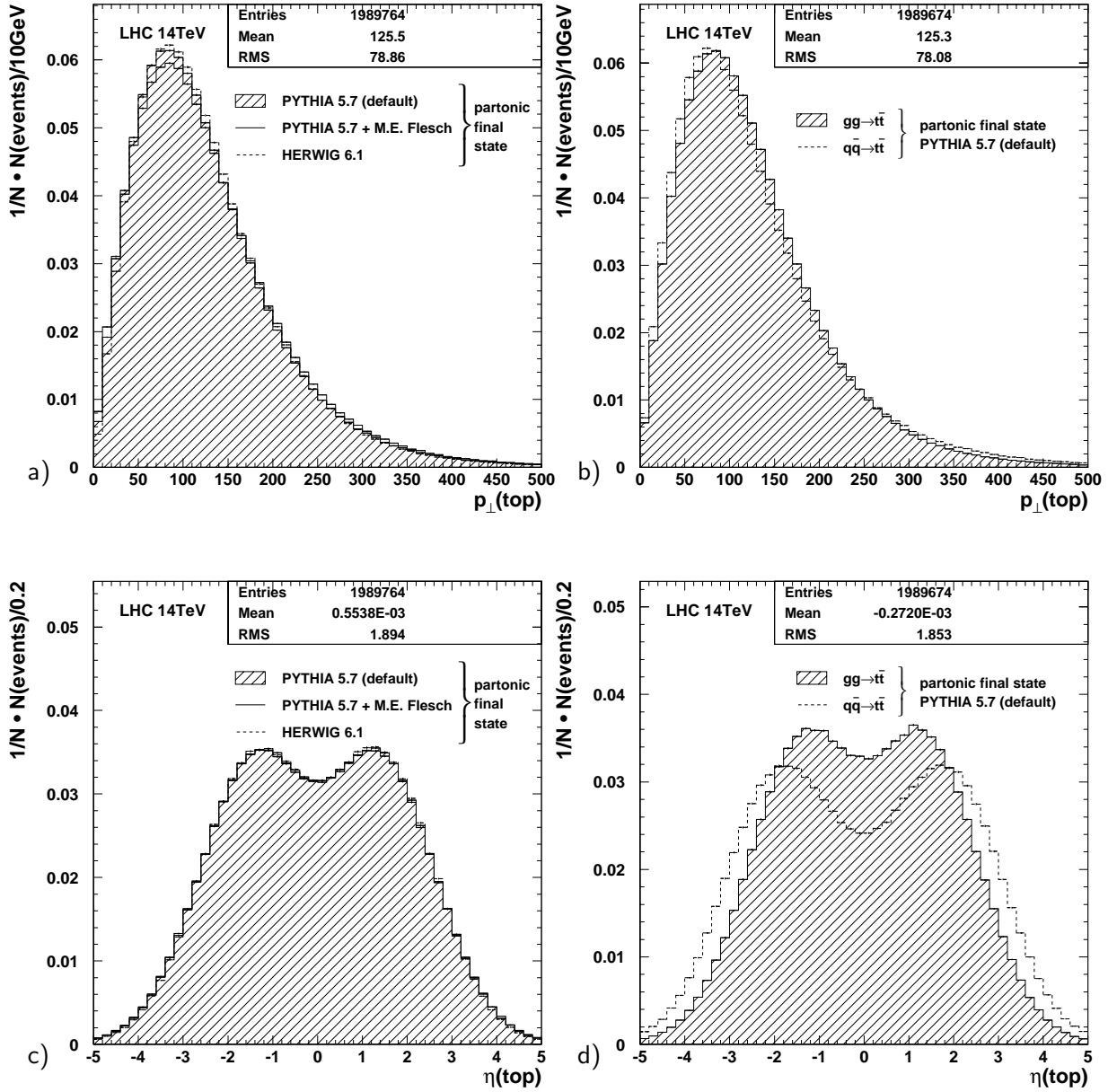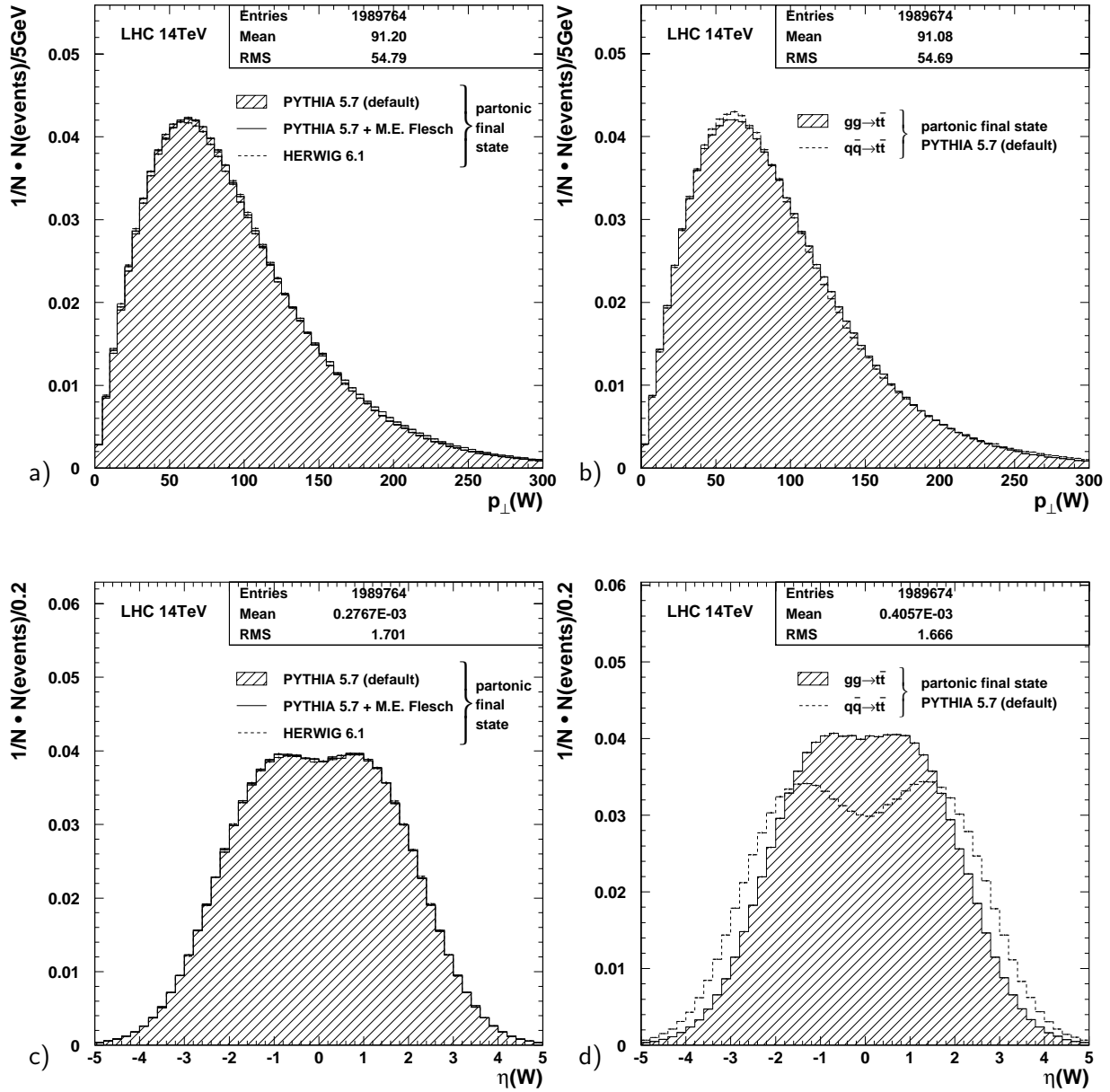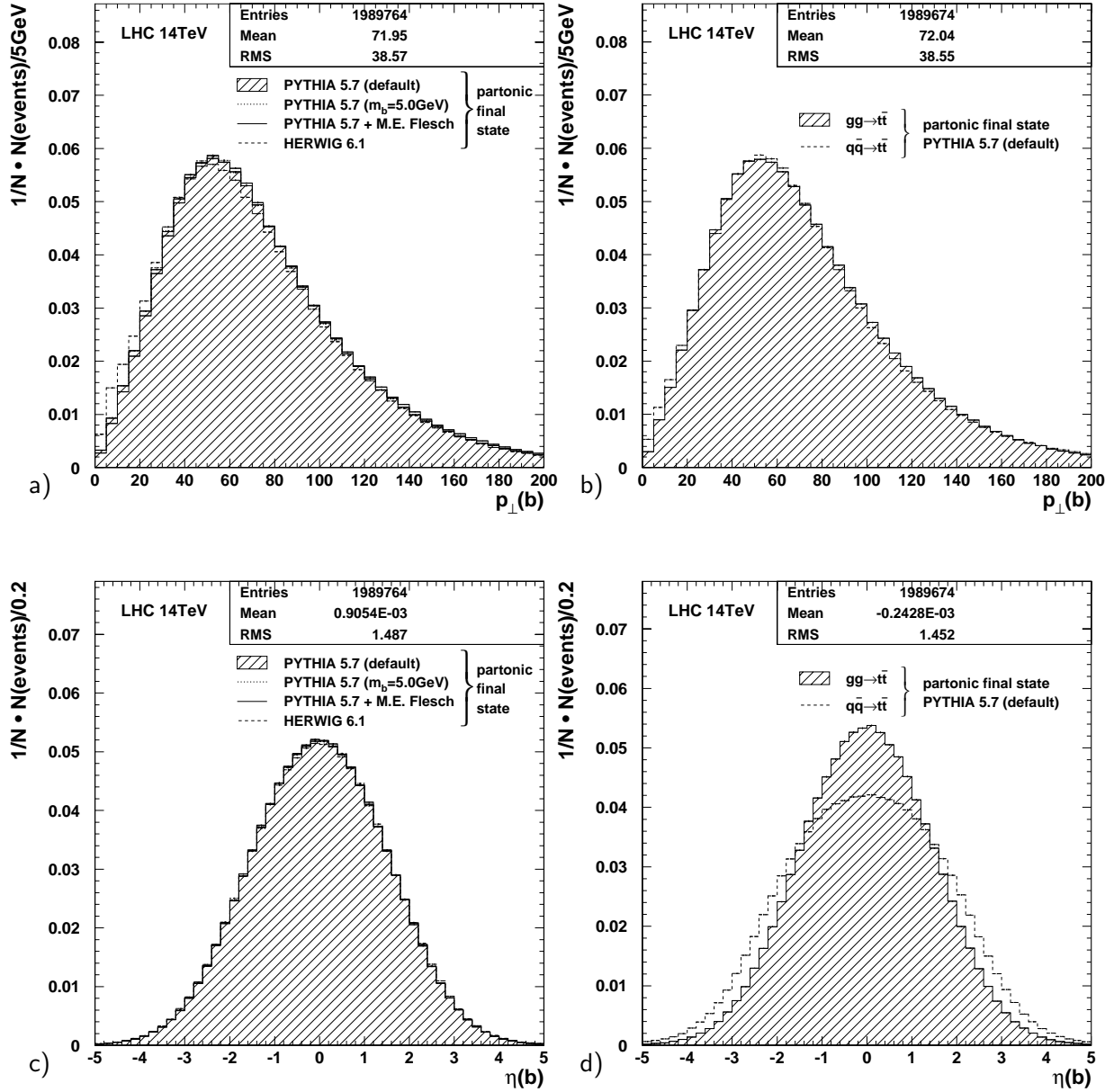
Figure 3.14: The b quark $p_\perp$ spectra (top) and the pseudo rapidity distributions (bottom) for different event generators (left) and separately for the gluon gluon fusion processes and the quark antiquark annihilation processes (right). In addition to the b quark mass value $m_b = 4.6\,GeV$ the distributions obtained with the PYTHIA 5.7 initial value $m_b = 5.0\,GeV$ are shown (left).
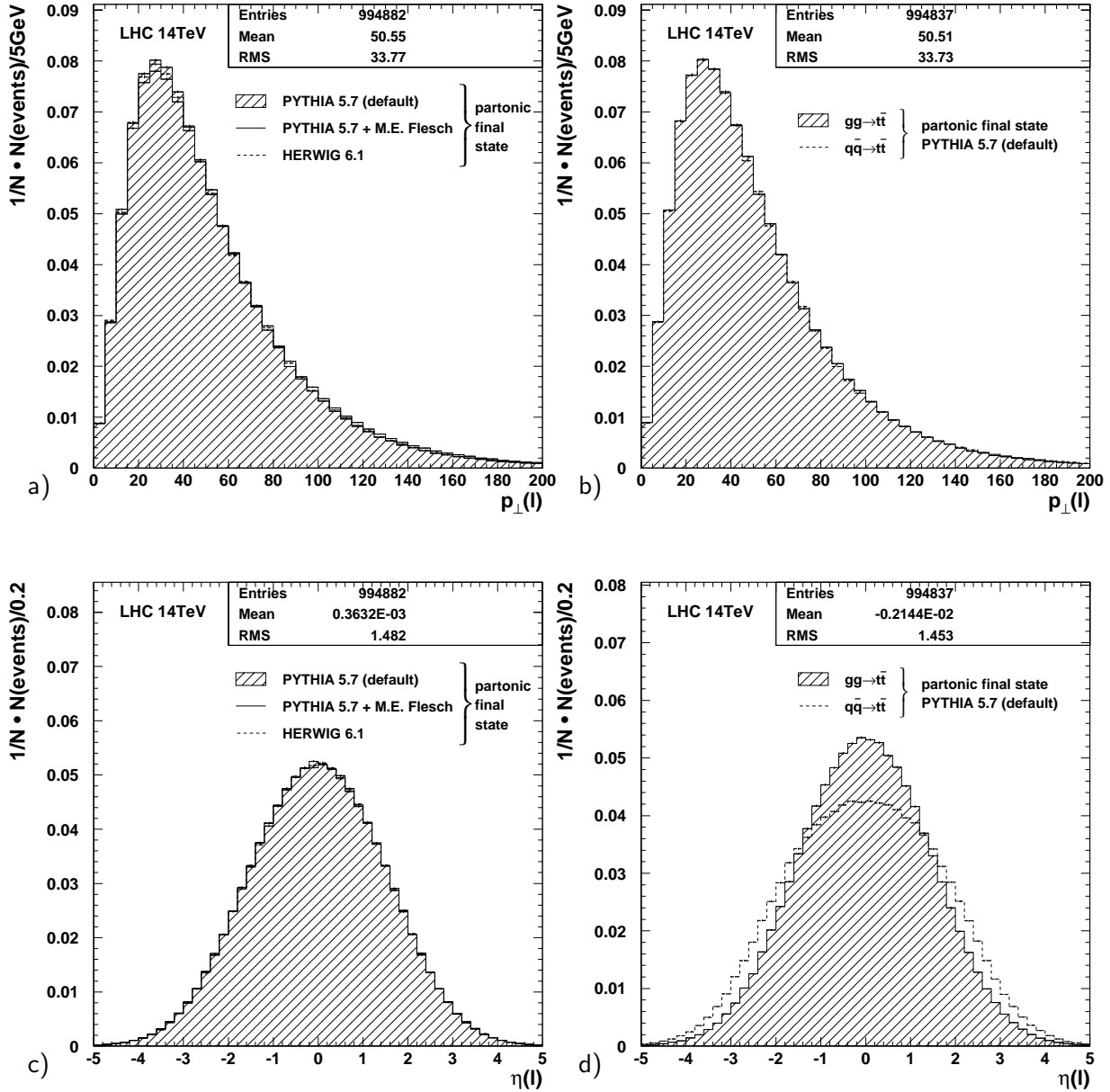
Figure 3.15: The $p_\perp$ spectra (top) and the pseudo rapidity distributions (bottom) of the leptons coming from a W boson of a top quark decay for different event generators (left) and separately for the gluon gluon fusion processes and the quark antiquark annihilation processes (right). The event generators agree very well and also the different $t\bar{t}$ production processes are consistent with each other.
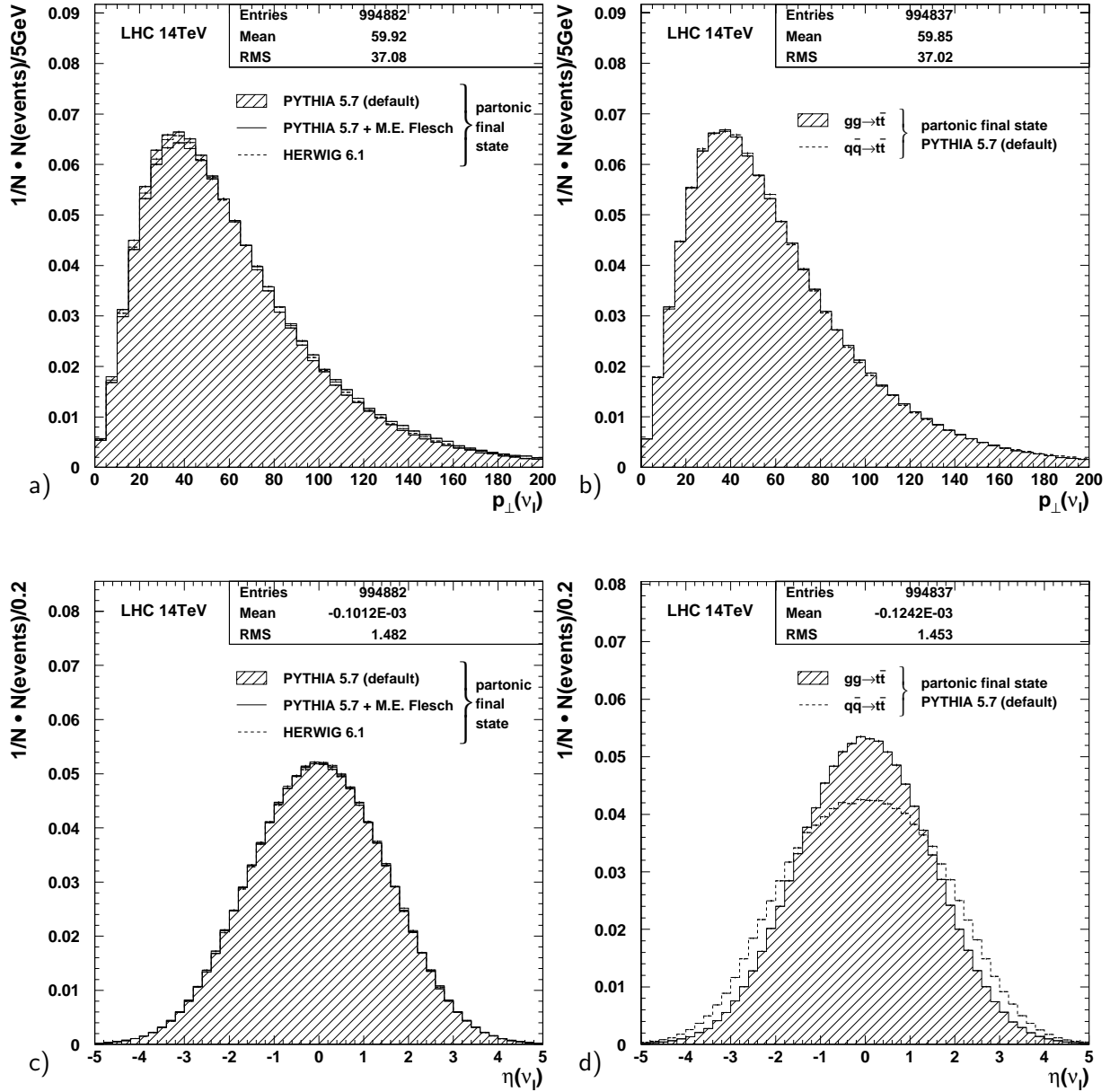
Figure 3.16: The $p_\perp$ spectra (top) and the pseudo rapidity distributions (bottom) of the neutrinos coming from a W boson of a top quark decay for different event generators (left) and the gluon gluon fusion processes in comparison to the quark antiquark annihilation processes (right). The event generators agree very well and also the different $t\bar{t}$ production processes show consistence with each other.
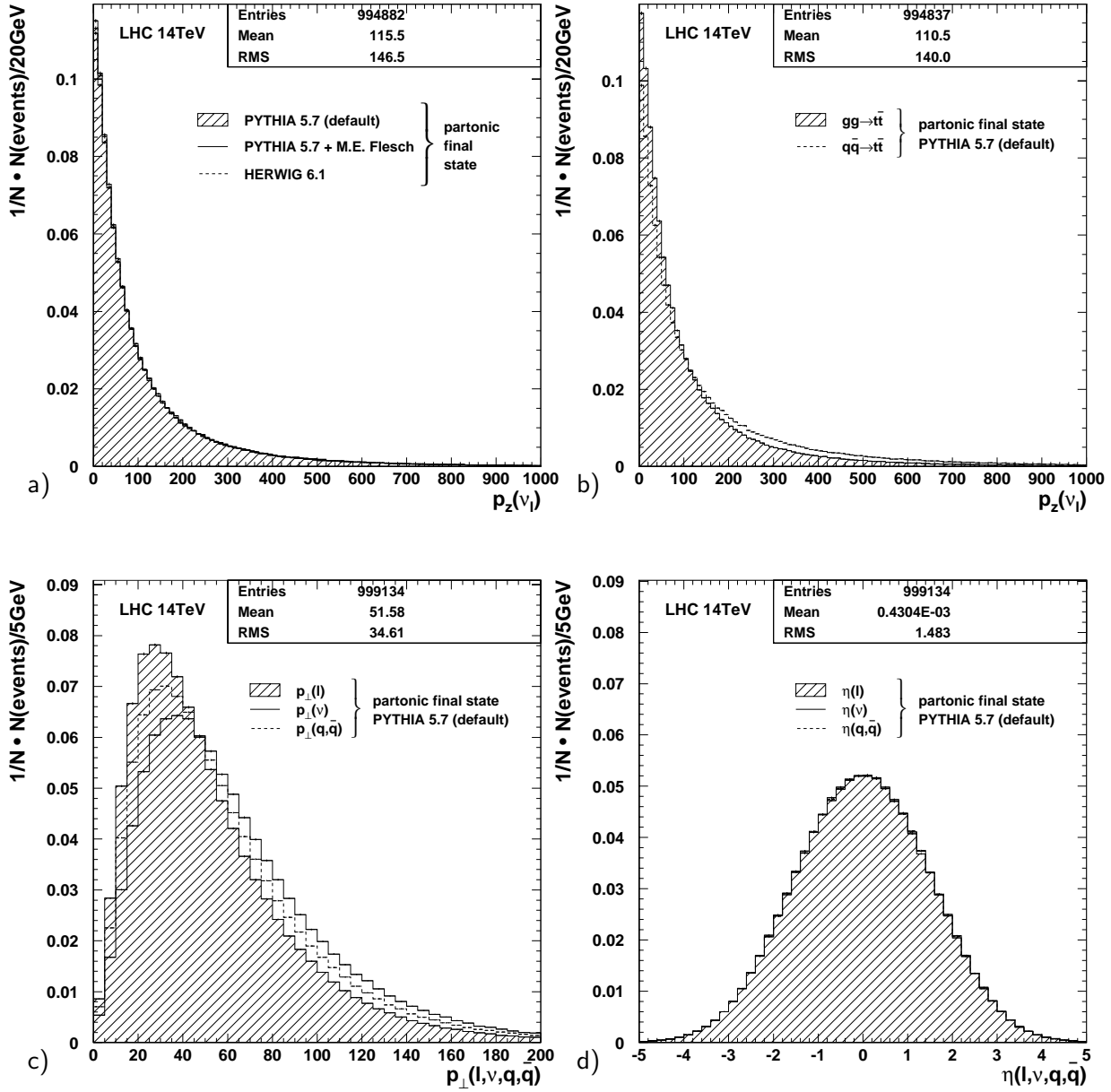
Figure 3.17: *The longitudinal momenta of the neutrinos (top) and the lepton and neutrino transverse momentum spectra and pseudo rapidity distributions (bottom) in comparison. The W boson does not decay isotropically in the standard model. Therefore the distributions of the neutrinos and the corresponding leptons of the weak isospin doublets are different. The summed and averaged distributions of the isospin partners are represented by the distribution of the quarks and antiquarks coming from a W boson of a top quark decay.*

where P_1, P_2 and P_3 correspond to the fit parameters shown in figure 3.11 a) and b). The total decay width of the top can be determined through $\Gamma = |P_3/P_2|$. The resulting widths are $\Gamma_t = 1.54\,\text{GeV}$ and $\Gamma_W = 2.06\,\text{GeV}$. The fit functions can not be distinguished from the coinciding distributions of the two event generators HERWIG 6.1 and PYTHIA 5.7 since the masses are exactly generated according to the fit function. In figure 3.11 (bottom) the longitudinal momenta of the top quarks from the hard subprocess in the partonic center of mass system are compared. The event generators used and the $2 \rightarrow 6$ on-shell matrix elements implemented in PYTHIA agree very well. At lower longitudinal momenta the contribution from gluon gluon processes dominates while towards higher momenta the quark antiquark annihilation processes gain and beyond the crossing point at about $300\,\text{GeV}$ they dominate the spectrum.

The transverse momentum and pseudo rapidity spectra of the top quarks agree quite well for the different event generators as shown in figure 3.12. The $p_\perp$ spectrum of the top quarks from quark antiquark annihilation is slightly softer than for the top quarks from gluon gluon fusion. The pseudo rapidity distributions are symmetric around $\eta = 0$ and the maxima of the distribution are reached at about $\eta = -2$ and $\eta = +2$ giving the distribution the shape of a double hump. The distribution of the pseudo rapidities of the top quarks produced by the gluon fusion is narrower and the dip at the center is less pronounced.

The transverse momentum and pseudo rapidity spectra of the W bosons show a quite similar picture (see figure 3.13). The event generators agree very well and the pseudo rapidity distribution of the W bosons of the gluon gluon fusion processes are narrower in comparison to those of the quark antiquark annihilation processes. The dip in the center of the distribution is almost gone.

The same distributions for the b quarks from the top decay are shown in figure 3.14. For the PYTHIA 5.7 default matrix elements the $p_\perp$ spectra coincide independently of the used b quark mass which has been varied from $m_b = 4.6\,\text{GeV}$ to $m_b = 5.0\,\text{GeV}$. The implemented $2 \rightarrow 6$ on-shell matrix elements agree also very well. The event generator HERWIG 6.1 shows a slightly softer $p_\perp$ spectrum. The spectrum does not depend on the $t\bar{t}$ production process as was already the case for the W boson but it is broader. The pseudo rapidity distributions for the different event generators and b quark masses agree very well. The distributions reach their maximum at the center ($\eta = 0$) and for the gluon gluon fusion processes the distribution is narrower in comparison to the quark antiquark annihilation processes.

Now the decay products of the W bosons from the top quark decays have to be discussed. First the observable charged leptons (see figure 3.15). The used event generators and matrix elements agree very well for the $p_\perp$ spectra and the pseudo rapidity distributions. The $p_\perp$ spectrum is independent of the production process and relatively narrow in comparison to those of the b quarks and also of the W bosons. The pseudo rapidity distributions are quite similar to those of the b quarks.

For the neutrinos of the W bosons which in turn come from the top quarks of the hard subprocess the transverse momenta and pseudo rapidities of figure 3.16 are comparable

to the distributions of the leptons. To see a difference they have to be compared directly. First however the longitudinal momenta of the neutrinos are compared.

The longitudinal momenta p_z of the neutrinos reach their maximum at vanishing momenta as can be seen in figure 3.17 a) and b). Towards higher momenta the shape of the distribution follows the form $1/p_z$ leading to an approximation of the abscissa. The neutrinos in the gluon gluon fusion processes show a higher maximum and the distribution falls more steeply with a crossing point at about $p_z(\nu_\ell) = 100\,\mathrm{GeV}$. In figure 3.17 c) and d) the $p_\perp$ spectra and the pseudo rapidity distributions of the leptons, the neutrinos and also the quarks (antiquarks) of the W bosons are compared. While the pseudo rapidity distributions coincide perfectly, the $p_\perp$ spectra can be distinguished significantly. This is because of the anisotropic decay of the W boson within the standard model. This point is subject of investigation in chapter 5. The leptons have the highest maximum at lower momenta leading to a softer momentum spectrum while the neutrinos have a smaller maximum at higher momenta leading to the hardest momentum spectrum. The momentum spectrum of the quarks and antiquarks from the W bosons take their course exactly between the spectra of the leptons and the neutrinos which build a weak isospin doublet. This is because the quarks and antiquarks build the averaged sum of the isospin doublet partners.

3.7 Detector simulation

The response of a detector is most accurately simulated with the detector description and simulation tool GEANT [Goo94]. The program simulates the passage of elementary particles through matter taking into account geometrical volume boundaries of a given detector and physical effects according to the nature of the particles themself, their interactions with matter and the magnetic field in the detector. In case of the CMS detector the detailed GEANT simulation (based on Fortran) is embedded in the software package CMSIM[1] [Kar00] which allows event generation, particle tracking in the detector with the recording of hits, pile-up of several events, signal and noise simulation and the reconstruction and analysis of events. In addition CMSIM provides an interface to the event display CMSCAN [Alv97] which shows the digitized energy depositions and hits of particle tracks of an event in the detector. The processing of events through the detailed GEANT simulation is very time-consuming and therefore not applicable if millions of events as expected for the $t\bar{t}$ production have to be investigated. To avoid this shortcoming the parameterised fast detector response CMSJET [Abd99] obtained from detailed GEANT simulations of the CMS detector using CMSIM has been built. In comparison to the detailed GEANT simulation the CMSJET detector simulation gains about three orders of magnitude in speed. The parameterised simulation includes the acceptance of the detector as well as degraded response regions due to cracks between barrel and endcap. The track of particles and their point of entry into the calorimeters is calculated taking the magnetic field into account in case of charged particles. The particle momenta and directions are Gaussian

---

[1]**CMS Sim**ulation

smeared according to the parameterizations in the electromagnetic, the hadronic, the very forward calorimeter and the muon system. CMSJET also contains parameterizations of the lateral and longitudinal shower development allowing a hadronic shower to start in the electromagnetic calorimeter with consequent prolongation in the hadronic calorimeter and depositing energy in both calorimeters. The energy depositions are stored in a grid of calorimeter cells according to the CMS detector geometry.

Since the energy scales of the electromagnetic and the hadronic calorimeter are fixed in CMSJET an adjustable absolute energy scale has been implemented for each calorimeter separately. This is important since the absolute energy scale is only known within the uncertainty of its calibration and reconstructed objects as jets and invariant masses of several jets will be affected by the variation of these scales. It should be mentioned that beside the reliable Fortran packages CMSIM and GEANT the transition to object oriented software packages in the programming language $C++$ like ORCA[2] [ORC00] and GEANT4 [Fol00] is forthcoming, but since they also rely on the time-consuming detailed GEANT simulation they couldn't be used here for the investigation of $t\bar{t}$ events either.

In addition, a parametrised tracker response simulation [Dro00] taking into account the precision of reconstructing the track transverse momentum, the angle of direction and the impact parameter was used to measure the impact parameters and its errors for b tagging with the help of the impact parameter method.

The trigger is not simulated but studies based on detailed GEANT simulations show that the trigger efficiency of the process $pp \rightarrow t\bar{t} \rightarrow eX$ achieves 99.3 % [Das98]. This constitutes an important issue for the statistical error in the top mass determination through the semileptonic $t\bar{t}$ decay channel. The detailed analysis of the trigger efficiency in the dileptonic decay channel is not accomplished so far, but there is no reason to expect dramatically reduced efficiencies supposing two high $p_\perp$ leptons and b jets as well as non negligible missing $p_\perp$.

3.8   The cone jet algorithm

A jet can be defined as a certain amount of hadronic and electromagnetic energy within a small opening angle [Cat93]. However, any precise analysis needs to have an exact definition of jets which has to be given by a jet algorithm. Such a jet algorithm should match the intuitive definition of a jet. Different jet algorithms differ in the assignment of the particles to the jets and in the treatment of low energetic particles. These differences are relevant for a comparison of the data with the theory. The comparison is best suited done with a jet algorithm which provides an unambiguous jet configuration for the theoretical predictions and the experimental results.

The cone jet algorithm discussed here [Sey94] builds the four vector of a jet from the four vectors of the particles according to the Snowmass convention [Hut90]. It defines the

---

[2]**O**bject oriented **R**econstruction for **CMS A**nalysis

transverse energy $E_\perp = E \sin \theta$, the pseudo rapidity η and the azimuthal angle ϕ of a jet by

$$E_{\perp \text{ jet}} = \sum_{i \in \text{jet}} E_{\perp i} \,, \tag{3.62}$$

$$\eta_{\text{jet}} = \sum_{i \in \text{jet}} E_{\perp i} \eta_i / E_{\perp \text{jet}} \,, \tag{3.63}$$

$$\phi_{\text{jet}} = \sum_{i \in \text{jet}} E_{\perp i} \phi_i / E_{\perp \text{jet}} \,, \tag{3.64}$$

where the sum runs over the particles i belonging to the jet. According to this definition the jets are treated as massless. The distance between two particles i and j can be expressed by the longitudinal invariant opening angle

$$R_{ij} = \sqrt{(\eta_i - \eta_j)^2 + (\phi_i - \phi_j)^2} \tag{3.65}$$

in η, ϕ space. The invariance reveals its advantage at hadron colliders like the LHC where the partonic center of mass system is in general longitudinally boosted against the hadronic center of mass system.

The algorithm begins with the initialisation of all four vectors above a transverse energy threshold as jet seed. At LHC energies with its large particle multiplicities (about 700 final state particles in the semileptonic decay channel of the $t\bar{t}$ production) the threshold is typically set to $E_\perp = 1\,\text{GeV}$. $E_{\perp\text{jet}}$, η_{jet} and ϕ_{jet} are calculated for every jet seed according to the equations 3.64, where a particle i belongs to a jet if it lies within a radius R to the jet axis, i.e.

$$i \in \text{jet} \iff R_{i,\text{seed}} = \sqrt{(\eta_i - \eta_{\text{seed}})^2 + (\phi_i - \phi_{\text{seed}})^2} < R \,. \tag{3.66}$$

In other words, R is a parameter of the algorithm which defines a cone around the jet axis in which the four vectors have to be taken into account. If the new determined jet axis does not coincide with the old one of the jet seed the new jet axis is taken as jet seed and the jet quantities are calculated once again. This procedure is repeated until the jet axis gets a stable position. In practice this is the case after three to four iterations. All jets obtained in this way are put into a list of proto jets. Jets below a cut-off transverse energy $E_{\perp\text{min}}$ are deleted from the list. A cut-off value of $E_{\perp\text{min}} = 10\,\text{GeV}$ was applied. Among the remaining jets those which lose a fraction f of transverse energy to a jet with higher transverse energy are also canceled from the list of proto jets. Here the parameter f is set to 0.75 as used by the CDF collaboration [CDF92]. Finally all four vectors shared between several proto jet axes are assigned to the proto jet closer in η, ϕ space. The quantities 3.64 of the relevant proto jets are recalculated and the list of proto jets is checked a last time for jets dropping below the transverse momentum threshold $E_{\perp\text{min}}$.

The transverse energy of the reconstructed jets produced in $t\bar{t}$ events are shown in appendix B, figures B.1, B.2 and B.3 for the cone sizes $R = 0.5$ and $R = 0.7$. The jet
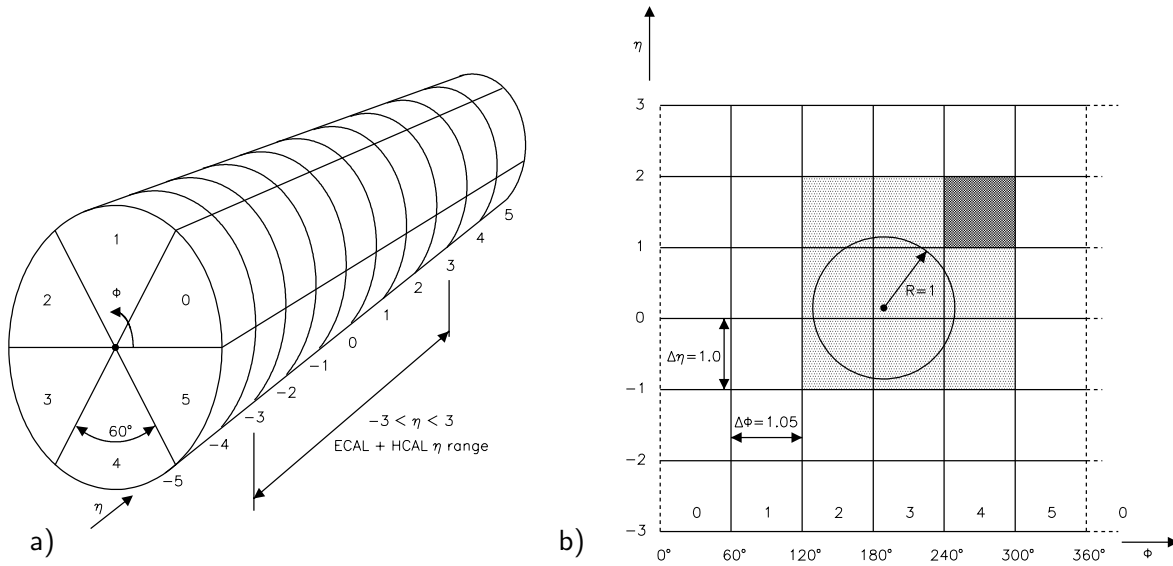
Figure 3.18: The η, ϕ space in which the four vectors are combined to jets. The azimuthal angle is periodical, the pseudo rapidity is not. The cylindrical presentation of the phase space (a) illustrates the periodicity in ϕ. It is divided into a grid of equidistant units as can be seen from the homogeneous plane of the transformed phase space (b). If the unit lengths are taken at least as large as the parameter R of the cone algorithm, which has been taken here to be 1, only neighbouring unit areas to the jet axis can contribute to the jet (dotted squares). Some of them may also be excluded (dark dotted square). This fact can be used to consider only four vectors in the relevant unit areas, which reduces the CPU time by the jet algorithm considerably.

algorithm was applied to the hits in the electromagnetic and the hadronic calorimeter clusters of the parameterised CMS detector simulation.

The method of jet finding with an iterative cone algorithm is in common use by experiments like CDF, H1 and OPAL [Adl99]. In contrast to these experiments the particle multiplicity at the LHC, operating at considerably higher energies, is remarkably enhanced and the CPU time needed by the jet algorithm increases roughly with the second power of the number of jet seeds. Therefore the benefit of infrared safeness [Sey97] through the consideration of the middle of all jet pairs as jet seeds beside the iterative procedure could not be applied for the investigations done in the chapters below. However, no noticable influence can be observed for the reconstructed top, the shape of its invariant mass distribution and the fitted central value of its mass.

The performance of the cone jet algorithm can be improved by dividing the η, ϕ space in a grid as indicated in figure 3.18. There the phase space is exemplary subdivided into equidistant unit areas of length $\Delta\phi = \pi/3 \simeq 1.05$ and height $\Delta\eta = 1.0$, suitable for the cone algorithm with cone size $R = 1$. Choosing the unit lengths of the grid at least as large as the parameter R restricts the four vectors corresponding to a jet with a given axis to the immediately neighbouring unit areas. This can be exploited for an

efficient assignment of four vectors to a jet, where only the relevant unit areas have to be considered. In practice the cone parameter $R = 0.5$ has been used for the determination of the top quark mass (see chapter 4). Here the most efficient division of the grid has turned out to be $\Delta\phi = \pi/12 \simeq 0.26$ and $\Delta\eta = (3 - (-3)/12) = 0.5$. Choosing these values the CPU time needed by the cone jet algorithm could be reduced by a factor of two. It should be mentioned that the refinement of the grid for a better approximation of the cone does help to improve the efficiency but the time needed due to the additional administrative expense dominates.

3.9   The impact parameter method

The tagging of jets arising from the shower and fragmentation of b quarks is accomplished with the impact parameter method which relies on the reconstruction of tracks coming from secondary vertices which can be spatially distinguished (of the order of a few mm's) from the primary vertex due to the long lifetime of mesons and baryons containing a b quark. The tracks are reconstructed with the help of the pixel vertex detector and the impact parameters are determined as the shortest distance between the nominal interaction point and the extrapolation of the reconstructed track. The transverse extension of the bunches is negligible in comparison to its longitudinal extension (see table 1.1). Moreover the alignment in transverse direction is less problematic than the exact timing of the bunch crossings to the nominal interaction point. Therefore only the information of the transverse impact parameter d_{xy} is used here. To take the precision of the measured transverse impact parameter into account it can be divided by its spatial uncertainty $\delta(d_{xy})$ so that more accurately measured impact parameters obtain a larger weight. The resulting expression
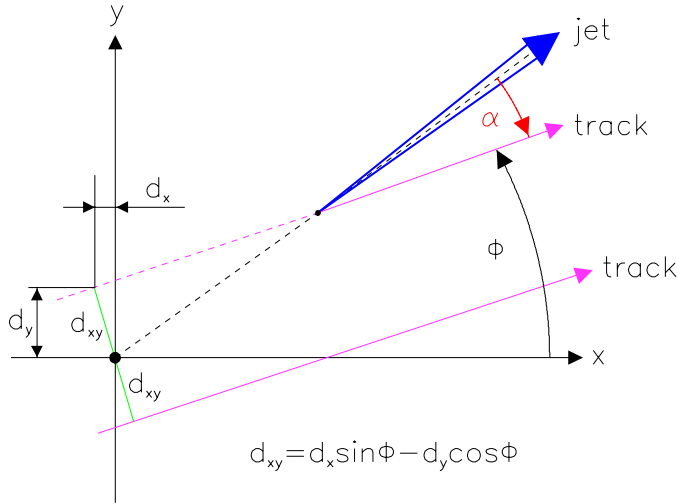
Figure 3.19: The transverse impact parameter d_{xy} from a track crossing the jet axis in front of and behind the primary vertex. The signs of d_{xy} are opposite for the two cases and this is used to distinguish them.

$$\sigma_{xy} = \frac{d_{xy}}{\delta(d_{xy})} \tag{3.67}$$

is called the significance. Now the sign of σ_{xy}, coming from the transverse impact parameter d_{xy} can be used in conjunction with the direction of a considered jet to take the decision if the track belongs to this jet or not, i.e. if it crosses the jet axis in front of the primary vertex or behind (see figure 3.19). In the first case the track is expected to belong to the jet, in the latter it is not. To get an expression with a positive sign in the case of a track belonging to the jet, the significance σ_{xy} is multiplied by the sign of the third component of the cross product $[\vec{p}_{\mathrm{jet}} \times \vec{p}_{\mathrm{track}}]_z$ between the jet axis and the track. This ensures that the sign of the product

$$\sigma_{xy}\mathrm{sign}\left([\vec{p}_{\mathrm{jet}} \times \vec{p}_{\mathrm{track}}]_z\right) \tag{3.68}$$

does not change if a rotation of the event by an arbitrary azimuthal angle ϕ is applied.

4

Top quark mass determination

In this chapter the selection of $t\bar{t}$ events in the semileptonic decay channel, the reconstruction of the top quarks and the determination of the top quark mass will be covered. The influence of potential systematic uncertainties is discussed extensively.

4.1 Event selection in the semileptonic $t\bar{t}$ decay channel

The selection consists of cuts exploiting the unique signature of a $t\bar{t}$ pair in the semileptonic decay channel. To identify the leptonically decaying W boson an isolated lepton and missing $p_\perp$ from the neutrino are required. At least two non b jets have to be found to be combined to the hadronically decaying W boson. To complete the event topology two additional jets have to be tagged as b jets. The selection procedure is shown here as an example for the event generator PYTHIA 5.7 assuming the $3.5 \cdot 10^6$ semileptonic decaying $t\bar{t}$ events expected in $10\,\text{fb}^{-1}$ according to NLO calculations. The huge amount of statistics allows hard cuts, predominantly in jet $E_\perp$ and in b jet identification, to get a clean event sample. There are no explicit cuts against background processes since their contribution is negligible. This will be shown later.

1. At least one charged lepton has to be found in the pseudo rapidity range $|\eta| < 2.4$ to be fully contained in the electromagnetic calorimeter ($|\eta_{\max}| = 2.5$) in case of an electron or in the muon chambers ($|\eta_{\max}| = 2.4$) in case of a muon. The transverse energy of the reconstructed leptons is shown in figure 4.1 a). Exactly one lepton has to lie above a transverse energy threshold of $20\,\text{GeV}$. The lepton requirement yields an efficiency of $53.3\,\%$ of all generated events.

2. The lepton ℓ is considered as isolated if within the radius $R_\ell = 0.3$ in η, ϕ space more than $90\,\%$ of the deposited transverse energy belongs to the reconstructed lepton. The radius chosen, provides enough statistics without degraded reconstruction. The distribution is shown in figure 4.1 b) and has an efficiency of $76.5\,\%$ reducing the sample to $40.8\,\%$ of all events.

3. A missing transverse momentum of at least $20\,\text{GeV}$ is required corresponding to the transverse momentum components of the neutrino from the leptonically decaying W boson. Therefore the barrel, endcap and very forward calorimeters are used to get the largest possible hermiticity of the detector up to $|\eta| = 5.3$. The applied
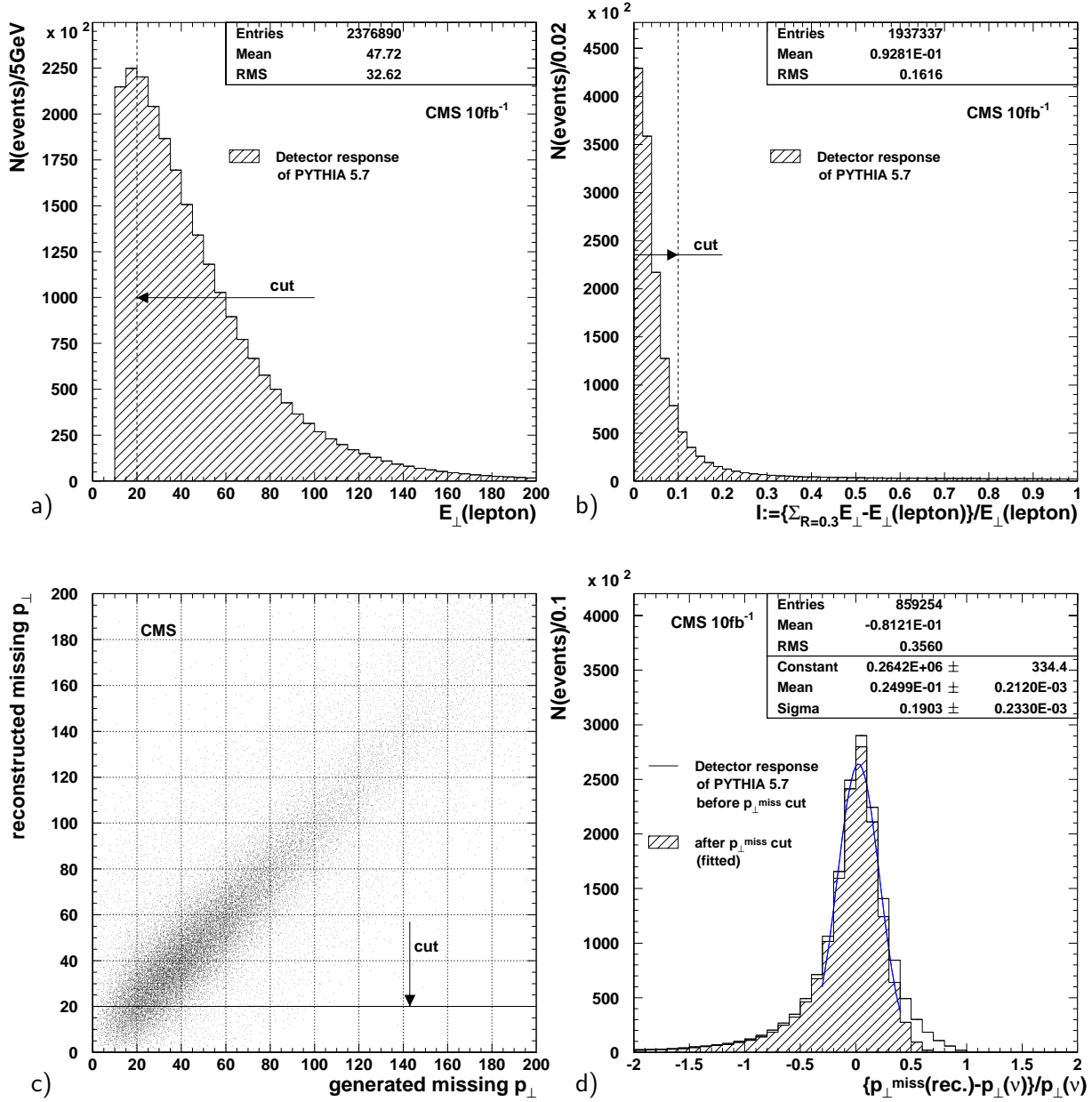
Figure 4.1: *The $p_\perp$ spectrum of the reconstructed lepton (with highest transverse momentum in the case of several ones) (a), the lepton isolation $I := ([\sum_{R=0.3}(E_\perp)] - E_\perp(\ell))/E_\perp(\ell)$ (b), the correlation between the transverse momentum of the neutrino coming from the leptonically decaying W boson and the measured missing $p_\perp$ in (c) and the fitted resolution of the missing $p_\perp$ after the cut (d).*
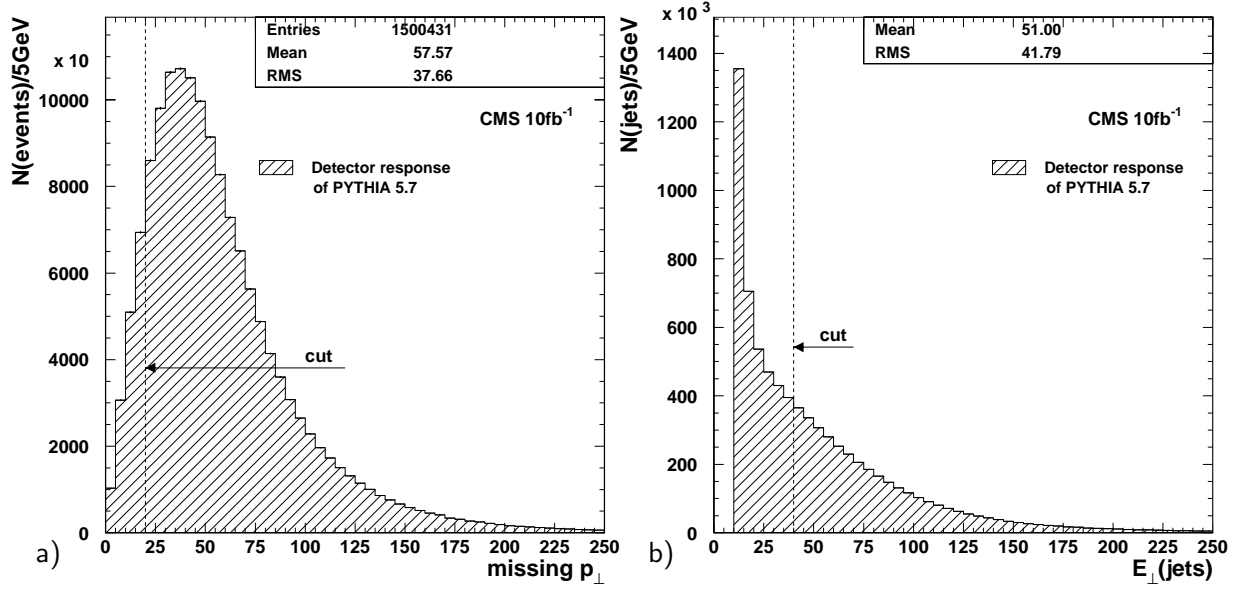
Figure 4.2: The spectrum of the reconstructed missing transverse momentum and the $E_\perp$ spectrum of the reconstructed jets.

cut shown in the figures 4.1 c) and 4.2 a) is kept soft since only the top in the hadronic decay channel will be used for the determination of the top quark mass in this analysis. Thus, the better resolution of the jet transverse energies compared to the missing $p_\perp$ can be exploited without unnecessary loss of statistics. The missing transverse momentum resolution is about 20 % as shown in figure 4.1 d). The cut has an efficiency of 89.2 % leaving 36.4 % of all generated events.

4. The jets are reconstructed with the cone jet algorithm explained in section 3.8 using the cone parameter $R = 0.5$. The $E_\perp$ spectrum of all reconstructed jets is shown in figure 4.2 b) (jets below 10 GeV in $E_\perp$ are not reconstructed). To reconstruct the hadronically decaying W boson and the b quarks at least four jets with a transverse energy of above 40 GeV are demanded. The hard cut decreases the dependence of the reconstructed top on the low $E_\perp$ contributions from the underlying event, multiple interactions and initial state radiation. The hardness of the cut is reflected in the efficiency of 18.1 %, after which 6.6 % of all generated events remain.

5. Exactly two out of these jets have to be identified as coming from a b quark. A jet is tagged as b jet using the impact parameter of tracks belonging to the jet as explained in section 3.9. Tracks within a radius of less than 0.5 around the jet axis are defined as belonging to the jet. If a track fulfils the condition for more than one jet, it is attributed to the jet closer in η, ϕ space. Every considered track needs to have a transverse impact parameter of $|d_{xy}| < 1.0$ mm to differentiate against background tracks from long living mesons as K_S^0 and Λ^0. To define a b jet two tracks with a signed significance of $\sigma_{xy}\text{sign}([\vec{p}_{\text{jet}} \times \vec{p}_{\text{track}}]_z) > +2.0$ are required. The distributions

63
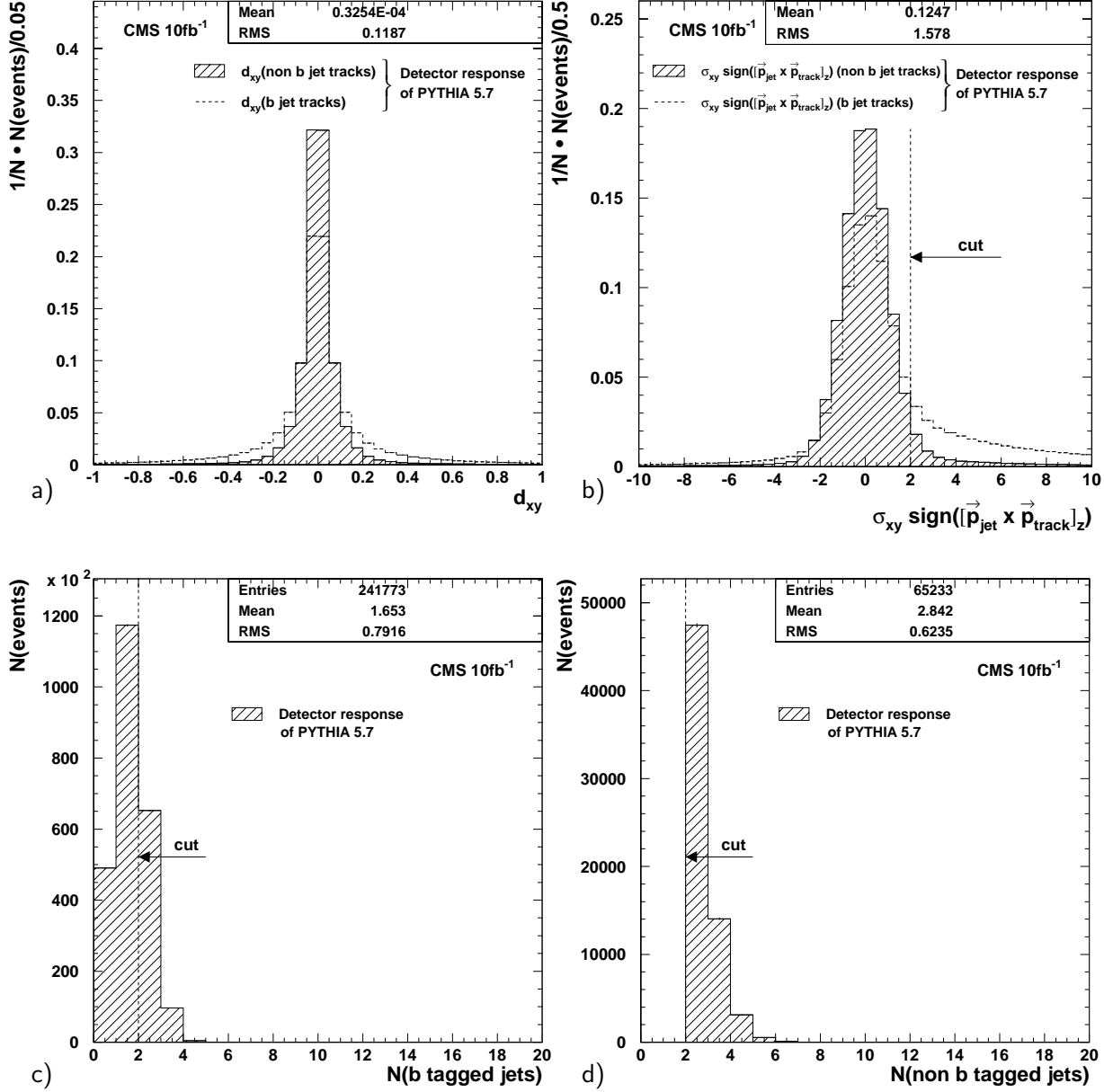
Figure 4.3: *The transverse impact parameter and the signed significance of tracks from b jets and non b jets in comparison (a) and b) and the number of b tagged and non b tagged jets (c) and d). The tracks from b jets tend to have larger transverse impact parameters and an accumulation of b jet tracks at enhanced positive values of the signed significance can be observed. In most cases less than two jets fulfil the b tagging criteria (c). Sometimes jets are mistagged as b jets and more than two b jets are found. After exactly two b tagged jets remain the number of non b tagged jets is obtained as shown in plot d). More than two jets arise from multiple interactions, final and initial state radiation.*
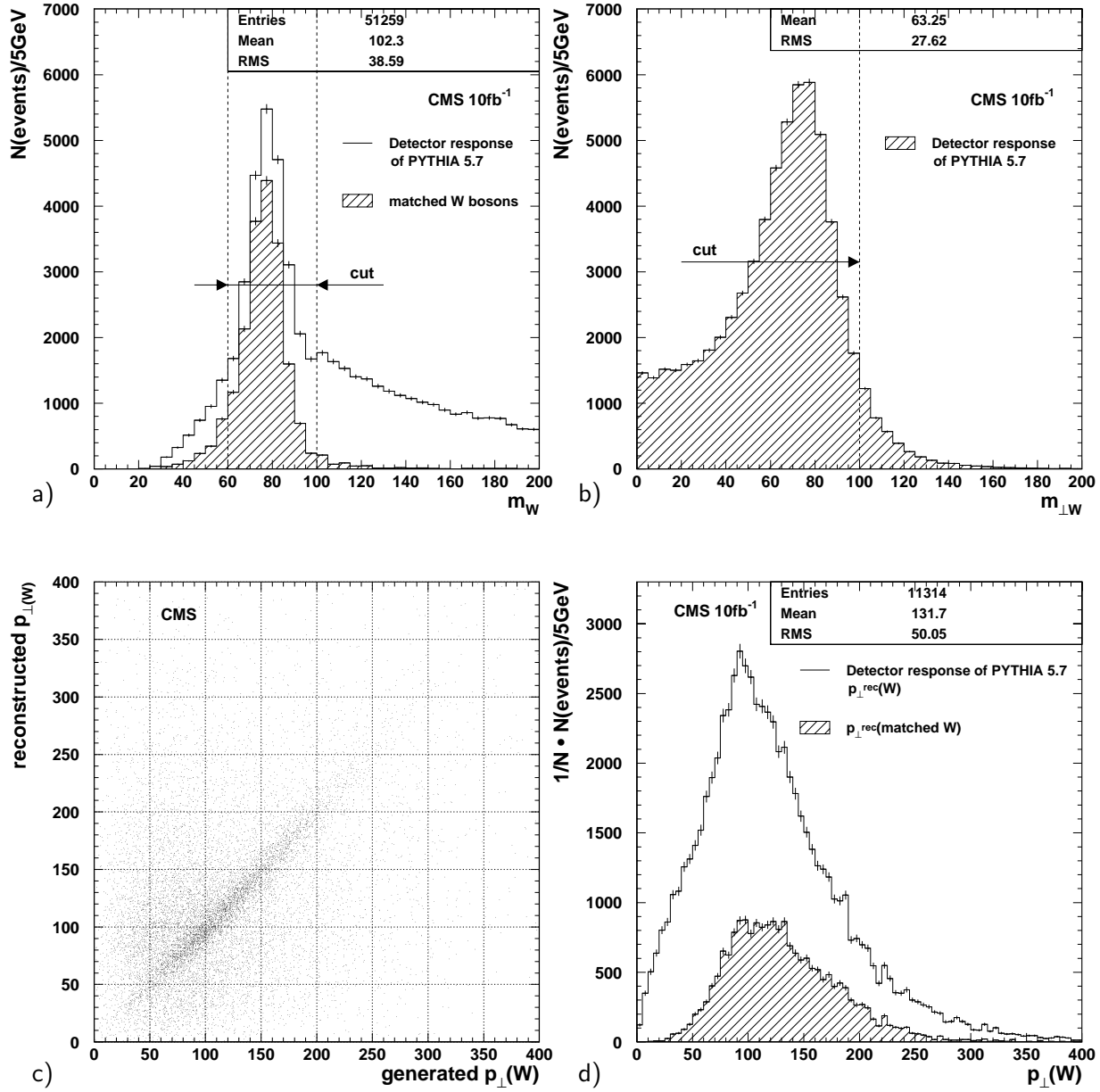
Figure 4.4: The W boson reconstructed from two non b jets (a), the transverse mass of the leptonically decaying W boson (b), the correlation of the transverse momentum of the generated and the reconstructed hadronically decaying W boson (c) and its transverse momentum spectrum with and without the matching condition $R_{W_{rec.}, W_{gen.}} < 0.2$ (d). The same condition was used for the mass distribution of the reconstructed W bosons in a) whose decay quarks match the non b jets.

of the transverse impact parameter and the signed significance are shown in figure 4.3 a) and b). In addition the b jets have to lie above a $50\,\mathrm{GeV}$ threshold in $E_\perp$ as their transverse momentum is on average much higher (more than $10\,\mathrm{GeV}$) than that of non b jets. In figure 4.3 c) and d) the number of identified b jets is compared to that of non b jets. This procedure has an efficiency of $27.3\,\%$ and $1.8\,\%$ of all events remain. With two expected b jets per event the efficiency to tag one b jet is about $52\,\%$. About $20\,\%$ of the tagged b jets cannot be matched to a b quark from the decay of a top quark by using the matching condition $R_{b,\mathrm{jet}} < 0.2$.

6. Once two b jets have been tagged, the invariant mass of the W boson can be reconstructed, combining two of the remaining non b jets. Responsible for the appearance of more than two non b jets in the $t\bar{t}$ signal events are above all the final state radiation, the initial state radiation and multiple interactions. The requirement of exactly two non b jets does not improve the resolution of the reconstructed W boson resonance and the suppression of background processes. It would only reduce the number of events considerably. Therefore the non b jet pair with an invariant mass closest to the mass of the W boson is chosen among all remaining non b jets. To improve the resolution of the reconstructed top quark, events with solutions outside the $20\,\mathrm{GeV}$ window around the well known W boson mass are rejected as indicated in figure 4.4 a). The Gaussian part of the reconstructed W boson has a width of $9.2\,\mathrm{GeV}$. Matching the reconstructed boson to the generated one by requiring a distance smaller than 0.2 in η, ϕ yields a width of $7.6\,\mathrm{GeV}$. The correlation between the transverse momenta of the reconstructed and the generated W bosons and the $p_\perp$ spectra of the reconstructed and the matched reconstructed W bosons are shown in figure 4.4 c) and d). The cut on the mass of the reconstructed W boson has an efficiency of $40.0\,\%$ and $0.72\,\%$ of all events are kept.

7. The transverse mass of the leptonically decaying W boson $m_\perp(W) = \sqrt{((E_\perp(\ell) + \not{E}_\perp)^2 - (p_x(\ell) + \not{p}_x)^2 - (p_y(\ell) + \not{p}_y)^2)}$ can be reconstructed from the lepton and the missing transverse momentum (see figure 4.4 b). The transverse mass , which should not exceed the W boson mass is required to lie below $100\,\mathrm{GeV}$ to take into account the broad mass resolution of the reconstructed W boson. The cut has an efficiency of $93.8\,\%$ and $0.68\,\%$ of all events are kept.

4.2   Reconstruction of the top

After the selection of events some additional cuts are applied to improve the reconstruction of the top quarks. Some decisions have to be taken to solve the combinatorical ambiguities in the arrangement of objects to reconstruct a top quark.

1. The leptonically decaying W boson cannot fully be reconstructed since from the neutrino only the transverse momentum can be infered from the missing transverse momentum $\not{p}_\perp$ of the event, but with the W mass constraint the longitudinal momentum p_z of the neutrino can be determined up to a twofold ambiguity. It turns

out that in 66 % of all cases the smaller solution of p_z is the correct one and thus it is used for the reconstruction of the W boson.

2. After the cuts on the mass of the reconstructed hadronically decaying W boson have been applied the four vectors of the two corresponding jets are rescaled to match the well known mass of the W boson. This is done in multiplying the energy and momenta of the jets with the ratio of the generated on-shell to the reconstructed W boson mass $m_W^{\text{on-shell}}/m_W^{\text{rec.}}$. In this way the dependence of the two jets on the calorimeter energy scale can be almost eliminated.

3. Finally a twofold ambiguity remains to combine the b quark jets to the reconstructed W bosons. As possible decision criteria the transverse and longitudinal momenta of the top quarks (see figure 4.5) are considered. To prevent an enhanced sensitivity to the $p_\perp$ spectrum of the top quarks, it is not used to take a decision about the assignment. Instead the b jets are assigned to the W bosons in minimizing the longitudinal momenta of the top quarks. As can be extracted from plot d) of figure 3.11 the longitudinal momentum of the top quarks is a broad distribution, monotonically increasing towards lower longitudinal momenta. The shapes of the transverse and the longitudinal top momentum distributions are reproduced after the reconstruction as shown in figure 4.5.

4. Once the $t\bar{t}$ system is reconstructed, a cut can be applied to the alignment of the tops. Neglecting the initial state radiation and multiple interactions, which attribute an additional transverse momentum to the $t\bar{t}$ system, the top quarks should be
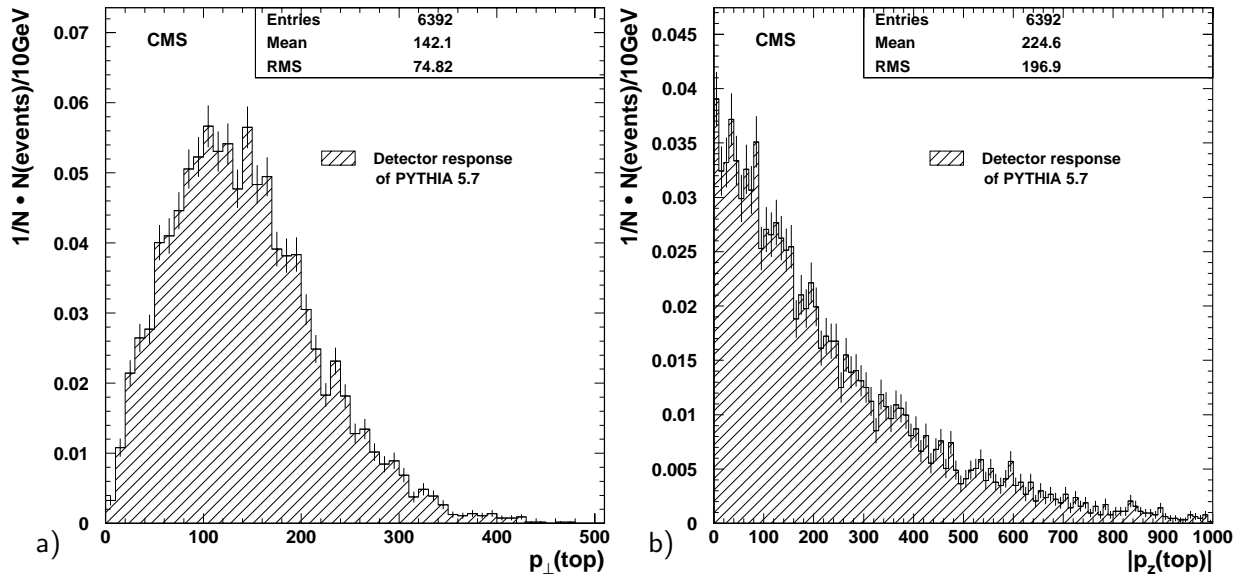
Figure 4.5: Momentum spectra of the reconstructed tops in analogy to those of the top quarks in the hard scattering process (see figure 3.11 c) and d). The characteristic shapes of the distributions are reproduced by the reconstructed top quarks.
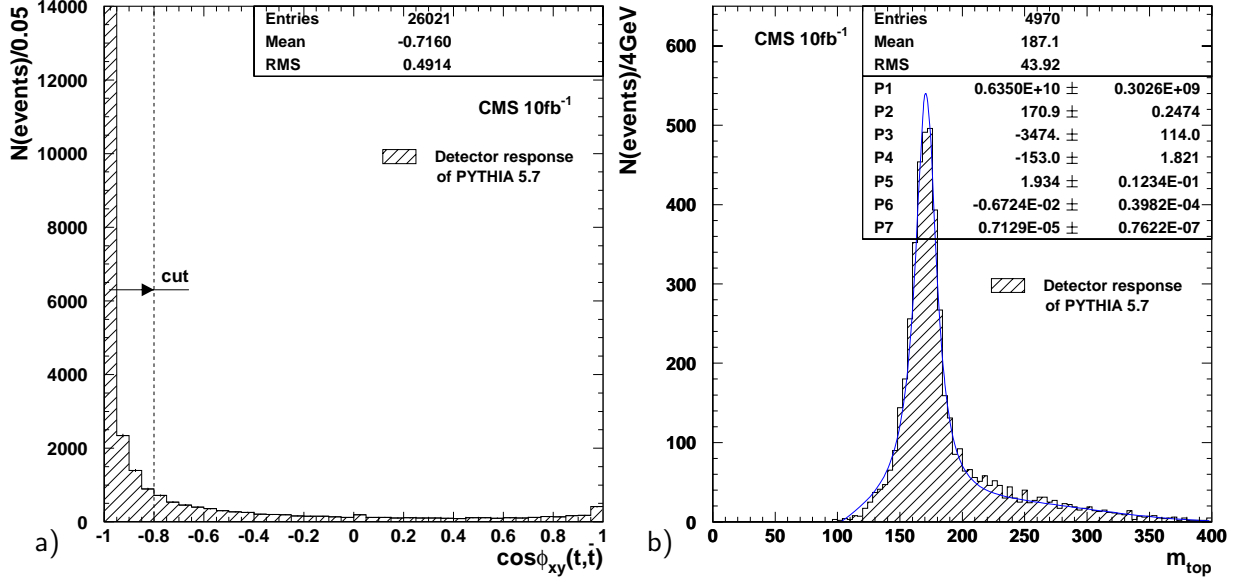
Figure 4.6: The cosine of the azimuthal angle ϕ between the two reconstructed top quarks and the reconstructed top with the hadronically decaying W boson (a). The top mass in b) was fitted with a relativistic Breit-Wigner function multiplied by a polynomial of degree four. The reconstructed mass and its statistical error can be extracted from the fit parameter P_2.

back to back in the xy plane transverse to the beam axis. The $t\bar{t}$ system is generally boosted along the beam axis and therefore not fully balanced in the lab system. The balance of the top quarks in the transverse plane is exploited to suppress strongly misreconstructed $t\bar{t}$ pairs in requiring the cosine of the azimuthal angle ϕ to fulfil $\cos\phi_{t\bar{t}} \leq -0.8$ (see figure 4.6 a). The cut efficiency is 75.0 % and 0.51 % of all events remain after this cut.

5. The last cut is dedicated to reduce combinatorical background, i.e. events with wrongly assigned b jets or wrongly chosen solutions of the neutrino p_z. Since the mass of the top quark will be determined, this information cannot be used as selection criteron but the difference in the masses of the two reconstructed top quarks should not differ too much since within the standard model the natural width of the top quark is about 1.5 GeV. The reconstruction broadens the width up to about 10 GeV with a Gaussian fit or to about 20 GeV using the relativistic Breit-Wigner fit shown in figure 4.6 b), where the distribution of the reconstructed mass of the top with the hadronically decaying W boson is plotted. Therefore a cut demanding the mass difference of the two reconstructed top quarks not to exceed 25 GeV is applied. The efficiency of this cut is 27.5 % and finally 0.14 % of all generated events are kept.

In figure 4.7 a) and b) a $t\bar{t}$ event in the semileptonic decay channel passing all the cuts is shown as seen with the CMS detector described by the detailed detector geometry of
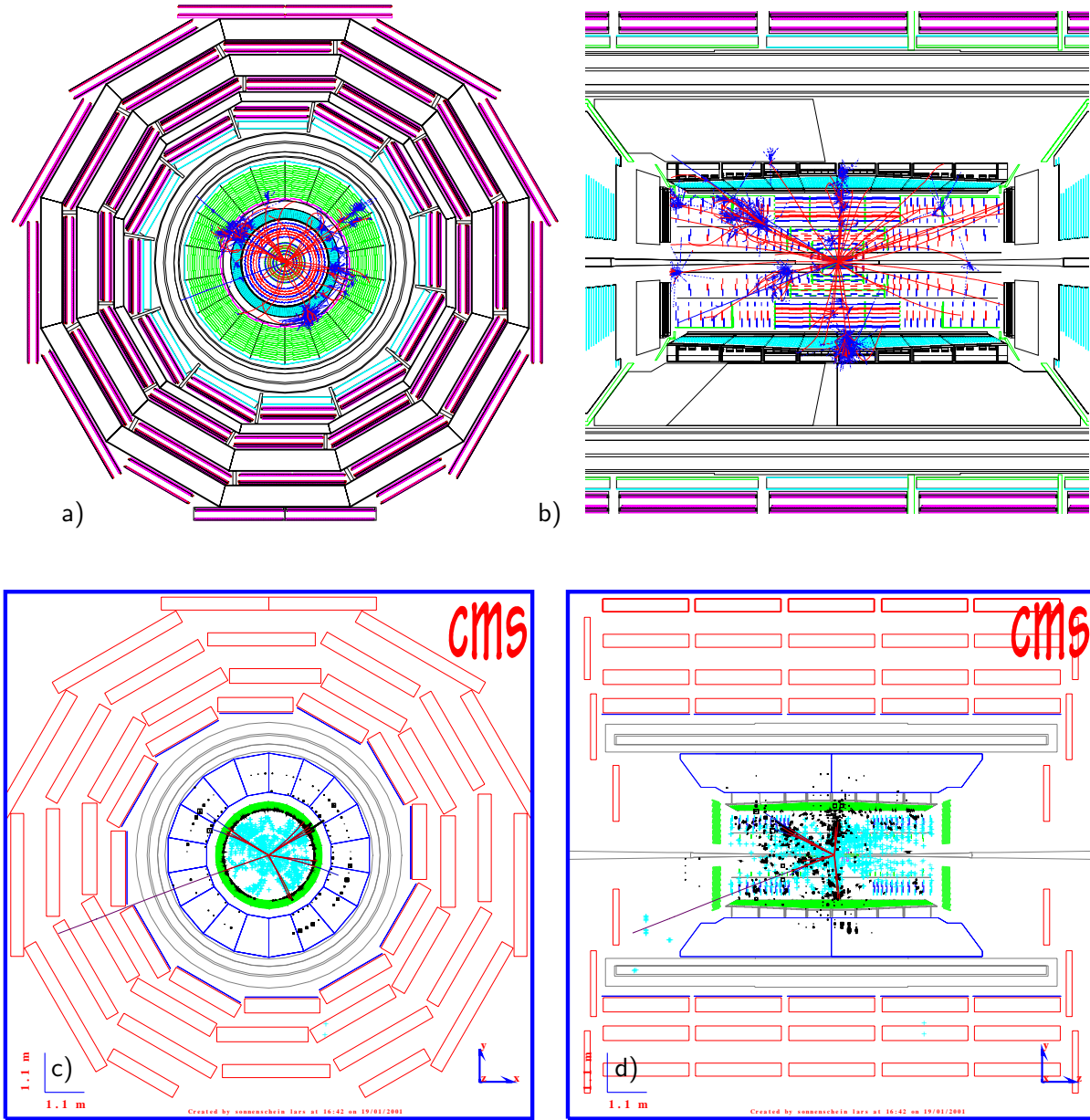
Figure 4.7: $t\bar{t}$ event in the semileptonic decay channel, displayed in the x, y (left) and the y, z plane (right) with detailed prolongation of particles via GEANT (version CMSIM118) through the material of the CMS detector geometry (top). The neutral particles are excluded from the picture to make the jets distinguishable. On the bottom the same $t\bar{t}$ event displayed with the event viewer CMSCAN based on the same GEANT simulation of the CMS detector. The energy depositions in the hadronic calorimeter are accumulated in a few representative towers for a better recognition of the event. The μ^- and the four high energetic jets, two b jets and two non b jets, of the simulated event which passed all cuts are clearly visible.

Final state particles				Reconstructed objects		
	$E_\perp$[GeV]	η[/]	ϕ[rad]		$E_\perp$[GeV]	η[/]	ϕ[rad]
μ^-	93.01	-0.81	-2.82	μ^-	92.43	-0.81	-2.82
$\bar{\nu}_\mu$	43.01	0.05	-1.84	$E\!\!\!/_\perp$	48.05	-0.24	-1.71
b	129.16	0.04	0.63	b jet	130.87	0.04	0.64
$\bar{b}$	111.64	-0.83	2.61	b jet	114.31	-0.84	2.60
u	76.58	0.09	-1.07	q jet	78.92	0.09	-1.05
$\bar{d}$	43.21	-0.59	-0.17	q jet	43.19	-0.57	-0.20

Table 4.1: Final state partons of a particular $t\bar{t}$ event in the semileptonic decay channel and the corresponding reconstructed objects.

GEANT. The simulation CMSIM (version 118) was used to describe the particle propagation through the detector material. Neutral particles from the event are not shown in the GEANT detector geometry so that the jets can be distinguished. The event viewer CMSCAN shows the same event in figure 4.7 c) and d). For a better visibility only tracks above a $p_\perp$ of 1 GeV, reconstructed from the simulated hits within the tracker and the muon chamber volumes are drawn. The energy depositions in the calorimeters are presented with a reduced resolution, accumulating the energies in distinguishable clusters. Ghost hits of the muon track and some energy depositions in the hadronic calorimeter are remnants from the other perspective of the detector. The hard subprocess of the event consists of a b and a $\bar{b}$ quark, a μ^- and its corresponding antineutrino and a u and a $\bar{d}$ quark. The direction and momenta of the particles and the corresponding reconstructed objects are listed in table 4.1.

Cut	Remaining fraction of generated events		
	$\ell = e, \mu$	$\ell = \tau$	$\ell = e, \mu, \tau$
At least 1 lepton with $|\eta_\ell| < 2.4$	81.0 %	36.9 %	66.3 %
Exactly 1 lepton with $p_\perp(\ell) > 20$ GeV	70.6 %	18.6 %	53.3 %
Lepton isolation $I_{R=0.3} < 0.1$	57.5 %	7.5 %	40.8 %
Missing transverse momentum $p\!\!\!/_\perp > 20$ GeV	51.2 %	6.9 %	36.4 %
At least 4 jets with $E_\perp > 40$ GeV	9.2 %	1.4 %	6.6 %
Exactly 2 b jets with $E_\perp > 50$ GeV	2.5 %	0.4 %	1.8 %
$60 < m_W^{\text{rec.}} < 100$ GeV	0.99 %	0.17 %	0.72 %
Transverse mass $m_\perp(W_{\text{lep.}}) < 100$ GeV	0.94 %	0.16 %	0.68 %
Azimuthal angle between rec. tops: $\cos\phi_{t\bar{t}} \leq -0.8$	0.70 %	0.13 %	0.51 %
Rec. top mass difference $|m_t - m_{\bar{t}}| < 25$ GeV	0.19 %	0.03 %	0.14 %

Table 4.2: Cuts for the selection of $t\bar{t}$ events in the semileptonic decay channel and for the reconstruction of the top quarks (The last two cuts). The different efficiencies for $t\bar{t}$ events with a W boson decaying into a τ lepton are separately indicated.
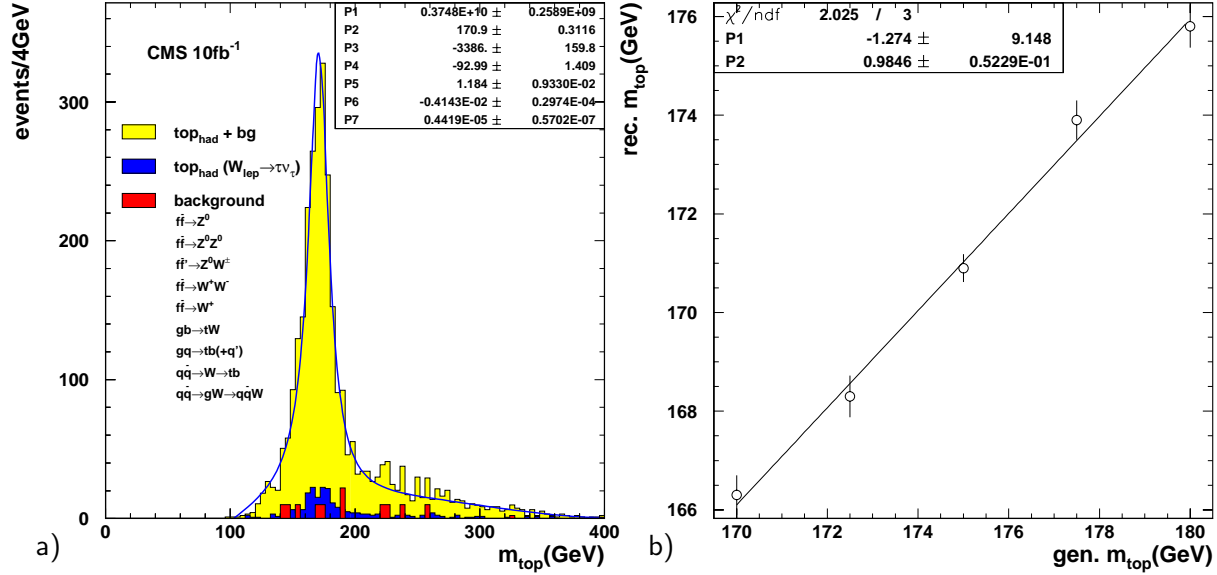
Figure 4.8: The mass of the reconstructed top after all cuts including the contribution of background processes as indicated (a). The contributing fraction of signal events with τ leptons from the leptonically decaying W boson and the negligible background are superimposed. Both, the signal and the background correspond to the integrated luminosity of $10\,fb^{-1}$ according to the LO cross sections. The dominant background process is the W production. Due to the huge cross section not all events could be generated but they are scaled to the expected number respectively. The dependence of the reconstructed top mass on the generated top quark mass is shown in b). It turns out to be linear.

After the selection and reconstruction has been applied to signal and background events, the mass of the hadronically decaying top is obtained as shown in figure 4.8 a). The four vectors of the two non b jets are scaled so that their invariant mass matches the on-shell mass of the W boson. Thus the uncertainty in the calibration of the non b jet energies can be eliminated. To exploit this the following concentrates on the top in the hadronic decay branch of the $t\bar{t}$ event. The other top is not considered here. The fitted histogram shows the sum of the signal and the very small background, where the signal consists of all semileptonic $t\bar{t}$ events ($\ell = e, \mu, \tau$). In addition the contribution of signal events with τ leptons from the leptonically decaying W boson is shown separately. Due to the dominating decay of the τ lepton into hadrons (about 65 %) the efficiencies of the cuts are degraded (see table 4.2). The signal events for $\ell = e, \mu$ and all leptons together ($\ell = e, \mu, \tau$) yield the same top mass of $m_t = 170.9$ GeV. The NLO cross sections for all considered background processes have not been calculated yet. Thus to be consistent all background processes and the signal are generated according to their LO cross section (see table 4.4 for the values). On the bottom of the histogram the pure background processes are plotted. Since the W production gives the dominant contribution and only a part of the large number of events could be generated, it had to be normalised to the corresponding cross section.

With a given top quark mass of 175.0 GeV a top mass of 170.9 ± 0.31 GeV is reconstructed. This comes predominantly from the b jets which are not calibrated (see appendix B for the transverse jet energy reconstructed and its resolution). The mass value is extracted from the fit function. It is a relativistic Breit-Wigner function with a superimposed polynomial of degree four to fit the tails due to combinatorical background and also minor the background processes. The central value of the resonance parameter (P2 in the plot) yields the mass of the reconstructed top and its statistical error gives the error on the mass. This error should not be confused with the reconstructed width of the top which is much larger. ATLAS simulations [ATL99] accomplished to reconstruct the top quark use a Gaussian fit to determine the top mass width. The results are comparable to the value of about 10 GeV achieved here applying a Gaussian fit as well. It may be possible to improve it slightly but its determination is not subject of investigation here.

To conclude from the reconstructed to the generated mass value of the top it is essential to translate also the error on the top mass. Therefore the knowledge of the functional dependence is essential. Here it is a linear dependence as shown in figure 4.8 b), facilitating the translation. The reconstructed top has a mass of about 2% below the generated value and therefore the gradient of the fitted line is expected to lie below 1. Its value turns out to be 0.985 and thus the error of the reconstructed value can be translated by simple multiplication with the inverse gradient 1.015. This has to be kept in mind considering the systematic error sources in the next section.

4.3 Systematic uncertainties

A lot of parameters enter into the generation of scattering processes via Monte-Carlo event generators. Those which are believed to have a considerable influence on the reconstruction of the top and thus on the determination of its mass are discussed below. The multitude of items are thematically ordered from the comparison of different event generators, over the investigation of multiple interactions to the influence of background processes.

1. One of the most important systematic investigations is the comparison of different event generators which should provide consistent results. Therefore the HERWIG 6.1 event generator is compared to PYTHIA 5.7 which has been chosen as default for most investigations (indicated as a dashed line in the graphical error summaries figure 4.9 and 4.10). The comparison of HERWIG 6.1 has to be done to PYTHIA 5.7 without multiple interactions (see the first item (MI off) in figure 4.10), since this feature is not included in HERWIG yet. The emphasis of HERWIG lies in the detailed simulation of the parton shower and it uses a cluster fragmentation model in contrast to the Lund string fragmentation model of PYTHIA. The top mass prediction of the two event generators agree very well within 100 MeV.

2. Next the event generator PYTHIA 6.1 is considered. It differs from PYTHIA 5.7 in more than the change from real to double precision. Among others an approximate

$1 - 2.5\alpha_s/\pi$ QCD correction factor has been introduced for the width of the top decay $t \rightarrow bW$ and the baryons are produced according to an advanced popcorn scheme [Sjo00]. Several extensions with new parameters are added and a lot of existing parameters changed their initial settings. Thus it cannot be expected that PYTHIA 6.1 reproduces PYTHIA 5.7 perfectly well. Nonetheless, merely a shift of 200 MeV is observed in the top mass. HERWIG 6.1 has a smaller deviation from PYTHIA 5.7 and therefore the larger shift in the top mass of 200 MeV from PYTHIA 6.1 has been taken into account. See also the error table 4.3 for the numerical results.
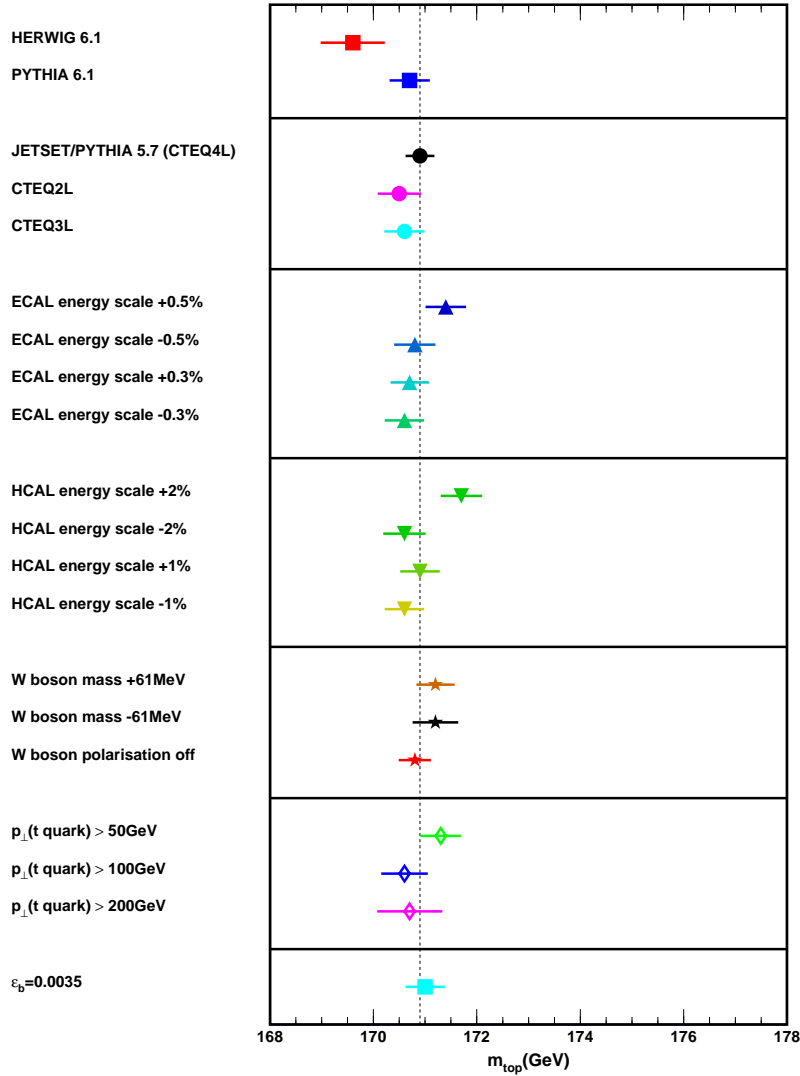
Figure 4.9: *Systematic uncertainties of the top mass. The mass value of* 170.9 GeV *obtained with the default event generator PYTHIA 5.7 is indicated as dashed line.*

Source of uncertainty		top mass	stat. error	syst. error
Event generators	HERWIG 6.1 (no MI)	169.6 GeV	±0.62 GeV	200 MeV
	PYTHIA 6.1	170.7 GeV	±0.39 GeV	
Parton density function (PYTHIA 5.7)	CTEQ4L (used as default)	170.9 GeV	±0.31 GeV	300 MeV
	CTEQ2L	170.5 GeV	±0.42 GeV	
	CTEQ3L	170.6 GeV	±0.39 GeV	
ECAL energy scale	$+0.5\,\%$	171.4 GeV	±0.39 GeV	300 MeV
	$-0.5\,\%$	170.8 GeV	±0.40 GeV	
	$+0.3\,\%$	170.7 GeV	±0.37 GeV	
	$-0.3\,\%$	170.6 GeV	±0.38 GeV	
HCAL energy scale	$+2\,\%$	171.7 GeV	±0.40 GeV	300 MeV
	$-2\,\%$	170.6 GeV	±0.41 GeV	
	$+1\,\%$	170.9 GeV	±0.38 GeV	
	$-1\,\%$	170.6 GeV	±0.39 GeV	
W boson ($m = 80.41\,\mathrm{GeV}$)	$m_W = m + 61\,\mathrm{MeV}$	171.2 GeV	±0.37 GeV	< 300 MeV
	$m_W = m - 61\,\mathrm{MeV}$	171.2 GeV	±0.44 GeV	
	No polarisation (isotropic decay)	170.8 GeV	±0.31 GeV	
Transverse momentum of the top quark	$p_\perp(t) > 50\,\mathrm{GeV}$	171.3 GeV	±0.39 GeV	< 300 MeV
	$p_\perp(t) > 100\,\mathrm{GeV}$	170.6 GeV	±0.45 GeV	
	$p_\perp(t) > 200\,\mathrm{GeV}$	170.7 GeV	±0.63 GeV	
b quark fragmentation	Peterson parameter $\epsilon_b = 0.0035$	171.0 GeV	±0.38 GeV	100 MeV
Multiple interaction (MI)	off	169.5 GeV	±0.39 GeV	200 MeV
	UA5 model	171.1 GeV	±0.54 GeV	
Initial state radiation	off	170.2 GeV	±0.35 GeV	100 MeV
	$Q_{\min}(\mathrm{ISR}) = 2\,\mathrm{GeV}$	170.7 GeV	±0.42 GeV	
	$Q_{\min}(\mathrm{ISR}) = 1.1\,\mathrm{GeV}$	171.0 GeV	±0.40 GeV	
	$Q_{\min}(\mathrm{ISR}) = 0.9\,\mathrm{GeV}$	170.9 GeV	±0.40 GeV	
Final state radiation	off	173.5 GeV	±0.22 GeV	100 MeV
	$Q_{\min}(\mathrm{FSR}) = 2\,\mathrm{GeV}$	170.7 GeV	±0.39 GeV	
	$Q_{\min}(\mathrm{FSR}) = 1.1\,\mathrm{GeV}$	170.8 GeV	±0.40 GeV	
	$Q_{\min}(\mathrm{FSR}) = 0.9\,\mathrm{GeV}$	170.9 GeV	±0.38 GeV	
M.E. (ISR+FSR off)	PYTHIA 5.7	172.9 GeV	±0.20 GeV	100 MeV
	On-shell approximation (Flesch)	171.9 GeV	±0.17 GeV	
	Breit-Wigner (Slabospitsky)	172.8 GeV	±0.22 GeV	
M.E. CompHEP (ISR+FSR off)	$pp \to t\bar{t} \to WbWb$	176.0 GeV	±0.22 GeV	100 MeV
	$pp \to WbWb$	175.9 GeV	±0.27 GeV	
Minimum bias	PYTHIA 5.7	174.5 GeV	±0.44 GeV	200 MeV
	CMS settings	172.3 GeV	±0.41 GeV	
	LHCb settings	172.1 GeV	±0.39 GeV	
	CMS (low $p_\perp$ + diffractive)	172.7 GeV	±0.43 GeV	
Signal + background	$t\bar{t}, tW, tb, Z, ZZ, ZW, WW, W$	170.9 GeV	±0.32 GeV	< 100 MeV

Table 4.3: Summary of all investigated uncertainties on the mass of the top, reconstructed from three jets. The values which have to be taken into account as uncertainty on the top mass are indicated in the last column. As default PYTHIA 5.7 with the CTEQ4L set of parton density functions was used resulting in a statistical error of 310 MeV as indicated in the third row. Due to the large amount of CPU time needed by the jet algorithm and the detector simulation, the systematic uncertainties could only be investigated with a sample of 1 000 000 generated events. See the text for a detailed discussion of the uncertainties.

3. The mass of the reconstructed top depends to some extend on the used set of parton density functions since the different slopes of the gluon densities yield different top production kinematics (see figure 4.9). In addition, the ratio between gg fusion and $q\bar{q}$ annihilation processes contributing to the $t\bar{t}$ production varies for the different sets of parton density functions in the percent level. However the knowledge of the gluon density of the proton will be improved in future at the Tevatron (Run II) and at the LHC so that smaller uncertainties can be expected. Furthermore, assuming standard model couplings the $t\bar{t}$ spin correlation could be used to fix the ratio between the gg fusion and the $q\bar{q}$ annihilation processes. As shown in figure 4.9 the CTEQ2L set, which already has been retracted by the authors, gives rise to a top mass shift of 400 MeV in relation to the CTEQ4L set which has been used as default. The newer CTEQ3L set differs only by 300 MeV. This is the value taken for the calculation of the total error.

4. The variation of the absolute energy scale of the electromagnetic calorimeter according to the TDR[1] [CMS97b] design goal of about $\pm 0.5\,\%$ leads to an uncertainty of 500 MeV. Using the Z mass constraint, detected events with two isolated high transverse momentum leptons from the process $Z \to ee$ will allow to achieve a calibration precision of $0.3\,\%$ corresponding to an uncertainty of 300 MeV on the top mass. Due to the huge cross section of the single Z production background considerations turn out to be unimportant. Since the contribution of the electromagnetic calorimeter to the jets and therefore to the top reconstructed of three jets is small, the top mass depends only marginally on the energy scale and shows consistence with the central value of the default top mass within its statistical errors as can be seen in figure 4.9. Statistical fluctuations show up in asymmetric shifts around the default value of the top mass.

5. According to the expected precision of laser calibration and light injection [CMS97c], the absolute energy scale of the hadronic calorimeter was varied by $\pm 2\,\%$ which gives rise to an uncertainty of 800 MeV in the top mass. Exploiting signal events of τ leptons balanced by jets, resonances decaying into two jets and pions not interacting in the electromagnetic calorimeter in comparison to the momentum measured in the tracker, an accuracy of $1\,\%$ can be achieved [Kin97]. The variation of the absolute energy scale by $1\,\%$ results in a shift of the top mass by 300 MeV. The small shifts are achieved exploiting the energy scale independence of the two non b jets due to the scaling of their four vectors, so that their invariant mass reaches the well known pole mass of the W boson. Again the obtained top masses are consistent with the default value and statistical fluctuations provide asymmetric shifts around the default value of the top mass.

6. Since a pair of non b jets is scaled, so that their invariant mass coincides with the W boson mass, its value has to be varied inside its error. Here a variation of the W

---

[1]**T**echnical **D**esign **R**eport

mass by ± 61 MeV was carried out. The variation yields no conclusive tendency in the shift of the top mass but is still consistent with the reconstructed default top mass within the statistical errors. Therefore the change in the top mass of 300 MeV can be considered as a fluctuation. A mass shift of 100 MeV is obtained by switching off the polarization of the W boson. However the polarization of the W boson will be measured at the LHC within an accuracy at the percent level and the uncertainty on the W mass will also become smaller. Nonetheless to be sure that the influence will not be underestimated the uncertainty of 300 MeV is taken into account.

7. The theoretical discussion in [Alt00] about the kinematic properties of the $t\bar{t}$ production shows the expected uncertainties the prediction of the top $p_\perp$ spectrum,
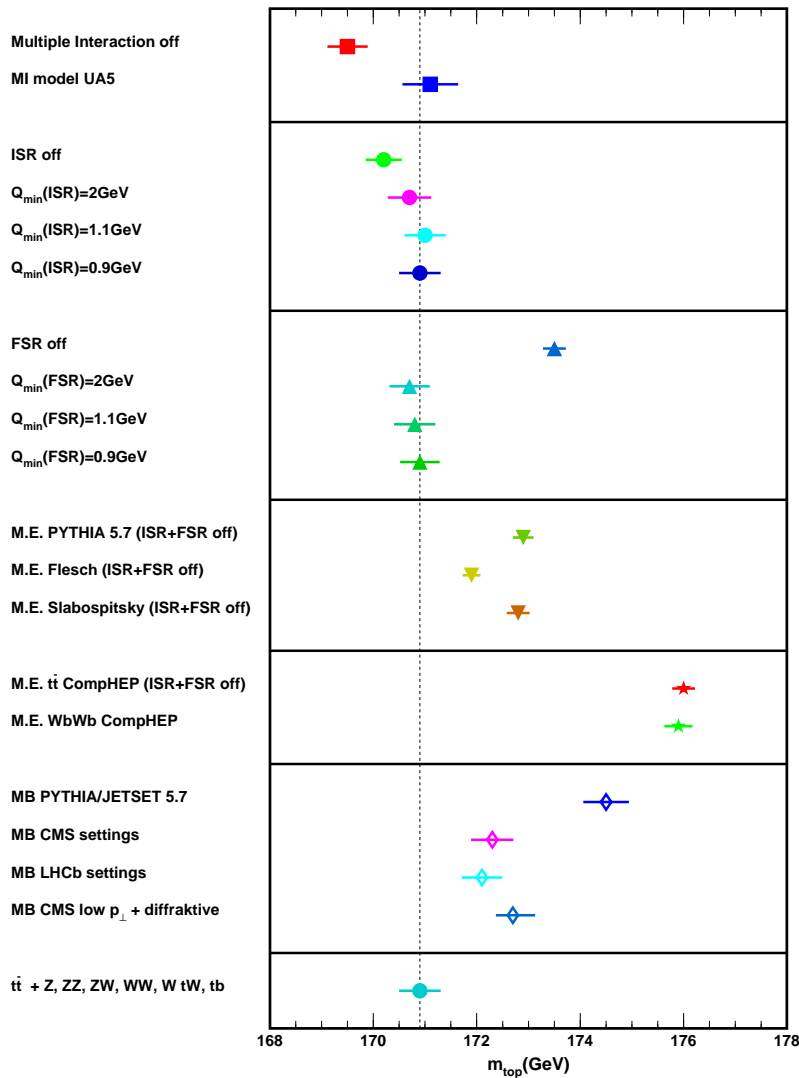

Figure 4.10: Systematic uncertainties of the top mass (continued).

comparing LO to NLO calculations. To show the stability of the determined top mass on the transverse momentum of the generated top quark, the analysis including the detector response has been carried out in three bins of different top quark transverse momenta ($p_\perp(t)$ greater than $50, 100$ and $200\,\mathrm{GeV}$). The largest deviation of $400\,\mathrm{MeV}$ is obtained with $p_\perp(t) > 50\,\mathrm{GeV}$. This uncertainty due to the choice of different kinematic regions is strongly correlated to that of the parton density functions and therefore partially double counted. Anyway higher order calculations will help to reduce the uncertainty in the future and the $400\,\mathrm{MeV}$ which are taken into account constitute already the largest contribution to the systematic uncertainties.

8. For the decay of the b quark the Peterson fragmentation function was used in the PYTHIA event generator. The default value of the parameter $\epsilon_b = 0.005$ was changed to the LEP tuned value $\epsilon_b = 0.0035$ [Abb98]. The uncertainty of $100\,\mathrm{MeV}$ shows that in this analysis the fragmentation of the b quark is not a critical issue. Nonetheless it has to be mentioned that recent measurements of the b quark fragmentation cannot be well fitted with the Peterson parameterization of the fragmentation function [Abe99]. The uncertainty of $100\,\mathrm{MeV}$ was taken as contribution to the systematic error.

9. Some contributions to the jets come from multiple interactions (MI), i.e. the scattering of a second parton pair coming from the same proton pair as the signal process. Switching off the multiple scattering of PYTHIA 5.7 with its default model assuming an equal probability in all events and an effective minimum transverse momentum of $p_{\perp\mathrm{min}} = 1.4\,\mathrm{GeV}$ leads to the rather big deviation of a $1.4\,\mathrm{GeV}$ lower top mass (see figure 4.10). However using the UA5 model assuming a varying impact parameter and a hadronic matter overlap consistent with a Gaussian matter distribution with an continuous turn off in the cross section at $p_{\perp 0} = 1.55\,\mathrm{GeV}$ already yields a small shift of $200\,\mathrm{MeV}$ in the top mass. Future studies at the Tevatron and the LHC will provide improved models with still smaller uncertainties than those between the used default model and the completely different UA5 model such that the uncertainty of $200\,\mathrm{MeV}$ can be considered as as a conservative estimate.

10. Switching off the initial state radiation (ISR) results in a $700\,\mathrm{MeV}$ lower top mass due to the lack of additional contributions to the jets. The default invariant mass cut-off Q_{min} is adjusted to $1.0\,\mathrm{GeV}$. A value twice as large, i.e. $Q_{\mathrm{min}} = 2\,\mathrm{GeV}$ results in a shift of $200\,\mathrm{MeV}$. Variation of the default invariant mass cut-off value by $\pm 100\,\mathrm{MeV}$ leads to a $100\,\mathrm{MeV}$ uncertainty in the top mass. Also the uncertainty due to the initial state radiation converges quickly while getting closer to the default invariant mass cut-off value.

11. Switching it off the final state radiation (FSR) yields a shift of $2.6\,\mathrm{GeV}$ towards upper top masses since no radiated partons can fall outside of the cone of the jet algorithm. The default invariant mass cut-off has the same value than for the initial state radiation ($Q_{\mathrm{min}} = 1.0\,\mathrm{GeV}$). The choice of $Q_{\mathrm{min}} = 2.0\,\mathrm{GeV}$ results in a shift

of 200 MeV. This variation of a factor of two is certainly to large and the shift is overestimated. The variation of $Q_{min} = 1.0$ GeV by ± 100 MeV yields a shift in the top mass of 100 MeV. The dependence of the top mass on the invariant mass cut-off value is not linear but it converges quickly while getting closer to the default value $Q_{min} = 1.0$ GeV.

12. To investigate the influence of the spin correlation between the decay products of the top quarks the $2 \to 2$ matrix elements $gg, q\bar{q} \to t\bar{t}$ of PYTHIA 5.7 which do not include the spin correlation are compared to the $gg, q\bar{q} \to t\bar{t} \to 6$ matrix elements [Ber98a] [Sla01] including the spin correlation. Due to selection cuts and the different kinematics in different edges of the phase space of correlated decay products, there may be an influence on the mass of the reconstructed top. To get a maximized sensitivity to this effect the final and initial state radiation are switched off. The prediction of the top mass of the $2 \to 6$ matrix elements in on-shell approximation from [Ber98a] is about 1 GeV lower than the prediction of the $2 \to 2$ matrix elements of PYTHIA 5.7. However this deviation is mainly due to the on-shell approximation and not due to the spin correlation, because the matrix elements from [Sla01] with a Breit-Wigner smeared top mass and off-shell W boson masses, which are more comparable to the off-shell treatment of PYTHIA 5.7, yield a tiny mass shift of about 100 MeV purely due to the spin correlation. This uncertainty is taken into account for spin correlation effects as indicated in table 4.3. It should be mentioned that with lower jet $E_\perp$ cuts the shift in the top mass does slightly increase. With $E_\perp(\text{jets}) \geq 20$ GeV, $E_\perp(b\,\text{jets}) \geq 30$ GeV a shift of 300 MeV is obtained.
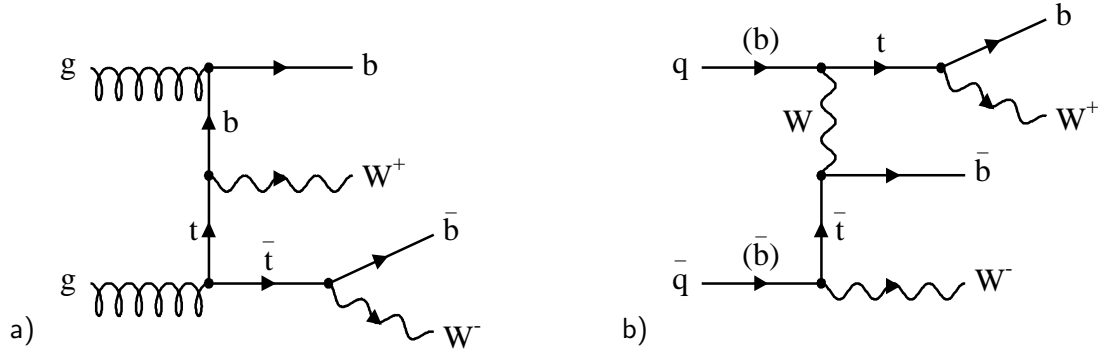
Figure 4.11: *Two examples of Feynman graphs presenting $2 \to 4$ processes with the same final state as the resonant $t\bar{t}$ production, namely two W bosons and two b quarks. The gluon gluon induced process in a) can be obtained from the resonant $2 \to 4$ process by attaching one gluon to a b quark instead of to a top quark. Also quark antiquark annihilation processes as depicted in b) contribute to single and non resonant processes with identical final state. The two processes shown here are single resonant with one highly virtual top quark.*

13. By using the matrix elements $gg, q\bar{q} \to bW^+\bar{b}W^-$ from CompHEP with PYTHIA 5.7 it is possible to generate the non resonant, the single and the double resonant $2 \to 4$ processes with two b quarks and two W bosons in the final state. The example for a single resonant process would be the constellation where one of the two incoming gluons couples to an outgoing b quark so that the corresponding top quark is highly virtual. This and another $2 \to 4$ process with a quark antiquark pair as incoming partons are shown in figure 4.11 a) and b) respectively. Since CompHEP uses its own choice of the Q^2 scale for the initial state radiation and only the independent fragmentation model works in the used version, it cannot be compared to the prediction of default PYTHIA 5.7. Instead CompHEP was used for the investigation exclusively, whereas final and initial state radiation have been switched off. The comparison between the resonant $t\bar{t}$ production from CompHEP and the sum of resonant and non resonant processes from CompHEP show a small effect of about $100\,\mathrm{MeV}$ in the fitted top mass as listed in table 4.3.

14. Every signal event is expected to be superimposed by 1.7 low $p_\perp$ scattering events on average at low luminosity which is considered in this work. The number can be obtained by application of equation 3.14. Therefore the relevant cross section of low $p_\perp$ scattering processes given by PYTHIA (MSEL=1), the specific (low) luminosity and the frequency of bunch crossings have to be inserted. The number is then given by

$$< N >= \frac{\sigma \cdot L}{f} = \frac{54\,\mathrm{mb} \cdot 10^{33}\mathrm{cm}^{-2}\mathrm{s}^{-1}}{40\,\mathrm{MHz} \cdot \frac{2835}{3564}} \simeq 1.7 \tag{4.1}$$

taking into account that only 2835 of 3564 possible bunch places will be filled. The time integration over $25\,\mathrm{ns}$ (the distance between two bunch crossings) is here done by division with the revolution frequency at low luminosity. The number of minimum bias events is Poisson distributed around the central value 1.7 and their additional contribution to the jets leads (with the PYTHIA 5.7 default settings) to a top mass of $174.5\,\mathrm{GeV}$ as listed in table 4.3. This relatively high value in comparison to the other models is mainly due to the abrupt cross section cut-off at the low value $p_{\perp 0} = 1.4\,\mathrm{GeV}$. Extrapolations from S$\bar{\mathrm{p}}$pS (UA1) and Tevatron (CDF) energies to $\sqrt{s} = 14\,\mathrm{TeV}$ at the LHC resulted already in first parameter settings for LHCb and CMS [See00]. At LHCb settings the same multiple interaction model as for UA5 is used with a continuous turn-off in the cross section at $p_{\perp 0} = 3.47\,\mathrm{GeV}$. Superimposing this kind of minimum bias events, the top mass reaches $172.1\,\mathrm{GeV}$. In case of CMS tuning a multiple interaction model assuming a varying impact parameter and a hadronic matter overlap consistent with a double Gaussian matter distribution with a continuous turn-off in the cross section at $p_{\perp 0} = 3.2\,\mathrm{GeV}$ is used. This gives rise to a top mass of $172.3\,\mathrm{GeV}$ which differs only by $200\,\mathrm{MeV}$ from that obtained using the LHCb tuned minimum bias events. After the start-up phase of the LHC the extrapolations will be replaced by measurements. These measurements have to be done very carefully to yield convergence in the parameter settings, predominantly the value of the transverse momentum threshold $p_{\perp 0}$. It

Process	Cross section (LO) PYTHIA 5.7	N(events) $\mathcal{L}_{\text{int}} = 10\text{fb}^{-1}$	Selected events after all cuts	
			$E_\perp(\text{jets}) \geq 20\,\text{GeV}$ $E_\perp(b\,\text{jets}) \geq 30\,\text{GeV}$	$E_\perp(\text{jets}) \geq 40\,\text{GeV}$ $E_\perp(b\,\text{jets}) \geq 50\,\text{GeV}$
$gg, q\bar{q} \to t\bar{t} \to b\bar{b}q\bar{q}\ell\nu_\ell,\ \ell = e, \mu$	160 pb	$1.6 \cdot 10^6$	11798 ± 108	2861 ± 53
$gg, q\bar{q} \to t\bar{t} \to b\bar{b}q\bar{q}\tau\nu_\tau$	80 pb	$0.8 \cdot 10^6$	875 ± 30	230 ± 15
$gg, q\bar{q} \to t\bar{t} \to b\bar{b}\tau\nu_\tau\ell\nu_\ell,\ \ell = e, \mu$	26.7 pb	$0.27 \cdot 10^6$	253 ± 16	36 ± 6
$gg, q\bar{q} \to t\bar{t} \to b\bar{b}\ell\nu_\ell\ell'\nu'_\ell,\ \ell = e, \mu$	26.7 pb	$0.27 \cdot 10^6$	63 ± 8	6 ± 2
$gg, q\bar{q} \to t\bar{t} \to b\bar{b}\tau\nu_\tau\tau\nu_\tau$	6.6 pb	$6.6 \cdot 10^4$	24 ± 5	3 ± 2
$gg, q\bar{q} \to t\bar{t} \to b\bar{b}q\bar{q}q\bar{q}$	240 pb	$240 \cdot 10^6$	3 ± 2	2 ± 1
$f\bar{f} \to Z$	49 000 pb	$4.9 \cdot 10^8$	6 ± 4	1 ± 1
$f\bar{f} \to ZZ$	11.3 pb	$11.3 \cdot 10^5$	2 ± 1	< 1
$ff' \to ZW$	26.7 pb	$26.7 \cdot 10^5$	3 ± 2	< 1
$f\bar{f} \to WW$	70.3 pb	$70.3 \cdot 10^5$	1 ± 1	< 1
$ff' \to W, gW, \gamma W$ $fg \to f'W$	520 000 pb	$5.2 \cdot 10^9$	660 ± 81	120 ± 35
$gb \to tW$	43.0 pb	$4.3 \cdot 10^5$	41 ± 7	2 ± 1
$gq \to tbq'$	204 pb	$2.0 \cdot 10^6$	10 ± 3	1 ± 1
$q\bar{q} \to W \to tb$	6.9 pb	$6.9 \cdot 10^4$	4 ± 1	< 1
$q\bar{q} \to gW \to b\bar{b}W$	396.5 pb	$4.0 \cdot 10^6$	1 ± 1	< 1

Table 4.4: *Contribution of background processes to the signal (first row). For consistency all cross sections are taken according to LO calculations. The last two columns show in comparison the remaining events after the event selection for different $E_\perp$ jet cuts.*

should be mentioned that also elastic, single and double diffractive events contribute with 0.8 events on average to each signal event. This leads to a central value of 2.5 for the Poisson distributed number of minimum bias events per signal event. With the CMS settings a slightly elevated top mass of 172.7 GeV will be achieved. This is the mass value which would be measured at CMS finally. Only the small discrepancy between the two models of LHCb and CMS is relevant as estimate for the uncertainty in the measured top mass.

15. Background processes are considered as listed in table 4.4. The first two rows show the $t\bar{t}$ signal process subdivided into the contribution of events with electrons and muons in the partonic final state on the one hand and events with tau leptons on the other hand. This is useful to reveal the different efficiencies of the applied event selection. The reconstructed top in the hadronic decay branch has a mass of 170.9 ± 0.25 GeV. The contribution of the Z and Z pair production as well as the ZW and W pair production, even with lower jet transverse energy cuts is negligible compared to the semileptonically decaying $t\bar{t}$ signal events. Due to the huge cross section of the single Z production and the W production partially accompanied by a quark, gluon or photon in the hard scattering, and additional jets by initial state radiation, it gives the biggest contribution to the background. As already mentioned not all events but the relevant fraction of them could be generated by imposing cuts on the center of mass energy and the transverse momentum of the

hard scattering process to allow the production of the demanded high $E_\perp$ objects in the final state. In case of the single Z production a center of mass energy of $\sqrt{\hat{s}} > 120\,\text{GeV}$ was required to reduce the cross section to $341.1\,\text{pb}$. In case of single W production $\sqrt{\hat{s}} > 140\,\text{GeV}$ and a transverse momentum of $\hat{p}_\perp > 40\,\text{GeV}$ yield a reduced cross section of $14\,000\,\text{pb}$. The number of generated events was normalised to the appropriate cross section and as shown in figure 4.8 the contribution does not affect the fitted top mass value at all.

Jets produced through initial state radiation differ in the lower part of the transverse momentum spectrum from jets produced in the hard scattering process. Therefore it is important to estimate the contribution of single top and W production processes including additional final state partons, predominantly quarks, in the matrix element. This is carried out with the implementation of the matrix elements of figure 4.12 and 4.13 into PYTHIA 5.7 [Sla01]. These are the single top production accompanied by an additional b and a non b jet in figure 4.12 a), the single top production accompanied by an additional W boson decaying into a pair of fermions in the same figure b), the single top production via a highly virtual W boson which decays into a resonant top quark and a b quark in figure 4.13 a) and the single W boson production accompanied by an additional quark antiquark pair arising from a gluon in the same figure b) [Sla01]. The cross section of all processes is of the same order of magnitude as the signal except for the single top production via the highly virtual W boson with $\sigma \simeq 6.9\,\text{pb}$. Nonetheless only few events remain even after the lower cuts in jet transverse energy for all considered processes. Furthermore a part of the contribution of the implemented $2 \to 5$ and $2 \to 4$ processes of the single top and W production is already covered with the default W boson production processes of PYTHIA. The sum of all investigated background processes contribute marginally to the signal even though some are double counted. The shift of the top mass is expected to be less than $100\,\text{MeV}$ as indicated in table 4.3.
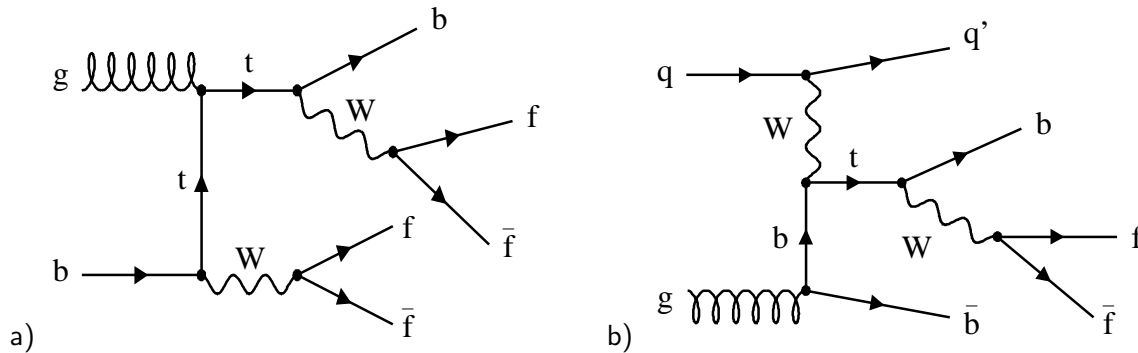
Figure 4.12: Processes of the single top production with five fermions in the final state, three coming from the top quark decay.
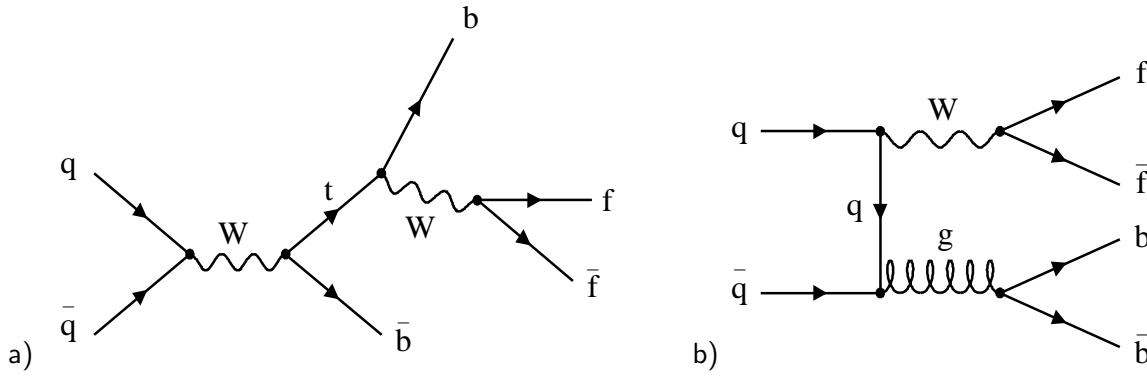
Figure 4.13: Single top production (a) and W production associated with a gluon (b) with four fermions in the final state, two coming from the W boson decay respectively.

Once all relevant error sources have been investigated the total error on the top mass can be determined. Taking the errors as normal distributed and uncorrelated the total error is simply obtained by the quadratic sum of all the errors. For each individual error source it could be shown that the uncertainty in the top mass will be small assuming the variation of the parameters in a reasonable range. Following the arguments of the preceding survey a total uncertainty in the top mass even below 900 MeV is not unrealistic. The dominating contribution of 400 MeV comes from the dependence of the reconstructed top mass on the $p_\perp$ of the generated top quarks. Assuming that not the best calibration precision of the calorimeters will be achieved, i.e. only within $\pm0.5\,\%$ for the electromagnetic calorimeter and $\pm2\,\%$ for the hadronic calorimeter the total uncertainty on the top mass would still be kept below 1.3 GeV. All the other considered error sources can only become better than the precision on the W boson mass, the knowledge of the b quark fragmentation and the amount of statistics.

The considerations made here do not include the statistical error on the central value of the investigated systematic uncertainties, which is in most cases about 400 MeV (see table 4.3). More available CPU time in the future will reduce this error remarkably[2]. Nevertheless, taking the statistical error into account, the total uncertainty on the top mass increases to 1 GeV, assuming the best calibration precision of the calorimeters will be achieved and to 1.36 GeV with the slightly degraded calibration precision also investigated above.

---

[2]Over two years of CPU time (on a SUN ULTRA 10) were needed to achieve the rather exhaustive survey of systematic uncertainties presented here. Available CPU's will be about one order of magnitude faster at the scheduled start time of the LHC.

5

Helicity of the W boson

The weak decays of the top quark are described by the universal $V - A$ charged current interactions within the standard model. The top quark mass far above the W boson production threshold shows up in a fundamentally different polarization of the W boson in a top quark decay compared to the weak decay of the lighter quarks via the charged current.

The W boson polarisation can be measured with the help of the lepton helicity angle explained in the next section. The polarizations as implemented in the event generator PYTHIA and the $2 \rightarrow 6$ matrix elements are discussed since the study is based on them. Following the technical issues, the event selection and the reconstruction of the lepton helicity angle is covered in the next section. Finally, systematic uncertainties are discussed in the last section.

5.1   The lepton helicity angle

The polarisation can be measured with the helicity angle of the lepton coming from a W boson which in turn comes from a top quark. The helicity angle θ^* is obtained by measuring the angle of the lepton direction of flight in the rest frame of its parent W boson with respect to the W boson direction of flight in the rest frame of its parent top quark. In figure 5.1 the angle and how it can be obtained is illustrated. The normalised
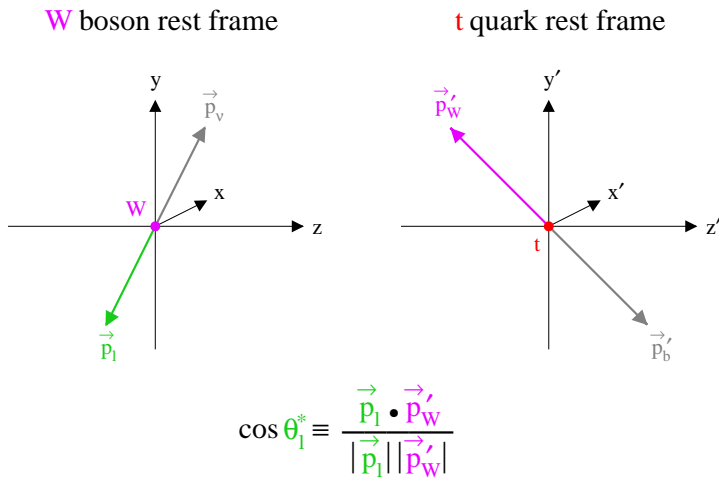
Figure 5.1: The lepton helicity angle can be obtained by measuring the opening angle between the lepton momentum vector in its parent W boson rest frame and the W boson momentum vector in its parent top quark rest frame. The cosine of the angle is given by the scalar product of the normalised lepton and W boson momentum vectors, i.e. their directions of flight.

Polarisation	Helicity state
left circular	$h_W = -1$
longitudinal	$h_W = 0$
right circular	$h_W = +1$

Table 5.1: *The different polarisations and the corresponding helicity states of the W boson including the $h_W = +1$ state which is strongly suppressed within the standard model.*

distribution of the lepton helicity angle within the standard model is given by

$$\frac{1}{N}\frac{dN}{d\cos\theta^*} = \frac{3}{8}\frac{1}{1+f}(1-\cos\theta^*)^2 + \frac{3}{4}\frac{f}{1+f}\sin^2\theta^* \tag{5.1}$$

at tree level. Neglecting the b quark mass the factor f is given by

$$f = \frac{m_t^2}{2m_W^2} \;. \tag{5.2}$$

The first term of the distribution corresponds to left circular polarized W bosons while the second term arises from longitudinal polarized W bosons. The contribution of right circular polarized W bosons is suppressed in top decays with a pure $V - A$ coupling by a chiral factor of the order m_b^2/M_W^2. In the non standard model decay of the top with a non vanishing contribution of right circular polarized W bosons a term proportional to $(1+\cos\theta^*)^2$ would have to be added to the normalised distribution 5.1. The polarizations and the corresponding helicity states of the W boson are listed in table 5.1. With the used top quark and W boson masses of table 3.1 the ratio of the two helicity states $h_W = 0, -1$ can be written as

$$\frac{\Gamma(h_W = 0)}{\Gamma(h_W = -1)} = \frac{1}{2}\left(\frac{m_t}{m_W}\right) = 2.37 \tag{5.3}$$

at tree level within the standard model and the resulting individual fractions are given by

$$\frac{\Gamma(h_W = -1)}{\Gamma_{\text{tot}}} = 0.297$$

$$\frac{\Gamma(h_W = 0)}{\Gamma_{\text{tot}}} = 0.703 \tag{5.4}$$

$$\frac{\Gamma(h_W = +1)}{\Gamma_{\text{tot}}} = 0 \;\;.$$

In figure 5.2 the distribution of the lepton helicity angle within the standard model and its decomposition into the longitudinal and left circular polarizations are shown. Recent measurements of the W boson helicity from CDF yield $\Gamma(h_W = 0)/\Gamma_{\text{tot}} = 0.91 \pm 0.39$ consistent with the standard model expectations [Aff00]. An improved measurement of the W boson helicities provides a unique test of the standard model and decreases
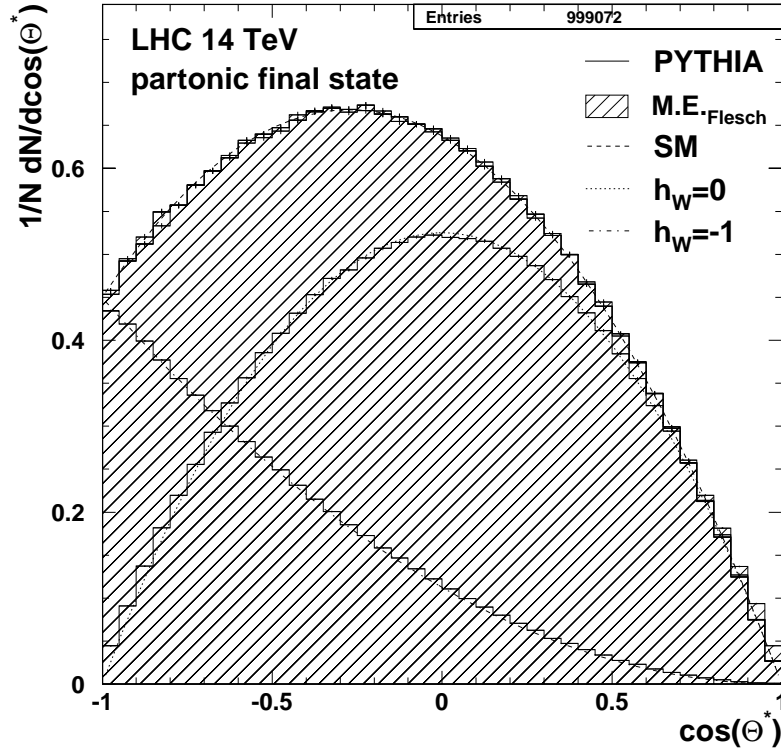
Figure 5.2: Cosine of the lepton helicity angle θ^* within the standard model and its decomposition into the longitudinal and the left circular polarizations for the predictions of the event generator PYTHIA 5.7 and the implemented $2 \to 6$ matrix elements in on-shell approximation. The theoretical predictions of formula (5.1) are indicated as smooth lines. The partonic final state of the compared matrix elements describe perfectly well the standard model predictions. While default PYTHIA achieves the anisotropic W boson decay by weights, it is accurately calculated in the $2 \to 6$ matrix elements.

systematic uncertainties in other measurements (see for example the important influence of the W boson polarisation on the determination of the top mass in leptonic final states with J/Ψ [Kha99]).

5.2 W boson helicity states in PYTHIA

The $2 \to 2$ default matrix elements of PYTHIA do not include the decay of the top quark and the W boson. This is implemented in the framework of the parton shower approach. By setting the variable MSTP(47) the W boson is allowed to decay according to the standard model (MSTP(47)=1) or isotropically (MSTP(47=0)). The angular distribution of the standard model is achieved with the acceptance rejection method. First PYTHIA provides a W boson decay of given angle θ^*. Then a random number is chosen between zero and the absolute maximum of the lepton helicity angle distribution of figure 5.1.

Helicity state	Decay particle flavour	Switch
$h_W = -1$	all weak isospin members with $I = -\frac{1}{2}$	MSTP(47)=2
	only charged leptons, no quarks	MSTP(47)=5
$h_W = 0$	all weak isospin members with $I = -\frac{1}{2}$	MSTP(47)=3
	only charged leptons, no quarks	MSTP(47)=6
$h_W = +1$	all weak isospin members with $I = -\frac{1}{2}$	MSTP(47)=4
	only charged leptons, no quarks	MSTP(47)=7

Table 5.2: *The additional possibilities implemented in PYTHIA for the separate investigation of the different W boson helicities. The helicities can be chosen for all or only the leptonic W boson decays i.e. the hadronic W boson decays take place according to the standard model.*

If the random number chosen is smaller than the distribution evaluated at the given angle θ^* the decay will be accepted. Due to the relatively smooth behaviour of the distribution a phase space transformation is not applied. In addition to the choices offered by PYTHIA the possibility to switch on the individual W boson helicity states separately were implemented as listed in table 5.2. The modified source code necessary to achieve this is shown in appendix C. Technically the lepton helicity angle can be obtained by the convenient expression

$$\cos\theta^* \simeq \frac{p_b \cdot (p_\ell - p_{\nu_\ell})}{p_b \cdot (p_\ell + p_{\nu_\ell})} \tag{5.5}$$

of the four vectors of the partons b, ℓ and ν_ℓ which avoids the numerical boosts with its uncertainties due to finite computing precision. The equation holds also for the antiparticles where the helicity state $h_{W^+} = -1$ corresponds to the helicity state $h_{W^-} = +1$ and therefore the distributions are identical.

5.3   Determination of the lepton helicity angle θ^*

The analysis is accomplished exactly the same way as for the determination of the top mass. Merely the cuts on the already reconstructed jets of the semileptonic $t\bar{t}$ events were loosened to improve the statistics and to release the strongly restricted and imbalanced phase space of the reconstructed angular distributions. The transverse energy of the non b and b jets were required to lie above the threshold $E_\perp = 20\,\text{GeV}$ and $E_\perp = 30\,\text{GeV}$ respectively. After the top quarks are reconstructed an additional cut was implied on the top masses obtained to avoid misreconstructed events with an enhanced top mass as shown in figure 5.3 a). In this figure the mass of the reconstructed top quarks with a hadronically and leptonically decaying W boson are compared. The shapes are quite similar due to the balanced transverse momentum cuts on the non b jets, the lepton and the missing $p_\perp$. The less pronounced peak of the top with the leptonically decaying W boson is a result of the degraded resolution of missing $p_\perp$ as compared to the transverse
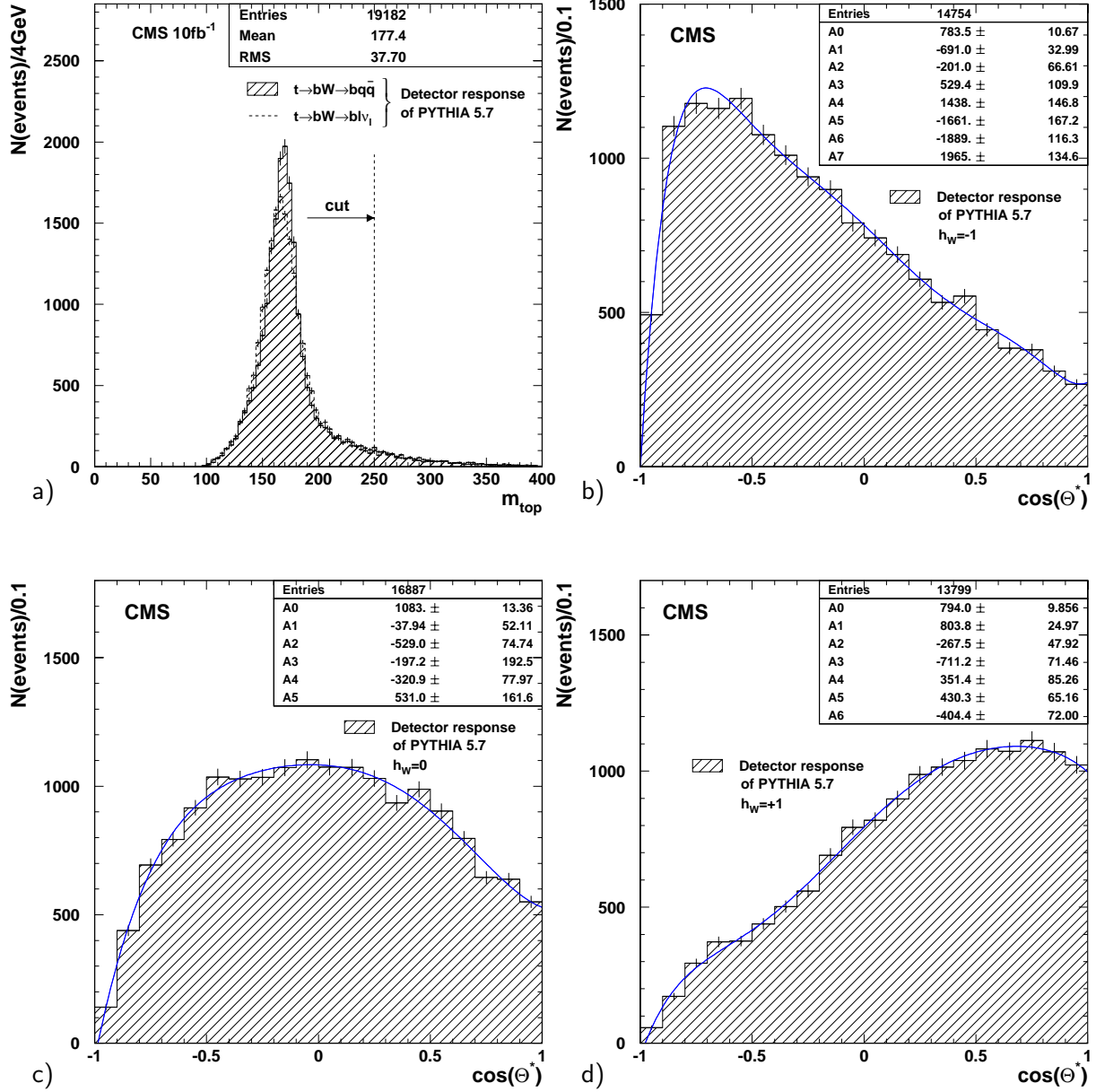
Figure 5.3: Masses of the reconstructed top quarks in the semileptonic decay channel (a) and the cosine of the reconstructed lepton helicity angle θ*, obtained from top with the leptonically decaying W boson. Each individual helicity state including the $h_W = +1$ state of a right circular polarized W boson, suppressed in the standard model is generated separately. The reconstructed observables for the left (a), long (b) and right circular polarized W bosons (c) are fitted with a polynomial of degree seven, five and six respectively. The values of the polynomial fit parameters are indicated in the plots. Their statistical errors are neglected with respect to the error estimation of the observable. Within the frame of a real measurement the statistics will be improved so that the contribution of the statistical errors of the fit parameters will be marginal.
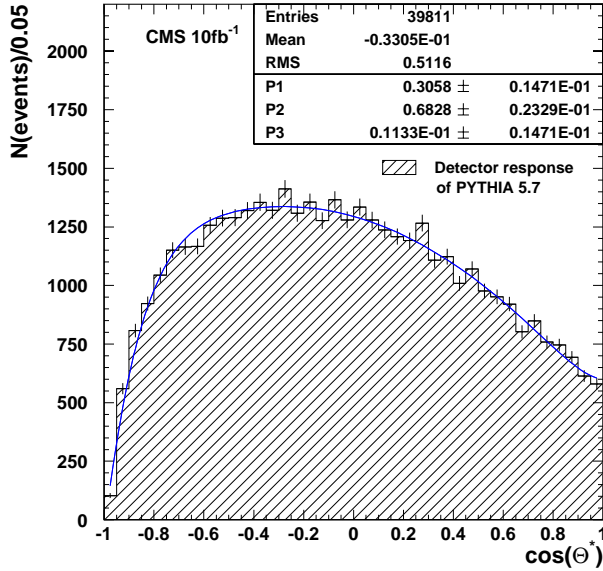
Figure 5.4: The reconstructed cosine of the lepton helicity angle θ^* predicted by the event generator PYTHIA 5.7 including the CMS detector response. The distorted phase space due to the cuts is compensated by the fit functions which are applied to the individual reconstructed W boson helicities, using the same cuts. The fitted parameter values P_1, P_2 and P_3 correspond to the fractions of the helicity states $h_W = -1$, $h_W = 0$ and $h_W = +1$ respectively.

momentum of jets. The long tail towards higher top masses of strongly misreconstructed $t\bar{t}$ events is avoided by the cut $m_t^{\text{rec.}} < 250\,\text{GeV}$. If at least one of the two reconstructed top quarks in an event exceeds this limit the event will be discarded.

The analysis is not optimized in the sense that the knowledge of the already precisely determined top mass was not exploited to resolve the ambiguities in the reconstruction of the top quarks. The reason is the limited available CPU time. The histograms of the W boson helicity are filled in the same jobs as used for the determination of the top mass whenever possible. An optimized analysis will predominantly decrease the statistical error, which is not a critical issue as will be shown below.

To determine the contributions of the different helicity states of the W boson decay, three event samples, each with one of the individual helicity states of the W boson have been generated. The resulting distributions of the lepton helicity angles are fitted with polynomial functions f as shown in figure 5.3 b), c) and d). Now the distribution obtained from a simulated data sample as shown in figure 5.4 can be fitted with the function

$$(\; P_1 \cdot f(h_W\!=\!-1) + P_2 \cdot f(h_W\!=\!0) + P_3 \cdot f(h_W\!=\!-1) \;) \; \cdot \; c_{\text{norm}} \; , \qquad (5.6)$$

where P_1, P_2 and P_3 are the fit parameters and c_{norm} is a constant necessary to normalise the sum of the three fit parameters to unity. A technical complication appears when the hadronically and the leptonically decaying W bosons of the $t\bar{t}$ events in the semileptonic decay channel are both forced to decay according to one and the same individual helicity state. The decomposition of the measured helicity angles differ somewhat from the generated ones. This is because of the fact that several classes of events with different kinematics and cut efficiencies are missing. These classes consist of events with leptonically and hadronically decaying W bosons in different helicity states. The helicity states of the hadronically decaying W bosons are not distinguished here. Therefore all classes of events can be generated in forcing only the leptonically decaying W boson to an individual

helicity state. These decay modes are listed in table 5.2 (MSTP(47)=5,6,7). The resulting fit functions of the three individual lepton helicity angle distributions have already been shown in figure 5.3 b), c) and d). The fit functions reproduce the lepton helicity angle distribution of a generated decomposition (here the decomposition is assumed to be the standard model prediction) better than in case of both W boson decays according to the same helicity state. This in turn means that a deviation of the standard model enforces an iterative approach to measure the lepton helicity angle of a given decomposition. The reconstructed fractions of the different helicity states are

$$\frac{\Gamma(h_W = -1)}{\Gamma_{\text{tot}}} = 0.306 \pm 0.015$$

$$\frac{\Gamma(h_W = 0)}{\Gamma_{\text{tot}}} = 0.683 \pm 0.023 \tag{5.7}$$

$$\frac{\Gamma(h_W = +1)}{\Gamma_{\text{tot}}} = 0.011 \pm 0.015 ,$$

where the errors correspond to an integrated luminosity of $10\,\text{fb}^{-1}$. The fractions within their errors are consistent with the standard model expectations.

5.4   Systematic uncertainties

The systematic uncertainties which are expected to have a noticeable effect on the measurement of the lepton helicity angle are listed in table 5.3. The influence of the spin correlation turned out to lie within the permille level even with the lower jet cuts as already discussed during the top mass determination. Therefore it is not considered in the

Source of uncertainty	$\Gamma(h_W = -1)/\Gamma_{\text{tot}}$	$\Gamma(h_W = 0)/\Gamma_{\text{tot}}$	$\Gamma(h_W = +1)/\Gamma_{\text{tot}}$
CTEQ2L	0.350 ± 0.026	0.652 ± 0.040	-0.002 ± 0.025
CTEQ3L	0.330 ± 0.025	0.687 ± 0.039	-0.017 ± 0.024
PYTHIA 5.7 (CTEQ4L)	0.306 ± 0.015	0.683 ± 0.023	0.011 ± 0.015
HERWIG 6.1	0.319 ± 0.024	0.646 ± 0.038	-0.036 ± 0.024
PYTHIA 6.1	0.326 ± 0.024	0.675 ± 0.038	-0.001 ± 0.024
$m_W + 61\,\text{MeV}$	0.323 ± 0.025	0.681 ± 0.039	0.004 ± 0.024
$m_W - 61\,\text{MeV}$	0.304 ± 0.024	0.695 ± 0.038	0.001 ± 0.024
$m_t = 177.5\,\text{GeV}$	0.302 ± 0.024	0.683 ± 0.038	0.015 ± 0.024
$m_t = 172.5\,\text{GeV}$	0.315 ± 0.024	0.681 ± 0.039	0.004 ± 0.024
$\epsilon_b = 0.0035$	0.314 ± 0.026	0.669 ± 0.040	0.017 ± 0.025
MI Model UA5	0.294 ± 0.024	0.692 ± 0.039	0.014 ± 0.025
MI off	0.345 ± 0.027	0.647 ± 0.042	0.007 ± 0.027

Table 5.3: Fractions of the W boson helicity states and their errors obtained through a fit to the reconstructed lepton helicity angle.

error analysis below. The items discussed here are obtained by the generation of $1\,000\,000$ events respectively and subsequent processing through the detector simulation.

1. The use of different parton density functions shows non negligible effects, where the density function set CTEQ2L already retracted again shows the greatest deviation. It is not taken into account for the error estimate. Instead the parton density function set CTEQ3L is used.

2. The event generator PYTHIA 6.1 agrees very well with the default predictions of PYTHIA 5.7. HERWIG 6.1 has to be compared to PYTHIA 5.7 without multiple interactions (see last row). The agreement is worse, but HERWIG is almost consistent within its errors with the default prediction. The large deviation of the helicity state $h_W = -1$ is probably only a statistical fluctuation. Nonetheless this and the deviations of the other helicity states are taken into account as systematic uncertainty.

3. The W boson mass of $80.41\,\text{GeV}$ has been varied within $61\,\text{MeV}$ as in the determination of the top mass. The results are consistent with the default predictions and the larger deviations are chosen as contribution to the systematic errors.

4. Also the top mass with an assumed central value of $175\,\text{GeV}$ was varied within the mass window of $\pm 2.5\,\text{GeV}$ which is certainly too large following the analysis of chapter 4. The central values are very close to the default predictions and the larger deviations which are taken into account provide a conservative estimate.

5. The dramatic change of the Peterson fragmentation parameter from $\epsilon_b = 0.005$ to $\epsilon_b = 0.0035$ shows up in slightly different predictions which are nonetheless consistent with the default values. The deviations from the central values have been added to the systematic errors.

6. The usage of the different multiple interaction model UA5 turned out to be small in the determination of the top mass. As a cross check that this is not by chance its influence on the measurement of the W boson helicity states is also investigated here. The predictions agree very well with those obtained using default settings.

The errors are assumed to be uncorrelated and Gaussian distributed as before in the top mass determination. Treating the systematic uncertainties in the same way leads to the reconstructed decomposition of the W boson helicity states and their corresponding error estimates

$$
\begin{aligned}
\frac{\Gamma(h_W = -1)}{\Gamma_{\text{tot}}} &= 0.306 \pm 0.015(\text{stat}) \pm 0.043(\text{syst}) \\
\frac{\Gamma(h_W = 0)}{\Gamma_{\text{tot}}} &= 0.683 \pm 0.023(\text{stat}) \pm 0.022(\text{syst}) \\
\frac{\Gamma(h_W = +1)}{\Gamma_{\text{tot}}} &= 0.011 \pm 0.015(\text{stat}) \pm 0.053(\text{syst}) \,,
\end{aligned}
\tag{5.8}
$$

where the statistical errors correspond to $10\,\mathrm{fb}^{-1}$. The systematic uncertainties provide a conservative estimate due to the variation of parameter values in a wide range. In fact almost all investigated error sources are consistent within their errors with the prediction of the PYTHIA 5.7 event generator using default settings. For an optimized and more detailed analysis more CPU time is necessary.

6

$t\bar{t}$ spin correlation

The top quark decays via an on-shell W boson in contrast to the much lighter d, u, s, c and b quarks which are not able to decay in such a way. Therefore the decay width of the top quark (see equation 2.1) is rather large, corresponding to an extremely short life time. Hence the top quark decays before it can form hadronic bound states. This unique feature can be used to investigate the spin of the top quark which is not possible in the case of the lighter quarks where the spin information gets diluted by hadronisation. Moreover the time for a spin-flip is much larger than the top quark life time such that the probability of a spin-flip by the emission of one or several gluons via a chromomagnetic dipol transition is very small. Thus the measurement of angular distributions of the top quark decay products allow to deduce the top quark spin and to look for deviations of the standard model couplings.

Here the spin correlation is measured in the dileptonic $t\bar{t}$ decay channel with the help of a double differential lepton angular distribution. The observable and its measurement are explained in the section below. In addition some explicit values are discussed for the LHC and the Tevatron. Subject of the next section is the event selection and the reconstruction of top quarks. The $t\bar{t}$ spin correlation is determined in the following section. A correction is applied for the distortion of the phase space. Then a functional dependence can be established between the values of the generated and the diluted reconstructed spin correlation. Moreover the influence of a neutral Higgs boson as discussed in chapter 7 is investigated. In the last section systematic uncertainties are discussed. The dominant contribution comes from the current uncertainty of the gluon density of the proton.

6.1 Spin sensitive observables

The spin of the top and antitop quarks can be inferred from their parity violating weak decay. For a decay particle f the angular distribution of its direction of flight in the rest frame of its polarized parent top quark with respect to the top spin vector can be written as

$$\frac{1}{N}\frac{dN}{d\cos\theta_{\pm}} = \frac{1}{2}(1 + \kappa_f \cos\theta_{\pm}) \ . \tag{6.1}$$

The indices of the angle θ correspond to the top quark (+) and the antitop quark (-) respectively and the coefficient κ_f determines the spin-analyser quality of the top quark daughter particle as listed in table 6.1. For the antitop quark the spin-analyser qualities

f	$\ell^+,\ \bar{d},\ \bar{s}$	$\nu_\ell,\ u,\ c$	b	W	low energy $q,\ \bar{q}$
κ_f	1	-0.31	-0.41	0.41	0.51

Table 6.1: *Spin-analyser quality κ_f of the top quark daughter particle f for the $V-A$ charged current. In the last column the coefficient κ of the W boson daughter particle with the lower energy in the corresponding top rest frame is given.*

are obtained by reverting the sign of the coefficient κ_f, e.g. $\kappa_{\ell^-} = -\kappa_{\ell^+} = -1$. The order α_s QCD corrections to the decays $t \to b\ell\nu$ and $t \to Wb$ of polarized top quarks are small for top and antitop quark polarisation observables [Cza91], [Sch96], [Fis99]. Therefore the investigation of the $t\bar{t}$ spin correlation can be accomplished with the leading order matrix elements of [Ber98a], [Sla01] implemented in PYTHIA 5.7. In the $t\bar{t}$ production the spin correlation between the decay products of the top quarks is most significant in the dileptonic decay channel since the spin-analyser quality of the leptons is maximal as can be extracted from table 6.1. Thus dileptonic $t\bar{t}$ events are predestinated for the investigation of the spin correlation.

Neglecting higher order QCD corrections the normalised double differential angular distribution of the two leptons is given by

$$\frac{1}{N}\frac{d^2N}{d\cos\theta^*_{\ell^+}\,d\cos\theta^*_{\ell^-}} = \frac{1}{4}(1 - \mathcal{A}\cos\theta^*_{\ell^+}\cos\theta^*_{\ell^-})\ . \tag{6.2}$$

The asymmetry coefficient

$$\mathcal{A} = \frac{N(t_L\bar{t}_L + t_R\bar{t}_R) - N(t_L\bar{t}_R + t_R\bar{t}_L)}{N(t_L\bar{t}_L + t_R\bar{t}_R) + N(t_L\bar{t}_R + t_R\bar{t}_L)} \tag{6.3}$$
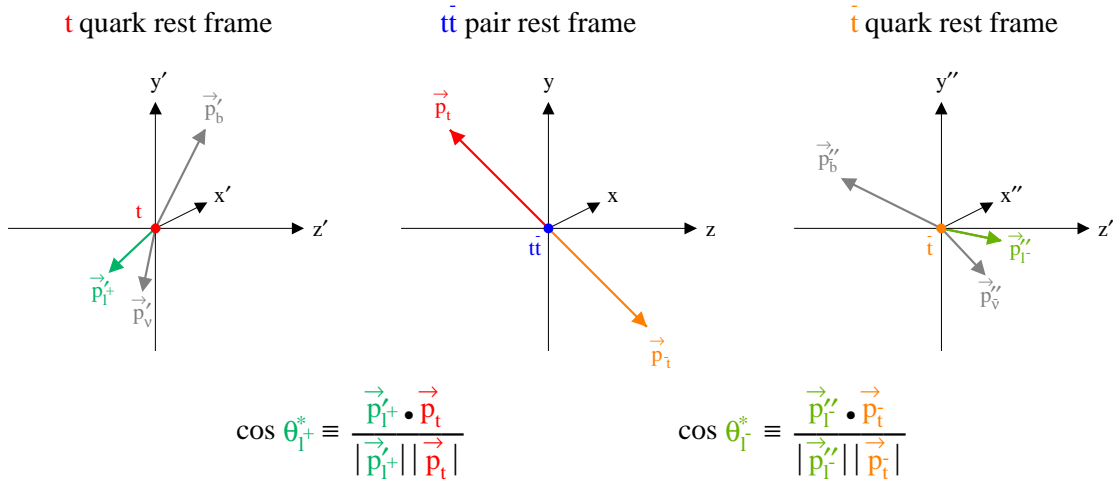
Figure 6.1: *The lepton angles of the helicity basis are obtained by measuring the opening angle between the (anti-)lepton momentum vector in its parent (anti-)top quark rest frame and the (anti-)top quark momentum vector in the $t\bar{t}$ quark pair rest frame. The cosine of the angles is given by the scalar product of the normalised (anti-)lepton and (anti-)top quark momentum vectors. This is the scalar product of their directions of flight.*

Figure 6.2: *Double differential distribution of the cosine of the lepton angles $\theta_{\ell\pm}^*$ in the helicity basis (see text). The $2 \to 6$ on-shell matrix elements from [Ber98a] implemented in PYTHIA 5.7 yield for the quark antiquark annihilation the correlation of plot a) which yield the fitted asymmetry coefficient $\mathcal{A} = -0.469 \pm 0.003$. For the gluon gluon fusion, the correlation of plot b) is obtained with the corresponding asymmetry coefficient $\mathcal{A} = 0.431 \pm 0.002$. At the LHC the correlation of plot c) with an asymmetry coefficient of $\mathcal{A} = 0.313 \pm 0.002$ is expected using the parton density functions of CTEQ4L which provide 87 % of the produced $t\bar{t}$ pairs by the gluon gluon fusion. The default $2 \to 2$ matrix elements of PYTHIA provide no correlation as can be seen in plot d). The value of the fitted asymmetry coefficient is $\mathcal{A} = -0.001 \pm 0.003$ consistent with zero.*

is the normalised difference between like-spin and unlike-spin $t\bar{t}$ quark pairs. In the helicity basis used here, the angle of a (anti-)lepton θ_ℓ^* is evaluated in the rest frame of its parent (anti-)top quark with respect to the (anti-)top quark direction of flight in the $t\bar{t}$ rest frame. In figure 6.1 the lepton angles and their determination are illustrated. Using the matrix elements from [Ber98a] and the parton density functions of CTEQ4L the prediction for the asymmetry coefficient of the partonic final state expected at the LHC is $\mathcal{A} = 0.312 \pm 0.003$. This value is extracted with the fit function

$$P_1 \cdot (1 - P_2 \cos\theta_{\ell+}^* \cos\theta_{\ell-}^*) \tag{6.4}$$

from plot 6.2 c). The value depends to some extent (to the percent level) on the parton density functions and the matrix elements (on-shell or Breit-Wigner) used as will be shown in the discussion of the systematic uncertainties. In the following the CTEQ4L parton densities and the matrix elements from [Ber98a] have been used. The most significant correlation is obtained with only one type of $t\bar{t}$ production mechanism since the different mechanisms show opposite correlations, i.e. $\mathcal{A} = 0.431 \pm 0.002$ for the gluon gluon fusion and $\mathcal{A} = -0.469 \pm 0.003$ for the quark antiquark annihilation (see figure 6.2 a) and b). The default $2 \rightarrow 2$ matrix elements from PYTHIA do not include the spin correlation as shown in figure 6.2 d). The resulting fitted asymmetry coefficient of $\mathcal{A} = -0.001 \pm 0.003$ is consistent with zero. To improve the significance of the correlation it would be desirable to find a basis in which the asymmetry coefficient $\mathcal{A}$ could reach its extreme values ± 1. Unfortunately no spin quantisation axis exists for the gluon gluon fusion processes, which dominate at the LHC, with respect to which the top and antitop quark spins are $100\,\%$ correlated [Alt00].

An optional upgrade of the LHC with proton proton collisions at $28\,\mathrm{TeV}$ would lead to a slightly enlarged fraction of $t\bar{t}$ events produced by the gluon gluon fusion (about $5\,\%$ using the parton densities of CTEQ4L) resulting in the enhanced asymmetry coefficient $\mathcal{A} = 0.347 \pm 0.003$ which corresponds to a gain of more than $10\,\%$. In contrast, at

Collider	Hadronic c.m.s. energy $\sqrt{s}$	Basis	Asymmetry coefficient $\mathcal{A}$ (standard model expectation)
Tevatron	1.8 TeV	helicity	$\mathcal{A} = -0.43$
	2.0 TeV		$\mathcal{A} = -0.41$
	1.8 TeV	optimal	$\mathcal{A} = -0.88$
	2.0 TeV		$\mathcal{A} = -0.85$
LHC	14 TeV	helicity	$\mathcal{A} = 0.31$
	28 TeV		$\mathcal{A} = 0.35$

Table 6.2: Standard model expectations of the asymmetry coefficient A as defined in equation (6.2) for different colliders and hadronic center of mass energies. The predictions in the helicity basis are obtained with the $2 \rightarrow 6$ matrix elements in the on-shell approximation using the CTEQ4L parton densities. The asymmetry coefficient in the optimal basis at a collider energy of $\sqrt{s} = 1.8$ TeV is taken from [Gro00]. The value in the optimal basis for a collider energy of $\sqrt{s} = 2.0$ TeV is extrapolated.
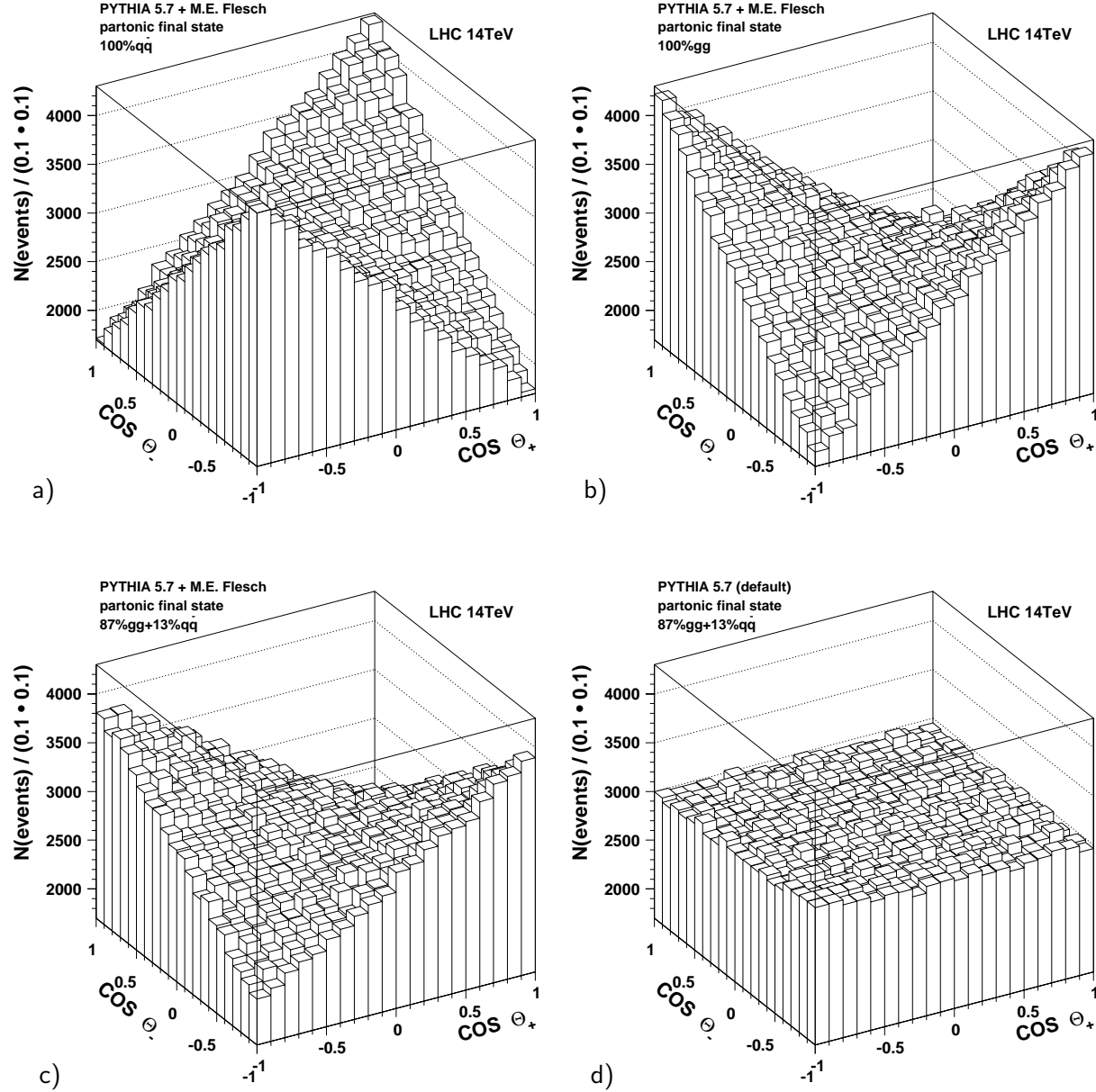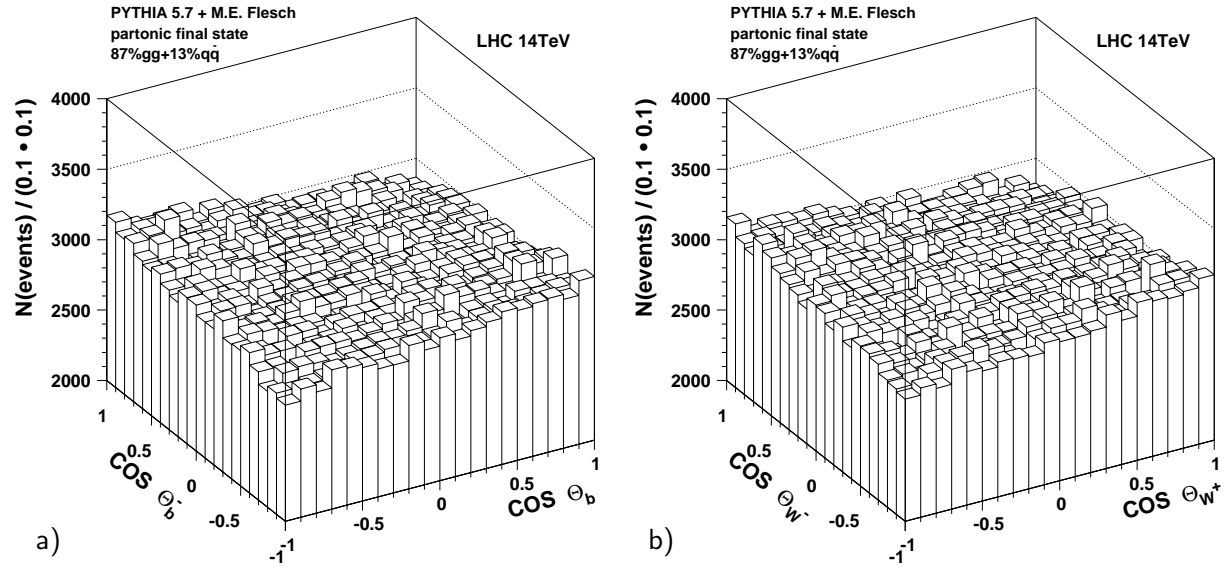
Figure 6.3: Double differential distribution of the cosine of the b quark and W boson angles θ^* in the helicity basis (see text) for the $2 \rightarrow 6$ on-shell matrix elements from [Ber98a] which include the $t\bar{t}$ spin correlation. The distributions are obtained using the parton density functions of CTEQ4L. The distribution of the b quarks and the W bosons yield the same asymmetry coefficient $\mathcal{A} = 0.048 \pm 0.002$ within the errors. This is because the b quarks and the W bosons are back-to-back in the corresponding top quark rest frame so that the single differential distributions have to be inverted for the particles and the antiparticles. The double inversion then yields the same correlation. Compared to the lepton case the correlation is more than six times weaker.

the Tevatron where proton antiproton collisions take place at a hadronic center of mass energy of $1.8\,\text{TeV}$ (recent Run I) an asymmetry coefficient of $\mathcal{A} = -0.430 \pm 0.003$ as defined here in the helicity basis is achieved. Due to the dominating quark antiquark annihilation processes (about $90\,\%$) an optimal basis which would yield $\mathcal{A} = -1$ in case of $100\,\%$ quark antiquark annihilation processes can be applied there. The standard model prediction for the asymmetry coefficient in the optimal basis at the Tevatron (Run I) is $\mathcal{A} = -0.88$ [Gro00] (Keep in mind that the double differential cross section of equation 6.2 is defined here for the LHC with a negative sign in front of the asymmetry coefficient $\mathcal{A}$, oppositely to the definition in [Gro00] and [Cho99]). At the Tevatron in Run II with a collider energy of $\sqrt{s} = 2.0\,\text{TeV}$ the fraction of quark antiquark annihilation processes will be reduced by about $2\,\%$ which will result in a slight decrease of the asymmetry coefficient of about $4\,\%$ to the value $\mathcal{A} = -0.414 \pm 0.003$ evaluated in the helicity basis. However, this minor loss in significance will be more than compensated by the enhanced statistics in Run II. In table 6.2 the standard model predictions for the asymmetry coefficient expected at the Tevatron and the LHC are given for different energies.

The correlation of the b quarks and the W bosons which have the same absolute value of the spin-analyser quality but with opposite sign are shown in the helicity basis for the

LHC in figure 6.3 a) and b). The asymmetry coefficient shrinks to $\mathcal{A} = 0.048 \pm 0.002$ which is more than six times smaller than what is achieved using the correlations between the leptons. The values of the coefficients are identical for the b quarks and the W bosons since they are back to back in the corresponding top quark rest frame and therefore both single differential angular distributions, for the particle and the antiparticle have to be inverted.

6.2   Selection and reconstruction of dileptonic $t\bar{t}$ events

Before the asymmetry factor can be determined, $t\bar{t}$ events in the dileptonic decay channel have to be selected. After the selection, the top quarks have to be reconstructed to produce the double differential distribution of the lepton angles in the helicity basis.

1. At least two charged leptons have to be found in the pseudo rapidity range of $|\eta| < 2.4$ to be fully contained in the electromagnetic calorimeter and the muon chambers. Exactly two charged leptons have to lie above a transverse energy threshold of $20\,\mathrm{GeV}$.

2. The charges of the two high transverse momentum leptons, deduced from the bending of their tracks in the magnetic field of the solenoid are required to have opposite signs.

3. The leptons are considered as isolated if within the radius of 0.3 in the η, ϕ space more than $90\,\%$ of the deposited transverse energy belongs to the reconstructed lepton.

4. A missing transverse momentum above $20\,\mathrm{GeV}$ is required to reflect the fact that two neutrinos are involved in the W boson decays of dileptonic $t\bar{t}$ events. This cut improves the selection of signal events against background but the phase space of the angular distributions becomes unbalanced since the transverse momentum components of the two neutrinos can compensate each other. The correction for this will be given in section 6.3.

5. The jets are reconstructed with the cone jet algorithm, as for the top mass determination and the analysis of the W boson helicity. To gain some statistics the transverse energy threshold of the jets has been set to $20\,\mathrm{GeV}$ and the cone size parameter has been set to R=0.7. At least two jets have to be found, among which exactly two have to be tagged as b jets. As before at least two tracks with an impact parameter of $|d_{xy}| < 1.0\,\mathrm{mm}$ and a signed significance of $\sigma_{xy}\mathrm{sign}([\vec{p}_{\mathrm{jet}} \times \vec{p}_{\mathrm{track}}]_z) > +2.0$ are required for a jet to be tagged as b jet.

The two neutrinos of an dileptonic event cannot be reconstructed since only the missing $p_\perp$ of the event is accessible (the longitudinal boost of the hard subprocess along the beam axis does not allow the determination of the sum of the longitudinal neutrino momenta).

With the help of kinematic constraints imposed by the known W boson and top quark masses the set of two linear and four quadratic equations

$$
\begin{aligned}
\not{p}_x &= p_x(\nu) + p_x(\bar{\nu}) = -(\,p_x(b) + p_x(\bar{b}) + p_x(\ell^+) + p_x(\ell^-)\,) \\
\not{p}_y &= p_y(\nu) + p_y(\bar{\nu}) = -(\,p_y(b) + p_y(\bar{b}) + p_y(\ell^+) + p_y(\ell^-)\,) \\
m_W^2 &= (\,E(\ell^+) + E(\nu)\,)^2 \\
&\quad -(\,p_x(\ell^+) + p_x(\nu)\,)^2 \\
&\quad -(\,p_y(\ell^+) + p_y(\nu)\,)^2 \\
&\quad -(\,p_z(\ell^+) + p_z(\nu)\,)^2 \\
m_W^2 &= (\,E(\ell^-) + E(\bar{\nu})\,)^2 \\
&\quad -(\,p_x(\ell^-) + p_x(\bar{\nu})\,)^2 \\
&\quad -(\,p_y(\ell^-) + p_y(\bar{\nu})\,)^2 \\
&\quad -(\,p_z(\ell^-) + p_z(\bar{\nu})\,)^2 \\
m_t^2 &= (\,E(\ell^+) + E(\nu) + E(b)\,)^2 \\
&\quad -(\,p_x(\ell^+) + p_x(\nu) + p_x(b)\,)^2 \\
&\quad -(\,p_y(\ell^+) + p_y(\nu) + p_y(b)\,)^2 \\
&\quad -(\,p_z(\ell^+) + p_z(\nu) + p_z(b)\,)^2 \\
m_t^2 &= (\,E(\ell^-) + E(\bar{\nu}) + E(\bar{b})\,)^2 \\
&\quad -(\,p_x(\ell^-) + p_x(\bar{\nu}) + p_x(\bar{b})\,)^2 \\
&\quad -(\,p_y(\ell^-) + p_y(\bar{\nu}) + p_y(\bar{b})\,)^2 \\
&\quad -(\,p_z(\ell^-) + p_z(\bar{\nu}) + p_z(\bar{b})\,)^2
\end{aligned}
\tag{6.5}
$$

with the six unknown variables $p_x(\nu)$, $p_y(\nu)$, $p_z(\nu)$, $p_x(\bar{\nu})$, $p_y(\bar{\nu})$ and $p_z(\bar{\nu})$ has to be solved. The energy of the neutrinos, assumed to be in very good approximation massless, can be obtained by $E(\nu, \bar{\nu}) = \sqrt{p_x^2(\nu, \bar{\nu}) + p_y^2(\nu, \bar{\nu}) + p_z^2(\nu, \bar{\nu})}$. The system of equations with up to 16 ambiguities due to the eight quadratic equations has to be solved numerically. This is a non trivial task since the reconstructed objects do not coincide perfectly with the corresponding variables of the partons. Furthermore the phase space for possible initial values of the unknown variables is enormous. Applying the Newton-Raphson method for nonlinear systems of equations [Pre94] or even the globally convergent multidimensional secant method of Broyden fails in most cases, i.e. the solution efficiency is too low. Therefore a semianalytical algorithm optimized for this problem [Sim99a] is used here. Its principle is to step through a one dimensional interval and then compute the other unknown variables. In case of no solutions at all, the masses of the top and antitop quarks are relaxed within a mass window of $15\,\mathrm{GeV}$. Without discrimination between b quark and b antiquark jets as used in this analysis, two solutions are obtained in $2\,\%$ of all cases, four solutions in $82\,\%$ of all cases, six solutions in $1\,\%$ of all cases and eight solutions in $15\,\%$ of all cases. If more than one solution is obtained, the most probable solution is
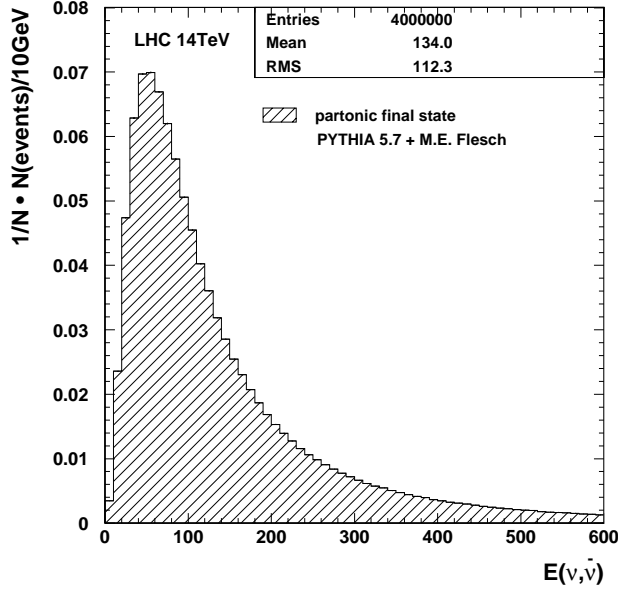
Figure 6.4: *Energy spectrum of the neutri-*
nos and antineutrinos arising from the W
bosons of $t\bar{t}$ events in the dileptonic decay
channel. The normalised distribution is
used twice as probability function for the
solution of the reconstructed energy of the
neutrinos and the antineutrinos (See the
text for details).

chosen. The probability of a solution is defined by

$$P_{\text{solution}} = P_{\cos\hat{\theta}} \cdot P_{E_\nu} \cdot P_{E_{\bar{\nu}}} \tag{6.6}$$

with the normalised distributions $P_{\cos\hat{\theta}}$ of the hard subprocess scattering angle of figure 3.2 and the neutrino energy spectra $P_{E_{\nu,\bar{\nu}}}$ shown in figure 6.4. The correct solution is obtained in about 68 % of cases. While the scattering angle which depends to some extend on the ratio of the $t\bar{t}$ production mechanisms as discussed in section 3.6 can be measured in the semileptonic decay channel, the neutrino energy spectrum has to be deduced indirectly. This gives rise to additional systematic uncertainties which remain to be investigated.

The double differential distributions of the lepton angles in the helicity basis after event selection and choice of the most probable solution are shown in figure 6.5 for the expectation at the LHC (a) and with vanishing generated asymmetry coefficient (b), obtained by a mix of 50 % gluon gluon fusion and 50 % quark antiquark annihilation processes. Both distributions are obtained using the on-shell matrix elements. The Breit-Wigner matrix elements yield the distribution shown in plot (c) and the result of the default PYTHIA 5.7 matrix elements without spin correlation is shown in plot (d). The standard model prediction of the distributions a) and c) agree very well. In contrast, the reconstructed lepton helicity angles shown in plot b) and d), which feature in the partonic final state of the same flat distribution, are not consistent with each other. At first sight one would expect identical reconstructed observables but the gluon gluon fusion processes have different kinematics compared to quark antiquark annihilation processes resulting in different selection efficiencies. Now, in the case of the $2 \rightarrow 6$ matrix elements including the spin correlation, the two production mechanisms populate different regions of the lepton angle phase space differently strong. Therefore the reconstructed observable with spin correlation differs from that without spin correlation. Thus the observable is able to confirm or disprove the spin correlation and to measure the asymmetry coefficient in case of spin correlation.

Figure 6.5: Uncorrected double differential distributions of the cosine of the lepton angles θ^* in the helicity basis of the $2 \to 6$ on-shell matrix elements from [Ber98a] (a) and b), of the $2 \to 6$ Breit-Wigner matrix elements from [Sla01] (c), and of the default matrix elements implemented in PYTHIA 5.7 (d). In each case the parton density function set CTEQ4L is used. The phase space is strongly distorted due to the selection cuts. The fitted asymmetry factors of the reconstructed distributions are therefor not very significant. The standard model predictions for the on-shell matrix elements of a) and the Breit-Wigner matrix elements of c) show consistence with each other. The distributions shown in plot b) and d) differ significantly, though both distributions of the partonic final state can be perfectly described by a horizontal plane. The gluon gluon fusion processes have different kinematics compared to the quark antiquark annihilation processes resulting in different selection efficiencies. Now, in the case of spin correlation the two production mechanisms populate different regions of the lepton angle phase space differently strong. Thus the reconstructed observables with and without spin correlation show differences.

6.3   Determination of the $t\bar{t}$ spin correlation

Once the dileptonic $t\bar{t}$ events have been reconstructed the correlation between the two leptons can be investigated. The uncorrected double differential angular lepton distributions in the helicity basis of figure 6.5 do not have very significant asymmetry coefficients. To reduce the influence of the limited detector acceptance and the different cut efficiencies of events in different phase space regions of the double differential angular lepton distributions, they are divided by a simulated reference sample which passes the same cuts. With equal fractions of gluon gluon fusion and quark antiquark annihilation processes the matrix elements including the spin correlation on the parton level result in a flat distribution. Therefore the reconstructed distribution of figure 6.5 b) with equal fractions of gluon gluon fusion and quark antiquark annihilation processes has been chosen as reference sample. The error of the resulting distributions is obtained by Gaussian error propagation taking into account the statistical error of the simulated data and the statistical error of the reference sample, bin by bin. It turns out, that the distributions obtained this way have an additional inclination beside the asymmetry. The inclination depends on the ratio to which gluon gluon fusion and quark antiquark annihilation pro-

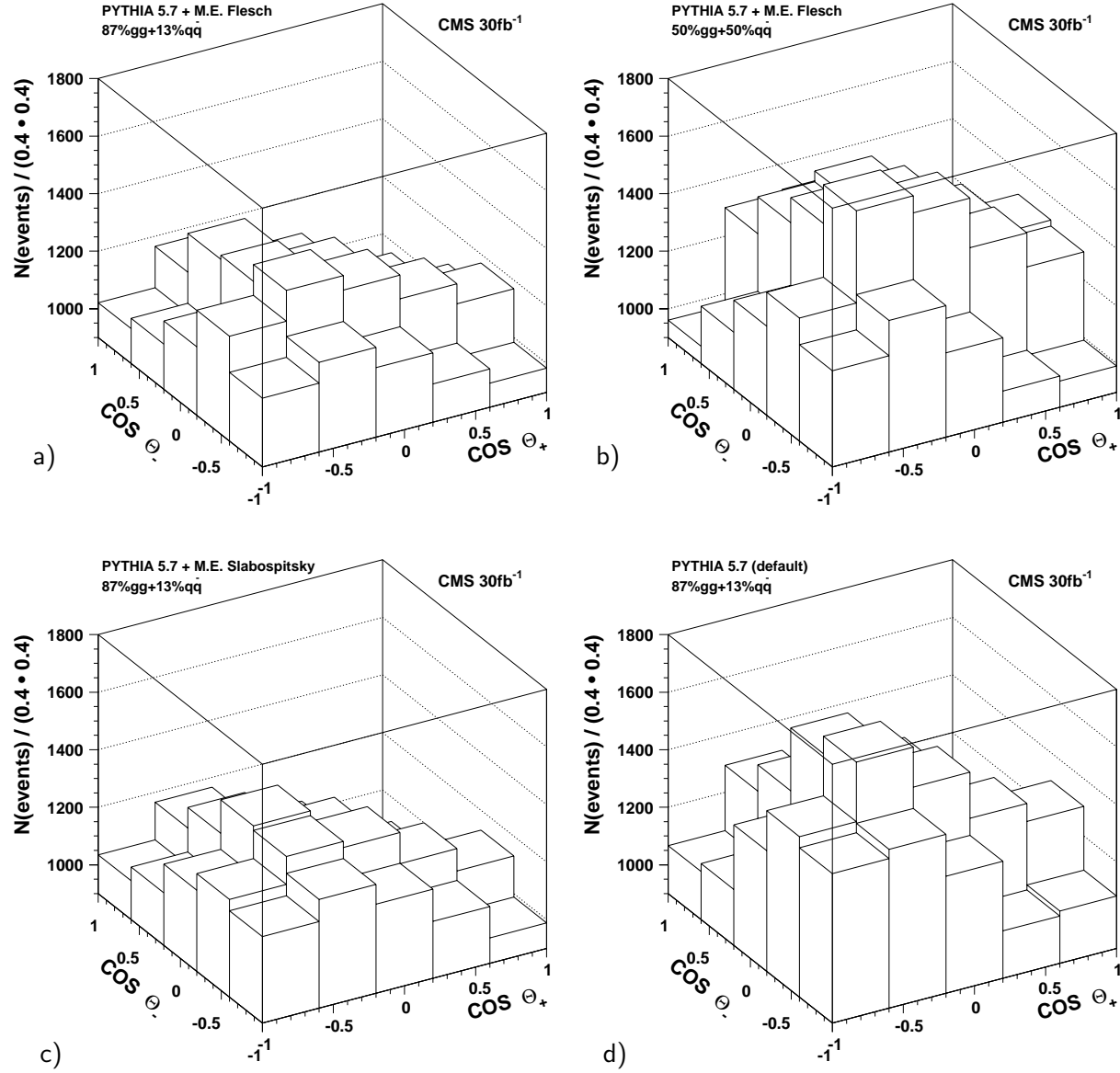Figure 6.6: *Double differential distribution of the cosine of the lepton angles θ^* in the helicity basis of the $2 \to 6$ on-shell matrix elements from [Ber98a] including the coherent contribution of a neutral Higgs boson with a mass of $400\,GeV$ decaying into a $t\bar{t}$ pair (the Higgs boson sector is discussed in chapter 7). In a) a Higgs boson with standard model couplings and in b) a CP violating Higgs without coupling to vector bosons are shown. The two simulated processes yield the asymmetry coefficients $\mathcal{A} = 0.309 \pm 0.002$ and $\mathcal{A} = 0.320 \pm 0.002$ respectively. The values differ by less than three percent from the standard model prediction without a Higgs boson.*

cesses contribute to the cross section. This comes, similar to the discussion at the end of the last section, from different cut efficiencies of the gluon gluon fusion and quark anti-quark annihilation processes on the one hand, and different population of different lepton angle phase space regions of the two processes on the other hand. The inclination can be described by a plane proportional to the function $c_{\mathrm{norm}} \cdot (\cos\theta^*_{\ell+} + \cos\theta^*_{\ell-})$. However, the value of the asymmetry coefficient obtained by a fit of the double differential angular lepton distribution, either with the fit function of equation (6.4) which is proportional to the normalised double differential cross section of equation (6.2) or with the expanded fit function

$$P_1 \cdot (\ 1 - P_2 \cos\theta^*_{\ell+} \cos\theta^*_{\ell-} + P_3(\cos\theta^*_{\ell+} + \cos\theta^*_{\ell-})\ ) \tag{6.7}$$

remains invariant since the original fitting function 6.4 and the expansion are orthogonal, i.e the integral of the product of the two functions over the whole phase space of the lepton helicity angles vanishes.

Moreover, the contribution of a neutral Higgs boson resonance above the $t\bar{t}$ production threshold as discussed in chapter 7 could become important. A possible CP violating contribution from a non standard model Higgs boson with a mass above the $t\bar{t}$ production threshold as given in figure 6.6 b) is not distinguishable from the standard model expectation without a Higgs boson (figure 6.2 c). The same holds for a standard model Higgs boson (figure 6.6 a). Thus the applied observable is not sensitive to CP violating effects of a Higgs boson.

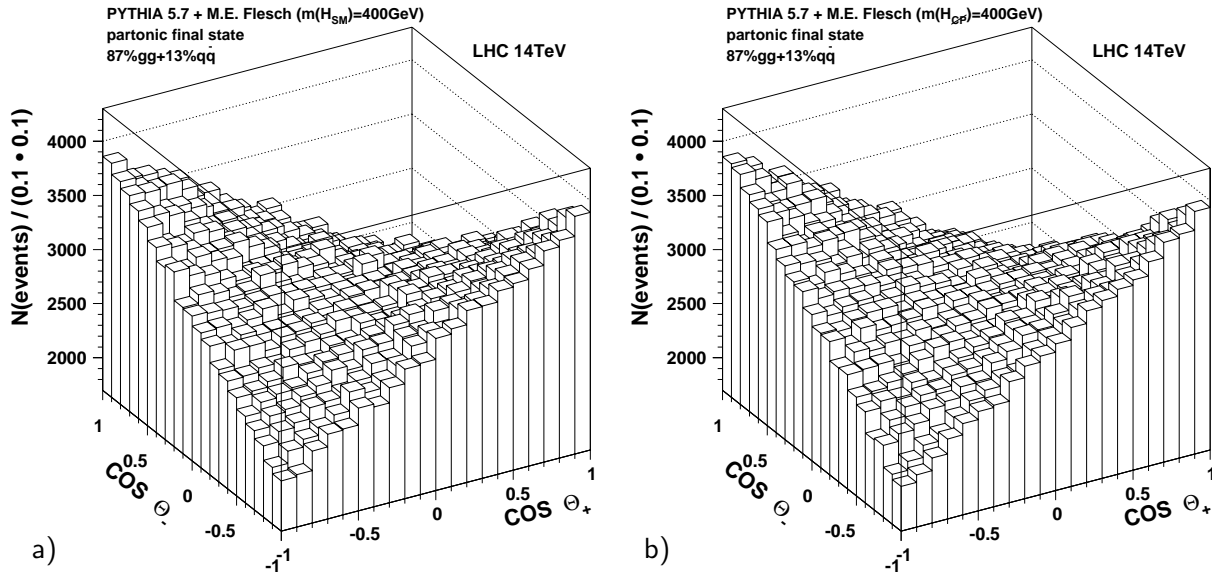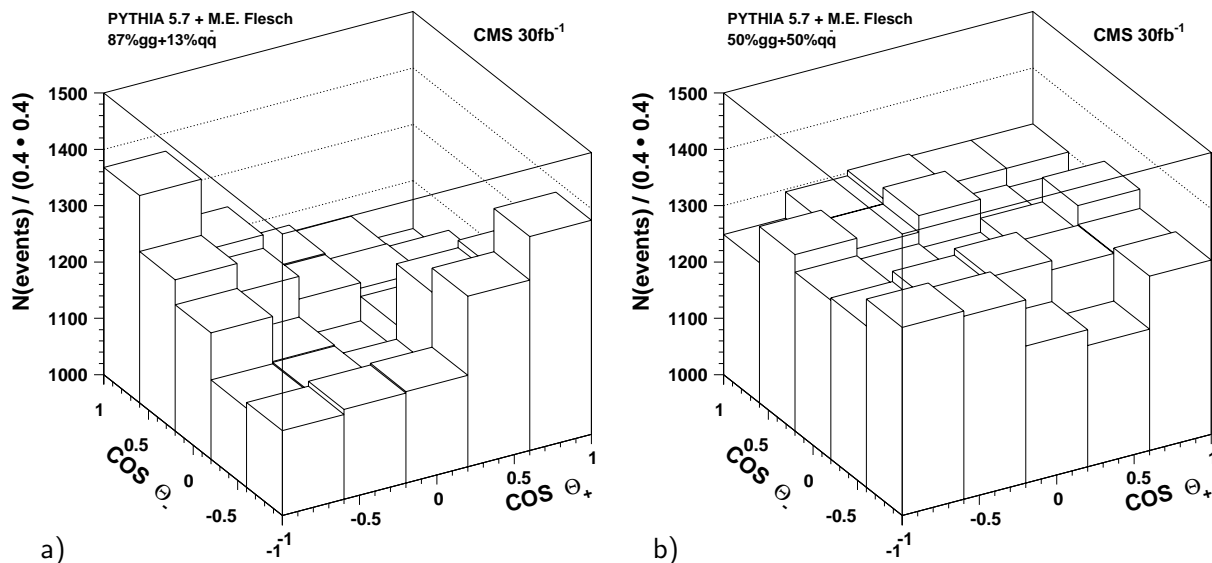*Figure 6.7: For distortion corrected double differential distributions of the cosine of the lepton angles θ^* in the helicity basis of the $2 \rightarrow 6$ on-shell matrix elements from [Ber98a]. The standard model expectation is shown in (a). Balanced fractions of gluon gluon fusion and quark antiquark annihilation processes are shown in (b). Both distributions are obtained using the parton density function set of CTEQ4L.*

P1	0.1225E-03 ±	0.4065E-02
P2	0.4615 ±	0.9885E-02
P3	0.1369 ±	0.3780E-01
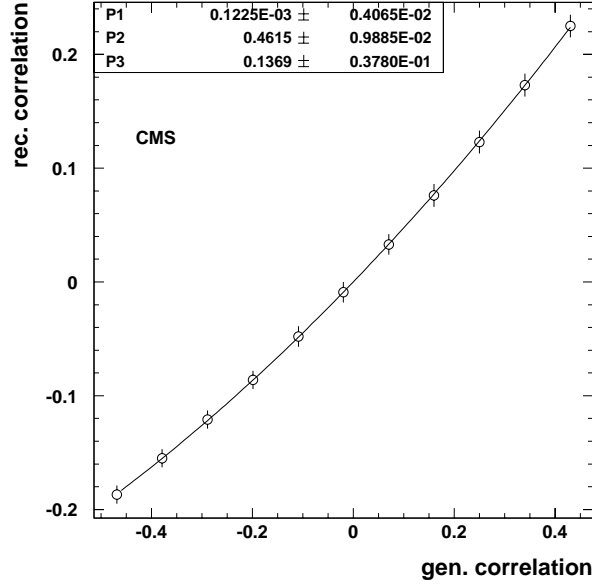
Figure 6.8: Functional dependence of the reconstructed asymmetry coefficient on the given value of the asymmetry obtained by the appropriate mixture of the gluon gluon fusion and the quark antiquark annihilation processes. The dependence can be well described by a second order polynomial with the fitted coefficients as indicated. The reconstructed asymmetry coefficients are smaller than the generated ones because they are diluted due to misreconstructed events.

Finally the reconstructed and for distortion of the phase space corrected distributions are shown in figure 6.7 after adjustment of the additional inclination which does not affect the fitted asymmetry coefficient. The obtained value for the fitted asymmetry coefficient of the standard model expectation (figure 6.7 a) is given by $\mathcal{A} = 0.159 \pm 0.019$ and a simulated data sample with balanced contributions of gluon gluon fusion and quark antiquark annihilation processes yields $\mathcal{A} = -0.016 \pm 0.017$ consistent with a vanishing asymmetry within the errors. The statistics of $30\,\mathrm{fb}^{-1}$ assumed here corresponds to three years running at low luminosity.

Beside the influence of misreconstructed $t\bar{t}$ events in the dileptonic decay channel, the spin correlation gets diluted due to wrongly chosen solutions in the event reconstruction. This can not be avoided since the topology of the events with their two neutrinos is obtained on a probability basis. Merely a moderate improvement can be expected using further variables as additional probability distributions, e.g. the lepton helicity angle in the W boson decay of chapter 5. Therefore the functional dependence of the reconstructed asymmetry coefficient on the generated value has to be examined. It turns out that the dependence can be described by a polynomial of degree two as shown in figure 6.8. According to Gaussian error propagation the statistical error of the simulated raw data sample is quadratically added to the statistical error of the reference sample by which it has been divided. The reconstructed diluted asymmetry coefficient with its errors is then translated according to the inverse function of the fitted polynomial

$$\mathcal{A}_{\mathrm{cor.}} = -\frac{P_2}{2P_3} + \sqrt{\frac{\mathcal{A}_{\mathrm{rec.}} - P_1}{P_3} + \frac{P_2}{2P_3}} \tag{6.8}$$

with the fit parameters P_1, P_2 and P_3 as indicated in figure 6.8. The reconstructed diluted asymmetry coefficient $\mathcal{A} = 0.159 \pm 0.019$ translates in this way to $\mathcal{A} = 0.315^{+0.034}_{-0.035}$. The asymmetrical errors arise from the non linearity of the function.

6.4   Systematic uncertainties

The systematic uncertainties which have an important influence on the asymmetry coefficient are considered below. Each item has been investigated using the statistics of $1\,000\,000$ generated events. To have an estimate of the influence imposed by theory only the partonic final state has been generated, except for the investigation of background processes.

1. As already explained the gluon gluon fusion processes provide the opposite correlation of the quark antiquark annihilation processes. Therefore the uncertainty of the proton gluon density constitutes the dominating contribution to the errors until its measurement at low x will be improved at the Tevatron in Run II and at the LHC. The fraction of $t\bar{t}$ pairs produced by the gluon gluon fusion and the slope of the gluon density of the proton influence the asymmetry coefficient. Six different sets of parton density functions as listed in table 6.3 have been tested. The resulting asymmetry coefficients vary from $\mathcal{A} = 0.288 \pm 0.003$ using CTEQ5L with the lowest fraction of contributing gluon gluon fusion processes ($83\,\%$) to $\mathcal{A} = 0.324 \pm 0.003$ using CTEQ3L with the highest fraction of contributing gluon gluon fusion processes ($89\,\%$). The value $\mathcal{A} = 0.312 \pm 0.003$ of CTEQ4L has been used as central value, resulting in a maximal deviation of 0.024 to the prediction of CTEQ5L which has been taken into account as theoretical uncertainty.

Source of uncertainty	Asymmetry coefficient $\mathcal{A}$	$t\bar{t}$ production processes
CTEQ2L	0.310 ± 0.003	$88\,\%$ gg + $12\,\%$ $q\bar{q}$
CTEQ3L	0.324 ± 0.003	$89\,\%$ gg + $11\,\%$ $q\bar{q}$
CTEQ5L	0.288 ± 0.003	$83\,\%$ gg + $17\,\%$ $q\bar{q}$
MRST99	0.316 ± 0.003	$87\,\%$ gg + $13\,\%$ $q\bar{q}$
CTEQ4L (default)	0.312 ± 0.003	
$m_W + 61\,\mathrm{MeV}$	0.315 ± 0.003	
$m_W - 61\,\mathrm{MeV}$	0.316 ± 0.003	
$m_t = 170\,\mathrm{GeV}$	0.318 ± 0.003	
$m_t = 180\,\mathrm{GeV}$	0.308 ± 0.003	$87\,\%$ gg + $13\,\%$ $q\bar{q}$
$t\bar{t} + H_{\mathrm{SM}}(400\,\mathrm{GeV})$	0.309 ± 0.003	
$t\bar{t} + H_{\mathrm{CP}}\,(400\,\mathrm{GeV})$	0.320 ± 0.003	
M.E. Slabospitsky	0.324 ± 0.002	
$t\bar{t}$ (signal) + $ZZ(\to b\bar{b}\,\ell^+\ell^-)$ (bg)	0.311 ± 0.035	

Table 6.3: Systematic uncertainties on the asymmetry coefficient $\mathcal{A}$. The by far dominating contribution comes from the uncertainty of the proton gluon density at low x, relevant for the $t\bar{t}$ production at the LHC.

2. The variation of the W boson mass ($80.41\,\text{GeV}$) within $61\,\text{MeV}$ leads to the marginal deviation of 0.004, almost consistent with the default value within the errors.

3. The top mass with an assumed central value of $175\,\text{GeV}$ has been varied in the wide range of $\pm 5\,\text{GeV}$ resulting in the marginal shift of 0.006.

4. The influence of an intermediate neutral Higgs boson with a mass above the $t\bar{t}$ production threshold (here a mass of $m_H = 400\,\text{GeV}$ was assumed) leads to the minor shift of 0.008. As already discussed, the observable is not sufficiently sensitive to be used for the investigation of the CP property of a Higgs boson. If a neutral Higgs boson in the relevant mass range will be discovered its small influence on the asymmetry coefficient can be taken into account in the analysis and the uncertainty vanishes.

5. The $2 \to 6$ matrix elements from [Sla01] using the Breit-Wigner approach show up in a slightly enhanced asymmetry coefficient of $\mathcal{A} = 0.324 \pm 0.002$. In the future, when higher order corrections are available, the deviation may decrease. Furthermore the enhanced value of the asymmetry obtained with the Breit-Wigner approach will help to increase the significance of the measured asymmetry coefficient. Here the deviation of 0.012 has been taken as an estimate of the expected uncertainty of the different approaches used.

6. The investigation of background processes on the parton level is restricted to processes with the same final state as the signal. However, as could already be shown for the determination of the top mass no such processes are expected to contribute noticeably to the reconstructed signal events. In contrast, the production of ZZ pairs with a cross section of about $8\,209\,\text{pb}$ could provide a non negligible contribution since the subsequent decay into two charge conjugated pairs, one lepton pair and one b quark pair, provide the essential objects which are necessary for the reconstruction of the $t\bar{t}$ events in the dileptonic decay channel. The missing transverse momentum required at the event selection can be easily obtained by the production of neutrinos e.g. within jets. The decay channel required decreases the cross section to the marginal value of $112.5 \cdot 10^{-3}\,\text{pb}$, corresponding to about 3400 events in $30\,\text{fb}^{-1}$. Among $100\,000$ generated and simulated events only five remain which fulfil the cuts. The supression is better than in the top mass determination. Other processes with remarkably larger cross sections like the single Z and W boson production are assumed to give similar contributions with respect to the semileptonic decay channel of the top mass determination. In this case the contributions within the percent level can be neglected. If the contributions are slightly enhanced the uncertainty can be restricted to the change in the measured asymmetry coefficient due to the uncertainty in the cross section of the considered background process.

   Moreover, higher order corrections may reveal different kinematics of the partons which are simulated in event generators like PYTHIA by initial and final state radiation. This could give rise to additional uncertainties. However for the determination

of the top quark mass it could be shown that the single top quark and W boson production processes, partially accompanied by additional partons, do not give rise to any additional uncertainty even if the cross sections are of the same order as the signal.

After all the uncertainty in the gluon density of the proton provides by far the greatest uncertainty in the measurement of the spin correlation. The statistical uncertainty of the translation function (6.8) has not been taken into account since more statistics will be generated and simulated for the measurement of the asymmetry coefficient at the LHC so that this contribution can be neglected. However the systematic uncertainty due to the usage of different matrix elements (from [Sla01]) has been taken into account as discussed above. The deviation can be considered as systematic uncertainty of the translation function.

As before, the errors are treated as Gaussian distributed and $100\,\%$ uncorrelated. The quadratic addition of the systematic error estimates yields the reconstructed and translated asymmetry coefficient of

$$\mathcal{A} = 0.311^{+0.034}_{-0.035}(\text{stat}) \pm 0.028(\text{syst}) \tag{6.9}$$

exploiting the statistics of $30\,\text{fb}^{-1}$, corresponding to three years running at low luminosity. The statistical error is dominating so that the measurement at high luminosity will bring improvements. This holds especially since the systematic error is strongly dominated by the uncertainty of the proton gluon density which will be subject to measurement in the future, leading to an essentially reduced systematic uncertainty.

Another possibility to measure the spin correlation with an observable based on a simple differential distribution applied in the dileptonic decay channel of the $t\bar{t}$ production is shown in appendix D.

7

Higgs boson sector

New physics beyond the standard model is expected at the TeV scale. This energy range, essential for the production of new particles will be reached at the LHC. In the two Higgs doublet model or a supersymmetric extension of the standard model a heavy neutral Higgs boson may have a mass high enough to decay into $t\bar{t}$ pairs. Its observation via the decay into a $t\bar{t}$ pair is subject of investigation here. For a Higgs boson with standard model couplings the total decay width is too broad to distinguish the signal from the background. However, without coupling to vector bosons the Higgs could be observed. Therefore a very good knowledge of the $t\bar{t}$ background shape is crucial. Once higher order corrections to the $t\bar{t}$ production are available they have to be taken into account. Such a heavy neutral Higgs is a candidate for the pseudo scalar Higgs in supersymmetric models. To check this its CP properties have to be investigated [Ber98b].

In the section below the production of a neutral Higgs boson at the LHC, its decay into a $t\bar{t}$ pair and its implementation in the matrix elements of [Ber98a] are discussed. The next section explains the selection of $t\bar{t}$ events in the semileptonic decay channel and the reconstruction of the $t\bar{t}$ invariant mass. The sum of signal and background is compared to the background, resulting in a significance of about 16 with the statistics of $50\,\mathrm{fb}^{-1}$. However, the dominating contribution to the systematic uncertainties is expected to come from higher order corrections, which are not available yet.

7.1   Heavy neutral Higgs bosons at the LHC

At the LHC, Higgs bosons will be predominantly produced in the s channel through the gluon gluon fusion process (see appendix E figure E.1 for the cross sections of the different standard model Higgs production mechanisms at the LHC). Their coupling to
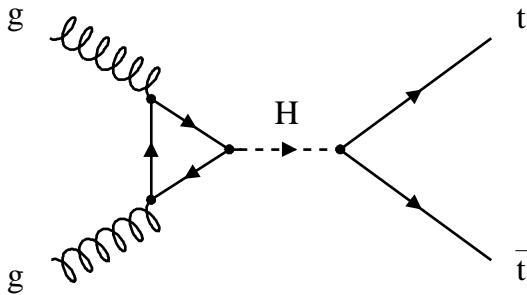
Figure 7.1: Feynman graph of the Higgs boson produced by the gluon gluon fusion via a fermion loop. The loop is predominantly realized by a virtual top quark since the coupling of the Higgs boson is proportional to the fermion mass. For a Higgs mass above the $t\bar{t}$ production threshold the Higgs boson can decay to an on-shell $t\bar{t}$ quark pair.

gluons is realized via a virtual fermion loop as shown in figure 7.1, since the Higgs itself does not couple strongly. This fermion loop consists predominantly of virtual top quarks since the coupling to the Higgs boson is proportional to the fermion mass. In case of supersymmetric extensions of the standard model the virtual loop between the gluons and a neutral Higgs boson may be realized by new particles like the stop quark.

A neutral Higgs boson as implemented in the matrix elements [Ber98a] (see figure A.1 a) and b) in the appendix for the Feynman graphs) becomes resonant in case of a mass above the $t\bar{t}$ production threshold (see the branching ratios of a standard model Higgs boson in dependence of its mass in figure E.2 b). The matrix elements calculate the coherent contribution of the resonant Higgs boson and the non resonant $t\bar{t}$ background. They are also valid in supersymmetric extensions of the standard model in case of squark masses above 400 GeV, since the contributions of such heavy squarks are negligible [Daw96]. The scalar and pseudo scalar couplings of the Higgs boson to top quarks can be described by the Yukawa interaction

$$\mathcal{L} = -(\sqrt{2}G_F)^{1/2} m_t \bar{\psi}_t (a_t + i\tilde{a}_t\gamma_5)\psi_t\varphi_H \tag{7.1}$$

with the Fermi constant G_F, the top quark mass m_t, the field ψ_t of the top quark, the scalar and pseudo scalar Yukawa couplings a_t and $\tilde{a}_t$ respectively and the field φ_H of the Higgs boson. The standard model couplings of the Higgs boson to the W and Z vector bosons are realized with a multiplicative factor g_{VV} which depends as the reduced Yukawa couplings in a two Higgs doublet model on the ratio of the vacuum expectation values of
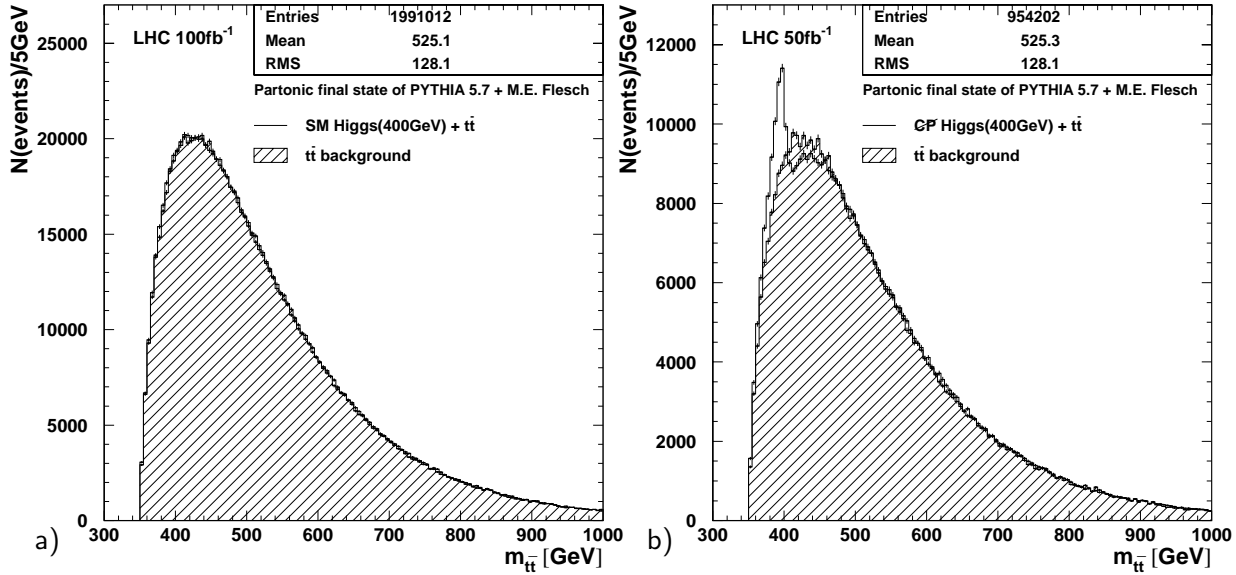
Figure 7.2: The invariant $t\bar{t}$ mass in the partonic final state of a 400 GeV Higgs boson within the standard model (a) and for a CP violating Higgs (b) without coupling to vector bosons ($g_{VV} = 0$, $a_t = 1$ and $\tilde{a}_t = -1$). The coherent sum of the signal plus $t\bar{t}$ background is compared to the background alone.

the Higgs doublets. In case of a standard model Higgs boson the couplings assume the values $g_{VV} = 1, a_t = 1, \tilde{a}_t = 0$. In contrast, a pseudo scalar Higgs (CP=-1, $a_t = 0$, $\tilde{a}_t = 1$) like in a supersymmetric extension of the standard model cannot couple to vector bosons at Born level due to C and P parity conservation. Thus the vector boson coupling g_{VV} assumes the value 0. The variable

$$\gamma_{\mathrm{CP}} = -a_t \tilde{a}_t \qquad (7.2)$$

gives a measure of the CP violation and assumes the value zero in case of a scalar or pseudo scalar Higgs boson. As an example a CP violating Higgs without coupling to vector bosons, i.e. $g_{VV} = 0$, $a_t = 1$ and $\tilde{a}_t = -1$ may be considered. The invariant $t\bar{t}$ mass spectrum is not sensitive to the CP properties of a Higgs, i.e. if the couplings are of the same order as in the examples of the CP violating and the pseudo scalar Higgs bosons above and their masses are the same, the invariant $t\bar{t}$ mass distribution is not affected. In figure 7.2 the invariant top antitop quark mass of the partonic final state is shown for two different Higgs bosons with a mass of 400 GeV. Within the standard model (a) the total decay width of $\Gamma_H \simeq 27$ GeV does not allow to distinguish the signal from the $t\bar{t}$ background. However, in case of a Higgs boson which does not couple to vector bosons ($g_{VV} = 0$) as discussed above, the width shrinks to $\Gamma_H \simeq 14.5$ GeV and the signal emerges from the background (b).

7.2 Event selection and reconstruction

The events are reconstructed in the semileptonic decay channel of the $t\bar{t}$ production since this channel has a unique signature and the available statistics is considerable.

The selection cuts are identical to those of the W boson helicity determination in chapter 5, where in addition to the lepton and missing $p_\perp$ above a transverse momentum threshold of 20 GeV, at least two non b jets and exactly two b jets above the transverse energy threshold of 20 GeV and 30 GeV respectively were required.

To improve the reconstruction of the event, the top mass has been assumed to be well known, which is adequate as could be shown in chapter 4. The assignment of the b jets to the reconstructed W bosons has been performed in minimizing the sum of the differences between the two reconstructed and the known on-shell top quark masses ($m_t^{\mathrm{on\text{-}shell}} = 175$ GeV). If the chosen solution for the reconstructed event has a top which differs in its mass by more than 50 GeV from the on-shell top quark mass, the event has been discarded.

Finally the reconstructed top quarks have to fulfil the angular condition $\cos \phi_{t\bar{t}} < -0.8$ in the plane transverse to the beam axis, i.e. the transverse momenta of the top quarks should be roughly back-to-back.

The reconstructed events are shown in figure 7.3 for a neutral Higgs boson of mass $m_H = 400$ GeV which does not couple to vector bosons (here a CP violating Higgs with $g_{VV} = 0$, $a_t = 1$ and $\tilde{a}_t = -1$ is assumed). For comparison the $t\bar{t}$ background is plotted superimposed. The statistics corresponds to $50\,\mathrm{fb}^{-1}$, accumulated in half a year running
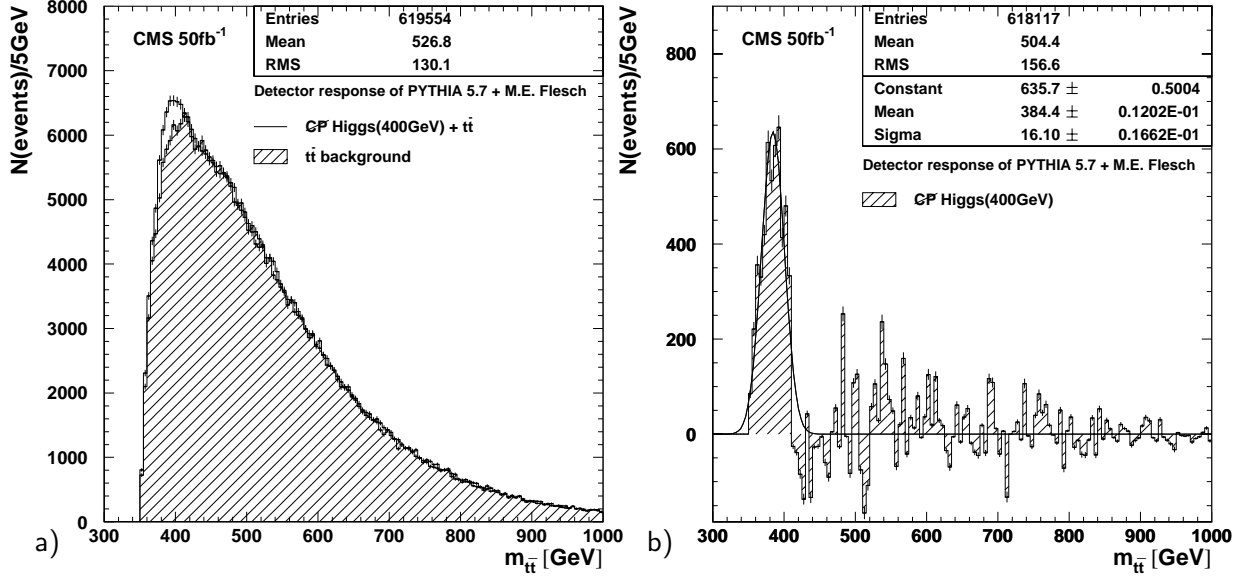
Figure 7.3: The CMS detector response of the invariant $t\bar{t}$ mass spectrum for a 400 GeV Higgs boson without coupling to vector bosons and the reduced Yukawa couplings $a_t = 1$ and $\tilde{a}_t = -1$ (a). The signal after subtraction of the $t\bar{t}$ background is shown in b). The fitted width of $\Gamma_H = 16.1$ GeV is slightly larger than the generated one due to the reconstruction and resolution of the detector.

at high luminosity ($\mathcal{L} = 10^{34}\,\mathrm{cm}^{-2}\mathrm{s}^{-1}$). The distributions with and without Higgs signal differ in the region around the Higgs mass only by about 10 % which puts strong demands on the accuracy of the cross sections and the invariant mass spectra since the Higgs signal peaks near the maximum of the invariant mass distribution of the $t\bar{t}$ background. Assuming both as well known, the signal after subtraction of the $t\bar{t}$ background is shown in figure 7.3 b). The reconstructed width of about $\Gamma_H = 16$ GeV, obtained by a Gaussian fit is merely about 10 % larger than the total decay width of the Higgs. Comparing the $t\bar{t}$ background to the Higgs signal in the invariant $t\bar{t}$ mass range below 400 GeV yields a significance of

$$\sigma \equiv \frac{N_S}{\sqrt{N_B}} \simeq 16 \ . \tag{7.3}$$

Considering this result one has to keep in mind that the precise knowledge of the $t\bar{t}$ background shape is crucial and higher order corrections to the $t\bar{t}$ production have to reveal fast convergence in the cross section and also in the shape of the $t\bar{t}$ invariant mass spectrum. Once NLO QCD corrections to the $t\bar{t}$ production are available they have to be compared to the LO predictions.

Summary

The analyses accomplished in this dissertation are dedicated to reveal the physics potential of the CMS experiment in the domain of top quark physics, exploiting the unmistakable signature of the $t\bar{t}$ production. The list of investigated subjects does not claim to be complete, but the most suggesting items are covered.

The investigations rely essentially on the implementation of matrix elements into the PYTHIA Monte-Carlo event generator. Accomodations applied to the event generator are explained whenever necessary. These technical issues and the kinematics of the $t\bar{t}$ production are discussed in detail as reference for future analyses.

The first analysis determines the top quark mass in the semileptonic decay channel of $t\bar{t}$ pairs. Based on the statistics of $3.5 \cdot 10^6$ $t\bar{t}$ events, corresponding to an integrated luminosity of $10\,\mathrm{fb}^{-1}$ expected in one year of data taking at low luminosity, the simulation shows that a total error of less than $900\,\mathrm{MeV}$ can be achieved. The statistical error contributes to only $250\,\mathrm{MeV}$. The dominant contribution to the systematic uncertainty ($400\,\mathrm{MeV}$) comes from the dependence on the $p_\perp$ spectrum of the generated top quarks. Even in case of degraded calibration precision of the calorimeters ($\pm 0.5\,\%$ and $\pm 2\,\%$ for the electromagnetic and the hadronic calorimeter respectively) the total uncertainty of the top mass would be below $1.3\,\mathrm{GeV}$. Most of the error sources are expected to decrease such as the statistical error, the knowledge about the b quark fragmentation and the uncertainty of the gluon density in the proton.

The top mass will also be measured with similar accuracies in the dileptonic [Kau01] and the fully hadronic decay channel [Wel00]. At first sight the fully hadronic decay channel may give rise to large systematic uncertainties due to the unavoidable influence of background processes, whose cross sections are not very well known. However, as shown in the analysis of [Wel00], they contribute only with a flat off-set to the invariant top mass distribution. Therefore the position of the reconstructed top mass is not affected at all. Moreover the results of the three decay channels of the two experiments ATLAS and CMS will be combined, so that the total error on the top mass will become still smaller.

In comparison to the Tevatron, with an expected achievable overall precision of about $2\,\mathrm{GeV}$ in Run II [Hal00], the LHC has the potential to improve the precision on the top quark mass by a factor of at least two. In respect of such small uncertainties one has to keep in mind the theoretical uncertainty in the concept of top quark pole mass by the order Λ_{QCD}.

After the top mass has been determined with high accuracy, the W boson helicity can be investigated. The $t\bar{t}$ production offers the opportunity to investigate the helicity states

of on-shell W bosons coming from top quark decays. The semileptonic decay channel with its unique signature provides a clean signal to determine the helicity states via the helicity angle of the lepton from the leptonically decaying W boson. Already with the data of one year at low luminosity $(10\,\mathrm{fb}^{-1})$ the systematic uncertainties dominate. The fractions of the different helicity states will be measured to the percent level and also a possible right circular polarized component of the W boson in contradiction to the standard model prediction can be investigated with a precision at the percent level. The expected accuracy in the determination of the W boson helicity will significantly improve existing measurements [Aff00], [Hal00].

The dileptonic decay channel of the $t\bar{t}$ production has been exploited to analyse the $t\bar{t}$ spin correlation via the two leptons in the final state of the events. With the double differential distribution of the cosine of the lepton angles in the helicity basis the asymmetry of $\mathcal{A} = 0.313 \pm 0.002(\mathrm{stat}) \pm 0.028(\mathrm{syst})$ is expected at the LHC. The measurement of the asymmetry is the direct check of the top quark spin one half and therefore a fundamental test of QCD. With the statistics of three years at low luminosity $(30\,\mathrm{fb}^{-1})$, the asymmetry will be measured with a total uncertainty of less than $15\,\%$, where the statistical error gives the dominant contribution. This has to be compared with the only measurement of the asymmetry accomplished so far by DØ, based on six dileptonic $t\bar{t}$ events. Other observables as shown in appendix D turn out to be slightly more significant than the double differential lepton angles in the helicity basis. They allow to reduce the total uncertainty on the asymmetry coefficient with the same amount of data to about $10\,\%$, assuming that the systematic uncertainties will not change dramatically.

As last item a scenario with a neutral Higgs boson in the mass range above the $t\bar{t}$ production threshold is considered. If a neutral Higgs boson is found there, its CP properties have to be investigated [Ber98b]. Here a neutral Higgs boson, which does not couple to vector bosons like the pseudo scalar Higgs in supersymmetric models, has been assumed. With a mass of $400\,\mathrm{GeV}$ the total decay width of such a boson shrinks from $\Gamma_H \simeq 27\,\mathrm{GeV}$ (standard model Higgs boson) to $\Gamma_H \simeq 14.5\,\mathrm{GeV}$. This improves the significance, important for the observability. In a mass window of $20\,\mathrm{GeV}$ around the Higgs mass, the invariant $t\bar{t}$ mass distribution shows an excess of about $10\,\%$ over the $t\bar{t}$ background, resulting in a significance of $S/\sqrt{B} \simeq 16$. Thus the precise knowledge of the $t\bar{t}$ background shape is crucial. The dominant contribution to the systematic uncertainties is expected to come from higher order corrections to the $t\bar{t}$ production. Once they are available, they have to be taken into account.

The $t\bar{t}$ production offers rich possibilities for studying strong and electroweak interactions. Only a part of it could be covered here. To extend this study one could look at the total decay width of the top quark to check the standard model expectation. Moreover the precise determination of the $t\bar{t}$ production cross section is important for the search of new particles.

Appendix A

Matrix elements

A.1 Matrix element implementation into PYTHIA

The $2 \to 6$ matrix elements from [Ber98a] are implemented in PYTHIA 5.7 via a call of the routine PYUPEV which the user has to provide. The routine can also be implemented in PYTHIA 6.1. Therefore all variables declared in real precision have to be declared in double precision. In addition the PYUPR common block of 3.57 was slightly changed to

$$\text{COMMON/PYUPPR/NUP,KUP(20,7),NFUP,IFUP(10,2),PUP(20,5),Q2UP(0:10)} , \quad \text{(A.1)}$$

i.e. now the PUP array is located behind the integer variable NFUP and the array IFUP. Apart from these two differences the implementation is identical to that into PYTHIA 5.7. The matrix elements mentioned above also allow to switch on an intermediate neutral Higgs boson which becomes relevant if its mass lies above the $t\bar{t}$ production threshold. The relative strength of the vector boson coupling g_{VV} and the reduced scalar and pseudo scalar Yukawa couplings a_t and $\tilde{a}_t$ can be chosen independently. Thus the non vanishing CP violating product $a_t\tilde{a}_t$ can contribute to the $t\bar{t}$ production via a Higgs boson. If a Higgs is switched on, which is simply achieved by setting at least one of the coupling constants g_{VV}, a_t or $\tilde{a}_t$ to a value different from zero, the reaction consists of the coherent
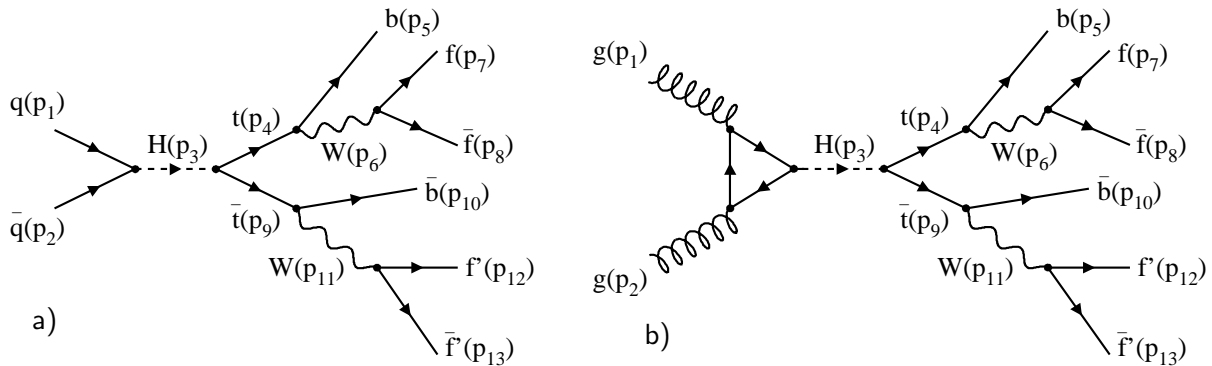

Figure A.1: The implemented matrix element $q\bar{q}(\to H) \to t\bar{t} \to 6f$ (a)) of the process number 193 and the matrix element $gg(\to H) \to t\bar{t} \to 6f$ (b)) of process number 194. The particle momenta are enumerated as used in the subroutine PYUPEV.

sum of the $t\bar{t}$ background and the Higgs signal. The relevant Feynman graphs indicating the numbering scheme of the particles used in the implementation are shown in figure A.1.

Running at different collider energies will result in lower generation efficiencies. This comes predominantly from a shift of the peak in the ξ distribution which is proportional to the logarithm of the ratio between the partonic ($\hat{s}$) and the hadronic (S) center of mass energy squared. It turned out that $\hat{s}$ peaks at about $(2.5\,m_t^{\mathrm{pol.}})^2$ so that the ξ distribution can universally be divided into two intervals below and above $\xi_i = \ln((2.5\,m_t^{\mathrm{pol.}})^2/s)$. Further improvements can be achieved in replacing the coefficient $c_3 = 1.9$ in the argument of the function which approximates the distribution of the hard subprocess scattering angle $\hat{\theta}$ by $c_3 = 2.27 - \exp(-0.0001(\sqrt{s} - 4\,000))$ and in replacing the coefficient $c_2 = 0.6$ in the argument of the function which approximates the y distribution by the expression $c_2 = 0.4 + 2\,300/\sqrt{s}$. These changes provide homogeneous generation efficiencies over the whole range of collider energies. The differences of the approximated distributions in proton proton collisions and proton antiproton collisions, both at $2\,\mathrm{TeV}$, show no considerable deviation which would make it necessary to apply different parameter values to the approximating functions of the generation phase space variables.

```
C************************************************************************

C...PYUPEV
C...Dummy routine, to be replaced by user. When called from PYTHIA
C...the subprocess number ISUB will be given, and PYUPEV is supposed
C...to generate an event of this type, to be stored in the PYUPPR
C...commonblock. SIGEV gives the differential cross-section associated
C...with the event, i.e. the acceptance probability of the event is
C...taken to be SIGEV/SIGMAX, where SIGMAX was given in the PYUPIN
C...call.

C %%%%%%%%%%%%%%%%%%%%%%%%%%%%%%%%%%%%%%%%%%%%%%%%%%%%%%
C       This routine is written by Lars Sonnenschein
C       It includes the matrixelement from M. Flesch et al.
C       Comments should be send to Lars.Sonnenschein@cern.ch
C %%%%%%%%%%%%%%%%%%%%%%%%%%%%%%%%%%%%%%%%%%%%%%%%%%%%%%


        SUBROUTINE PYUPEV(ISUB,SIGEV)

C...Double precision and integer declarations.
        IMPLICIT NONE

        INTEGER ISUB
        REAL SIGEV
C...Commonblocks.
        INTEGER MSTU,MSTJ
        REAL PARU,PARJ
        COMMON/LUDAT1/MSTU(200),PARU(200),MSTJ(200),PARJ(200)
Cls..common for branching of W
        INTEGER MDCY, MDME, KFDP
        REAL BRAT
        COMMON/LUDAT3/MDCY(500,3),MDME(2000,2),BRAT(2000),KFDP(2000,5)

cls...vint(1) to know CMS energy of collision
        INTEGER MINT
```

```
        REAL VINT
        COMMON/PYINT1/MINT(400),VINT(400)

cls...msti(52) finite tries for each event
        INTEGER MSTP, MSTI
        REAL PARP, PARI
        COMMON/PYPARS/MSTP(200),PARP(200),MSTI(200),PARI(200)

cls...Common block to be filled here with parton informations for PYTHIA
        INTEGER NUP,KUP,NFUP,IFUP
        REAL PUP,Q2UP
        COMMON/PYUPPR/NUP,KUP(20,7),PUP(20,5),NFUP,IFUP(10,2),Q2UP(0:10)
        SAVE /LUDAT1/,/PYUPPR/

        INTEGER KCHG
        REAL PMAS,PARF,VCKM
C...Particle properties + some flavour parameters.
        COMMON/LUDAT2/KCHG(500,3),PMAS(500,4),PARF(2000),VCKM(4,4)


        REAL Q2
        REAL xf1(-25:25), xf2(-25:25)

        REAL RLU
        REAL PS12, PS3

        REAL c_1, c_2, c_3, xi_a, xi_b, xi_i, xi, u
        REAL t_alpha_a, t_alpha_b, t_beta_a, t_beta_b, t_alpha, t_beta
        REAL PSa, PSb, y_a, y_b, y, r_a, r_b, r, den_t, den_u

cls...ALPAS from PYTHIA (PDFlib)
        REAL ULALPS

        INTEGER I, KPIND

        LOGICAL FIRST, BRFIRST
        SAVE FIRST, BRFIRST
        DATA FIRST /.TRUE./
        DATA BRFIRST /.TRUE./

        REAL BrWplus, BrWminus, BRANRNDM, BrPerm
        SAVE BrWplus, BrWminus, BrPerm


Cls... Some parameter declarations for the use of the matrix elements
c////////////////////////////////////////////////////
c       build # 0.73
c       'main' is a completely mutilated version of
c       a program by M. Flesch
c////////////////////////////////////////////////////

        REAL fgg,fqq,Gammah

        EXTERNAL Gammah

        REAL s,rs,eb
        REAL m,mh,Gamma,mhGh
        REAL Pi,Pi2,GeV2pb,v,alphas,a,as,gvv,mz,mw,kappa
        REAL a2,as2,mov2,mu,mh2,fact
        REAL cuttrap,cutpt
        REAL a_mh(1:4),a_aas(1:2,1:4),a_gvv(1:3)
        REAL par(1:11)

c*** 4-momenta in the lab frame ****
c       top and antitop quark
```

```
      REAL khcms(0:3) ,kbhcms(0:3)
c     lepton l^+ and l^-
      REAL lphcms(0:3),lmhcms(0:3)
c     b and bbar quark
      REAL bhcms(0:3),bbhcms(0:3)
c     neutrino and antineutrino
      REAL nuhcms(0:3),nubhcms(0:3)
c*** 4-momenta in the frame of initial partons ****
c     top and antitop quark
      REAL kpcms(0:3) ,kbpcms(0:3)
c     lepton l^+ and l^-
      REAL lppcms(0:3),lmpcms(0:3)
c     b and bbar quark
      REAL bpcms(0:3),bbpcms(0:3)
c     neutrino and antineutrino
      REAL nupcms(0:3),nubpcms(0:3)
c***

      LOGICAL scutrapit,scutpt

      COMMON/block1/s,rs,Gamma,v,m,mh,mhGh,mz,mw,mov2,mu,eb,mh2
      COMMON/block2/Pi,Pi2,GeV2pb,alphas,a,as,gvv,a2,as2,fact,kappa
      COMMON/block3/scutrapit,scutpt
      COMMON/block4/cuttrap,cutpt
      COMMON/block5/a_mh,a_aas,a_gvv


c*********************************************
c     proton-proton collisions at 14 TeV
c     rs=sqrt(s) in GeV

cls   rs = 14.E3
      rs = VINT(1)
c*********************************************

c
c     Cuts
c
c     cuttrapit = rapidity
c     of t and tbar quark;
c     cutpt = Pt cut in [GeV]
c     for visible particles in the final state.
c
c     These cuts are switched off, i.e. "put on comment"
c     in the subroutines "ggtt" and "qqtt".
c
c***************************
      scutrapit = .TRUE.
      cuttrap = 3.0

      scutpt = .TRUE.
      cutpt = 20.0

c***************************
cls     end of matrix element parameter declaration,
c/////////////////////////////////////////////////

c_____
cls     beginning of phase space variable generation


c     safety query of PYTHIA parameter settings
      IF(MSTI(52).GE.1 .AND. MSTI(52).LE.4) RETURN
```

```
c       original variables x_1 and x_2
c       par(1)=RLU(1.)
c       par(2)=RLU(1.)


        xi_a=LOG((2*PMAS(6,1)/rs)**2)
        xi_i=-7
        xi_b=0
        c_1=2.0

        t_alpha_a=1/c_1*TANH(c_1*(xi_a-xi_i))
        t_alpha_b=0

        t_beta_a=pi/(2*c_1)
        t_beta_b=2/c_1*ATAN(EXP(c_1*(xi_b-xi_i)))

        PSa=t_alpha_b-t_alpha_a
        PSb=t_beta_b-t_beta_a

        IF((PSa+PSb)*RLU(1.).LE.PSa) THEN
comment: probability of PSa

          t_alpha=(t_alpha_b-t_alpha_a)*RLU(1.) + t_alpha_a
          xi=1/c_1*1/2*LOG((1+c_1*t_alpha)/(1-c_1*t_alpha))+xi_i
          PS12=COSH(c_1*(xi-xi_i))**2
        ELSE
comment: probability of PSb

          t_beta=(t_beta_b-t_beta_a)*RLU(1.) + t_beta_a
          xi=1/c_1*LOG(TAN(c_1*t_beta/2))+xi_i
          PS12=COSH(c_1*(xi-xi_i))
        ENDIF

        PS12=PS12*(PSa+PSb)


        y_a=xi/2
        y_b=-y_a
        c_2=0.6
        r_a=1/c_2*TANH(c_2*y_a)
        r_b=1/c_2*TANH(c_2*y_b)
        r=(r_b-r_a)*RLU(1.)+r_a
        y=1/c_2*1/2*LOG((1+c_2*r)/(1-c_2*r))
c       product of Jacobian determinant and partial phase space
        PS12=PS12*COSH(c_2*y)**2 * (r_b-r_a)


        par(1)=EXP(xi/2+y)
        par(2)=EXP(xi/2-y)


c       original variable cos(z)
c       par(3)=2*RLU(1.)-1
c       PS3=2.


        c_3=1.9
        u=SINH(c_3)/c_3*(2*RLU(1.)-1)
        par(3)=LOG(c_3*u+SQRT((c_3*u)**2+1))/c_3
c       product of Jacobian determinant and partial phase space
        PS3=1./cosh(c_3*par(3)) * 2.*SINH(c_3)/c_3

        VINT(23)=par(3)
```

```
      par(4)=RLU(1.)*PI
      par(5)=RLU(1.)*2*PI
      par(6)=RLU(1.)*PI
      par(7)=RLU(1.)*2*PI
      par(8)=RLU(1.)*PI
      par(9)=RLU(1.)*2*PI
      par(10)=RLU(1.)*PI
      par(11)=RLU(1.)*2*PI


      VINT(44)=par(1)*par(2)*VINT(1)**2 ! shat

      Q2=PMAS(6,1)**2 + 0.25*VINT(44)
     & * ( (1-2.*PMAS(6,1)**2/VINT(44))**2
     & - 4.*PMAS(6,1)**4/VINT(44)**2 )
     & * (1-par(3)**2)

      VINT(51)=SQRT(Q2)
      VINT(52)=Q2

c     Initialize !
      CALL INIT

      alphas=ULALPS(Q2)

      CALL PYSTFU(MINT(11), par(1), Q2, xf1)
      CALL PYSTFU(MINT(12), par(2), Q2, xf2)




c... ######### tt~ processes 191 and 192 #########
      IF(ISUB.EQ.191.OR.ISUB.EQ.192) THEN
c     couplings
        gvv = 0.
        a = 0.
        as = 0.
c... ######## Higgs processes 193 and 194 ########
      ELSEIF (ISUB.EQ.193.OR.ISUB.EQ.194) THEN
c     couplings
        gvv = 1.
        mh = PMAS(25,1)
        a = 1.
        as = 0.
c     Higgs width
        Gamma = Gammah(mh**2)
        mh2 = mh**2
        mhGh = mh * Gamma

        IF (FIRST.EQV..TRUE.) THEN
        FIRST=.FALSE.
        WRITE(*,*)
        WRITE(*,*) ' — Higgs mass ———————-'
        WRITE(*,*) ' m_H=',mh
        WRITE(*,*)
        WRITE(*,*) ' — couplings (a,as) —————'
        WRITE(*,*) ' a=',a,' as=',as
        WRITE(*,*)
        WRITE(*,*) ' — gVV ————————————-'
        WRITE(*,*) ' g_VV=',gvv
        WRITE(*,*)
        WRITE(*,*) ' Gammah(m_H^2)=',Gamma
        WRITE(*,*)
        ENDIF

      ELSE
```

```
          SIGEV=0.
          RETURN
        ENDIF


c     The following parameters are needed in the matrix
c     element subroutines "qqtt" and "ggtt".
c     They are kept in the common block

        a2 = a**2
        as2 = as**2

c     factor resulting from the b and bbar energy integrations
c     in eq. (4) of ref. [1] (see below);
c     factors 2 and Pi and alpha_s, and conversion 1/GeV^2 − > pb.

        fact = 24.0 * mu**2 / (1.0 + 2.0*mu)
        fact = fact**2 /(32.*Pi**3) * alphas**2
        fact = fact * GeV2pb
C ****************************
C choice W decays
        IF (BRFIRST.EQ..TRUE.) THEN
          BRFIRST=.FALSE.
          CALL Weight(BrPerm, BrWplus, BrWminus)
          WRITE(*,*)
          WRITE(*,*)'PYUPEV(Flesch): BRUNCH(1.W)=',BrWplus,
     &       ' BRUNCH(2.W)=',BrWminus,' BrPerm=',BrPerm
          WRITE(*,*)
        ENDIF

        IF (ISUB.EQ.191.OR.ISUB.EQ.192) THEN
          KPIND=0
        ELSE
          KPIND=1 ! one index more for Higgs
        ENDIF

C choice qqbar or gg!
        IF (ISUB.EQ.191.OR.ISUB.EQ.193) THEN
          call qqtt(par,khcms,kbhcms,lphcms,lmhcms,nuhcms,nubhcms,
     +      bhcms,bbhcms,fqq)
          SIGEV=(xf1(1)*xf2(-1) + xf1(-1)*xf2(1) +
     &      xf1(2)*xf2(-2) + xf1(-2)*xf2(2) +
     &      xf1(3)*xf2(-3) + xf1(-3)*xf2(3) +
     &      xf1(4)*xf2(-4) + xf1(-4)*xf2(4) +
     &      xf1(5)*xf2(-5) + xf1(-5)*xf2(5) +
     &      xf1(6)*xf2(-6) + xf1(-6)*xf2(6) ) *
     &      fqq * 1.0E-9
     &      * BrWplus * BrWminus * BrPerm
     &      * 16*PI**8
     &      * PS12
     &      * PS3

          IF (.NOT.(SIGEV.GE.0..AND.SIGEV.LT.1.)) THEN
            PRINT*,'Should never happen: SIGEV[mb]=', SIGEV
            SIGEV=0.
          ENDIF

          IF (RLU(1.).LT.0.666) THEN
c... KF(u)=2
            KUP(1,2)=2
            KUP(2,2)=-2
          ELSE
c... KF(d)=1
            KUP(1,2)=1
            KUP(2,2)=-1
```

```
           ENDIF
           KUP(1,6)=4+KPIND
           KUP(2,6)=0
           KUP(1,7)=0
           KUP(2,7)=9+KPIND

           KUP(4+KPIND,4)=1
           KUP(4+KPIND,5)=0

           KUP(9+KPIND,4)=0
           KUP(9+KPIND,5)=2

        ELSEIF (ISUB.EQ.192.OR.ISUB.EQ.194) THEN
           call ggtt(par,khcms,kbhcms,lphcms,lmhcms,nuhcms,nubhcms,
     +        bhcms,bbhcms,fgg)
           SIGEV= xf1(21) * xf2(21) *
     &        fgg * 1.0E-9
     &        * BrWplus * BrWminus * BrPerm
     &        * 16*PI**8
     &        * PS12
     &        * PS3

           IF (.NOT.(SIGEV.GE.0..AND.SIGEV.LT.1.)) THEN
             PRINT*,'Should never happen: SIGEV[mb]=', SIGEV
             SIGEV=0.
           ENDIF

c... KF(g)=21
           KUP(1,2)=21
           KUP(2,2)=21
           den_t=2*(khcms(0)*par(1)*rs/2-khcms(3)*par(1)*rs/2)
           den_u=2*(khcms(0)*par(2)*rs/2+khcms(3)*par(2)*rs/2)
           IF (den_t.LT.den_u) THEN
             KUP(1,6)=4+KPIND
             KUP(1,7)=2

             KUP(2,6)=1
             KUP(2,7)=9+KPIND

             KUP(4+KPIND,4)=1
             KUP(4+KPIND,5)=0

             KUP(9+KPIND,4)=0
             KUP(9+KPIND,5)=2
           ELSE
             KUP(1,6)=2
             KUP(1,7)=9+KPIND

             KUP(2,6)=4+KPIND
             KUP(2,7)=1

             KUP(4+KPIND,4)=2
             KUP(4+KPIND,5)=0

             KUP(9+KPIND,4)=0
             KUP(9+KPIND,5)=1
           ENDIF

        ENDIF

c... settings common to initial partons
           KUP(1,1)=1
           KUP(1,3)=0
           KUP(1,4)=0
           KUP(1,5)=0
```

```
      KUP(2,1)=1
      KUP(2,3)=0
      KUP(2,4)=0
      KUP(2,5)=0

      PUP(1,1)=0.0
      PUP(1,2)=0.0
      PUP(1,3)=par(1)*rs/2
      PUP(1,4)=par(1)*rs/2
      PUP(1,5)=0.0

      PUP(2,1)=0.0
      PUP(2,2)=0.0
      PUP(2,3)=-par(2)*rs/2
      PUP(2,4)=par(2)*rs/2
      PUP(2,5)=0.0

c***********************


Comment...Final particle stuff.....................

c... Higgs comment line (KPIND=1)
      IF (KPIND.EQ.1) THEN
      KUP(3,1)=2
      KUP(3,2)=25
      KUP(3,3)=2
      KUP(3,4)=0
      KUP(3,5)=0
      KUP(3,6)=0
      KUP(3,7)=0

      PUP(3,1)=khcms(1)+kbhcms(1)
      PUP(3,2)=khcms(2)+kbhcms(2)
      PUP(3,3)=khcms(3)+kbhcms(3)
      PUP(3,4)=khcms(0)+kbhcms(0)
      PUP(3,5)=SQRT(PUP(3,4)**2-PUP(3,1)**2-PUP(3,2)**2-PUP(3,3)**2)
      ENDIF

c... t and t~ (comment lines)
      PUP(3+KPIND,1)=khcms(1)
      PUP(3+KPIND,2)=khcms(2)
      PUP(3+KPIND,3)=khcms(3)
      PUP(3+KPIND,4)=khcms(0)
      PUP(3+KPIND,5)=PMAS(6,1)

      KUP(3+KPIND,1)=2
      KUP(3+KPIND,2)=6
      KUP(3+KPIND,3)=1+2*KPIND
      KUP(3+KPIND,4)=0
      KUP(3+KPIND,5)=0
      KUP(3+KPIND,6)=0
      KUP(3+KPIND,7)=0

      PUP(8+KPIND,1)=kbhcms(1)
      PUP(8+KPIND,2)=kbhcms(2)
      PUP(8+KPIND,3)=kbhcms(3)
      PUP(8+KPIND,4)=kbhcms(0)
      PUP(8+KPIND,5)=PMAS(6,1)

      KUP(8+KPIND,1)=2
      KUP(8+KPIND,2)=-6
      KUP(8+KPIND,3)=2+KPIND
      KUP(8+KPIND,4)=0
```

```
      KUP(8+KPIND,5)=0
      KUP(8+KPIND,6)=0
      KUP(8+KPIND,7)=0


c... b and b~
      PUP(4+KPIND,1)=bhcms(1)
      PUP(4+KPIND,2)=bhcms(2)
      PUP(4+KPIND,3)=bhcms(3)
      PUP(4+KPIND,4)=bhcms(0)
      PUP(4+KPIND,5)=PMAS(5,1)

      KUP(4+KPIND,1)=1
      KUP(4+KPIND,2)=5
      KUP(4+KPIND,3)=3+KPIND

      KUP(4+KPIND,6)=0
      KUP(4+KPIND,7)=0

      PUP(9+KPIND,1)=bbhcms(1)
      PUP(9+KPIND,2)=bbhcms(2)
      PUP(9+KPIND,3)=bbhcms(3)
      PUP(9+KPIND,4)=bbhcms(0)
      PUP(9+KPIND,5)=PMAS(5,1)

      KUP(9+KPIND,1)=1
      KUP(9+KPIND,2)=-5
      KUP(9+KPIND,3)=8+KPIND

      KUP(9+KPIND,6)=0
      KUP(9+KPIND,7)=0


c... W+ and W- (comment lines)
      PUP(5+KPIND,1)=lphcms(1)+nuhcms(1)
      PUP(5+KPIND,2)=lphcms(2)+nuhcms(2)
      PUP(5+KPIND,3)=lphcms(3)+nuhcms(3)
      PUP(5+KPIND,4)=lphcms(0)+nuhcms(0)
      PUP(5+KPIND,5)=PMAS(24,1)

      KUP(5+KPIND,1)=2
      KUP(5+KPIND,2)=24
      KUP(5+KPIND,3)=3+KPIND
      KUP(5+KPIND,4)=0
      KUP(5+KPIND,5)=0
      KUP(5+KPIND,6)=0
      KUP(5+KPIND,7)=0

      PUP(10+KPIND,1)=lmhcms(1)+nubhcms(1)
      PUP(10+KPIND,2)=lmhcms(2)+nubhcms(2)
      PUP(10+KPIND,3)=lmhcms(3)+nubhcms(3)
      PUP(10+KPIND,4)=lmhcms(0)+nubhcms(0)
      PUP(10+KPIND,5)=PMAS(24,1)

      KUP(10+KPIND,1)=2
      KUP(10+KPIND,2)=-24
      KUP(10+KPIND,3)=8+KPIND
      KUP(10+KPIND,4)=0
      KUP(10+KPIND,5)=0
      KUP(10+KPIND,6)=0
      KUP(10+KPIND,7)=0


c... 4 vectors for W+ and W- products
      PUP(6+KPIND,1)=nuhcms(1)
```

```
      PUP(6+KPIND,2)=nuhcms(2)
      PUP(6+KPIND,3)=nuhcms(3)
      PUP(6+KPIND,4)=nuhcms(0)

      PUP(7+KPIND,1)=lphcms(1)
      PUP(7+KPIND,2)=lphcms(2)
      PUP(7+KPIND,3)=lphcms(3)
      PUP(7+KPIND,4)=lphcms(0)

      KUP(6+KPIND,1)=1
      KUP(6+KPIND,3)=5+KPIND
      KUP(6+KPIND,6)=0
      KUP(6+KPIND,7)=0

      KUP(7+KPIND,1)=1
      KUP(7+KPIND,3)=5+KPIND
      KUP(7+KPIND,6)=0
      KUP(7+KPIND,7)=0

      PUP(11+KPIND,1)=nubhcms(1)
      PUP(11+KPIND,2)=nubhcms(2)
      PUP(11+KPIND,3)=nubhcms(3)
      PUP(11+KPIND,4)=nubhcms(0)

      PUP(12+KPIND,1)=lmhcms(1)
      PUP(12+KPIND,2)=lmhcms(2)
      PUP(12+KPIND,3)=lmhcms(3)
      PUP(12+KPIND,4)=lmhcms(0)

      KUP(11+KPIND,1)=1
      KUP(11+KPIND,3)=10+KPIND
      KUP(11+KPIND,6)=0
      KUP(11+KPIND,7)=0

      KUP(12+KPIND,1)=1
      KUP(12+KPIND,3)=10+KPIND
      KUP(12+KPIND,6)=0
      KUP(12+KPIND,7)=0


c...common parton shower stuff
      NUP=12+KPIND
      NFUP=1

      IFUP(1,1)=4+KPIND
      IFUP(1,2)=9+KPIND

c... Q2 scale for initial state radiation
      Q2UP(0)=4.*(Q2-PMAS(6,1)**2)

c... Q2 scale for final state showers of b, b~, qq~ (of W+) and qq~ (of W-)

      Q2UP(1)=PMAS(6,1)**2

      CALL Wtreatment

C... End of main program
      END



c..._____
c...subroutine W treatment
      SUBROUTINE Weight(BrPerm, BrWplus, BrWminus)
c       decay table for W's
      INTEGER MDCY, MDME, KFDP
```

```
      REAL BRAT
      COMMON/LUDAT3/MDCY(500,3),MDME(2000,2),BRAT(2000),KFDP(2000,5)

      BrPerm=2.
      BrWplus=0.
      BrWminus=0.
      DO I=172,191
        IF (MDME(I,1).EQ.1) THEN
          BrWplus=BrWplus+BRAT(I)
          BrWminus=BrWminus+BRAT(I)
          BrPerm=1.
        ELSEIF (MDME(I,1).EQ.2) THEN
          BrWplus=BrWplus+BRAT(I)
        ELSEIF (MDME(I,1).EQ.3) THEN
          BrWminus=BrWminus+BRAT(I)
        ENDIF
      ENDDO
      END
c...~~~~~~~~~~~~~~~~~~~~~~~~~~~~~~~~~~~~~~~~~~~~~~~~~~~~~~~~~~~~~~~~~~~~

c...━━━━━━━━━━━━━━━━━━━━━━━━━━━━━━━━━━━━
c...subroutine W daughters parton shower treatment (Q^2, colour flow)
      SUBROUTINE Wtreatment

      INTEGER NUP,KUP,NFUP,IFUP
      REAL PUP,Q2UP
      COMMON/PYUPPR/NUP,KUP(20,7),PUP(20,5),NFUP,IFUP(10,2),Q2UP(0:10)

      INTEGER I
      DO I=3,NUP
        IF (ABS(KUP(I,2)).EQ.24) CALL Wsubtreat(I)
      ENDDO

      END
c...~~~~~~~~~~~~~~~~~~~~~~~~~~~~~~~~~~~~~~~~~~~~~~~~~~~~~~~~~~~~~~~~~~~~

c...━━━━━━━━━━━━━━━━━━━━━━━━━━━━━━━━━━━━
c...subroutine W daughters parton shower treatment (Q^2, colour flow)
      SUBROUTINE Wsubtreat(WPlace)

      INTEGER WPlace, DaPlace, DbPlace, Wsign
I
C...Particle properties + some flavour parameters.
      INTEGER KCHG
      REAL PMAS,PARF,VCKM
      COMMON/LUDAT2/KCHG(500,3),PMAS(500,4),PARF(2000),VCKM(4,4)

c decay table for W's
      INTEGER MDCY, MDME, KFDP
      REAL BRAT
      COMMON/LUDAT3/MDCY(500,3),MDME(2000,2),BRAT(2000),KFDP(2000,5)

      INTEGER NUP,KUP,NFUP,IFUP
      REAL PUP,Q2UP
      COMMON/PYUPPR/NUP,KUP(20,7),PUP(20,5),NFUP,IFUP(10,2),Q2UP(0:10)

      REAL BRANRNDM

      DaPlace=0
      DbPlace=0
      DO I=NUP,3,-1
        IF (KUP(I,3).EQ.WPlace) THEN
          IF (DbPlace.GT.0) DaPlace=I
          IF (DbPlace.EQ.0) DbPlace=I
        ENDIF
```

```
      ENDDO

      IF (KUP(WPlace,2).EQ.24) THEN
c... W+ decay
        BRANRNDM=0.
        DO I=172,191
          IF (MDME(I,1).EQ.1.OR.MDME(I,1).EQ.2) THEN
            BRANRNDM=BRANRNDM+BRAT(I)
          ENDIF
        ENDDO
        BRANRNDM=BRANRNDM*RLU(1.)
        PUP(DbPlace,5)=0.
        DO I=172,191
          IF (MDME(I,1).EQ.1.OR.MDME(I,1).EQ.2) THEN
            BRANRNDM=BRANRNDM-BRAT(I)
          ENDIF
          IF (BRANRNDM.LE.0..AND.PUP(DbPlace,5).EQ.0.) THEN
            KUP(DaPlace,2)=KFDP(I,2)
            PUP(DaPlace,5)=PMAS(ABS(KFDP(I,2)),1)
            KUP(DbPlace,2)=KFDP(I,1)
            PUP(DbPlace,5)=PMAS(ABS(KFDP(I,1)),1)
          ENDIF
        ENDDO

        IF (ABS(KUP(DaPlace,2)).EQ.12.OR.
     &       ABS(KUP(DaPlace,2)).EQ.14.OR.
     &       ABS(KUP(DaPlace,2)).EQ.16) THEN
          KUP(DaPlace,4)=0
          KUP(DaPlace,5)=0
          KUP(DbPlace,4)=0
          KUP(DbPlace,5)=0
        ELSEIF (ABS(KUP(DaPlace,2)).EQ.2.OR.
     &       ABS(KUP(DaPlace,2)).EQ.4.OR.
     &       ABS(KUP(DaPlace,2)).EQ.6) THEN
          KUP(DaPlace,4)=DbPlace
          KUP(DaPlace,5)=0
          KUP(DbPlace,4)=0
          KUP(DbPlace,5)=DaPlace
        ENDIF

      ELSEIF (KUP(WPlace,2).EQ.-24) THEN
c... W- decay
        BRANRNDM=0.
        DO I=172,191
          IF (MDME(I,1).EQ.1.OR.MDME(I,1).EQ.3) THEN
            BRANRNDM=BRANRNDM+BRAT(I)
          ENDIF
        ENDDO
        BRANRNDM=BRANRNDM*RLU(1.)
        PUP(DbPlace,5)=0.
        DO I=172,191
          IF (MDME(I,1).EQ.1.OR.MDME(I,1).EQ.3) THEN
            BRANRNDM=BRANRNDM-BRAT(I)
          ENDIF
          IF (BRANRNDM.LE.0..AND.PUP(DbPlace,5).EQ.0.) THEN
            KUP(DaPlace,2)=-KFDP(I,2)
            PUP(DaPlace,5)=PMAS(ABS(KFDP(I,2)),1)
            KUP(DbPlace,2)=-KFDP(I,1)
            PUP(DbPlace,5)=PMAS(ABS(KFDP(I,1)),1)
          ENDIF
        ENDDO

        IF (ABS(KUP(DaPlace,2)).EQ.12.OR.
     &       ABS(KUP(DaPlace,2)).EQ.14.OR.
     &       ABS(KUP(DaPlace,2)).EQ.16) THEN
```

```
        KUP(DaPlace,4)=0
        KUP(DaPlace,5)=0
        KUP(DbPlace,4)=0
        KUP(DbPlace,5)=0
       ELSEIF (ABS(KUP(DaPlace,2)).EQ.2.OR.
     &       ABS(KUP(DaPlace,2)).EQ.4.OR.
     &       ABS(KUP(DaPlace,2)).EQ.6) THEN
        KUP(DaPlace,4)=0
        KUP(DaPlace,5)=DbPlace
        KUP(DbPlace,4)=DaPlace
        KUP(DbPlace,5)=0
       ENDIF

      ELSE
        PRINT*,'Mistake: Wsign=',Wsign
      ENDIF

      NFUP=NFUP+1
      IFUP(NFUP,1)=DaPlace
      IFUP(NFUP,2)=DbPlace

      Q2UP(NFUP)=PUP(WPlace,5)**2

      END
c...~~~~~~~~~~~~~~~~~~~~~~~~~~~~~~~~~~~~~~~~~~~~~~~~~~~~~~~~~~~~~~~~~~~~



c
c**************************************************
c     subroutine INIT fills arrays and puts constants.
c     The LHC c.m. energy rs = 14 TeV is provided in the main program
c**************************************************
      SUBROUTINE INIT

      IMPLICIT NONE

C...All real arithmetic in double precision.
      INTEGER KCHG
      REAL PMAS,PARF,VCKM
C...Particle properties + some flavour parameters.
      COMMON/LUDAT2/KCHG(500,3),PMAS(500,4),PARF(2000),VCKM(4,4)

      REAL s,rs,eb
      REAL m,mh,Gamma,mhGh
      REAL Pi,Pi2,GeV2pb,v,alphas,a,as,gvv,mz,mw,kappa
      REAL a2,as2,mov2,mu,mh2,fact
      REAL a_mh(1:4),a_aas(1:2,1:4),a_gvv(1:3)

      COMMON/block1/s,rs,Gamma,v,m,mh,mhGh,mz,mw,mov2,mu,eb,mh2
      COMMON/block2/Pi,Pi2,GeV2pb,alphas,a,as,gvv,a2,as2,fact,kappa
      COMMON/block5/a_mh,a_aas,a_gvv

cls...ALPHAS from PYTHIA (PDFlib)
      REAL ULALPS

c- constants
      Pi = 4.0*ATAN(1.0)
      Pi2 = Pi**2

c- conversion 1/Gev^2 -> pb
      GeV2pb = 0.3893856848E9

c- c.m. energy^2 [GeV^2]
      s = rs**2
```

```
c– SM Higgs v.e.v. [GeV]
      v = 246.

c– QCD coupling alpha_s (taken here at the scale of 2*m_top)
cls       alphas = 0.1

c– top mass m, Z mass mz, W mass mw [GeV]
      m = PMAS(6,1)
      mz = PMAS(23,1)
      mw = PMAS(24,1)
c       write(*,*) 'm_t=',m,' m_z=',mz,' m_w=',mw

c– some factors which are also needed in the matrix
c       element subroutines "qqtt" and "ggtt", and which
c       are also kept in the common blocks
      mov2 = (m/v)**2
      mu = mw**2/m**2
      eb = (m**2-mw**2)/(2.0*m)
      kappa = (m**2-2.*mw**2)/(m**2+2.*mw**2)
c       factor resulting from the b and bbar energy integrations
c       in eq. (4) of ref. [1],
c       factors 2 and Pi and alpha_s, and conversion 1/GeV^2 – > pb.

      fact = 24.0 * mu**2 / (1.0 + 2.0*mu)
      fact = fact**2 /(32.*Pi**3) * alphas**2
      fact = fact * GeV2pb
c***********

      RETURN
      END
```

A.2 Characteristic distributions of the hard subprocess

In the following some additional distributions of the hard $t\bar{t}$ subprocess and its partons are provided. In figure A.2 a) and b) the normalised x and Q^2 distributions of the different matrix elements and event generators used are shown. In c) and d) the partonic center of mass energy squared is compared for the different matrix elements (event generators) and the different $t\bar{t}$ production mechanisms. In figure A.3 the Q^2 scale of the hard subprocess in dependence of the transverse momentum of the $t\bar{t}$ system (a) and b)) and the normalised $t\bar{t}$ transverse momentum distribution (c) for the different production mechanisms are shown. Finally in figure A.4 the transverse momenta and the pseudo rapidity distributions of the W boson daughter quarks are plotted. The different matrix elements and event generators are compared on the left hand side while the contribution of the different production mechanisms (gluon gluon fusion and quark antiquark annihilation) to the $t\bar{t}$ production are compared on the right.
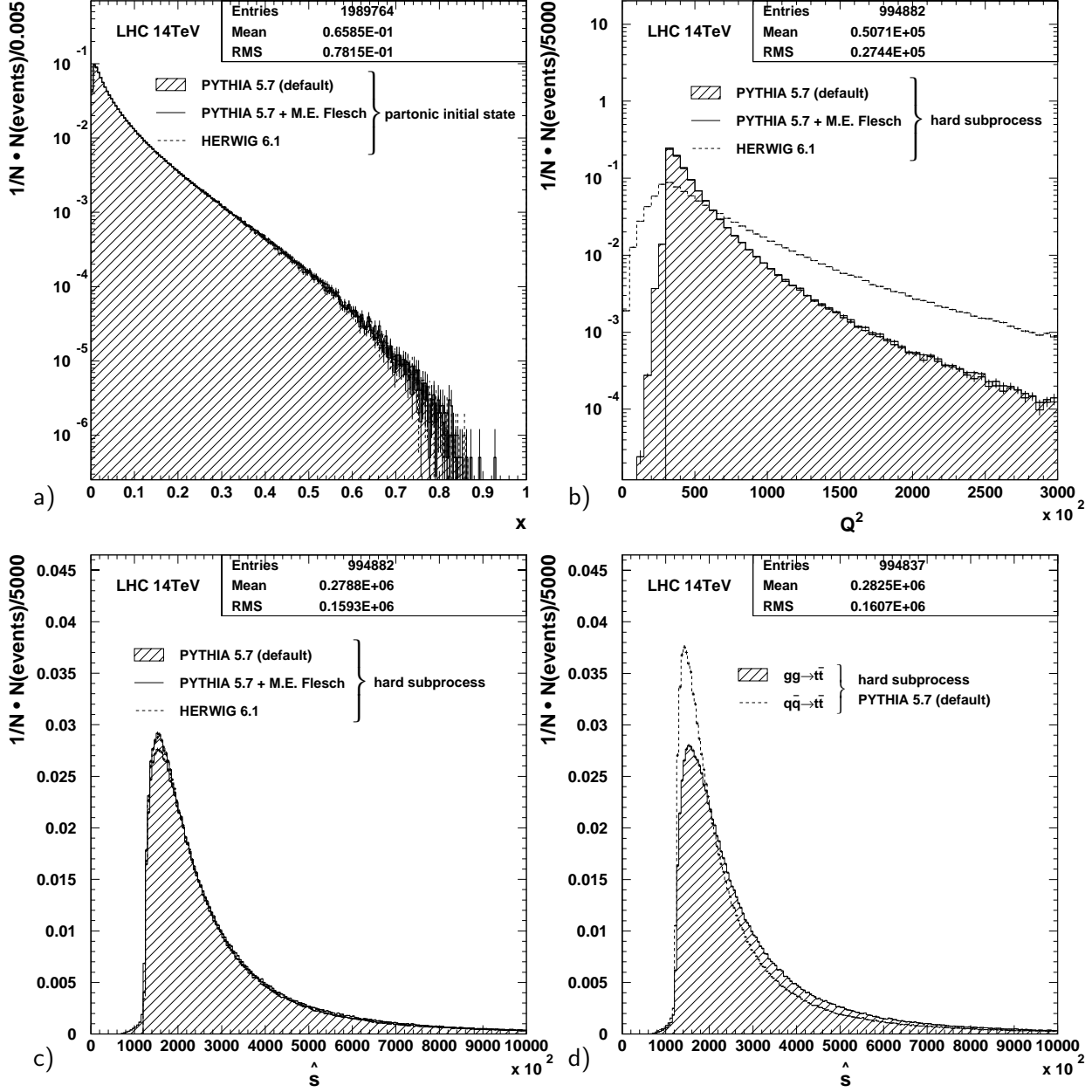
Figure A.2: Distributions of the generated proton momentum fractions $x_{1,2}$, the Q^2 scales of the hard subprocess and the partonic center of mass energy squared $\hat{s}$ for the used event generators and the $2 \rightarrow 6$ on-shell matrix elements implemented in PYTHIA. The predictions of the different matrix elements agree quite well for the x and the $\hat{s}$ distributions. The differences in the Q^2 distribution is due to different choices of the Q^2 scale. The peak of the $\hat{s}$ distribution is more pronounced for the quark antiquark annihilation.
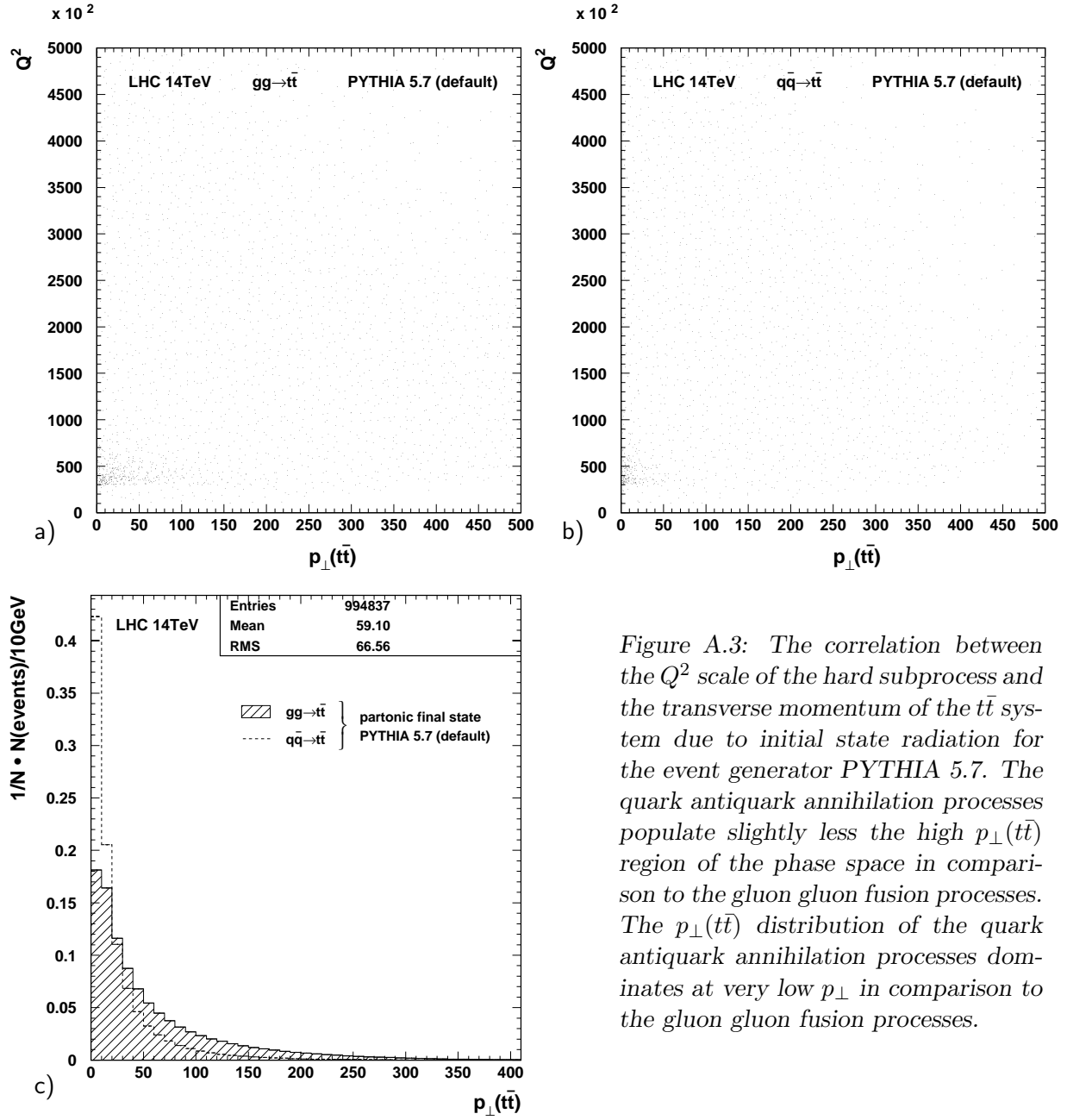
Figure A.3: The correlation between the Q^2 scale of the hard subprocess and the transverse momentum of the $t\bar{t}$ system due to initial state radiation for the event generator PYTHIA 5.7. The quark antiquark annihilation processes populate slightly less the high $p_\perp(t\bar{t})$ region of the phase space in comparison to the gluon gluon fusion processes. The $p_\perp(t\bar{t})$ distribution of the quark antiquark annihilation processes dominates at very low $p_\perp$ in comparison to the gluon gluon fusion processes.
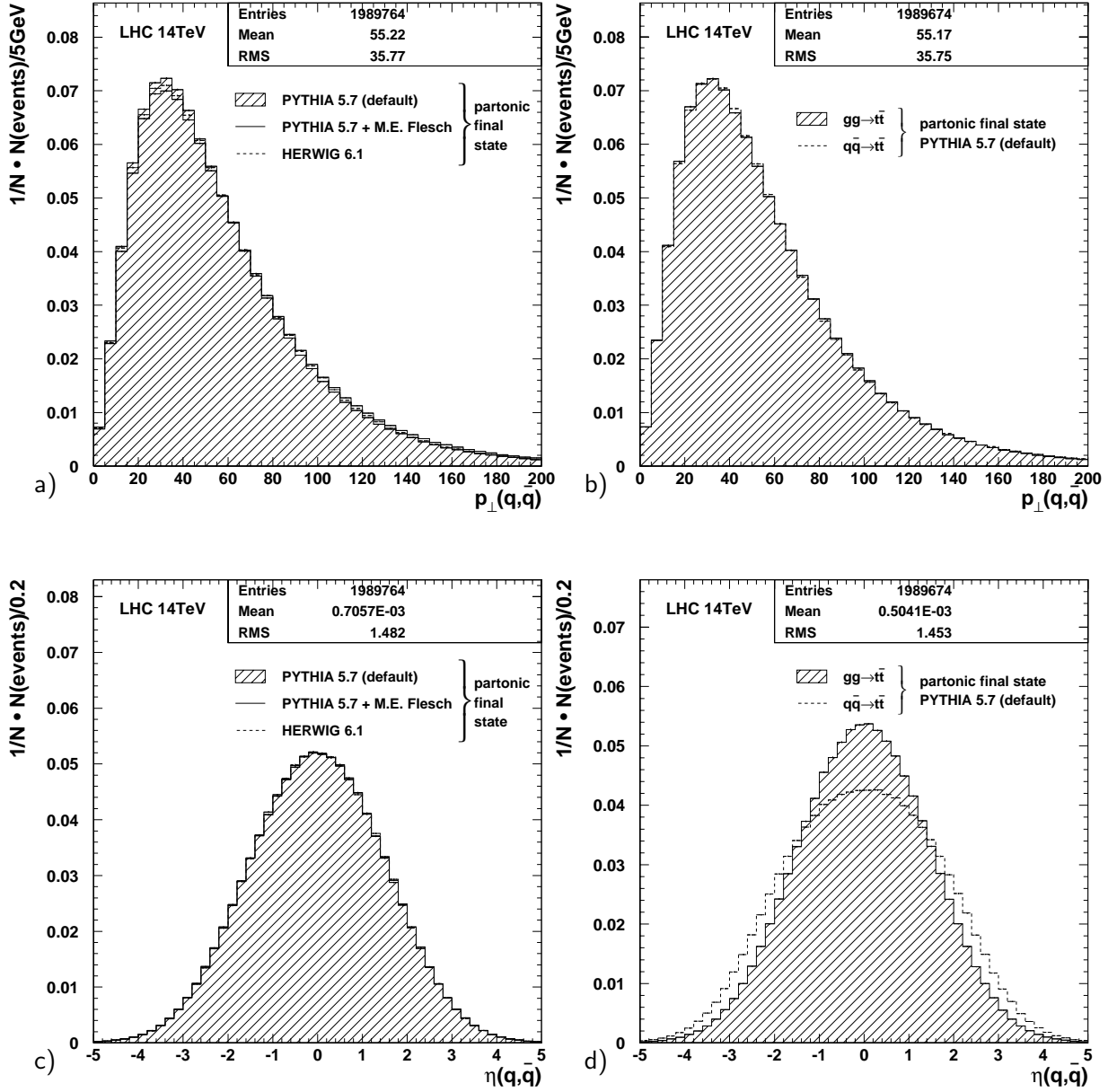
Figure A.4: The $p_\perp$ spectrum (top) and the pseudo rapidity distribution (bottom) of the W daughter quarks for different event generators (left) and the gluon gluon fusion processes compared to the quark antiquark annihilation processes (right). The distributions are the superposition of the two weak isospin doublet members (corresponding to the neutrino and lepton in the case of a leptonic W boson decay) since the quarks are not distinguished. The different event generators agree quite well. The quark antiquark annihilation processes show a slightly broader distribution in comparison to the gluon gluon fusion processes.

Appendix B

Jet energies and resolutions

Jets are reconstructed from the hits in the electromagnetic and hadronic calorimeter of the CMSJET detector response with the cone algorithm introduced in section 3.8. For the investigation, $t\bar{t}$ events in the semileptonic decay channel as used for the top mass determination (chapter 4) have been generated. Jets which coincide with a W boson daughter quark within $R_{\mathrm{jet},q} < 0.2$ in the η, ϕ space, are taken to determine the transverse energy resolution. As an example in figure B.1 the jets of a $100\,\mathrm{GeV}$ quark (within $1\,\%$), obtained using the jet algorithm with the cone size $R = 0.7$ is shown. The distribution can be fitted with a Gaussian and the mean value matches the generated quark transverse energy within one percent. The resolution is given by the Gaussian width and achieves about $9.5\,\%$ in this example. In figure B.2 the transverse energies and resolutions are shown for the cone size $R = 0.5$. On the left the light quarks from the W bosons are related to the jets while on the right the b quarks from the top quark decays have been matched to the jets. The reconstructed transverse jet energy depends linearly on the generated transverse energy of the quarks (see the straight line fit in a) and b)). The resolutions improve towards higher transverse energies as can be extracted from the plots c) and d). The same distributions are given for the cone parameter $R = 0.7$ in figure B.3.
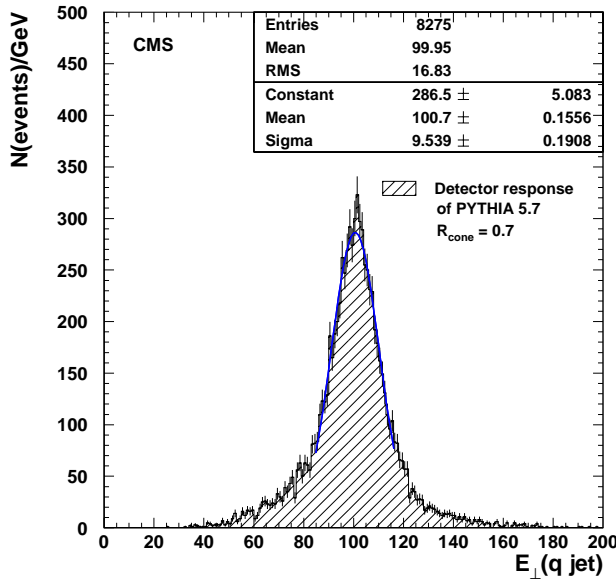

Figure B.1: Transverse energy of the light quark jets from $t\bar{t}$ events which match the W boson daughter quarks in the η, ϕ space within $R_{jet,q} < 0.2$. The quark energies are restricted to $E_{\perp}(q) = 100 \pm 1\,GeV$ and the cone size of $R = 0.7$ was chosen. The resolution determined by a Gaussian fit achieves about $9.5\,\%$.
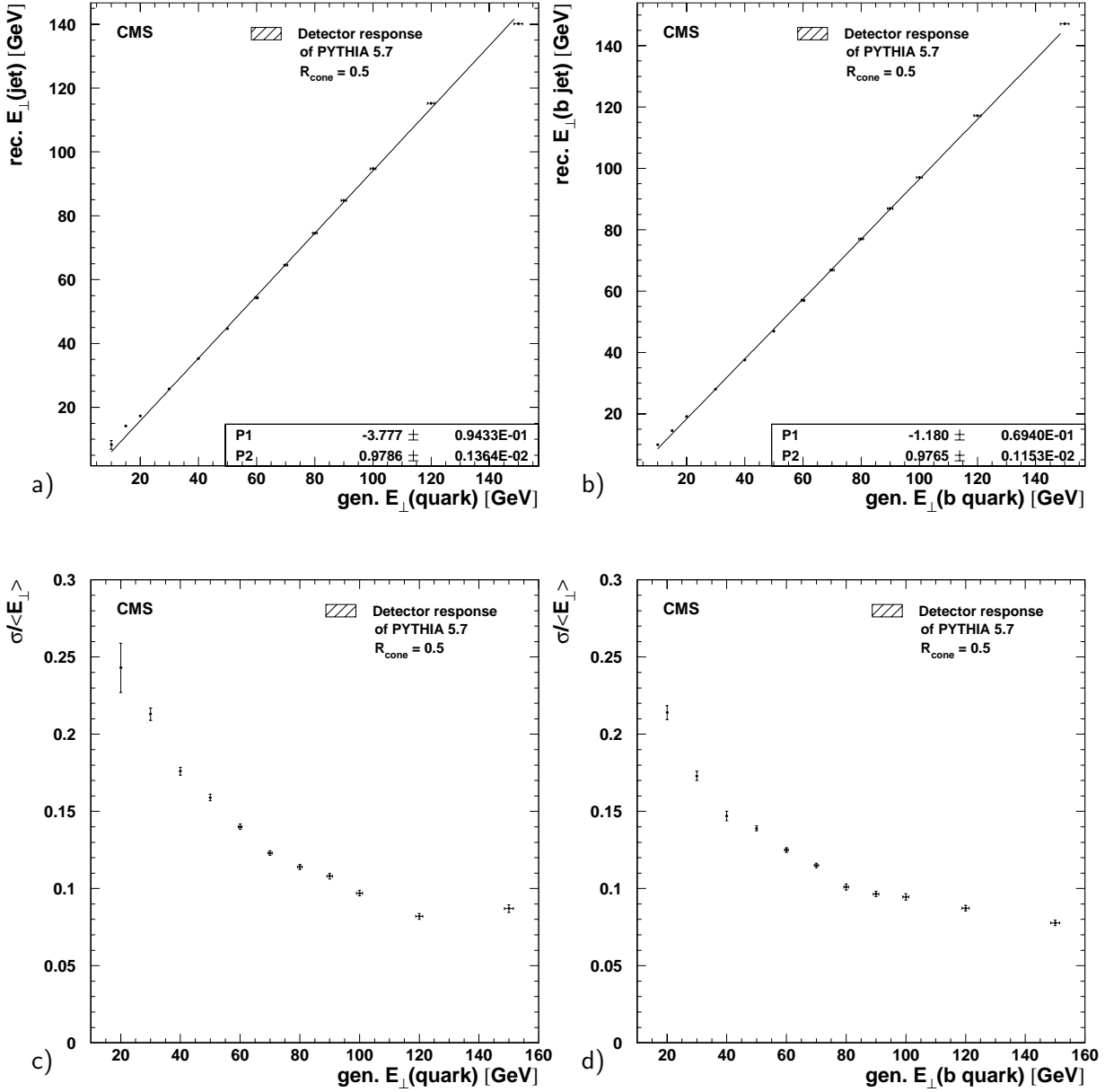
Figure B.2: *The transverse energy and its resolution of the jets reconstructed in $t\bar{t}$ events with the cone algorithm ($R = 0.5$). As matching condition between the quarks and the jets the distance $R_{jet,q} < 0.2$ in η, ϕ space has been applied. The dependence between the quark and the jet transverse energies (top) can be well approximated with a straight line. The fitted lines for non b jets (left) and b jets (right) are quite similar. The transverse momentum resolutions for the different kinds of jets are shown on the bottom. The resolution improves towards higher transverse energies.*
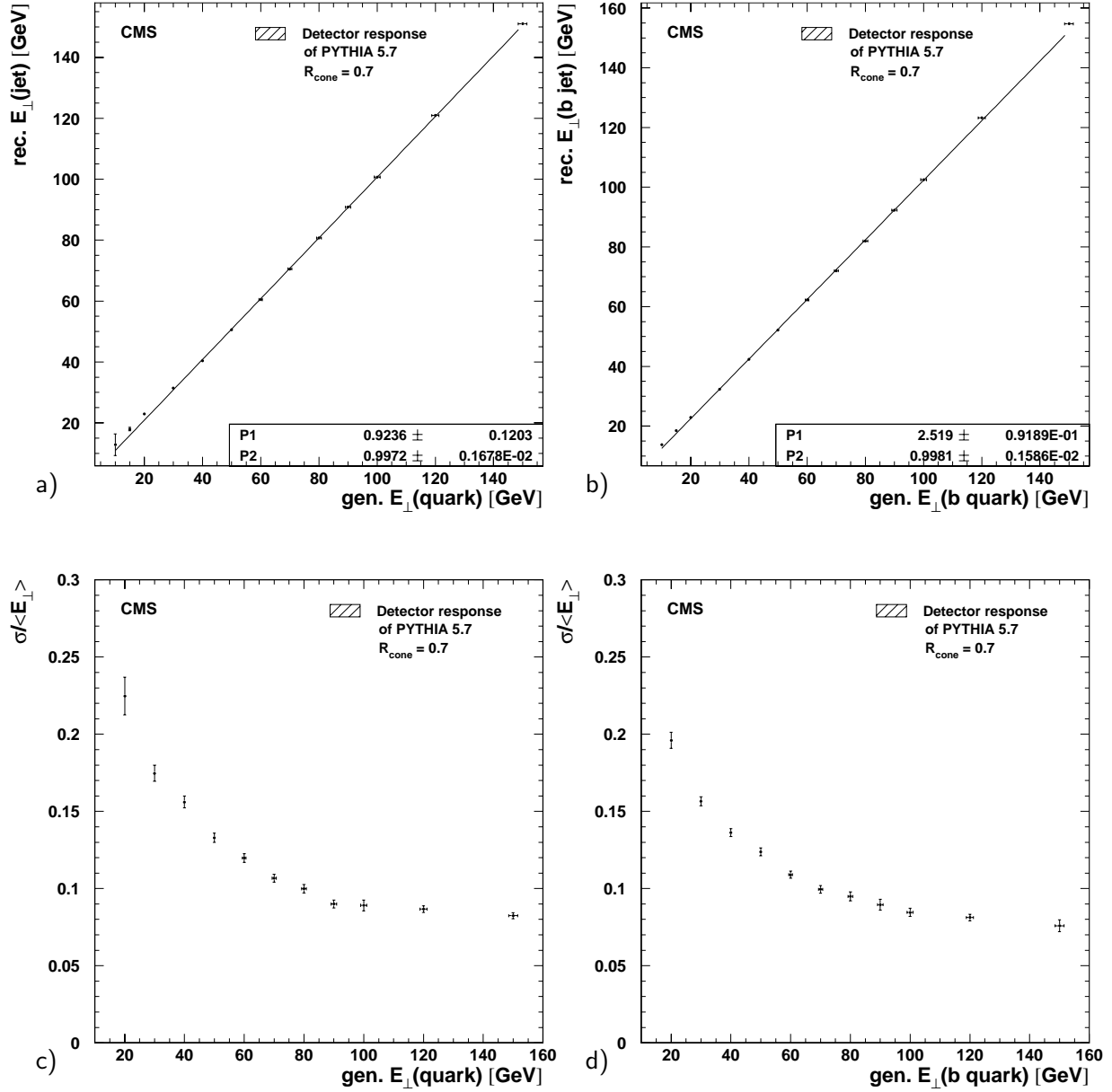
Figure B.3: The transverse energy and its resolution of the jets reconstructed in $t\bar{t}$ events with the cone algorithm using the cone parameter $R = 0.7$. The same matching condition between the quarks and the jets as for the cone size $R = 0.5$ is used ($R_{jet,q}(\eta, \phi) < 0.2$). The dependence between the quark and the jet transverse energies shows a linear behaviour and the reconstructed transverse momenta match the generated quark momenta within the percent level. The transverse momentum resolutions of the jets are quite similar to those of figure B.2 where the cone size $R = 0.5$ was used.

Appendix C
Helicity angles in W boson decays

The additionally implemented possibilities to choose an individual helicity of the decaying W boson are shown in the listing below, which is an extract of the PYTHIA 5.7 subroutine PYRESD.F. Therein the four vectors of the particles can be identified by the following indices. I1 corresponds to the top quark, I2 and I3 correspond to the charged lepton type and the neutrino type fermion of the W boson decay respectively and I4 corresponds to the b quark of the weak top quark decay. As can be extracted from the source code, the angular orientation of the W boson decay according to the standard model (MSTP(47)=1) is proportional to the product of the four vectors $(p_t \cdot p_\ell)(p_b \cdot p_{\nu_\ell})$.

```
     .
     .
     .

C...Angular correlation in f -> f' + W -> f' + 2 quarks/leptons.
      I1=IREF(IP,8)
      IF(MOD(KFAGM,2).EQ.0) THEN
        I2=N+1
        I3=N+2
      ELSE
        I2=N+2
        I3=N+1
      ENDIF
      I4=IREF(IP,2)

      if (MSTP(47).eq.1) then
        WT=(P(I1,4)*P(I2,4)-P(I1,1)*P(I2,1)-P(I1,2)*P(I2,2)-
     &      P(I1,3)*P(I2,3))*(P(I3,4)*P(I4,4)-P(I3,1)*P(I4,1)-
     &      P(I3,2)*P(I4,2)-P(I3,3)*P(I4,3))
        WTMAX=(P(I1,5)**4-P(IREF(IP,1),5)**4)/8.

      elseif (MSTP(47).EQ.2.OR.MSTP(47).EQ.3.OR.MSTP(47).EQ.4.OR.
     &    MSTP(47).EQ.5.OR.MSTP(47).EQ.6.OR.MSTP(47).EQ.7) then
cls...supplement polarisations
        mt2=P(I1,4)**2-P(I1,1)**2-P(I1,2)**2-P(I1,3)**2
        mW2=(P(I2,4)+P(I3,4))**2
     &     -(P(I2,1)+P(I3,1))**2
     &     -(P(I2,2)+P(I3,2))**2
     &     -(P(I2,3)+P(I3,3))**2
        f_tW=0.5*mt2/mW2
        costh=(P(I4,4)*(P(I2,4)-P(I3,4))
     &     - P(I4,1)*(P(I2,1)-P(I3,1))
     &     - P(I4,2)*(P(I2,2)-P(I3,2))
     &     - P(I4,3)*(P(I2,3)-P(I3,3)) )
     &     /(P(I4,4)*(P(I2,4)+P(I3,4))
     &     - P(I4,1)*(P(I2,1)+P(I3,1))
```

```
      &        - P(I4,2)*(P(I2,2)+P(I3,2))
      &        - P(I4,3)*(P(I2,3)+P(I3,3)) )

          if (MSTP(47).eq.2) then
            WT=3./8.*1./(1.+f_tW)*(1.-costh)**2 !only left
            WTMAX=3./2.*1./(1.+f_tW) !only left

          elseif (MSTP(47).eq.3) then
            WT=3./4.*f_tW/(1.+f_tW)*(1.-costh**2) !only longitudinal
            WTMAX=3./4.*f_tW/(1.+f_tW) !only longitudinal

          elseif (MSTP(47).eq.4) then
            WT=3./8.*1./(1.+f_tW)*(1.+costh)**2 !only right
            WTMAX=3./2.*1./(1.+f_tW) !only right

          elseif (MSTP(47).eq.5) then
            if (ABS(K(I2,2)).eq.11.or.ABS(K(I2,2)).eq.13.or.
      &          ABS(K(I2,2)).eq.15.or.ABS(K(I3,2)).eq.11.or.
      &          ABS(K(I3,2)).eq.13.or.ABS(K(I3,2)).eq.15) then
              WT=3./8.*1./(1.+f_tW)*(1.-costh)**2 !only left
              WTMAX=3./2.*1./(1.+f_tW) !only left
            else
              WT=(P(I1,4)*P(I2,4)-P(I1,1)*P(I2,1)-P(I1,2)*P(I2,2)-
      &          P(I1,3)*P(I2,3))*(P(I3,4)*P(I4,4)-P(I3,1)*P(I4,1)-
      &          P(I3,2)*P(I4,2)-P(I3,3)*P(I4,3))
              WTMAX=(P(I1,5)**4-P(IREF(IP,1),5)**4)/8.
            endif
          elseif (MSTP(47).eq.6) then
            if (ABS(K(I2,2)).eq.11.or.ABS(K(I2,2)).eq.13.or.
      &        ABS(K(I2,2)).eq.15.or.ABS(K(I3,2)).eq.11.or.
      &        ABS(K(I3,2)).eq.13.or.ABS(K(I3,2)).eq.15) then
              WT=3./4.*f_tW/(1.+f_tW)*(1.-costh**2) !only longitudinal
              WTMAX=3./4.*f_tW/(1.+f_tW) !only longitudinal
            else
              WTMAX=3./4.*f_tW/(1.+f_tW) !only longitudinal
              WT=(P(I1,4)*P(I2,4)-P(I1,1)*P(I2,1)-P(I1,2)*P(I2,2)-
      &          P(I1,3)*P(I2,3))*(P(I3,4)*P(I4,4)-P(I3,1)*P(I4,1)-
      &          P(I3,2)*P(I4,2)-P(I3,3)*P(I4,3))
              WTMAX=(P(I1,5)**4-P(IREF(IP,1),5)**4)/8.
            endif
          elseif (MSTP(47).eq.7) then
            if (ABS(K(I2,2)).eq.11.or.ABS(K(I2,2)).eq.13.or.
      &        ABS(K(I2,2)).eq.15.or.ABS(K(I3,2)).eq.11.or.
      &        ABS(K(I3,2)).eq.13.or.ABS(K(I3,2)).eq.15) then
              WT=3./8.*1./(1.+f_tW)*(1.+costh)**2 !only right
              WTMAX=3./2.*1./(1.+f_tW) !only right
            else
              WT=(P(I1,4)*P(I2,4)-P(I1,1)*P(I2,1)-P(I1,2)*P(I2,2)-
      &          P(I1,3)*P(I2,3))*(P(I3,4)*P(I4,4)-P(I3,1)*P(I4,1)-
      &          P(I3,2)*P(I4,2)-P(I3,3)*P(I4,3))
              WTMAX=(P(I1,5)**4-P(IREF(IP,1),5)**4)/8.
            endif

          endif
c...end of supplement polarisations~~~~~~~~~~~~~~~~~~~~~~~~~~~~~~~~~~
          endif

      IF(KFAGM.EQ.6.AND.MSTP(48).LE.1) WT=WTMAX
      IF(KFAGM.NE.6.AND.MSTP(49).LE.1) WT=WTMAX

        .
        .
        .
```

Appendix D

$t\bar{t}$ spin correlation observable

In chapter 6 the $t\bar{t}$ spin correlation has been investigated with the double differential distribution of the lepton angles in the helicity basis. Another possibility to measure the spin correlation between the two leptons in the dileptonic decay channel of the $t\bar{t}$ production is provided by the observable

$$\mathcal{O} = \hat{p}_{\ell+}^* \cdot \hat{p}_{\ell-}^* \tag{D.1}$$

from [Fle98]. It is the angle between the directions of flight of the two leptons in the rest frame of their corresponding top (antitop) quark. The advantage of this observable is that only a one dimensional distribution has to be fitted and, as can be extracted from the
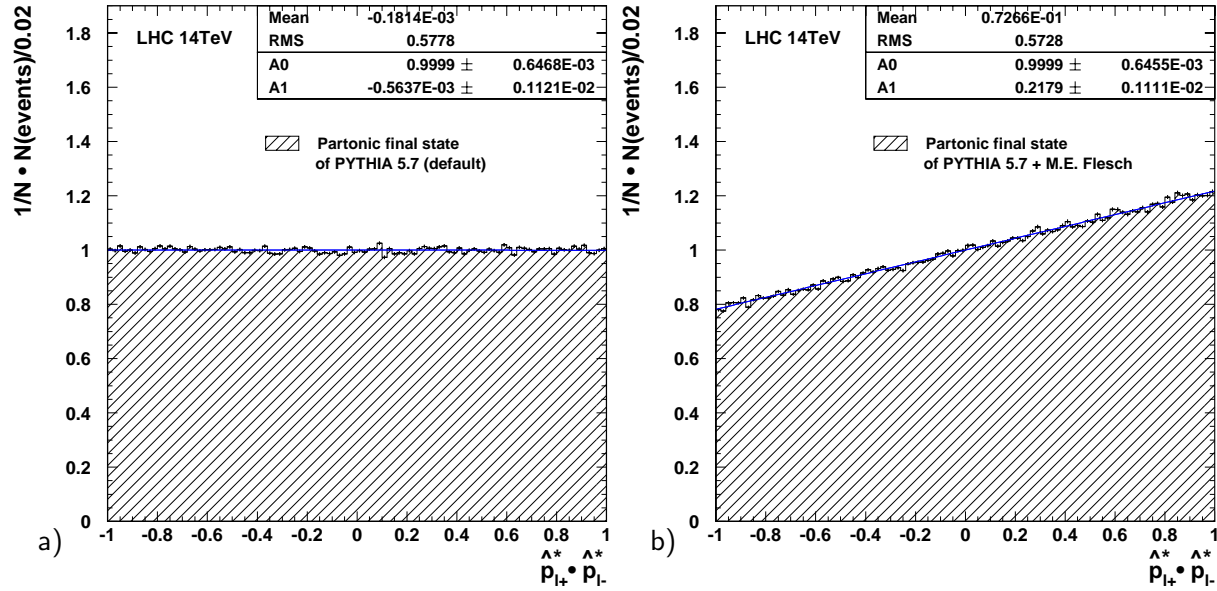

Figure D.1: The angle of the directions of flight of the two charge conjugated leptons of the non radiative partonic final state in their corresponding top (antitop) quark rest frame respectively. While the default $2 \rightarrow 2$ matrix elements implemented in PYTHIA without spin correlation show a flat distribution (plot a)), the $2 \rightarrow 6$ matrix elements from [Ber98a] result in a distribution which can be described by an inclined straight line (plot b)).
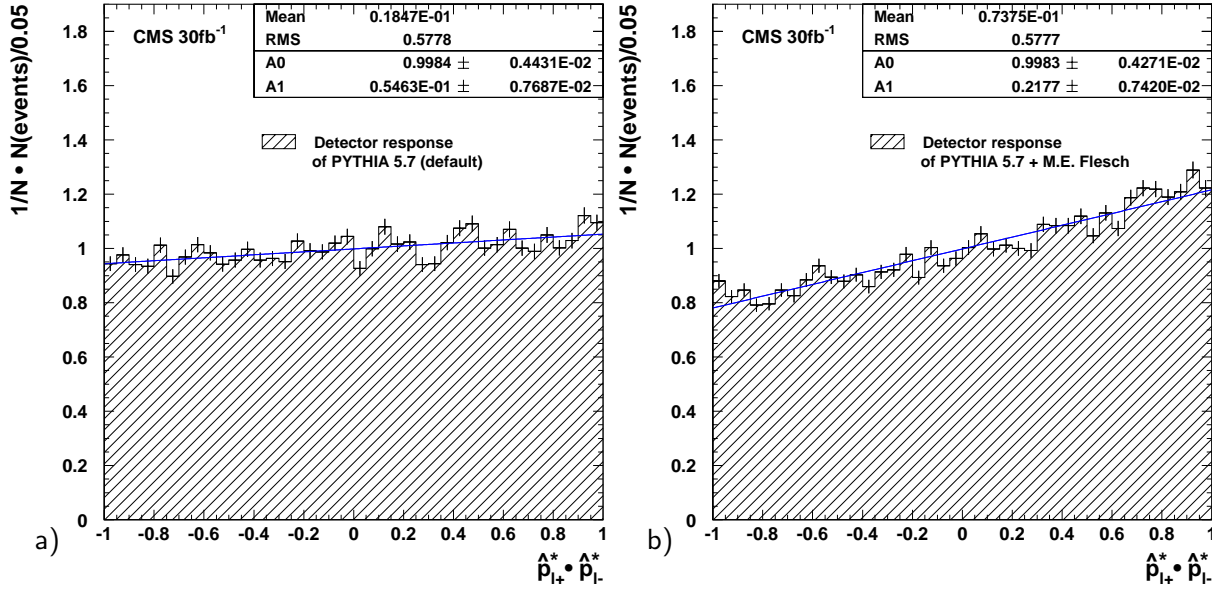
Figure D.2: The angle of the directions of flight of the two reconstructed charge conjugated leptons in the rest frame of their corresponding reconstructed top (antitop) quark. The distributions are fitted with a straight line. The inclination of the straight lines (fit parameter A_1) differ significantly between the case of no spin correlation (plot a)) and spin correlation according to the standard model (plot b)).

plots, a simple straight line fulfils the requirements. The expectations for the non radiative partonic final state at the LHC without and with spin correlation are shown in figure D.1 a) and b) respectively. The same distributions for the CMS detector response are given in figure D.2. The slope of the straight line with its errors is indicated in the plots as fit parameter A_1. The difference between the two cases with and without spin correlation is significant. The statistical error on the fit parameter of the detector response is less than $5\,\%$ for $30\,\mathrm{fb}^{-1}$. This indicates, that this observable may be better suited to measure the spin correlation at the LHC than the double differential lepton angle distribution in the helicity basis. This may not be true for the Tevatron, where an optimal basis of the double differential lepton angle distribution yields an enhanced significance. The disadvantage of this observable compared to the double differential angular lepton distribution discussed in chapter 6 is the missing second degree of freedom, which provides more information. This can become important in case of deviations from the spin correlations expected in the standard model.

Appendix E

Standard model Higgs boson at the LHC

The cross sections of the different production mechanisms for a standard model Higgs boson in dependence of its mass as given in [Spi97] are shown in figure E.1. Over the whole mass range the gluon gluon fusion gives the dominating contribution. Towards higher Higgs masses the associated Higgs production through quark quark scattering becomes more and more important. The total decay width in dependence of the mass is shown in figure E.2 a) and the branching ratios of the different decay channels are given in b). The plots are obtained using the program HDECAY [Djo97] assuming a top quark mass of 175 GeV.
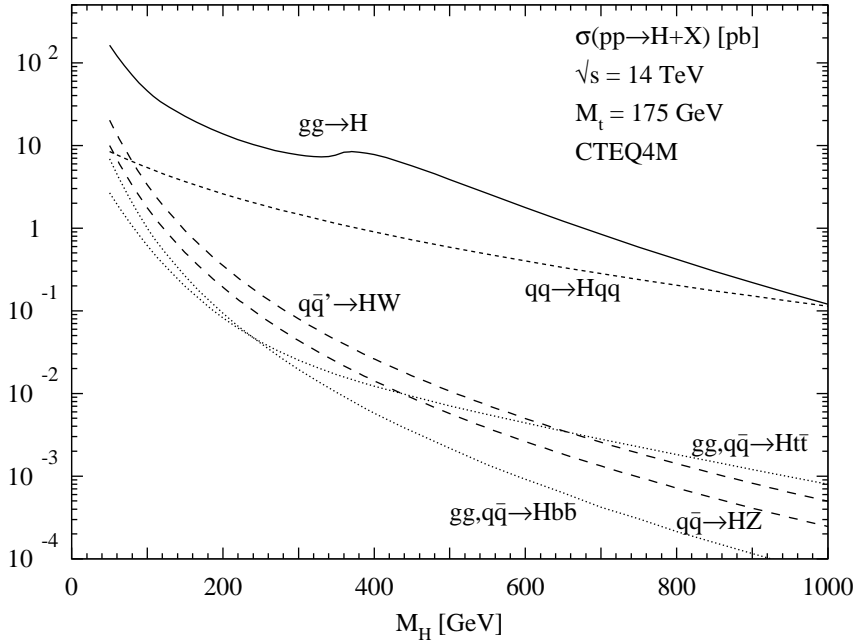

Figure E.1: *The most important production cross sections of the standard model Higgs boson at the LHC in dependence of the Higgs boson mass. The cross sections, obtained with parton density functions tuned to HERA data, include QCD next-to-leading order corrections. The gluon gluon fusion process dominates over the whole Higgs mass range. Close above the $t\bar{t}$ production threshold the cross section for this production process increases slightly while the other cross sections decrease strictly monotonously towards higher Higgs masses.*
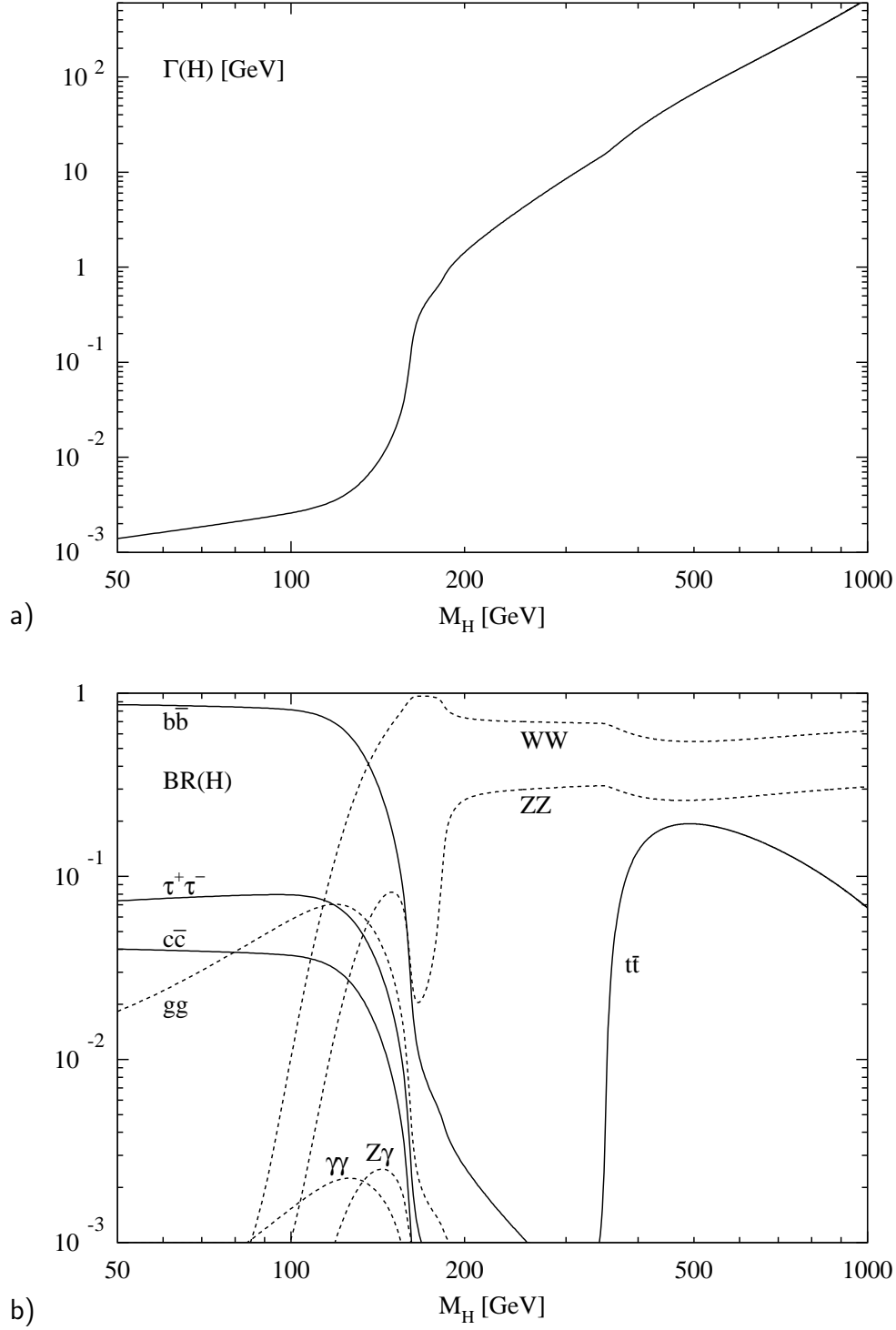
a)

b)

Figure E.2: The total decay width (a)) and the branching ratios (b)) of the standard model Higgs boson in dependence of its mass. The quantities are obtained with the program HDECAY including higher order QCD corrections.

Bibliography

[Abb98]   D. Abbaneo *et al.*, *Studies of Quantum Chromodynamics with the ALEPH detector,* Phys. Rep. 294, 1 (1998).

[Abb00]   D. Abbaneo *et al.*, *A Combination of Preliminary Electroweak Measurements and Constraints on the Standard Model,* CERN-EP-2000-016, CERN 2000.

[Abd99]   S. Abdullin, A. Khanov, N. Stepanov, *CMSJET,* CMS Technical Note, CMS TN/94-180, 1999.

[Abe99]   K. Abe *et al.*, *Measurement of the b Quark Fragmentation Function in Z^0 decays,* SLAC PUB 8153, Stanford 1999.

[Adl99]   C. Adloff *et al.*, Measurement of internal jet structure in dijet production in deep-inelastic scattering at HERA, *Nucl. Phys.* **B543**, (1999) 3.

[Aff00]   T. Affolder *et al.*, *Measurement of the Helicity of W Bosons in Top Quark Decays, Phys. Rev. Lett.* **84**, (2000) 216.

[Alt00]   G. Altarelli, M. L. Mangano *et al.*, *Proceedings of the Workshop on Standard Model Physics (and more) at the LHC,* CERN 2000-004, CERN 2000.

[Alv97]   G. Alverson, L. Taylor, *The CMSCAN Program,* CMS software group, Boston 1997.

[And86]   B. Andersson, G. Gustafson, B. Söderberg, *A probability measure on parton and string states, Nucl. Phys.* **B264** (1986) 29.

[ATL99]   ATLAS Collaboration, *Detector and Physical Performance Technical Design Report,* CERN/LHCC 99-15, ATLAS TDR 15, CERN 1999.

[Ber92]   C. Berger, *Teilchenphysik,* Springer-Verlag, Berlin 1992.

[Ber98a] W. Bernreuther, M. Flesch, P. Haberl, *Signatures of Higgs Boson in the Top Quark Decay Channel at Hadron Colliders, Phys. Rev.* **D58**, (1998) 114031.

[Ber98b] W. Bernreuther, A. Brandenburg, M. Flesch, *Effects of Higgs sector CP violation in top-quark pair production at the LHC,* hep-ph/9812387, CERN-TH-98-390, CERN 1998.

[Bro93]   E. Brouzet, K. Schindl, *The LHC Proton Injector Chain,* CERN/PS 93-39 (DI), CERN/SL 93-37 (AP), CERN 1993.

[Cat93]   S. Catani, *The $k_\perp$-algorithm for Jet Production and Fragmentation,* CERN-TH 6895, Geneva 1993.

[CDF92]   CDF Collaboration, *The topology of three jet events in $p\bar{p}$ collisions at $\sqrt{s} = 1.8\,TeV,$ Phys. Rev.* **D45**, (1992) 1448.

[CDF95]   CDF Collaboration, *Observation of Top Quark Production in $\bar{p}p$ Collisions,* Report No. FERMILAB-PUB-95/022-E, hep-ex/9503002, Fermilab 1995.

[Cho99]   S. Choi, *Spin Correlation in $t\bar{t}$ Production from $p\bar{p}$ Collisions at $\sqrt{s} = 1.8\,TeV,$* D∅ PhD thesis, Seoul 1999.

[Cla00]   R. Clare, *LEP Results on Electroweak and Heavy Quark Physics,* Talk given at the SLAC Summer Institute 2000, Stanford 2000.

[CMS94]   CMS Collaboration, *The Compact Muon Solenoid,* Technical Proposal, CERN/LHCC 94-38, LHCC/P1, CERN 1994.

[CMS97a]   CMS Collaboration, *The Magnet Project,* Technical Design Report, CERN/LHCC 97-10, CMS TDR 1, CERN 1997.

[CMS97b]   CMS Collaboration, *The Electromagnetic Calorimeter Project,* Technical Design Report, CERN/LHCC 97-33, CMS TDR 4, CERN 1997.

[CMS97c]   CMS Collaboration, *The Hadron Calorimeter Project,* Technical Design Report, CERN/LHCC 97-31, CMS TDR 2, CERN 1997.

[CMS97d]   CMS Collaboration, *The Muon Project,* Technical Design Report, CERN/LHCC 97-32, CMS TDR 3, CERN 1997.

[CMS98]   CMS Collaboration, *The Tracker Project,* Technical Design Report, CERN/LHCC 98-6, CMS TDR 5, CERN 1998.

[CMS99]   CMS/TOTEM, *Workshop on CMS/TOTEM Integration and the Luminosity Measurement at CMS,* Workshop, CERN Meeting 1999-100, CERN 1999.

[CMS00a]   CMS Collaboration, *Addendum to the CMS Tracker TDR,* CMS/2000-006 Document, CERN/LHCC 2000-016, CMS TDR 5 Addendum 1, CERN 2000.

[CMS00b]   CMS Collaboration, *The Trigger and Data Acquisition project, Volume I, The Level-1 Trigger,* Technical Design Report Volume 1: The Trigger Systems, CERN/LHCC 2000-038, CMS TDR 6.1, CERN 2000.

[ORC00]   CMS software group, *ORCA 4.4.0-User Guide,* CERN, Geneva 2000.

BIBLIOGRAPHY

[Cor99]   G. Corcella *et al. HERWIG 6.1,* hep-ph/9912396, 1999.

[Cza91]   A. Czarnecki, M. Jezabek, J.H. Kühn, *Lepton Spectra from Decays of polarized Top Quarks, Nucl. Phys.* **B351**, 70 (1991).

[Das98]   S. Dasu, W. Badgett, M. Jaworski, J. Lackey, W.H. Smith, *CMS Level-1 Calorimeter Trigger Detailed Simulation,* CMS Note, CMS NOTE 1998/027, CERN 1998.

[Daw96]   S. Dawson, A. Djouadi, M. Spira, *QCD corrections to SUSY Higgs production: The Role of squark loops, Phys. Rev. Lett.* **77**, 16 (1996).

[Djo97]   A. Djouadi, J. Kalinowski, M. Spira, *HDECAY: a Program for Higgs Boson Decays in the Standard Model and its Supersymmetric Extension,* DESY 97-079, hep-ph/9704448, Hamburg 1997.

[Don96]   J. F. Donoghue, E. Golowich, B. R. Holstein, *Dynamics of the Standard Model,* Cambridge University Press, 1996.

[Dro00]   V. Drollinger, V. Karimäki, S. Lehti, N. Stepanov, A. Khanov, *Upgrade of Fast Tracker Response Simulation, the FATSIM utility,* CMS Internal Note, CMS IN 2000/034, 2000.

[Ell96]   R. K. Ellis, W. J. Stirling, B. R. Webber, *QCD and Collider Physics,* Cambridge University Press, Cambridge 1996.

[Fie91]   R. D. Field, R. P. Feynman, *Quark elastic scattering as a source of high-transverse-momentum-mesons, Rev. Mod. Phys.* **63** (1991) 615.

[Fis99]   M. Fischer, S. Groote, J. G. Körner, M. C. Mauser, B. Lampe, *Polarized top decay into polarized W: t(pol.) –> W(pol.) + b at O(alpha(s)), Phys. Lett.* **B451**, 406 (1999)

[Fle98]   M. Flesch, *Top-Quark-Spineffekte in Hochenergiereaktionen,* RWTH PhD Thesis, Aachen 1998.

[Fol00]   G. Folger, S. Giani, *Introduction to GEANT4,*
http://wwwinfo.cern.ch/asd/geant4, CERN 2000.

[Goo94]   M. Goossens *et al., GEANT, Detector Description and Simulation Tool,* GEANT user's guide CERN, Geneva 1994.

[Gro00]   D. E. Groom *et al., Review of particle physics,* The European Physical Journal C, volume 15, number 1-4, 2000.

[Hal00]   R. Hall, *Top Quark Studies and Searches for New Phenomena at the Tevatron,* talk given at the SLAC Summer Institute 2000, Stanford, August 2000.

[Hut90]   J. E. Huth *et al.*, *Research Directions for a Decade, Proceedings of the Summer Study on High Energy Physics,* Snowmass, Colorado 1990.

[Jar90]   G. Jarlskog, D. Rein *Large Hadron Collider Workshop,* Proceedings Vol. I-III, Aachen 1990.

[Kar00]   V. Karimäki *et al.*, *CMS Simulation package CMSIM, User's Guide and Reference Manual,* CMS detector simulation software group, CERN, Geneva 2000.

[Kau01]   R. Kaur, S. B. Beri, J. M. Kohli, *Preliminary study of the top mass determination in the dilepton (e-mu) channel at LHC,* CMS CR Note 2001/002, CERN 2001.

[Kha99]   A. Kharchilava, *Top mass determination in leptonic final states with J/Ψ,* CMS Note 1999/065, CERN 1999.

[Kin97]   R. Kinnunen, A. Nikitenko, *Study of calorimeter calibration with pions from jets in CMS,* CMS Note, CMS NOTE 1997/097, CERN 1997.

[Kle88]   R. Kleiss, W. J. Stirling, *Top quark production at hadron colliders: some useful formulae, Z. Phys.* **C40**, (1988) 419.

[Lai97]   H. L. Lai *et al.*, *Improved Parton Distributions from Global Analysis of Recent Deep Inelastic Scattering and Inclusive Jet Data, Phys. Rev.* **D55**, 1280 (1997), hep-ph/9606399.

[Lef95]   P. Lefèvre, T. Pettersson, *The Large Hadron Collider, Conceptual Design,* CERN/AC 95-05 (LHC), CERN 1995.

[Ler93]   D. Leroy, R. Perin, G. de Rijk, W. Thomi, *Design of a high-field twin aperture superconducting dipole model,* IEEE Trans. Appl. Supercond. **3** (1993) 614.

[Loh90]   E. Lohrmann, *Einführung in die Elementarteilchenphysik,* Teubner Studienbücher, Stuttgart 1990.

[MRS99]   A. D. Martin, R. G. Roberts, W. J. Stirling, R. S. Thorne, *Parton Distributions and the LHC: W and Z Production,* RAL-TR-1999-047, hep-ph/9907231, 1999.

[Per86]   R. Perin, *Magnet R&D for the CERN LHC, Proceedings of the Workshop on Superconducting Magnets and Cryogenics,* Report BNL 52066, Brookhaven 1986.

[Pim90]   M. Pimiä *et al.*, *Compact Muon Solenoid,* in [Jar90] Vol. I (1990) 547.

[Pre94]   W. H. Press, S. A. Teukolsky, W. T. Vetterling, B. P. Flannery, *Numerical Recipes in FORTRAN,* Cambridge University Press, Cambridge 1994.

146

[Puk99]   A. Pukhov *et al.*, *CompHEP: a package for evaluation of Feynman diagrams and integration over multi-particle phase space. User's manual for version 3.3*, Preprint INP-MSU 98-41/542, Moscow 1999.

[Rys00]   M. G. Ryskin, Y. u. M. Shabelski, A. G. Shuvaev, *Heavy Quark Production in Hadron Collisions*, hep-ph/0011111, Lecture given at *XXXIV* PNPI Winter School, St. Petersburg 2000.

[Sch96]   C. R. Schmidt, *Top quark production and decay at next-to-leading order in e+ e- annihilation*, *Phys. Rev.* **D54**, 3250 (1996)

[See00]   C. Seez, *Minimum-bias pileup issues in electron-photon HLT studies*, CMS Internal Note, CMS IN 2000/001, CERN 2000.

[Sey94]   M. H. Seymour, *Searches for new particles using cone and cluster jet algorithms: a comparative study*, *Z. Phys.* **C62**, (1994) 127.

[Sey97]   M. H. Seymour, *Jet Phenomenology, Proceedings of Les Rencontres de la Valleé d'Aoste: Results and Perspectives in Particle Physics*, La Thuile 1997.

[Sim99a] V. Šimák, P. Homola, J. Valenta, R. Leitner, *Reconstruction of Top-Antitop System from 2 Leptons and 2 Jets Final States in Experiment ATLAS*, ATL-COM-PHYS-99-073, Geneva 1999.

[Sim99b] E. H. Simmons, *Top theories*, Proceedings of Heavy Flavours 8, Southampton 1999.

[Sjo94]   T. Sjöstrand *et al.*, *PYTHIA 5.7*, Comput. Phys. Commun. **82**, (1994) 74.

[Sjo00]   T. Sjöstrand *et al.*, *PYTHIA 6.1*, Description available at `http://www.thep.lu.se/ torbjorn/pythia/pythia6152.update`, August 2000.

[Sla01]   S. R. Slabospitsky, L. Sonnenschein, *TopRex 3.0 - a special generator for the production of top quarks and related processes in hadron collisions*, in preparation.

[Son01]   L. Sonnenschein, *Top Quark Physics at the LHC*, Talk given at the Spin 2000 Symposium Osaka, to be published in the Proceedings, Osaka 2000.

[Spi97]   M. Spira, P. M. Zerwas, *Electroweak Symmetry Breaking and Higgs Physics*, CERN-TH/97-379, Genf 1997.

[Tol98]   K. Tollefson, *Top Quark Production and Decay Measurements from CDF*, FERMILAB-CONF-98-389-E, Proceedings of the ICHEP 98, Vancouver 1998.

[UA183a] UA1 Collaboration, *Experimental Observation of Isolated Large Transverse Energy Electrons with Associated Missing Energy at* $\sqrt{s} = 540\,GeV$, *Phys. Lett.* **122B**, (1983) 103.

[UA283a] UA2 Collaboration, *Observation of Single Isolated Electrons of High Transverse Momentum in Events with Missing Transverse Energy at the CERN* $\hat{p}p$ *Collider, Phys. Lett.* **122B**, (1983) 476.

[UA183b] UA1 Collaboration, *Experimental Observation of Lepton Pairs of Invariant Mass around 95 GeV at the CERN SPS Collider, Phys. Lett.* **126B**, (1983) 398.

[UA283b] UA2 Collaboration, *Evidence for* $Z^0 \rightarrow e^+e^-$ *at the CERN* $\bar{p}p$ *Collider, Phys. Lett.* **129B**, (1983) 130.

[Web84] B. R. Webber, *A QCD model for jet fragmentation including soft gluon interference, Nucl. Phys.* **B238** (1984) 492.

[Wel00] T. Welters, *Bestimmung der Top-Quark-Masse aus dem Zerfallskanal* $pp \rightarrow t\bar{t} \rightarrow b\bar{b}W^+W^- \rightarrow 6$ *Jets am zukünftigen LHC Speicherring auf der Grundlage von Simulationen des CMS-Detektors,* RWTH Diploma Thesis, Aachen 2000.

Curriculum vitae

General Data

Born	31.07.1968 in Wuppertal, Germany
Nationality	German
Marital status	Married

Chronological career

Primary school	August 1974 - June 1978 in Dieringhausen
Secondary school	August 1978 - July 1984 in Wiehl-Bielstein
Vocational training	03.09.1984 - 17.07.1986 Electrician at L. & C. Steinmüller GmbH
	01.08.1986 - 31.01.1988 Electronician at C. & W. Berges GmbH & Co KG
Vocational practice	01.02.1988 - 30.06.1988 as electronician at Rainer Raymund Electrical and Industrial Installations
Grammar school emphasizing science and engineering	August 1988 - June 1991 in Gummersbach
Military service	01.07.1991 - 30.06.1992 as broadcast soldier at the radio and broadcast battalion Koblenz
Vocational practice	0.1.07.1991 - 30.09.1992 as electronician at PE-S Personal-Service GmbH
University	October 1992 - September 1994, RWTH Aachen Basic study
	October 1994 - September 1995, ULB Bruxelles Main study
	October 1995 - September 1996, RWTH Aachen Elementary particle physics and astronomy
	October 1996 - March 1998, DESY Hamburg Practical training and diploma thesis at the H1 experiment (for the RWTH Aachen, institute III B)
	May 1998 - spring 2001, CERN Geneva PhD thesis at the CMS experiment (for the RWTH Aachen, institute III B)

<u>Other education</u>

September 1984 - December 1996, Adult evening classes Gummersbach
Electronic certificate

February 1986, Professional association
Industrial safety seminar

October 1991 - December 1991, Chamber of handicrafts Koblenz
Technical higher mathematics

February 1992 - April 1992, Institute of data processing Koblenz
C programming language

August 1993, Université de Caen
French language course

October 1994 - July 1995, E.P.F.C. Bruxelles
French language course

July 1995 - August 1995, ULB Bruxelles
French language course

September 1997, Monschau
Belgian-Dutch-German school of elementary particle physics

August 2000, Stanford
SLAC Summer Institute

October 2000, Osaka
Spin 2000 Symposium

Acknowledgements

During my studies for the CMS experiment I appreciated very much the open and harmonic atmosphere of the collaboration and my home institute in Aachen. Unconfined support came from experimental physicists as well as from theorists within and outside of the collaboration whenever necessary. Here I wish to thank all of them. Furthermore I want to emphasise my special thank to the following persons:

First, I would like to thank my advisor Prof. G. Flügge, who gave me an opportunity and support to this exciting work. Without him this work would not have come off.

Great thanks to W. Bernreuther and S. Slabospitsky for providing matrix elements and prolific discussions about theoretical and technical issues. They facilitated the progress of the work considerably.

A. Nikitenko and N. Stepanov were always around to elucidate physical and technical questions. Thank you for this great cooperativeness.

Many thanks to D. Denegri for his support and exhaustive discussions in which he participated with diligence.

As well thanks to M. L. Mangano for gainful discussions and hints. He was always ready to offer support and to give useful suggestions.

Special thanks to S. Abdullin, R. Adolphi, V. Drollinger, A. Kharchilava, K. Rabbertz, R. Schulte, B. Schwering and T. Wengler for their support and helpful discussions.

Last but not least, acknowledgements to my family for their patience.